博士論文

High-Precision Measurements of the Fundamental Properties of the Antiproton

（反陽子の基礎物理量の高精度測定）

長濱　弘季

Abstract

In this thesis, high-precision measurements of the fundamental properties of the antiproton are presented, such as the direct measurement of the lifetime, the charge-to-mass ratio, and the magnetic moment. As a consequence, they provide stringent tests of CPT symmetry, which is one of the most fundamental symmetries in the Standard Model of particle physics.

Contents

List of Figures vii

List of Tables xi

I Introduction 1

1 Background 3

1.1 Personal contributions and overall structure of this thesis 5
1.2 CPT invariance 7
1.3 Standard Model Extension 8
1.4 Measuring the fundamental properties with Penning traps 9
  1.4.1 Charge-to-mass ratio 9
  1.4.2 g-factor 9

II Theoretical Basics 11

2 Penning trap 13

2.1 Particle motions in a Penning trap 13
2.2 Cylindrical Penning trap 16

3 Non-destructive detection of the eigenfrequencies 21

3.1 Principle of the detection system 21
3.2 Equation of the particle motion 25
3.3 Optimisation of the dip detection 29

3.4 Sideband coupling technique 32
3.5 Active feedback cooling 35

4 Non-destructive detection of the spin-state 37
4.1 Continuous Stern-Gerlach effect 37
4.2 Larmor resonance line-shape in the magnetic bottle 40
4.3 Spin-transition rates 41
4.4 Double trap method 42

III Experimental Setup 45

5 BASE experiment 47
5.1 Antiproton decelerator and antiproton transfer line 47
5.2 BASE apparatus 49
5.3 Superconducting magnet 50
5.4 Cryo-mechanical setup 51
5.5 Degrader system 53
5.6 Penning-trap system 56
  5.6.1 Precision trap (PT) and analysis trap (AT) 57
  5.6.2 Reservoir trap (RT) 58
  5.6.3 Cooling trap (CT) 58
5.7 Electron gun 58
5.8 Trap assembly 59
5.9 DC and RF wiring 59
  5.9.1 DC biasing for the Penning-trap electrodes 61
  5.9.2 Excitation lines 64
  5.9.3 Pinbase 65
  5.9.4 RF switch 65
  5.9.5 Feedback lines 65
  5.9.6 Spin-flip lines 65
  5.9.7 High voltage lines for capturing antiprotons 66
  5.9.8 DC biasing for the cryogenic amplifiers 66

6 **Single-particle detection systems** **67**
- 6.1 Axial detectors 67
  - 6.1.1 Superconducting axial resonators 68
  - 6.1.2 Axial amplifiers 71
  - 6.1.3 Implementation of the axial detectors to the BASE apparatus 76
- 6.2 Cyclotron detector for the precision trap 78
- 6.3 Q-tuner 81

IV Experimental Results **85**

7 **Reservoir trap for antiprotons** **87**
- 7.1 Catching and cooling of antiprotons 87
- 7.2 Cleaning procedure 90
- 7.3 Potential tweezer scheme 92

8 **Comparison of the antiproton-to-proton charge-to-mass ratio** **97**
- 8.1 Principle of the measurement 97
- 8.2 Preparation procedure 98
- 8.3 Measurement procedure 99

9 **Single antiproton in the analysis trap** **105**
- 9.1 Overview 105
- 9.2 Characterisation of the analysis trap 105
  - 9.2.1 Adiabatic shuttling of a single antiproton from the RT to the AT . . . 107
  - 9.2.2 Acceptance of the ring voltage and the tuning ratio 107
  - 9.2.3 Parametric excitation of the axial motion 108
  - 9.2.4 Direct measurement of the magnetic bottle 113

10 **Axial frequency stability in the magnetic bottle** **119**
- 10.1 Electron kickout scheme 120
- 10.2 Optimisation of the ground structure 121
- 10.3 Characterisation of the axial frequency stability 123
  - 10.3.1 Definition of the axial frequency fluctuation 123
  - 10.3.2 Allan deviation 125

10.4 Temperature measurements of the radial motions 129
  10.4.1 Temperature of the modified cyclotron mode 129
  10.4.2 Temperature of the magnetron mode 131

11 Measurement of the magnetic moment of the antiproton **133**
11.1 Principle of frequency measurements in the magnetic bottle 134
11.2 Line-shape study 136
11.3 Procedure of the g-factor measurement 137
11.4 Line-shape modifications 139
11.5 Drift effect studies 140
  11.5.1 External magnetic field drifts 140
  11.5.2 Voltage stability 141
  11.5.3 Cyclotron random walk 141
  11.5.4 Magnetron random walk 142
11.6 Larmor frequency ν_L measurement 143
11.7 Larmor frequency ν_L evaluation 146
11.8 Modified cyclotron frequency ν_+ measurement 148
11.9 Modified cyclotron frequency ν_+ evaluation 149
11.10 Final result 151
11.11 Application of the Standard Model Extension 152

12 Conclusion and Outlook **157**

Acknowledgements **159**

References **163**

List of Figures

1.1 Summary of high-precision tests of the fundamental charge, parity, time invariance of the Standard Model. 7

2.1 Electric/magnetic field configuration of a hyperbolic Penning trap. 14
2.2 Example of a quadrupolar voltage potential. 14
2.3 Schematic of the particle's eigenmotions in a Penning trap. 16
2.4 Schematic of a cylindrical Penning trap. 17
2.5 Orthogonality and compensation of a Penning trap. 19

3.1 Schematic of the image-current detection 22
3.2 Equivalent circuit of the trapped particle with the detection system. 26
3.3 Total impedance of the detection system together with a trapped particle. . . . 27
3.4 Example of a dip spectrum in the precision trap. 28
3.5 Equivalent circuit of the entire system, without a trapped particle. 29
3.6 Conversions of series to parellel RC and RLC circuit. 30
3.7 Conversions of an equivalent circuit of the entire system. 31
3.8 Schematic of a active feedback loop to manipulate the effective temperature as well as the Q-value of the detection system. 35

4.1 Schematic of the continuous Stern-Gerlach effect. 38
4.2 Simulated result of the magnetic bottle. 39
4.3 Procedure of the double trap method. 43

5.1 Top view drawing of the BASE experimental zone and the AD facility. 47
5.2 Schematic of the BASE beamline. 48

5.3 Overview of the BASE apparatus. 49
5.4 Magnetic field of the superconducting magnet measured with the co-magnetometer particle. 50
5.5 LN_2 and LHe stages of the BASE apparatus. 51
5.6 (a) Placement of the degrader foils at the upstream-side of the Penning-trap chamber. (b) Calculation of the structure generated by the copper mesh assembly. 54
5.7 Catching probability of 5.3 MeV antiprotons as function of the thickness of the aluminium degrader calculated with SRIM. 55
5.8 Schematic of the BASE Penning-trap assembly. 56
5.9 Entire assembly of the experiment. 59
5.10 Schematic of the electronics diagram 60
5.11 Configuration of the Penning-trap electrodes. 61
5.12 Continuous voltage measurement of UM 1-14 (*Stefan Stahl Electronics*), when it is operated in ultra-high precision mode. 62
5.13 Allan deviation of the voltage/frequency fluctuation, based on continuous voltage measurements of UM 1-14 for 10 hours. 63
5.14 Schematic of the filters at the pinbase 64
5.15 Schematic of the spinflip line 66

6.1 Schematic of the superconducting resonator 68
6.2 Schematic of the electronics chamber. 68
6.3 Schematic of the setup for measuring the properties of the unloaded resonators 69
6.4 Schematic of the axial amplifier 72
6.5 Schematic of the setup for characterising the amplifier 74
6.6 Result of the gain and noise of the amplifier 75
6.7 Detailed layout of the detection system 76
6.8 Spectrum of the RT detector 77
6.9 Schematic of the cyclotron detector 78
6.10 Schematic of the cyclotron amplifier 79
6.11 Resonance spectra of the cyclotron detector while tuning the varactor. 80
6.12 Schematic of the Q-tuner 82
6.13 (a) Dip with Q-tuner on and off. (b) Dip linewidth as a function of dissipated power 82
6.14 Characterisation of the axial frequency for different dip widths 83

7.1 Schematic of capturing antiproton in the reservoir trap. 88
7.2 Annihilation signal of antiprotons on the beam monitor. 89
7.3 (a) Scintillation signal of antiprotons due to the AD ejection. (b) Scintillation signal of 3000 antiprotons extracted from the reservoir. 89
7.4 FFT spectra taken during the antiproton preparation procedure. 91
7.5 z-axis potentials used for particle extraction from the reservoir trap. 93
7.6 (a) Results of the application of the potential tweezer scheme. (b) Dip-width as a function of extracted particles 95

8.1 Schematic of the charge-to-mass ratio measurement 98
8.2 (a) Detailed procedure of the charge-to-mass ratio measurement. (b) Potential configuration for antiproton cyclotron frequency measurement. (c) Potential configuration for H^- cyclotron frequency measurement 100
8.3 (a) All measured antiproton-to-H^- cyclotron frequency ratios as a function of time. (b) Measured ratios projected to a histogram. (c) Allan deviation of the measured ratios 102

9.1 Required precision to observe a particle signal. 108
9.2 Simulation on the parametrically excited axial motion 111
9.3 Measurement result of the parametric resonance scheme 112
9.4 Spectra of a peak signal of the parametrically excited particle and a dip after the drive is turned off 113
9.5 (a) Signal-to-noise ratio of the dip as a function of the tuning ratio. (b) Dip spectrum when the optimum tuning ratio and the ring voltage is applied. . . . 114
9.6 Orthogonality characterisation of the analysis trap 115
9.7 Experimental setup for the magnetic bottle measurement 115
9.8 Axial frequency fluctuation caused by external rf drives in the magnetic bottle 116
9.9 Direct measurement of the magnetic field in the AT 117

10.1 Schematic of the electron kickout 120
10.2 Comparison of the axial frequency stability between before improving the ground of the apparatus and after the action. 121
10.3 Monitoring the noise level on the resonance frequency of the cyclotron detector, while performing grounding actions. 122
10.4 Power cable distribution of the electric instruments 124

10.5 Comparison of the Allan and Standard variance by using H_{SV} and H_{AV} 127
10.6 (a) Simulation of the Allan deviation $\sigma_y(\tau)$ when a certain amount of white noise and the random walk are present. (b) Axial frequency stability characterised by using the Allan deviation $\sigma_y(t)$ 128
10.7 (a) Histogram of the energy distribution of the modified cyclotron mode. (b) Axial frequency distribution due to different cyclotron energies as a function of a number of measurements 130
10.8 Histogram of the magnetron energy measured in the AT by using sideband drives 132

11.1 Schematic of frequency measurements in the analysis trap (AT). 134
11.2 Examples of a measured cyclotron resonance and a Larmor resonance. 136
11.3 Schematic of the Penning-trap system used for the g-factor measurement of the antiproton 138
11.4 Measurement sequence of the g-factor. 139
11.5 Axial frequency fluctuation Ξ_z for different averaging times and different cyclotron energies E_+. 142
11.6 Schematic of the Larmor frequency measurement. 143
11.7 First observation of spinflips of a single trapped antiproton in BASE 145
11.8 Power characterisation of spin-flip drive. 145
11.9 Cumulative plot of frequency fluctuations for different spin-flip drive frequencies. 146
11.10 (a) 95 % confidence level of the distribution $\langle\nu_{\mathrm{L}}\rangle - \nu_{\mathrm{L,e}}$ as a function of the magnetron heating rate. (b) Distribution $\langle\nu_{\mathrm{L}}\rangle - \nu_{\mathrm{L,e}}$ for the magnetron heating rates which are observed in this experiment. 147
11.11 Measurement of the modified cyclotron frequency. 148
11.12 (a) Simulated walk of the cyclotron frequency. (b) Projection of the simulated result to frequency fluctuation $\Xi_z(\nu_{\mathrm{rf}})$. 150
11.13 Results of the six g-factor measurements 151
11.14 Standard Sun-centred inertial reference frame 153

List of Tables

1.1 Sensitivity of different CPT tests with respect to CPT violation in the framework of the Standard Model Extension. 8

5.1 Probability p of a particle to hit the massive part of N out of the six copper meshes of the mesh degrader. 55
5.2 Geometry parameters and magnetic field gradients of the four Penning traps in the BASE apparatus. 57

6.1 Geometry of the resonators 67
6.2 Summary of the characterisation measurements of the unloaded resonators. . . 70
6.3 Typical optimum biasing voltages for the amplifier 75
6.4 Gain and noise of the axial amplifiers at 4 K. 75
6.5 Input characteristics of the axial amplifiers at 1 MΩ. 76
6.6 Summary of the characterisation measurements of the axial detectors 78
6.7 Summary of the cyclotron detector parameters. 81

11.1 Summarises all measured modified cyclotron and Larmor frequencies. 152
11.2 Derived constraints on the Standard Model Extension parameters by the g-factor measurement. 155

Part I

Introduction

Chapter 1

Background

The current understanding of the Universe comes mainly from the fields of particle physics and cosmology. In particle physics, an almost perfect symmetry between matter and antimatter exists. On cosmological scales, however, a striking imbalance between matter and antimatter is observed [1]. This contradiction between the fields of particle physics and cosmology demands experiments to compare the fundamental properties of particles and antiparticles with high precision. Such comparisons provide stringent tests of charge, parity, and time (CPT) symmetry; - one of the most fundamental symmetries in the Standard Model of particle physics [2].

Despite its importance to our understanding of nature, only a few direct and precise tests of CPT symmetry are available [3–10] or are planned [11, 12]. Our experimental collaboration group, the Baryon Antibaryon Symmetry Experiment (BASE), aims to carry out such tests by comparing the fundamental properties of protons and antiprotons with high precision [13]. To realise this, BASE constructed a new experimental apparatus at the antiproton decelerator (AD) facility of the European Organisation for Nuclear Research (CERN), Geneva, Switzerland in 2013. The AD facility is the only place in the world which provides low energy antiprotons for physics experiments, and consequently allows physicists to capture, and even store antiprotons at rest. BASE utilises an advanced Penning-trap system formed of four Penning traps. One of these traps allows us to accumulate injected antiprotons in a reservoir for more than a year. Single antiprotons can be separated from the reservoir and adiabatically transported between the traps [14], and the physical properties of the particles can be measured by using highly sensitive superconducting detection systems [15].

Experiments with single particles in Penning traps allow high-precision measurements of particle properties and give access to stringent tests of fundamental symmetries [16]. Measurements in this field largely rely on the non-destructive detection of the trapped particle's eigenfrequencies [15]. For instance, the most precise measurements of atomic masses are based on Penning-trap experiments [17]. These measurements impact significantly on neutrino physics [17, 18], as well as on rigorous tests of relativistic energy-mass equivalence [19]. Electron g-factor measurements provide the most stringent tests of bound-state quantum electrodynamics [20]. The most precise value of the mass of the electron in atomic mass units has been extracted from a g-factor measurement of the electron bound to a highly-charged carbon ion [21]. Other Penning-trap based measurements provide the most stringent tests of the fundamental CPT symmetry. Electron and positron magnetic anomaly frequencies were compared with fractional precisions at a level of parts per billion (p.p.b.) [3], and the fundamental properties of protons and antiprotons, such as charge-to-mass ratios [6] and g-factors [22] were compared with 90 parts per trillion (p.p.t.) and 4.4 parts per million (p.p.m.) precision, respectively. Recently, BASE reported the most precise comparison of the proton-to-antiproton charge-to-mass ratio with a fractional precision of 69 p.p.t. [23], and the most precise measurement of the magnetic moment of the proton with a relative precision of 3.3 p.p.b. [24]. Additionally, the most precise measurement of the antiproton's magnetic moment was performed in early spring 2016 by BASE and its result will be published in January 2017 [25]. This specific measurement is the main subject of this thesis.

BASE's experiments form a part of the long history of enquiry and experiments to examine the magnetic moment of the proton and the antiproton. The first measurement of the proton magnetic moment was performed by Stern in the early 1930's, using the molecular beam techniques [26, 27]. This led to the discovery of the proton's g-factor unequal to 2, which implied the substructure of the proton. Due to this discovery, Stern was awarded the Nobel Prize in 1943. Further developments with molecular beams by Rabi improved the precision [28]. In the following decade, Purcell and Bloch developed nuclear magnetic resonance techniques [29,30], which led to a further improvement in the measurement precision of the magnetic moment of the proton. Afterwards, further progress in these precision measurements was made by Ramsey and Kleppner, determined from hyperfine spectroscopy of atomic hydrogen [31, 32]. In 1972, Kleppner improved the hydrogen maser technique and obtained the proton to electron magnetic moment ratio with a fractional precision of 10 p.p.b. [33], which was the highest precision measurement attained for over 40 years [34]. However, progress towards direct measurements of the proton magnetic moment has recently been achieved. The BASE companion experiment at the University of Mainz demonstrated the application of the double Penning-trap technique [35], and measured the proton magnetic moment with the highest precision to date [24].

Compared to the proton, there have only been a few attempts to measure the magnetic moment of the antiproton. The measurement of the antiproton's magnetic moment was carried out in 1988 from a spectroscopy of $n = 11 \rightarrow 10$ antiprotonic X-ray transition in ^{208}Pb [36], and in 2009 using super-hyperfine spectroscopy of antiprotonic helium atoms (3000 p.p.m.) [37]. In 2013, a new value was determined by the ATRAP collaboration using the first single-antiproton measurement with a cryogenic Penning trap (4.4 p.p.m.) [22]. As mentioned above, BASE improved the precision of these measurements to the sub-p.p.m. level in early spring 2016, which is the most precise value of the magnetic moment of the antiproton yet measured [25] (it is also the main result within my PhD studies). However, it is known that the magnetic moments can be determined in Penning traps with much higher precision using the double trap technique as was demonstrated by using a single trapped proton [24]. However, the implementation of this method is an extremely challenging task, since it affords complicated interplay and shuttling between two highly optimised Penning traps with very different properties. BASE is currently working on the implementation of this double trap method. Logically the double trap technique requires optimisation of the individual traps, leading automatically to single trap magnetic moment measurements. The implementation of these single trap methods, and a resulting sixfold improved measurement of the magnetic moment of the antiproton in the so-called analysis trap, is described within this thesis.

1.1 Personal contributions and overall structure of this thesis

I started working officially in BASE in February 2013, as one of the groups's initial members (alongside the team's other initial members: Dr Stefan Ulmer, Dr Christian Smorra, Mr Kurt Alan Franke, and Mr Georg Ludwig Schneider). As an initial member of BASE I was fortunate to participate across the broad spectrum of the project from the construction of the experimental apparatus to the operation of the experiment itself. On the technical side, I mainly contributed to the development of single particle detection systems, low noise electronics and the wirings of the entire apparatus. During the course of my PhD studies and work within BASE, we developed a novel antiproton reservoir trap technique [14]. This allowed us to accumulate antiprotons and transport single particles non-destructively to other traps within the trap system whenever needed. By implementing this new technique, it became possible to conduct measurements even when the accelerators were shutdown. High-precision measurements are usually very sensitive to noise and the antiproton decelerator generates electronic and magnetic field noise making it far, preferable to operate the measurements during the shutdown period. In addition, BASE compared antiproton-to-proton charge-to-mass ratio with higher precision than ever achieved before, and reported these results in 2015 [23]. In this experiment, we measured the cyclotron frequencies of a single trapped antiproton and an H^- ion using a newly developed fast shuttling method and sideband coupling. To date, this is the most stringent test of CPT invariance in the baryon sector. In the process of achieving these results, I contributed within BASE as a technical and experimental collaborator. I developed the axial detection system to monitor antiprotons in the reservoir trap as well as to measure the cyclotron frequencies of a trapped antiproton and an H^- ion. Participations in beamshifts, data-collection processes, and maintenance of the apparatus were other key parts of my role.

My main contribution to the experiment during the framework of my PhD studies was the measurement of the magnetic moment of the antiproton in the analysis trap (AT), where a strong inhomogeneous magnetic field was superimposed. I contributed by observing single proton and antiproton signals in the AT, detecting spin-transitions by means of the continuous Stern-Gerlach effect [38], and measuring its magnetic moment. The resultant fractional precision achieved is 0.8 p.p.m., which is a factor of six improvement compared to the previous result [22]. A manuscript which details this achievement has recently been accepted by the *Nature Communications* journal and is published in January 2017.

Having quoted my personal contribution to BASE, I would like to clearly emphasise that all these results are based on excellent teamwork of a group of eight people, each person working on the experiment with great dedication.

The overall structure of this thesis is as follows. It consists of four parts, such as I. Introduction, II. Theoretical Basics, III. Experimental Setup, and IV. Experimental Results. I. Introduction continues with a short description on CPT invariance and the Standard Model Extension [39], and ends with the principle of measuring the fundamental properties of the proton and the antiproton using Penning traps. II. Theoretical Basics consists of the principle of the Penning trap, non-destructive detection of the trapped particle's eigenfrequencies, and the spin-state. III. Experimental setup describes each device and the systems which are implemented in the BASE apparatus, including: the wirings, the low noise electronics, and the single particle detection systems. Finally, IV. Experimental Results presents my core achievement during my PhD studies, that is: the reservoir trap technique, comparison of the antiproton-to-proton charge-to-mass ratios, and experiments in the analysis trap.

1.2 CPT invariance

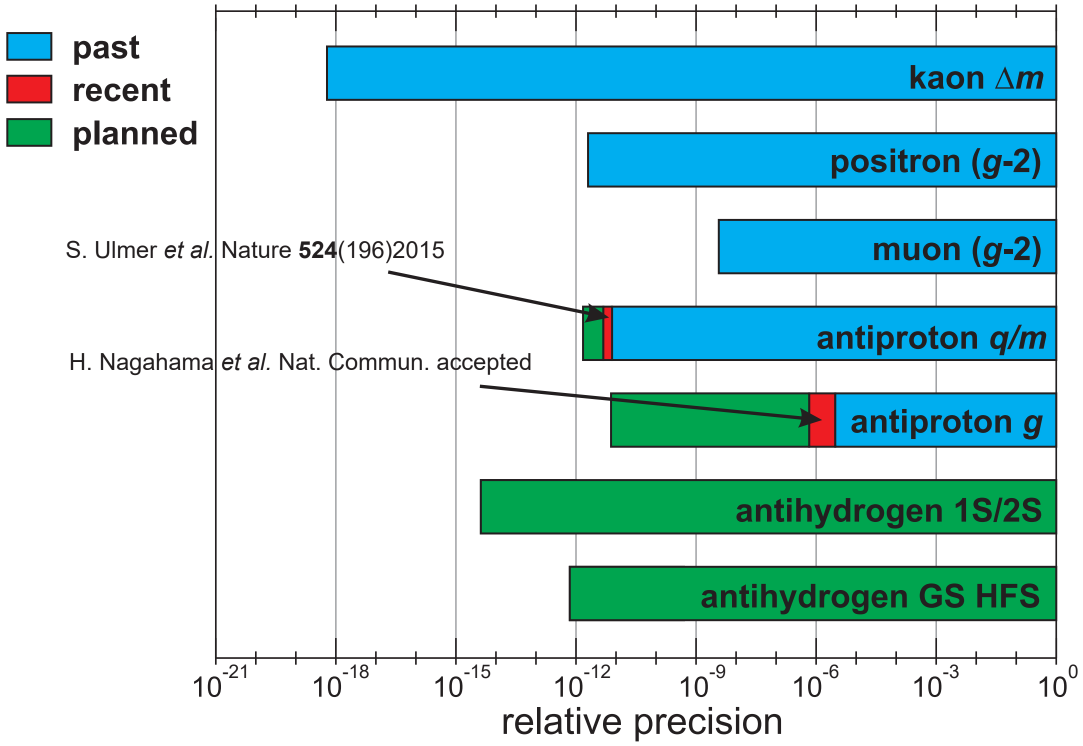

Fig. 1.1: Summary of high-precision tests of the fundamental charge, parity, time invariance of the Standard Model. BASE contributes measurements with single trapped antiprotons and targets measurements of charge-to-mass ratios and g-factors.

The CPT theorem states that any local, Lorentz-invariant quantum field theory is invariant under the combined transformation of CPT [2]. The CPT transformation consists of Charge conjugation (change matter to antimatter, and vice versa), Parity transformation (inverting the signs of spatial coordinate), and Time reversal (inversion of time). CPT symmetry is one of the most fundamental symmetries in the Standard Model of particle physics, which states that the fundamental properties of particles and their antiparticle conjugates, such as charge, mass, lifetime, and magnetic moment must be identical apart from signs. High-precision comparisons of the fundamental properties of particles and their antiparticle conjugates consequently provide stringent tests of CPT symmetry.

Figure 1.1 shows relative precisions achieved for different kinds of CPT tests on different systems performed up to now . The blue, red, and green bars indicate the past, recent, and future planned tests, respectively. According to this graph, up to now the most precise test comes from the comparison of decay channels of the neutral Kaon system, which allows the extraction of the mass difference of the particles with a fractional precision of 10^{-18} [4].

1.3 Standard Model Extension

High-precision measurements of the physical properties offered by experiments with Penning traps are suited to precision studies of fundamental symmetries, such as Lorentz and CPT symmetries. According to [40–42], tiny violations in Lorentz symmetry could unify gravity and quantum physics, and emerging strands of string theory. In the framework of the Standard Model Extension (SME) [9,39,43], investigations concerning possible Lorentz and CPT violations which could arise through experiments with Penning traps have been carried out. Within these studies, perturbation theory has been applied to determine the dominant Lorentz- and CPT-violating shifts in the anomaly and cyclotron frequencies of electrons, positrons, protons, and antiprotons. By utilising resultant precisions achieved by the Penning-trap experiments [22,24,25], it is possible to extract constraints on CPT violating SME coefficients. The application of this methodology is described in section 11.11. Moreover, in the framework of the SME, the sensitivity of different CPT tests is discussed using the measure $r_j = \Delta E/E$, where ΔE is the upper limit for the energy difference between given conjugate matter and antimatter systems and E is the energy-eigenvalue of the full relativistic Hamiltonian describing the system. Table 1.1 shows comparisons of this figure of merit between the Kaon system and single-particle measurements in Penning traps. Although the relative precisions which can be achieved by Penning-trap experiments are lower than that of the Kaon mass comparison, the sensitivity with respect to CPT violation in the SME framework is higher.

Table 1.1: Sensitivity of different CPT tests with respect to CPT violation in the framework of the Standard Model Extension.

measurement	relative precision	sensitivity r_j to CPT violation
kaon Δm [4]	$\sim 10^{-18}$	$\sim 10^{-18}$
electron/positron $g-2$ [3]	$\sim 10^{-12}$	$\sim 10^{-21}$
proton/antiproton g-factor [24,25]	$\sim 10^{-6}$	$\sim 10^{-22}$

1.4 Measuring the fundamental properties using Penning traps

1.4.1 Charge-to-mass ratio

The charge-to-mass ratio q/m of a particle is directly related to the free cyclotron frequency ν_c as

$$\frac{q}{m} = \frac{2\pi\nu_\mathrm{c}}{|\vec{B}_z|}, \tag{1.1}$$

where $|\vec{B}_z|$ is the external magnetic field (more detailed explanation will be given in section 2.1). Since ν_c can be derived by measuring the three eigenfrequencies of a particle trapped in a Penning trap, and subsequently applying the invariance theorem [44]

$$\nu_\mathrm{c} = \sqrt{\nu_+^2 + \nu_-^2 + \nu_z^2}, \tag{1.2}$$

it is experimentally accessible. As will be described in chapter 3, non-destructive measurements of these eigenfrequencies are possible by detecting induced image currents on the Penning-trap electrodes. In this way, a comparison of charge-to-mass ratios of the proton and the antiproton is possible by measuring the free cyclotron frequencies $\nu_{\mathrm{c,p}}$ and $\nu_{\mathrm{c,\bar{p}}}$ at the same magnetic field $\vec{B}$ and by taking the ratio of these two frequencies

$$\frac{\nu_{\bar{\mathrm{p}}}}{\nu_\mathrm{p}} = \frac{(q/m)_{\bar{\mathrm{p}}}}{(q/m)_\mathrm{p}}. \tag{1.3}$$

In 2015, BASE reported the most precise comparison of the antiproton-to-proton charge-to-mass ratios [23]. This result will be presented in chapter 8.

1.4.2 *g*-factor

The *g*-factor is a dimensionless quantity which relates the spin $\vec{S}$ of a particle to its magnetic moment

$$\vec{\mu}_\mathrm{s} = g\frac{q}{2m}\vec{S}. \tag{1.4}$$

The spin energy of a particle E_s in the presence of a magnetic field $\vec{B}_z$ is

$$E_\mathrm{s} = -\vec{\mu}_\mathrm{s} \cdot \vec{B}_z. \tag{1.5}$$

Inserting Eq. 1.4 into Eq. 1.5 and using the spin eigenvalues $\langle s_z \rangle = \pm\hbar/2$, the following equations are obtained

$$\begin{aligned} E_\mathrm{s} &= \pm g\frac{q}{2m}\frac{\hbar}{2}|\vec{B}_z| \qquad (1.6)\\ \Delta E_\mathrm{s} &= g\frac{q\hbar}{2m}|\vec{B}_z|, \qquad (1.7)\end{aligned}$$

where ΔE_s is the energy difference between the two spin-states. This difference can be associated with the precession frequency of the spin in a magnetic field $\vec{B}_z$, which is the so-called Larmor precession frequency

$$\nu_\mathrm{L} = \frac{1}{2\pi} \cdot \frac{g}{2} \cdot \frac{q}{m} |\vec{B}_z|. \tag{1.8}$$

Together with Eq. (1.1), the g-factor can be expressed as the ratio of the Larmor frequency ν_L and the free cyclotron frequency ν_c

$$\frac{g}{2} = \frac{\nu_\mathrm{L}}{\nu_\mathrm{c}}. \tag{1.9}$$

Note that Eq. (1.9) only holds when ν_c and ν_L are measured at a same magnetic field. Since the spin-precession does not induce image currents on the electrodes to allow a direct access, the Larmor frequency ν_L is determined by applying the continuous Stern-Gerlach effect in a Penning trap with a strong magnetic bottle superimposed at the trap centre. This scheme will be described in section 4.

These measurement principles are applied during my PhD studies for comparing the charge-to-mass ratio of the antiproton and the proton (chapter 8), and measuring the g-factor of the antiproton (chapter 11).

Part II

Theoretical Basics

Chapter 2

Penning trap

The fundamental properties of the proton and the antiproton, such as the charge-to-mass ratios and the magnetic moments (g-factor), are directly accessible by measuring the eigenfrequencies of a single trapped particle in a Penning trap. Aiming for measuring these physical quantities with high precision, the BASE experiment uses a cryogenic multi Penning-trap system. The system is enclosed in a chamber which is pinched off before cooling down to 4 K. This ensures a considerably high vacuum conditions inside the chamber $\approx 10^{-18}$ mbar at 4 K, and in this way the trapped particles experience no interactions with contaminants, and reach inherently long storage times. Additionally, superconducting magnets which are used to confine charged particles typically have the magnetic field stability of $dB/(B \cdot dt) \approx 10^{-11}$/month, leading to obtain a high frequency stability of trapped particles. Due to this reason, Penning traps are considered to be one of the most stabilisable tools for confining charged particles and to investigate their properties with high precision.

This chapter focuses on describing particle motions in a Penning trap, the cylindrical Penning traps geometry which is used in BASE, and how we eventually approach to the fundamental properties by using this particular tool.

2.1 Particle motions in a Penning trap

A particle of mass m and charge q in a homogeneous magnetic field $\vec{B}_z$ is constrained to a circular orbit called cyclotron motion. Choosing the z axis to be parallel or antiparallel to the field of the superconducting magnet $\vec{B}_z$, the cyclotron orbit is a rotation obeying the right-hand

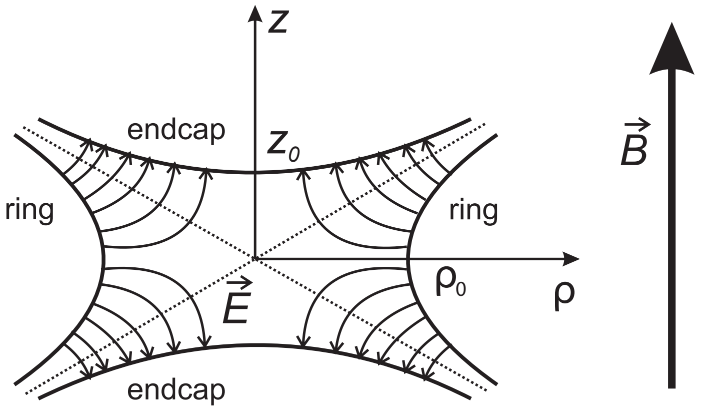

Fig. 2.1: Electric/magnetic field configuration of a hyperbolic Penning trap. The magnetic field confines a particle only in a radial direction ρ. Together with the electrostatic quadrupole potential, it allows to confine a particle also in the axial direction z. In total, three electrodes are required to generate the quadrupole potential. Two end cap electrodes on the top and the bottom, and one ring electrode in the centre.

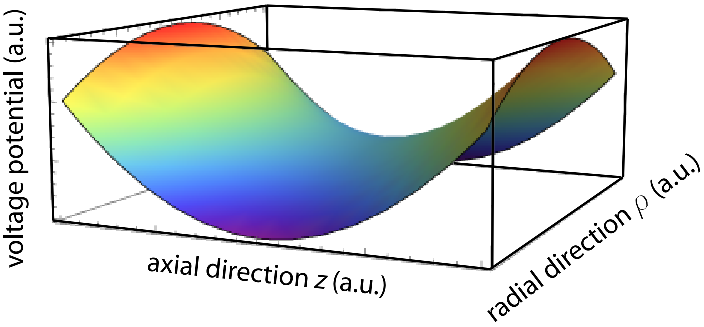

Fig. 2.2: Example of a quadrupolar voltage potential based on Eq. (2.4).

rule, in the radial direction. Its frequency ν_c is given by

$$\nu_\mathrm{c} = \frac{1}{2\pi}\frac{q|\vec{B}_z|}{m}. \tag{2.1}$$

The magnetic field $\vec{B}_z$ provides radial confinement. To prevent the particles to escape along the magnetic field lines, an electrostatic quadrupole potential is superimposed. Field configurations of a hyperbolic Penning trap with the surface reproducing the potential geometry is shown in Fig. 2.1. In practice, cylindrical Penning traps are used for the BASE experiment, and will be described in the next section 2.2. As shown in Fig. 2.1, at least three electrodes are required to generate a quadrupole potential, such as two end cap electrodes with one ring electrode located at the centre. The end cap electrodes and the ring electrode can be expressed as the hyperbola of revolution

$$z^2 = z_0^2 + \frac{\rho^2}{2} \quad \text{and} \tag{2.2}$$

$$z^2 = \frac{\rho^2 - \rho_0^2}{2}, \tag{2.3}$$

respectively. By applying a voltage V_0 to the ring electrode with respect to the end caps in such a geometrical configuration, a quadrupolar voltage potential $\Phi_V(z,\rho)$ is produced as

$$\Phi_V(z,\rho) = V_0 C_2 \left(z^2 - \frac{\rho^2}{2} \right), \tag{2.4}$$

where $\sqrt{C_2}$ a specific coefficient characterising the typical geometrical length scale of the trap (refer to section 2.2). An example of a quadrupole potential based on Eq. (2.4) is shown in Fig. 2.2. This provides stable storage of a charged particle with an axial harmonic oscillation frequency of

$$\nu_z = \frac{1}{2\pi}\sqrt{\frac{2qC_2V_0}{m}}. \tag{2.5}$$

Solving a full equation of particle motions in this field configuration leads to a modification of the cyclotron frequency ν_c [45]. This is caused by the radial field component of the electrostatic potential. The resulting eigenfrequency of this modified cyclotron motion is

$$\nu_+ = \frac{1}{2}\left(\nu_\mathrm{c} + \sqrt{\nu_\mathrm{c}^2 - 2\nu_z^2} \right). \tag{2.6}$$

From now on, we call ν_c as free cyclotron frequency to distinguish from the modified cyclotron frequency ν_+ when a particle is in fact confined in a Penning trap. In addition to these two modes, there is another radial mode called magnetron motion, which is caused by a $\vec{E} \times \vec{B}$ drift. The magnetron frequency ν_- is

$$\nu_- = \frac{1}{2}\left(\nu_\mathrm{c} - \sqrt{\nu_\mathrm{c}^2 - 2\nu_z^2} \right) \approx \frac{V_0 C_2}{|\vec{B}|}. \tag{2.7}$$

To first order, ν_- is independent on the physical properties of the trapped particle. It only depends on the electromagnetic fields. An illustration of the particle's eigenmotions in a Penning trap is shown in Fig. 2.3.

For $\nu_\mathrm{c}^2 > 2\nu_z^2$, a Penning trap provides stable trapping conditions. Typical Penning traps used for precision experiments are operated with parameters

$$\nu_+ \gg \nu_z \gg \nu_-. \tag{2.8}$$

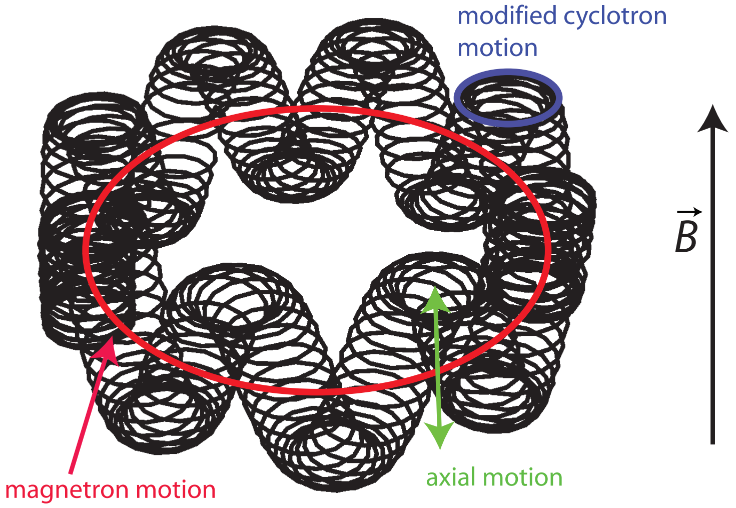

Fig. 2.3: Schematic of the particle's eigenmotions in a Penning trap. The entire motion is a superposition of the axial motion along the magnetic field lines, the modified cyclotron motion, and the magnetron motion.

Some useful relations between the eigenfrequencies are

$$\nu_- \simeq \frac{\nu_z^2}{2\nu_+} \tag{2.9}$$

$$\nu_c \simeq \nu_+ + \nu_- \tag{2.10}$$

$$\nu_c^2 = \nu_+^2 + \nu_-^2 + \nu_z^2. \tag{2.11}$$

Equation (2.10) and (2.11) only hold for ideal Penning traps, whereas Eq. (2.11) is also valid in presence of some specific first order trap errors, such as an elliptic deformation of the electrostatic quadrupole potential, and towards a tilt of the quadrupole potential with respect to the magnetic field lines [44]. However, it is sensitive to

- imperfect quadrupolar potential due to higher order multipolar corrections, and
- inhomogeneities of the magnetic field.

Specifically this so-called invariance theorem makes Penning traps strong tools in high-precision investigations of single particle properties.

2.2 Cylindrical Penning trap

In practice, BASE uses cylindrical Penning traps to confine charged particles. Cylindrical Penning traps provide - in an appropriately chosen trap geometry - a large homogeneous trapping

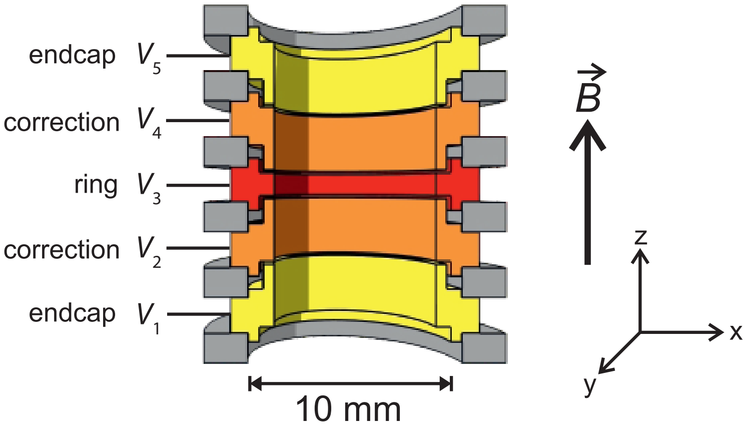

Fig. 2.4: Schematic of a cylindrical Penning trap. Taken and modified from [13].

region. In addition, compared to hyperbolic traps, cylindrical traps are much easier to machine. Practically the electrodes of a cylindrical trap can be manufactured with tolerances of order 5 μm. The geometrical configuration of a five-pole cylindrical Penning trap is shown in Fig. 2.4. It consists of a stack of gold-plated copper electrodes which are electrically separated with insulating sapphire rings. As will be described in the end of this section, this electrode configuration allows to generate a quadrupolar electric potential. In addition to a strong homogeneous magnetic field $\vec{B}$ generated by a superconducting magnet (see section 5.3), which is in parallel to z coordinate as shown in Fig. 2.4, charged particles can be stably confined inside the trap. However, in reality the trapping potentials are not identical to the theory which were introduced in a previous section 2.1. Therefore, certain amount of deviations exist compared to the theoretical optimum.

In order to produce a trapping potential which is close to the perfect quadrupole, the electrodes must be as ideal as possible and the magnetic field should be highly homogeneous. As shown in Fig. 2.4, the trap electrodes consist of a central *ring electrode* with length l_r, two neighbouring *correction electrodes* with length l_ce, and two *endcaps* with length l_e. The radius of the trap is a. By choosing adequate lengths and length-to-radius ratios, the Penning trap can be designed in a following way.

- The higher order potential coefficients C_4 and C_6 can be tuned to zero simultaneously. This is called the *compensated design*.

- The eigenfrequency of the particle is independent of the voltage applied to the correction electrodes. This is called the *orthogonality design*.

The field configuration of the voltage potential can be derived by solving the cylindrical Laplace equation

$$\nabla^2\Phi(\rho,z) = \frac{1}{\rho}\frac{\partial}{\partial\rho}\left(\rho\frac{\partial}{\partial\rho}\Phi(\rho,z)\right) + \frac{\partial^2}{\partial z^z}\Phi(\rho,z) = 0, \tag{2.12}$$

which has to be found for Dirichlet boundary conditions $\Phi(a,z) = V$. V is the voltage applied to the respective electrode. A variable separation method can be applied to Eq. (2.12) for allowing it to be reorganised as $\Phi(\rho,z) = R(\rho)Z(z)$. Therefore, it leads to two independent differential equations in order to satisfy Eq. (2.12)

$$\frac{1}{\rho}\frac{d}{d\rho}\left(\rho\frac{d}{d\rho}R(\rho)\right) - k^2R(\rho) = 0 \tag{2.13}$$

$$\frac{d^2}{dz^2}Z(z) + k^2Z(z) = 0. \tag{2.14}$$

Here, k is a separation constant. Equation (2.13) can be solved by introducing modified Bessel-functions $I_k(\rho)$, whereas Eq. (2.14) is solved by trigonometric functions, leading to the solution

$$\Phi(\rho,z) = \sum_{n=-\infty}^{\infty} I_0(k_n\rho)(A(k_n)\sin(k_nz)). \tag{2.15}$$

Where, $k_n = \frac{n\pi}{\Lambda}$, $n \in \mathbb{Z}$. Λ is the total length of the trap. $A(k_n)$ is defined by the Dirichlet boundary conditions and can be calculated by simple integration. Now the total potential of p stacked electrodes can be expressed as

$$\begin{aligned}\Phi(\rho,z) \quad &= \quad \frac{2}{\Lambda}\sum_{n=1}^{\infty}\left[\frac{V_1\cos(k_nz_0) - V_p\cos(k_n\Lambda)}{k_n} + \sum_{i=2}^{p}\frac{V_i - V_{i-1}}{k_n^2d}(\sin(k_nz_{2i}) - \sin(k_nz_{2i-1}))\right] \\ &\times \quad \frac{I_0(k_n\rho)}{I_0(k_na)}\sin(k_nz).\end{aligned} \tag{2.16}$$

Where d [m] is the length of the space between two adjacent electrodes, z_{2i} is the axial start coordinate of electrode i and z_{2i-1} the stop coordinate of electrode $i-1$. Equation (2.16) can be simplified when considering $p = 5$ as

$$\begin{aligned}\Phi(\rho,z,V_i) \quad &= \quad \frac{2}{\Lambda}\sum_{n=1}^{\infty}\left[\frac{V_1\cos(k_nz_0) - V_5\cos(k_n\Lambda)}{k_n} + \sum_{i=2}^{5}\frac{V_i - V_{i-1}}{k_n^2d}(\sin(k_nz_{2i}) - \sin(k_nz_{2i-1}))\right] \\ &\times \quad \frac{I_0(k_n\rho)}{I_0(k_na)}\sin\left(k_n\left(z + \frac{\Lambda}{2}\right)\right).\end{aligned} \tag{2.17}$$

Refer to Fig. 2.4 for the definition of each variables. Now, Eq. (2.17) is expanded in powers of the coordinates z^j as

$$\Phi(0,z) = V_0\sum_{j=0}^{n} C_jz^j, \tag{2.18}$$

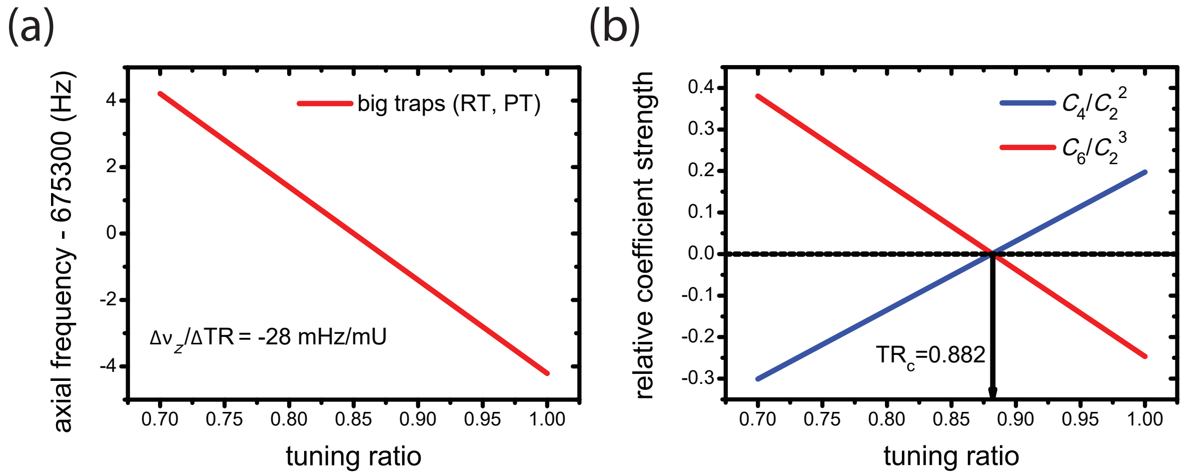

Fig. 2.5: Orthogonality and compensation of a Penning trap. (a) Axial frequency as a function of the tuning ratio ($\mathrm{TR} = V_{\mathrm{ce}}/V_0$). (b) Voltage potential coefficients C_4 and C_6 as a function of the TR. When $\mathrm{TR} = \mathrm{TR_c} = 0.882$, the both coefficients are tuned to zero simultaneously.

where the voltage potential coefficients C_j are defined by

$$\begin{aligned} C_j &= \frac{1}{j!\Lambda V_0} \sum_{n=1}^{\infty} \left[\frac{V_1 \cos(k_n z_0) - V_5 \cos(k_n \Lambda)}{k_n} + \sum_{i=2}^{5} \frac{V_i - V_{i-1}}{k_n^2 d} (\sin(k_n z_{2i}) - \sin(k_n z_{2i-1})) \right] \\ &\times \frac{(n\pi/\Lambda)^j}{I_0(k_n a)} \sin\left(\frac{\pi}{2}(n+j)\right). \end{aligned} \tag{2.19}$$

Now, we define the *tuning ratio* $\mathrm{TR} = V_{\mathrm{ce}}/V_0$, which is a ratio of the voltages $V_2 = V_4 = V_{\mathrm{ce}}$ applied to the correction electrodes and $V_3 = V_0$ applied to the ring electrode. During precision measurements, $V_1 = V_5 = 0$. Therefore, C_j can be expressed as $C_j = E_j + D_j \cdot \mathrm{TR}$ for every j. The coefficients E_j and D_j are defined by the dimensions of the trap electrodes. It is possible to make a condition where $D_2 \approx 0$ (*orthogonality*) and $C_4 = C_6 = 0$ (*compensation*) by varying the diameter of the trap a, the length of the ring electrode l_{r}, and the length of the correction electrodes l_{ce}. Figure 2.5 shows the characterisation of the orthogonality and the compensation for the big traps (reservoir trap (RT) and the precision trap (PT)). Figure 2.5 (a) shows the axial frequency ν_z as a function of the TR. With the design value of D_2, it has a slope of $\Delta\nu_z/\Delta\mathrm{TR} = -28\,\mathrm{mHz/mU}$, where mU stands for ”milliunit”, which defines a change of the dimensionless TR by 0.001. Figure 2.5 (b) shows the simultaneous compensation of C_4 and C_6. When $\mathrm{TR} = \mathrm{TR_c} = 0.882$, both coefficients vanish simultaneously. For smaller trap geometries, the axial frequency dependency on the TR is much more sensitive. As will be described in section 9.2.2, it leads to a situation where it requires to have high accuracies for V_0 and TR to observe particle signals. For the small traps used in BASE (an analysis trap (AT) and a cooling trap (CT)), $\Delta\nu_z/\Delta\mathrm{TR} = 37\,\mathrm{Hz/mU}$ is obtained. The BASE Penning-trap design is described in great detail in the Master thesis of Georg Schneider [46].

Chapter 3

Non-destructive detection of the eigenfrequencies

A single particle stored in a cryogenic Penning trap has three eigen-motions, such as the modified cyclotron motion, the magnetron motion, and the axial motion (for the details, see section 2.1). Information on these motions can be extracted by means of the image-current detection. The particle motion induces tiny currents in the trap electrodes on the order of fA. Our developed highly sensitive superconducting resonant detectors allow for non-destructive detection of these weak signals [15]. Since these detection systems are our only way to acquire frequency information non-destructively from the trapped particle, it is one of the crucial components for high precision experiments. In this chapter, the principle of non-destructive detection of the eigenfrequencies is described.

3.1 Principle of the detection system

The particle's eigenmotions induce tiny image-currents in the Penning-trap electrodes as

$$i_{\mathrm{p}} = \frac{2\pi q}{D} \cdot \nu_i \cdot \zeta_i, \tag{3.1}$$

where D is a trap specific length, ν_i the eigenfrequency, and ζ_i the coordinate of the respective eigenmotion. In order to detect an induced current i_{p}, a superconducting detector is connected directly to an appropriate Penning-trap electrode (refer to Fig. 5.10) as shown in Fig. 3.1. It consists of a superconducting resonator followed by a cryogenic low-noise amplifier. The resonator acts as a *RLC* parallel tuned circuit, which has a certain resonance frequency matched to

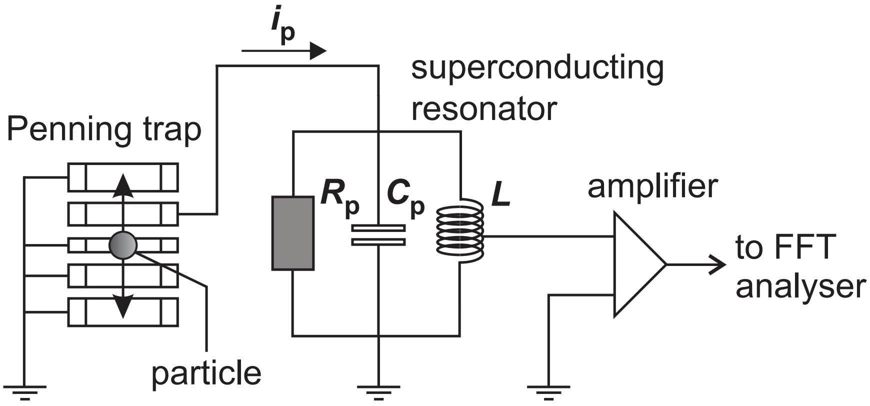

Fig. 3.1: Schematic of the image-current detection. A superconducting resonator followed by a cryogenic low-noise amplifier is connected to one of the Penning-trap electrodes to detect an induced image-current i_p, which is generated due to the interaction between the eigenmotion and the electrode. This schematic shows a detection of the axial motion. The equivalent circuit of the resonator can be considered as an *RLC* parallel tuned circuit. When at resonance ν_0, the reactances compensate each other, hence the resonator acts as a parallel resistor R_p. A voltage drop $V_\mathrm{p} = R_\mathrm{p} i_\mathrm{p}$ is amplified with the cryogenic amplifier and subsequently its transient is recorded by a fast fourier transform (FFT) analyser.

the eigenfrequency ν_i

$$\nu_0 = \frac{1}{2\pi\sqrt{LC_\mathrm{p}}}, \tag{3.2}$$

and a quality factor (Q-value)

$$Q_\mathrm{p} = \frac{2\pi E}{\Delta E} \approx \frac{\nu_0}{\Delta\nu}. \tag{3.3}$$

Here, E is the stored energy of the oscillating resonator, ΔE is the energy dissipated per cycle, and $\Delta\nu$ is the $-3\,\mathrm{dB}$ width of the resonance spectrum. Equation (3.3) becomes approximately equivalent when the Q-value becomes large. To discuss the relevant properties of the detection circuit, we derive the following correlation. The total impedance of the tuned circuit is

$$|Z_\mathrm{p}(\omega)| = \frac{1}{\sqrt{\frac{1}{R_\mathrm{p}^2} + \left(\omega C_\mathrm{p} - \frac{1}{\omega L}\right)^2}}, \tag{3.4}$$

where ω is the angular frequency. When on resonance $\omega = 2\pi\nu_0$, $|Z_\mathrm{p}|$ is at maximum $|Z_\mathrm{p,res}| = R_\mathrm{p}$. From the definition of Q-value (Eq. (3.3)), $|Z_\mathrm{p}(\omega)|/|Z_\mathrm{p,res}| = 1/\sqrt{2}$. Therefore,

$$\frac{|Z_\mathrm{p}(\omega)|}{|Z_\mathrm{p,res}|} = \frac{1}{\sqrt{1 + \left(\omega C_\mathrm{p} - \frac{1}{\omega L}\right)^2 R_\mathrm{p}^2}} = \frac{1}{\sqrt{2}}. \tag{3.5}$$

To satisfy this equation, it is necessary to solve ω which also satisfies

$$R_{\mathrm{p}}\left(\omega C_{\mathrm{p}}-\frac{1}{\omega L}\right)=\pm 1. \tag{3.6}$$

This can be solved by simple algebra. By defining $\Delta\nu=\nu_2-\nu_1(>0)$,

$$\begin{aligned}\nu_1 &= \frac{1}{4\pi L C_{\mathrm{p}} R_{\mathrm{p}}}\left(-L+\sqrt{L^2+4LC_{\mathrm{p}}R_{\mathrm{p}}^2}\right) && (3.7)\\ \nu_2 &= \frac{1}{4\pi L C_{\mathrm{p}} R_{\mathrm{p}}}\left(L+\sqrt{L^2+4LC_{\mathrm{p}}R_{\mathrm{p}}^2}\right) && (3.8)\end{aligned}$$

are obtained as the two independent solutions for Eq. (3.6). Inserting Eq. (3.7) and Eq. (3.8) to Eq. (3.3), the following relation is derived

$$Q_{\mathrm{p}}=2\pi\nu_0 C_{\mathrm{p}} R_{\mathrm{p}}=\frac{R_{\mathrm{p}}}{2\pi\nu_0 L}. \tag{3.9}$$

This relation is important for further discussions.

At resonance ν_0, the reactances compensate each other and the resonator acts as a parallel resistor R_{p}. When the resonance frequency ν_0 is matched to the eigenfrequency of the particle ν_i, a voltage drop over the *RLC* circuit occurs $V_{\mathrm{p}}=R_{\mathrm{p}}i_{\mathrm{p}}$ and is subsequently amplified by a cryogenic amplifier. Its transient will be recorded by a fast fourier transform (FFT) analyser. Since V_{p} is proportional to R_{p}, which is also proportional to Q_{p} as shown in Eq. (3.9), Q_{p} needs to be as large as possible to obtain a large voltage drop V_{p}. To achieve this, we have developed our handmade axial detectors and cyclotron detectors. The details on these detectors will be described in chapter 6. In practice, the parallel capacitance and the parallel resistance of the detector are not only contributed by the resonator, but also by the electrodes, feedthroughs, and the cryogenic amplifier. In order to distinguish them from the properties of the unloaded resonator, from now on we define R_{eff} as an effective parallel resistance, C_{eff} as an effective parallel capacitance, $\nu_{0,\mathrm{eff}}$ as a resonance frequency, and $Q_{\mathrm{p,eff}}=R_{\mathrm{eff}}/(2\pi\nu_{0,\mathrm{eff}}L)$ as an effective Q-value of the entire detection system. In this way, a total impedance of the detector can be expressed as

$$|Z_{\mathrm{eff}}(\omega)|=\frac{1}{\sqrt{\frac{1}{R_{\mathrm{eff}}^2}+\left(\omega C_{\mathrm{eff}}-\frac{1}{\omega L}\right)^2}}. \tag{3.10}$$

In addition to induced image-currents, there is some noise present in this system. The most significant contribution is the Johnson-Nyquist noise i_{th} [A/$\sqrt{\mathrm{Hz}}$], which is generated by the effective resistance R_{eff} as

$$i_{\mathrm{th}}=\sqrt{\frac{4k_{\mathrm{B}}T}{R_{\mathrm{eff}}}}, \tag{3.11}$$

where k_B is Boltzmann constant and T is the effective temperature of the system [47,48]. From Eq. (3.10) and Eq. (3.11), frequency dependent voltage drop $V_{\mathrm{th}}(\omega)$ $[\mathrm{V}/\sqrt{\mathrm{Hz}}]$ is obtained as

$$V_{\mathrm{th}}(\omega) = |Z_{\mathrm{eff}}(\omega)| i_{\mathrm{th}} = \sqrt{\frac{4k_B T}{\frac{1}{R_{\mathrm{eff}}} + R_{\mathrm{eff}}\left(\omega C_{\mathrm{eff}} - \frac{1}{\omega L}\right)^2}}. \tag{3.12}$$

Amount of voltage transmitted to the input of the amplifier depends on how strongly the resonator is coupled to the amplifier. This coupling strength is defined as a coupling factor κ $(0 < \kappa < 1)$ (the detailed definition is described in section 3.3). This is a crucial parameter which needs to be optimised to meet requirements for the application of each detection system. Before κV_{th} is amplified, the equivalent input noise of the amplifier e_n $[\mathrm{V}/\sqrt{\mathrm{Hz}}]$ is quadratically added. Within the frequency range of interest ($> 5.0 \times 10^5$ Hz), e_n can be considered approximately as white noise. These noise sources are transmitted through the apparatus and amplified again by an rf amplifier at room temperature. The signals of the detection system are down-mixed into the frequency range of an FFT analyser (SR780, SRS), which detects the dissipated power in its input impedance R as

$$P_{\mathrm{th}}(\omega) = 10\log\left(\frac{G^2\kappa^2\left(V_{\mathrm{th}}(\omega)\right)^2/R}{0.001}\right) \tag{3.13}$$

$$P_e = 10\log\left(\frac{G^2 e_n^2/R}{0.001}\right), \tag{3.14}$$

where $P_{\mathrm{th}}(\omega)$ [dBm/Hz] is the resultant dissipated power density of $V_{\mathrm{th}}(\omega)$, P_e [dBm/Hz] is the resultant dissipated power density of e_n, and G is the total gain of the amplifiers. For our experimental condition, $P_{\mathrm{th}}(\omega \to 2\pi\nu_{0,\mathrm{eff}}) \gg P_e$. Consequently, we can define a resonator signal-to-noise ratio SNRr [dB] as

$$\mathrm{SNRr} = P_{\mathrm{th}}(2\pi\nu_{0,\mathrm{eff}}) - P_e = 20\log\left(\frac{u_n}{e_n}\right) = 20\log\frac{\sqrt{4k_B T R_{\mathrm{eff}}}\cdot\kappa}{e_n}, \tag{3.15}$$

where $u_n = \kappa V_{\mathrm{th}}(2\pi\nu_{0,\mathrm{eff}})$. In Fig. 6.8, an example of a noise spectrum of the axial detector without any trapped particles is shown. In this case, SNRr = 30 dB. Also by extracting $\nu_{0,\mathrm{eff}}$ and Q-value from the obtained spectrum and inserting them into Eq. (3.15), an effective temperature T of the detector can be derived. When the particle motion is in thermal equilibrium to the detector, the motional amplitude is Boltzmann distributed and its line-shape depends on the temperature T.

3.2 Equation of the particle motion

The next step is to find out how the resonance spectrum looks like when a trapped particle is tuned in parallel to the detector. Since the particle dissipates its energy due to a voltage drop $V_{\mathrm{eff}} = R_{\mathrm{eff}} i_{\mathrm{p}}$, it is necessary to consider how the motional amplitude evolves in the time domain.

In this section, the interaction of the particle with the detection system, represented effectively by a parallel resistor is described. The equivalence of this system to a damped harmonic oscillator is shown. The particle energy decreases via the resistive cooling due to the detector resistance R_{eff}, as described in section 3.1. In this respect, it is inappropriate to detect directly the magnetron frequency ν_- with such a detection scheme, since the magnetron mode is a metastable mode and its radius increases while it looses its energy. The detector tuned to ν_- would damp the magnetron energy continuously and eventually the particle would collide with the trap electrode. Therefore, the non-destructive detection is only an excellent technique for detecting the axial frequency ν_z and the modified cyclotron frequency ν_+. During my PhD studies, I have developed image-current detection systems to detect the axial frequency [15]. The modified cyclotron frequency as well as the magnetron frequency were measured either by the sideband coupling technique (refer to section 3.4) or in the analysis trap, by making use of the magnetic bottle (see section 11.8). The axial detector was used for both techniques. A cyclotron detector is installed in the precision trap to resistively cool the modified cyclotron mode for spin-flip detections (see section 10.4). Note, that the cyclotron detector is also connected to one of the correction electrodes, however, the electrode is split in two segments.

From now on, characteristics of the axial dip detection will be focused only. The equation of the particle motion can be written as

$$m\frac{d^2z}{dt^2} = -m\left(\gamma\frac{dz}{dt} + \omega_z^2 z\right), \tag{3.16}$$

where γ is the damping constant and ω_z is the axial-angular frequency. By multiplying Eq. (3.16) by dz/dt, and subsequently time-integrating the result,

$$\frac{1}{2}m\left(\frac{dz}{dt}\right)^2 + \frac{1}{2}m\omega_z^2 z^2 = -\int m\gamma\left(\frac{dz}{dt}\right)^2 dt = -\int P dt \tag{3.17}$$

is obtained. P is the power dissipation of the image-current at R_{eff}. From (Eq. 3.17),

$$P = R_{\mathrm{eff}} i_{\mathrm{p}}^2 = m\gamma\left(\frac{dz}{dt}\right) \tag{3.18}$$

is derived, and also by solving for γ,

$$\gamma = \frac{R_{\mathrm{eff}} i_{\mathrm{p}}^2}{m(dz/dt)^2} \tag{3.19}$$

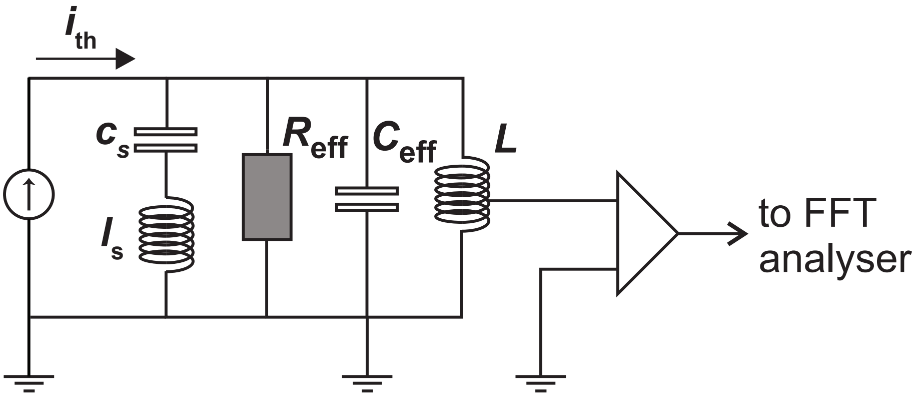

Fig. 3.2: Equivalent circuit of the trapped particle with the detection system. The particle acts as a *LC* series circuit, which has a resonance frequency same as the eigenfrequency $\nu_i = 1/\sqrt{l_s c_s}$.

is obtained. Together with Eq. (3.1), Eq. (3.19) can be rewritten as

$$\gamma = \frac{R_{\mathrm{eff}}}{m}\frac{q^2}{D^2} \Longleftrightarrow \tau = \frac{m}{R_{\mathrm{eff}}}\frac{D^2}{q^2}. \tag{3.20}$$

τ is the cooling time constant, which defines the amount of time required for a particle to decrease its energy down to a fraction $1/e$ of the initial energy. By combining Eq. (3.16) and Eq. (3.19),

$$m\frac{D^2}{q^2}\frac{d}{dt}i_{\mathrm{p}} + R_{\mathrm{eff}}i_{\mathrm{p}} + m\omega_z^2\int\frac{D^2}{q^2}i_{\mathrm{p}}dt = 0 \tag{3.21}$$

is obtained. By replacing $l_{\mathrm{s}} = m\frac{D^2}{q^2}$ and $c_{\mathrm{s}} = \frac{1}{m\omega_z^2}\frac{q^2}{D^2}$, Eq. (3.21) is rewritten as

$$l_{\mathrm{s}}\frac{d}{dt}i_{\mathrm{p}} + R_{\mathrm{eff}}i_{\mathrm{p}} + \frac{1}{c_{\mathrm{s}}}\int i_{\mathrm{p}}dt = 0. \tag{3.22}$$

Equation (3.22) indicates that the particle behaves as a series *LC* circuit with a resonance frequency of ν_z. When the particle is in thermal equilibrium to the detector, an equivalent circuit including the particle in a Penning trap can be shown as in Fig. 3.2. The total impedance $|Z_{\mathrm{total}}(\omega)|$ of this system is

$$|Z_{\mathrm{total}}(\omega)| = \left|\frac{Z_{\mathrm{s}}Z_{\mathrm{eff}}}{Z_{\mathrm{s}} + Z_{\mathrm{eff}}}\right| \tag{3.23}$$

$$Z_{\mathrm{s}} = j\omega l_{\mathrm{s}} + \frac{1}{j\omega c_{\mathrm{s}}} \tag{3.24}$$

$$\nu_z = \frac{1}{2\pi\sqrt{l_{\mathrm{s}}c_{\mathrm{s}}}}. \tag{3.25}$$

Figure 3.3 shows the total impedance $|Z_{\mathrm{total}}(\omega)|$ for different axial frequencies ν_z. When the axial frequency is tuned to the resonance frequency $\nu_0 = \nu_z$, the impedance shows a dip at ν_0

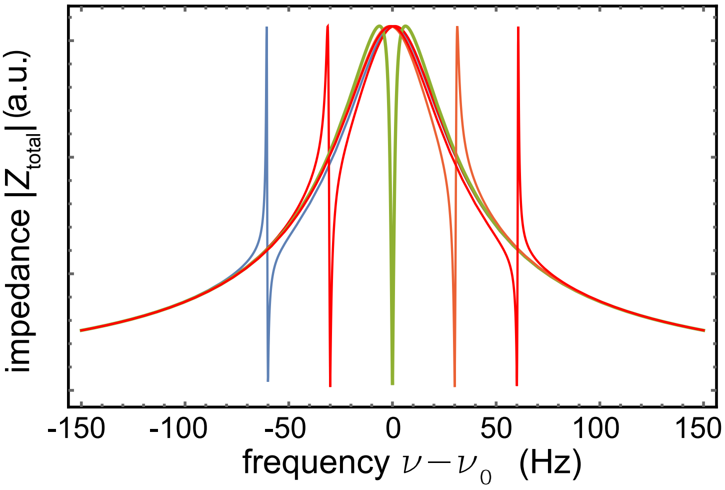

Fig. 3.3: Total impedance of the detection system together with a trapped particle. It shows different impedances by varying the axial frequency ν_z of the particle. When $\nu_0 = \nu_z$ (green curve), reactances of the detector vanish at ν_z and the system can be considered approximately as a simple *RLC* series tuned circuit near the resonance frequency ν_0. By measuring a dip-width $\Delta\nu_{z,\mathrm{N}}$ of the spectrum, it is possible to determine a number of the stored particles (see Eq. (3.27) and the text).

as represented by the green curve. In this situation, reactance components of the detector L and C_{eff} vanish at ν_z, as a consequence the system can be considered approximately as a simple *RLC* series tuned circuit near the resonance frequency ν_0. We define a -3 dB dip-width of the resonance curve $\Delta\nu_z$ as

$$\Delta\nu_z = \frac{\nu_z}{Q_\mathrm{s}} = \frac{R_\mathrm{eff}}{2\pi l_\mathrm{s}} = \frac{1}{2\pi}\frac{R_\mathrm{eff}}{m}\frac{q^2}{D^2}, \tag{3.26}$$

where Q_s is the quality factor for *RLC* series tuned circuit, which can be derived as a same way as for Q_p (refer to section 3.1). Equation (3.26) represents the dip-width of a single trapped particle, however this can be extended for more than one particles. Assuming N identical particles are stored in a Penning trap, this particle cloud has a mass Nm and a charge Nq. Therefore, the expected dip-width $\Delta\nu_{z,\mathrm{N}}$ can be expressed as

$$\Delta\nu_{z,\mathrm{N}} = \frac{1}{2\pi}\frac{R_\mathrm{eff}}{Nm}\frac{(Nq)^2}{D^2} = N \cdot \Delta\nu_z. \tag{3.27}$$

$\Delta\nu_{z,\mathrm{N}}$ is proportional to the number of trapped particles N. This relation is exceptionally important, since it indicates that the number of trapped particles can be measured non-destructively by measuring the dip-width from the obtained spectrum.

If we gather all the information which described up to now, the accumulated noise amplitude u_total $[\mathrm{V}/\sqrt{\mathrm{Hz}}]$ which is expected to be transmitted through the FFT analyser when the particle

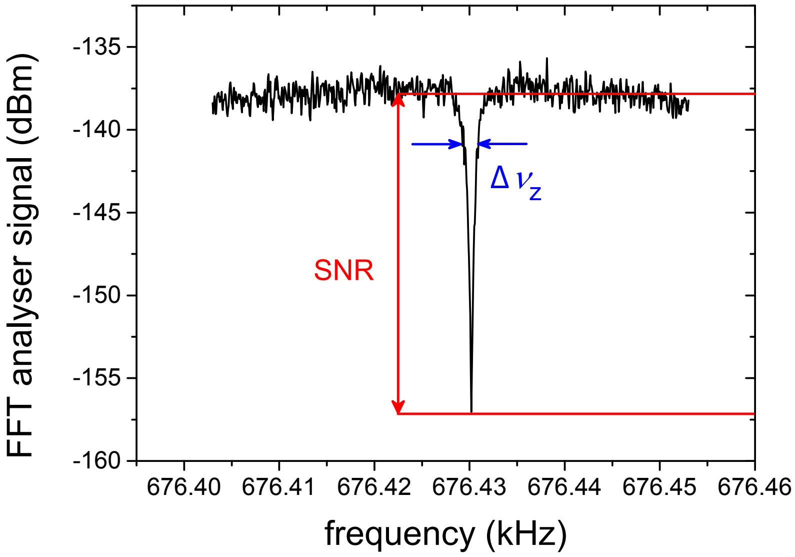

Fig. 3.4: Example of a dip spectrum in the precision trap. A signal-to-noise ratio (SNR) and a dip-width ($\Delta\nu_z$) are important characteristics which contribute to an axial frequency scatter as shown in Eq. (3.30).

is in thermal equilibrium to the detector temperature T can be expressed as

$$u_{\text{total}}^2 = (G_1 G_2 \kappa |Z_{\text{total}}| i_{\text{th}})^2 + (G_1 G_2 e_{\text{n}})^2 + (G_2 z_{\text{n}})^2 + s_{\text{n}}^2. \tag{3.28}$$

Here, G_1 is the gain of the cryogenic amplifier, G_2 is the gain of the rf amplifier outside of the apparatus, z_{n} the equivalent input noise of the rf amplifier, and s_{n} the equivalent input noise of the FFT analyser. When $\nu = \nu_z = \nu_0 \Rightarrow |Z_{\text{total}}| = 0$, the noise level is $u_{\text{total},0} \approx G_1 G_2 e_{\text{n}}$. Moreover, the noise level at $\nu = \nu_0$ when there is no particle trapped is $u_{\text{total,res}} \approx G_1 G_2 \kappa |Z_{\text{eff}}| i_{\text{th}}$. Now, we define the dip signal-to-noise ratio SNR [dB] as

$$\text{SNR} = 10 \log \left(\frac{u_{\text{total,res}}^2 / R}{0.001} \right) - 10 \log \left(\frac{u_{\text{total},0}^2 / R}{0.001} \right) = 20 \log \left(\frac{\sqrt{4 k_{\text{B}} T R_{\text{eff}}} \cdot \kappa}{e_{\text{n}}} \right). \tag{3.29}$$

This is the same definition as for SNRr (see Eq. 3.15). However, SNR = SNRr holds only when assuming that the axial frequency ν_z is infinitely stable during the measurement time. In practice the fluctuations of the particle frequency smear out the dip signal, hence SNR < SNRr.

Figure 3.4 shows an example of an axial frequency dip spectrum. By fitting the dip with the appropriate line-shape, the axial frequency ν_z, the particle number N, and SNR are extracted. The expected axial frequency scatter σ obtained from this fit is evaluated as

$$\sigma \propto \sqrt{\frac{1}{4\pi} \frac{\Delta\nu_z}{t_{\text{avg}}} \frac{1}{\sqrt{\text{SNR}}}}, \tag{3.30}$$

where t_{avg} is the averaging time. Therefore, $\Delta\nu_z$ and SNR should be optimised so that σ becomes sufficiently small for fixed t_{avg}. This is one of the most important factors which needs to be considered to achieve antiproton spin-transition spectroscopy in the analysis trap (see chapter 10).

3.3 Optimisation of the dip detection

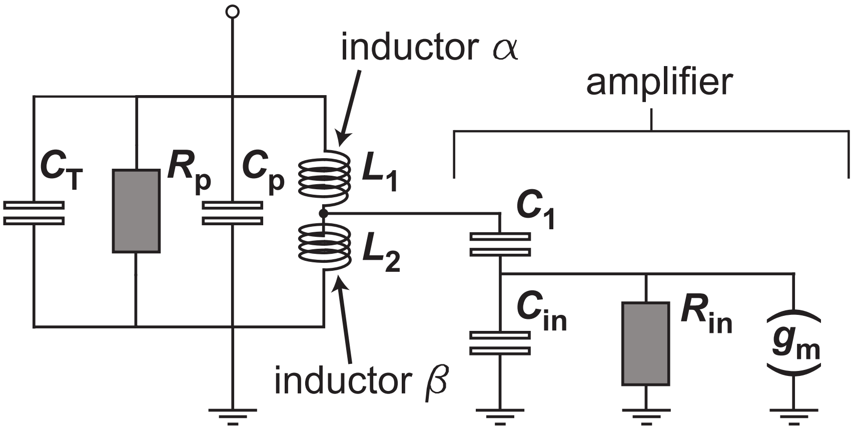

Fig. 3.5: Equivalent circuit of the entire system, without a trapped particle. C_{T} is the parasitic trap capacitance, C_1 is the input capacitor of the amplifier, C_{in} is the parasitic input capacitance of the amplifier, R_{in} is the parasitic input resistance of the amplifier, and g_{m} is the transconductance of the amplifier. Inductor α and β are effective inductors due to the tapping, which have N_1 and N_2 number of turns, respectively.

This section will be focusing on optimisations of the dip detection, mainly by using Eq. (3.30). For our convenience, we rewrite below the definitions on the dip-width $\Delta\nu_z$ [Hz] and the dip signal-to-noise ratio SNR [dB]

$$\Delta\nu_z = \frac{1}{2\pi}\frac{R_{\mathrm{eff}}}{m}\frac{q^2}{D^2} \tag{3.31}$$

$$\mathrm{SNR} = 20\log\left(\frac{\sqrt{4k_{\mathrm{B}}TR_{\mathrm{eff}}}\cdot\kappa}{e_{\mathrm{n}}}\right). \tag{3.32}$$

Obviously, R_{eff} and κ need to be defined in the first place. In Fig. 3.5, it shows an equivalent circuit of the entire system without any trapped particles. We define inductor α and inductor β as effective inductors due to the tapping, which have N_1 and N_2 number of turns, respectively. Therefore $L_1 = k\cdot N_1^2$, $L_2 = k\cdot N_2^2$, where k is a scaling factor. Regarding the definitions for each

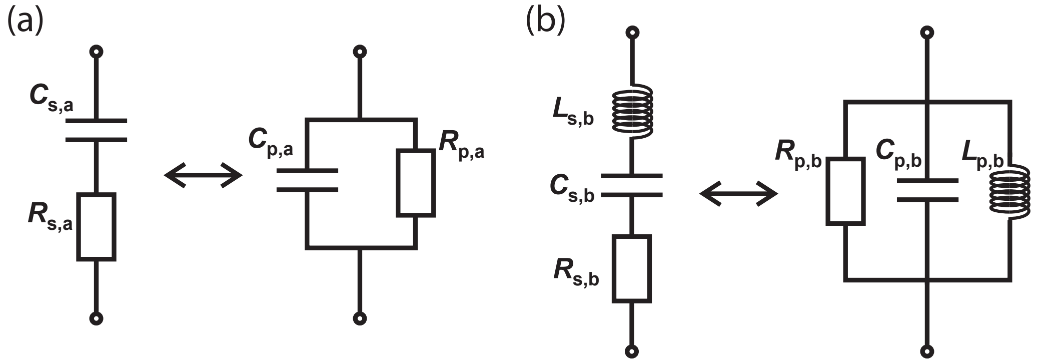

Fig. 3.6: Conversions of series to parellel (a) RC and (b) RLC circuit.

component, see the figure caption. The coupling constant κ is now defined as

$$\kappa = \kappa_l \cdot \kappa_c = \frac{N_2}{N_1 + N_2} \cdot \frac{C_1}{C_1 + C_{\mathrm{in}}}. \tag{3.33}$$

Note, that κ is tunable by varying N_1, N_2 and C_1. Next, a conversion of the equivalent circuit (Fig. 3.5) to a simple *RLC* parallel circuit is required in order to define R_{eff}. To realise this, we first consider simple conversions between the two cases as shown in Fig. 3.6. Figure 3.6 (a) shows the conversion between a series and a parallel *RC* circuit, and Fig. 3.6 (b) shows the case for *RLC* series and parallel circuits. Correlations between series and parallel components can be derived by calculating a total impedance for each circuits, and subsequently use the fact that the impedances are identical. From the calculation,

$$R_{\mathrm{p,a}} = \frac{1}{\omega^2 C_{\mathrm{p,a}}^2 R_{\mathrm{s,a}}} \tag{3.34}$$

$$C_{\mathrm{s,a}} = \frac{1 + \omega^2 R_{\mathrm{p,a}}^2 C_{\mathrm{p,a}}^2}{\omega^2 R_{\mathrm{p,a}}^2 C_{\mathrm{p,a}}} \tag{3.35}$$

$$R_{\mathrm{p,b}} = \frac{\omega_0^2 L_{\mathrm{p,b}} L_{\mathrm{s,b}}}{R_{\mathrm{s,b}}} \tag{3.36}$$

are obtained. Figure 3.7 shows a schematic of how the conversions can take place from the initial equivalent circuit to an effective *RLC* parallel circuit. By utilising Eq. (3.34), Eq. (3.35), and Eq. (3.36), eventually $R_{\mathrm{p,2}}$ (see Fig. 3.7 (g)) is calculated as

$$\begin{aligned} R_{\mathrm{p,2}} = \frac{L}{L_2} \cdot \left(\frac{C_{\mathrm{in}}}{C_{\mathrm{s,2}}}\right)^2 \cdot R_{\mathrm{in}} &= \left(\frac{N_1 + N_2}{N_2}\right)^2 \cdot \left(\frac{C_1 + C_2}{C_1}\right)^2 \cdot \left(\frac{\omega^2 R_{\mathrm{in}}^2 C_{\mathrm{in}}^2}{1 + \omega^2 R_{\mathrm{in}}^2 C_{\mathrm{in}}^2}\right)^2 \cdot R_{\mathrm{in}} \\ &\approx \frac{R_{\mathrm{in}}}{\kappa^2}. \end{aligned} \tag{3.37}$$

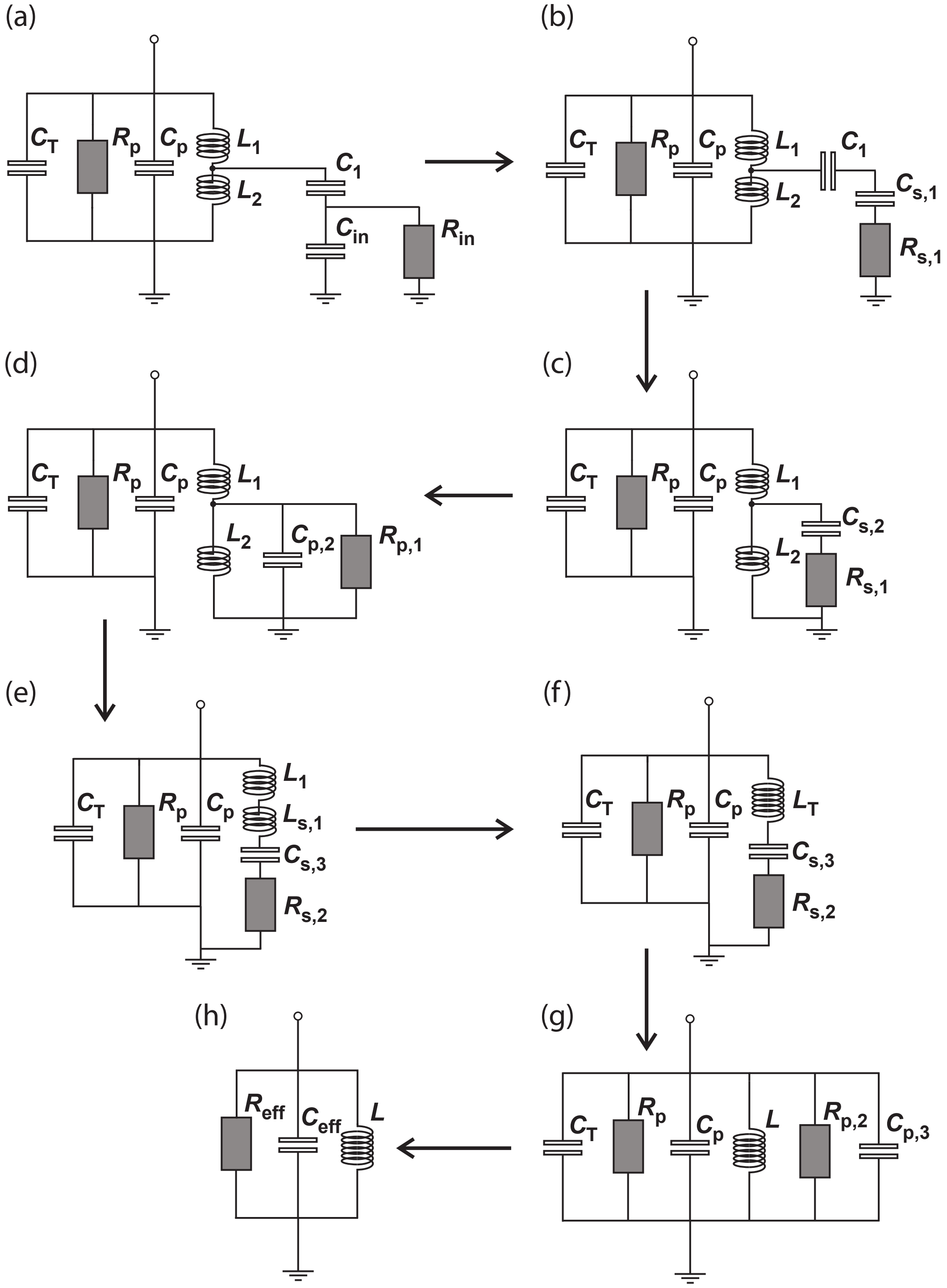
(a)
C_T
R_p
C_p
L_1
L_2
C_1
C_{in}
R_{in}
(b)
C_T
R_p
C_p
L_1
L_2
C_1
$C_{s,1}$
$R_{s,1}$
(d)
C_T
R_p
C_p
L_1
L_2
$C_{p,2}$
$R_{p,1}$
(c)
C_T
R_p
C_p
L_1
$C_{s,2}$
L_2
$R_{s,1}$
(e)
C_T
R_p
C_p
L_1
$L_{s,1}$
$C_{s,3}$
$R_{s,2}$
(f)
C_T
R_p
C_p
L_T
$C_{s,3}$
$R_{s,2}$
(h)
R_{eff}
C_{eff}
L
(g)
C_T
R_p
C_p
L
$R_{p,2}$
$C_{p,3}$

Fig. 3.7: Conversions of an equivalent circuit of the entire system by using Fig. 3.6.

This assumption holds when dealing with high frequencies more than several MHz, and the parasitic input resistance R_{in} is more than several MΩ. Therefore, R_{eff} is derived as

$$R_{\mathrm{eff}} = \frac{R_{\mathrm{p}} R_{\mathrm{p},2}}{R_{\mathrm{p}} + R_{\mathrm{p},2}} \approx \frac{R_{\mathrm{p}} R_{\mathrm{in}}/\kappa^2}{R_{\mathrm{p}} + R_{\mathrm{in}}/\kappa^2}. \tag{3.38}$$

By inserting Eq. (3.38) into Eq. (3.31) and Eq. (3.32), it turns out that $\Delta\nu_z$ decreases as κ increases, and SNR increases while κ increases. $\Delta\nu_z$ can be tuned in a range of $1 \sim 5\,\mathrm{Hz}$, depending on the requirement for each trap systems. Therefore, the parallel resistance R_{p} of the resonator as well as the parasitic input resistance R_{in} of the cryogenic amplifier must be as large as possible to obtain a large SNR for the same $\Delta\nu_z$. As a consequence, the axial frequency scatter σ improves for fixed averaging time t_{avg}, and dip-width $\Delta\nu_z$ (see Eq. (3.30)).

By also taking a look once again on Eq. (3.32), the equivalent input noise e_{n} of the amplifier needs to be small as possible to obtain a high SNR. To understand which component contributes the most to e_{n}, it is necessary to consider how the amplifier board is developed. As will be described in the experimental setup part in chapter 6, the amplifier consists of a common-source circuit for the input stage and a source-follower circuit for the output stage. By defining an equivalent noise of the input stage and the output stage as $e_{\mathrm{n},1}$ and $e_{\mathrm{n},2}$ respectively,

$$e_{\mathrm{n}} = \sqrt{e_{\mathrm{n},1}^2 + \frac{e_{\mathrm{n},2}^2}{G_1^2}} \tag{3.39}$$

is obtained. Therefore, $e_{\mathrm{n}} \approx e_{\mathrm{n},1}$ holds when $G_1 \gg 1$. As a conclusion, it is necessary to adopt a FET for the input stage which has not only large R_{in}, but also small e_{n} as much as possible. The characterisation of e_{n} of our cryogenic amplifiers is described in section 6.1.2.

3.4 Sideband coupling technique

The sideband coupling technique is frequently applied to determine the radial eigenfrequencies ν_+ and ν_-, cooling the radial modes n_+ and n_-, and determination of the effective temperatures. In references [45, 49], the technique is described in detail. In this section, the principle of this method is summarised.

By applying an rf-drive with a frequency ω_{rf} and a quadrupolar field amplitude E_0 to the trap electrodes, it couples two modes

$$\vec{E}(x_j, x_k) = \mathrm{Re}(E_0 \exp(i\omega_{\mathrm{rf}} t))(x_j \vec{e}_k + x_k \vec{e}_j) \tag{3.40}$$

at the sum and the difference frequency $\omega_{\rm rf} = \omega_j \pm \omega_k$ of the two modes, which are described by the coordinates x_j and x_k, and frequencies ω_j and ω_k. Therefore, following differential equations are obtained describing the corresponding dynamics

$$\frac{d^2x_j}{dt^2} + \omega_j^2 x_j = \frac{qE_0}{m}\exp(i\omega_{\rm rf}t)x_k \tag{3.41}$$

$$\frac{d^2x_k}{dt^2} + \omega_k^2 x_k = \frac{qE_0}{m}\exp(i\omega_{\rm rf}t)x_j. \tag{3.42}$$

Assuming that the rf-field amplitude E_0 is smaller than the field strengths defining the unperturbed mode dynamics, which is applicable for our experimental condition, the transformation

$$x_j \to \frac{X_j(t)}{\sqrt{\pi m\omega_j}}\exp(i\omega_j t) \tag{3.43}$$

$$x_k \to \frac{X_j(t)}{\sqrt{\pi m\omega_k}}\exp(i\omega_k t) \tag{3.44}$$

leads to a non-diagonal system matrix with vanishing trace and complex eigenvalues, which turns out to be equivalent to an oscillating system. The energy transfer rate is defined by the drive strength and can be expressed in terms of a Rabi frequency

$$\Omega_0 = \frac{qE_0}{2m\sqrt{\omega_j\omega_k}}. \tag{3.45}$$

For instance, the coupling of the magnetron mode to the axial mode is described as following. Assume that the initial axial amplitude of the trapped particle is zero, and the magnetron mode has a certain amplitude. In this condition, a resonant coupling drive with a frequency $\omega_{\rm rf} = \omega_z + \omega_- + \delta$ ($\delta = 0$) is applied. Due to the energy transfer between the modes, the mode trajectories can be parameterised as

$$z(t) = z_0 \sin\left(\frac{\Omega_0}{2}t\right)\sin(\omega_z t + \phi_z) \tag{3.46}$$

$$\rho(t) = \rho_{-,0} \sin\left(\frac{\Omega_0}{2}t\right)\sin(\omega_- t + \phi_-), \tag{3.47}$$

where ϕ_z and ϕ_- are absolute phases. The mode amplitudes z_0 and $\rho_{-,0}$ are modulated with the frequency $\Omega_0/2$. By performing a fourier transformation to Eq. (3.46), it gives modified eigenfrequencies $\omega_{\rm l,r} = \omega_z \mp \Omega_0/2$. This indicates that the axial frequency dip in the noise spectrum of the axial resonator (see Fig. 3.4) splits into two dips.

If the drive is not resonant $\delta \neq 0$, the following relation can be considered

$$\omega_{\rm l} + \omega_{\rm r} = 2\omega_z - \delta = \omega_z + \omega_{\rm rf} - \omega_-. \tag{3.48}$$

Therefore, by measuring ν_z, ν_l and ν_r from the spectra, the magnetron frequency ω_- is obtained from Eq. (3.48). This method is applicable for obtaining the modified cyclotron frequency ω_+, except for the sign in the drive frequency. If the particle is driven with a sideband $\omega_\mathrm{rf} = \omega_+ - \omega_z + \delta$ the same argumentation holds as following:

$$\omega_\mathrm{l} + \omega_\mathrm{r} = 2\omega_z - \delta = \omega_z - \omega_\mathrm{rf} + \omega_+. \tag{3.49}$$

The precision of the free cyclotron frequency ν_c is dominated by the measured precision of the modified cyclotron frequency ν_+. This is verified by applying a Gaussian error propagation to the invariance theorem as

$$\Delta\nu_\mathrm{c} = \sqrt{\left(\frac{\nu_+}{\nu_\mathrm{c}}\Delta\nu_+\right)^2 + \left(\frac{\nu_z}{\nu_\mathrm{c}}\Delta\nu_z\right)^2 + \left(\frac{\nu_-}{\nu_\mathrm{c}}\Delta\nu_-\right)^2}. \tag{3.50}$$

In order to measure ν_c with a fractional precision in the p.p.b. range, the measurement precision of the magnetron frequency of about 100 Hz is sufficient. Therefore, in most of the cases the magnetron frequency ν_- is neglected for the measurement cycle and determined only once per day [23,50,51].

The sideband coupling technique described above can be applied to cool the radial modes. This is due to the fact that the frequencies are measured by mode coupling to the thermal bath of the axial detector, which has an effective temperature T_z. If the initial state of the trapped particle is (n_z, n_-) and interacts with an photon with energy $\hbar(\omega_z + \omega_-)$, two ways of the transition is possible

$$(n_z, n_-) \rightarrow (n_z + 1, n_- - 1) \tag{3.51}$$

$$(n_z, n_-) \rightarrow (n_z - 1, n_- + 1) \tag{3.52}$$

Equation (3.51) implies that this process increases the magnetron amplitude ("heating"), whereas Eq. (3.52) shows that the amplitude decreases ("cooling") for this process. Considering the fact that the transition rate of Eq. (3.51) and Eq. (3.52) scale with $\propto (n_z + 1)n_-$ and $\propto n_z(n_- + 1)$ respectively, the cooling process dominates as long as $n_- > n_z$ until the equilibrium state $n_z = n_-$ is reached. For the limit effective temperature, the relation

$$T_- = \frac{\omega_-}{\omega_z} T_z \tag{3.53}$$

is found. As will be presented in section 10.4, the effective magnetron temperature of $T_- \approx 0.1\,\mathrm{K}$ can be achieved. In this condition, the magnetron energy can be cooled down to $T_- =$

$|E_-|/k_B \approx 100\,\mu\mathrm{K}$ within few minutes. This argument also holds for the modified cyclotron frequency as

$$T_{+,\mathrm{SB}} = \frac{\omega_+}{\omega_z} T_z \approx 350\,\mathrm{K}, \tag{3.54}$$

which is a factor of 40 larger than the temperature achieved by resistive cooling with the cyclotron detector $T_+ \approx 8\,\mathrm{K}$ (see section 10.4.1).

3.5 Active feedback cooling

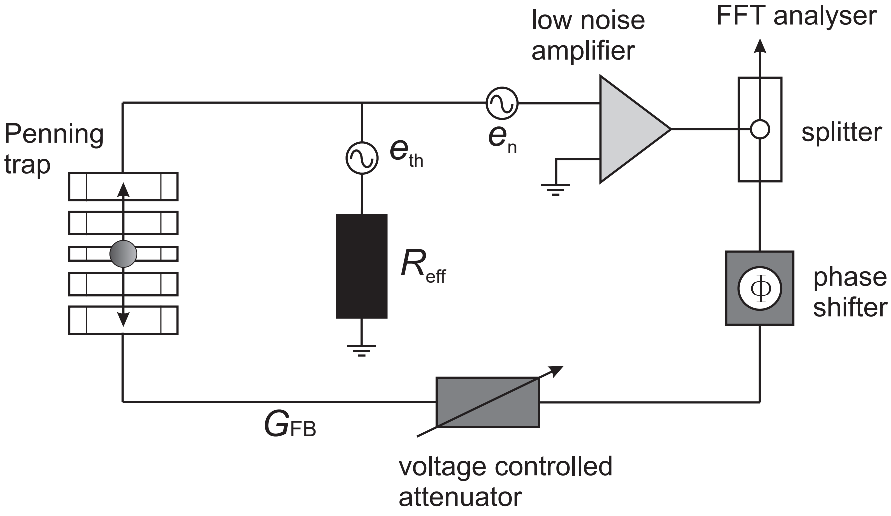

Fig. 3.8: Schematic of a active feedback loop to manipulate the effective temperature as well as the Q-value of the detection system.

Decreasing the temperature of the trapped antiproton leads to a decrease of the line-width of the cyclotron resonance and the Larmor resonance, consequently it leads to increase the experimental precision. By applying active feedback cooling method [52], it is possible to manipulate the detector temperature T by controlled feedback. A schematic of the technique is presented in Fig. 3.8. The detector is represented by the effective parallel resistance R_{eff} in series to the thermal noise source e_{th}. The low noise amplifier is represented by the equivalent input noise e_{n}. The accumulated noise is picked up, amplified and fed back to the trap via a splitter, phase shifter, and a voltage controlled attenuator. The feedback gain G_{FB} can be adjusted by the voltage controlled attenuator.

Considering that a voltage drop V_{p} occurred when the particle current i_{p} flows through the resistor R_{eff}, the feedback signal manipulates the particle motion. The signal is instantaneously fed back to the particle with feedback-gain G_{FB}. Seen from the particle, the effect of G_{FB} looks like a resistor with modified absolute value $R_{\mathrm{eff,mod}}$.

Taking into account that V_{p} is identical to $V_{\mathrm{p,mod}}$, the relation to these effective values is evaluated as

$$V_{\mathrm{p}} = i_{\mathrm{p}} R_{\mathrm{eff}} \pm G_{\mathrm{FB}} i_{\mathrm{p}} R_{\mathrm{eff}} \tag{3.55}$$

$$V_{\mathrm{p,mod}} = i_{\mathrm{p}} R_{\mathrm{eff,mod}} \tag{3.56}$$

$$R_{\mathrm{eff,mod}} = R_{\mathrm{eff}}(1 \pm G_{\mathrm{FB}}). \tag{3.57}$$

Equation (3.57) is derived by equating Eq. (3.55) and Eq. (3.56). The effective temperature T_{eff} is derived by the same argument as for the case of the resistors, and it can be written as

$$T_{\mathrm{eff}} = T_0(1 \pm G_{\mathrm{FB}}), \tag{3.58}$$

where T_0 is the temperature of the detection system. From Eq. (3.58), applications of the feedback affects the temperature of the particle. Negative feedback [53] reduces its temperature, whereas the positive feedback increases. In practice, we apply feedback on the axial mode to reduce the line-width of the cyclotron and Larmor resonances. Negative feedback is in particular also important for the cyclotron mode to effectively cool the particle to a subthermal energy. This is essential for the spin-transition detection because not only the spin, but also the cyclotron energy E_+ couples. A cyclotron quantum transition Δn_+ shifts the axial frequency by 63 mHz, which leads to axial frequency fluctuations. This eventually limits the detectability of the spin-state. The rate of the quantum jump dn_+/dt is low while the cyclotron energy is small (see section 10.4.1). Therefore, aiming for a high resolution on the antiproton spin-state spectroscopy, an efficient cooling of the cyclotron mode is crucial.

Chapter 4

Non-destructive detection of the spin-state

The first observation of spin-flips of the proton was demonstrated at the University of Mainz and reported in 2011 [54,55]. The basic principle of this measurement can be directly applied to the antiproton. In this chapter, the principle of the non-destructive detection of the antiproton's spin-transition is described in detail.

4.1 Continuous Stern-Gerlach effect

Spin-transitions of a trapped antiproton can be induced by an rf field. Since the spin precession does not induce any image-currents in the electrodes as the three eigenmotions, the transition is not accessible by using image-current detections (see chapter 3). To overcome this difficulty, a quadratic inhomogeneity in the magnetic field, which we call the *magnetic bottle*, is produced by a ferromagnetic ring electrode at the centre of the analysis trap (AT). In this condition, the magnetic field $\vec{B}(\rho,z)$ at the centre of the trap can be expressed as

$$\vec{B}(\rho,z) = B_0\vec{e}_z + B_2\left(\left(z^2-\frac{\rho^2}{2}\right)\vec{e}_z - \rho z\vec{e}_\rho\right). \tag{4.1}$$

Note that Eq. (4.1) represents an expansion up to the second-order, which is the leading magnetic field perturbation. The equation of motion of an antiproton stored in a Penning trap with such a superimposed magnetic bottle is

$$\begin{aligned} F(z) = -\frac{\partial\Phi_\mathrm{V}(z)}{\partial z} - \frac{\partial\Phi_\mathrm{M}(z)}{\partial z} &= -2C_2qV_0z - \frac{\partial}{\partial z}\left(\mu_\mathrm{total}(B_0+B_2z^2)\right) \\ &= -(2C_2qV_0 + 2\mu_\mathrm{total}B_2)z. \end{aligned} \tag{4.2}$$

Here, Φ_V is the voltage potential, Φ_M is the magnetic field potential and $\mu_\mathrm{total} = \mu_+ + \mu_- + \mu_\mathrm{s}$ is the total magnetic moment which is the sum of angular momenta of the cyclotron mode μ_+

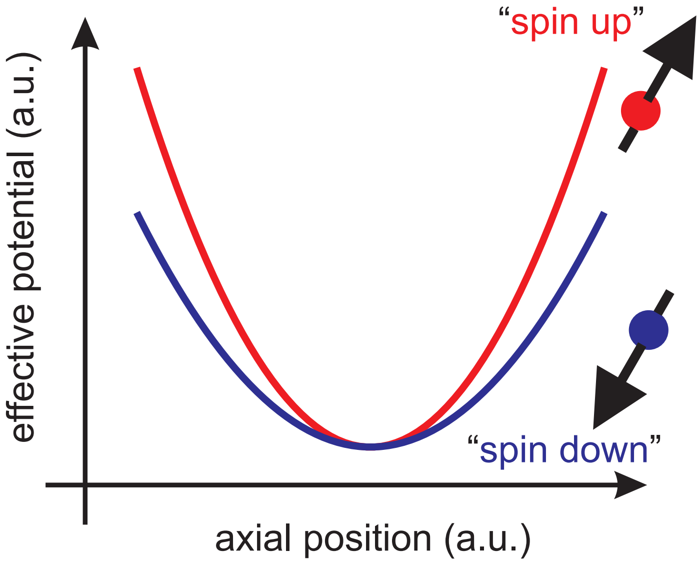

Fig. 4.1: Schematic of the continuous Stern-Gerlach effect. In the magnetic bottle, the effective axial potential is dependent on the particle's spin-state. In the case of the antiproton, the axial frequency ν_z is larger for the spin-up state than that of the spin-down state. By using this principle, the non-destructive detection of spin-transitions become possible.

and the magnetron mode μ_- as well as a spin magnetic moment μ_s. Equation (4.2) is nothing but a simple harmonic oscillator with an angular axial frequency ω_z of

$$\omega_z = \omega_{z,0}\sqrt{1+\frac{2\mu_\mathrm{total}B_2}{m_\mathrm{p}\omega_{z,0}^2}}. \tag{4.3}$$

Here, $\omega_{z,0}$ is the angular axial frequency in absence of the magnetic bottle $B_2 \approx 0$. Equation (4.3) can be approximated by performing a first order of Taylor expansion as

$$\begin{aligned} \nu_z &\approx \nu_{z,0}+\frac{\mu_\mathrm{total}B_2}{4\pi^2 m_\mathrm{p}\nu_{z,0}} \\ &= \nu_{z,0}+\frac{h\nu_+}{4\pi^2 m_\mathrm{p}\nu_{z,0}}\cdot\frac{B_2}{B_0}\cdot\left(n_+ + \frac{1}{2} + \frac{\nu_-}{\nu_+}\left(n_- + \frac{1}{2}\right) + \frac{g m_\mathrm{s}}{2}\right), \end{aligned} \tag{4.4}$$

where n_+, n_- and $m_\mathrm{s} = \pm\frac{1}{2}$ is the principal quantum number of the cyclotron mode, the magnetron mode and the spin-state, respectively. This is one of the most important relations when dealing with a magnetic bottle, since it implies that the axial oscillation frequency ν_z depends not only on the trapping voltage potential, but also on n_+, n_- and m_s. Therefore, when a spin-transition occurs $\Delta m_\mathrm{s} = \pm 1$, the axial frequency ν_z will be shifted by

$$\Delta\nu_{z,\mathrm{SF}} = \frac{\mu_\mathrm{s}B_2}{2\pi^2 m_\mathrm{p}\nu_{z,0}} = g\frac{q\hbar B_2}{8\pi^2 m_\mathrm{p}^2\nu_{z,0}}. \tag{4.5}$$

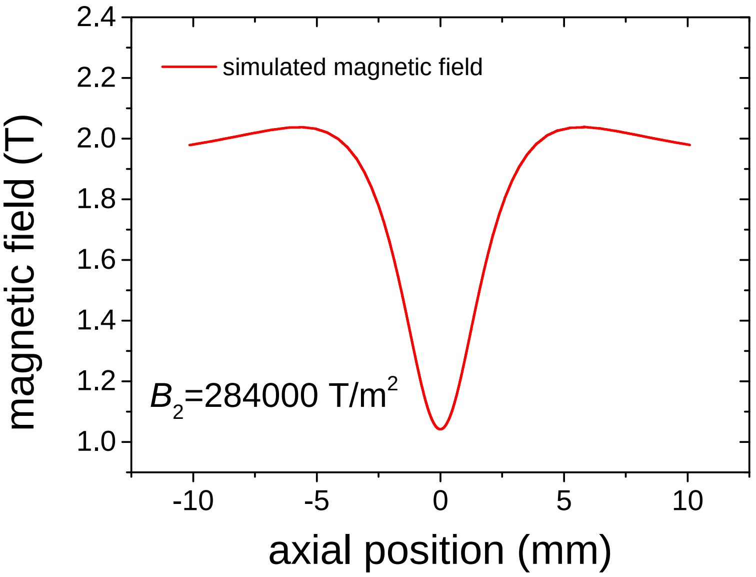

Fig. 4.2: Simulated result of the magnetic bottle. By fitting this curve, $B_2 = 284000\,\mathrm{T/m^2}$ is extracted. The magnetic field configuration for the entire Penning-trap assembly is shown in Fig. 5.8.

By using this method, basically it is possible to clearly identify the spin-state by recording the axial frequency ν_z. This principle of identifying the spin-state is called the *continuous Stern-Gerlach effect* (a schematic of this effect is shown in Fig. 4.1). It has been introduced and applied by Hans Dehmelt, who measured the magnetic moments of the electron and the positron by using this method [38]. However, the application of this technique to the proton/antiproton is very challenging since a spurious noise on the trap electrodes induces the quantum transitions in the radial modes as $\Delta n_+ = 62\,\mathrm{mHz}$ and $\Delta n_- = 42\,\mu\mathrm{Hz}$, which consequently unstabilise the axial frequency. Additionally, for given B_0 and B_2, $\Delta\nu_{z,\mathrm{SF}}$ is about ten thousand times smaller for the antiproton than for the electron and the positron. This indicates that it is incredibly challenging to resolve spin-flips for the proton/antiproton system compared to the electron/positron system. In order to overcome this challenge, the BASE experiment utilises a ferromagnetic material of FeCo for the ring electrode of the AT to create the strongest magnetic bottle which has ever been superimposed on a Penning trap $B_2 \approx 284\,000\,\mathrm{T/m^2}$ (the value is derived from a simulation as shown in Fig. 4.2). With this condition, $\Delta\nu_{z,\mathrm{SF}} \approx 180\,\mathrm{mHz}$ out of $675\,\mathrm{kHz}$ is achieved, which is large enough to resolve spin-flips as long as the axial frequency ν_z is sufficiently stable (see chapter 10).

In the strong magnetic bottle, the radial frequencies are also dependent on the energy of the eigenmotions. From Eq. (4.1), the following relations are derived by using simple algebra:

$$\Delta\omega_+ = \frac{\omega_+}{m_p\omega_{z,0}^2}\cdot\frac{B_2}{B_0}\left(-\frac{\omega_z^2}{\omega_+^2}\Delta E_+ - 2\Delta E_- + 2\Delta E_z\right) \tag{4.6}$$

$$\Delta\omega_- = \frac{\omega_-}{m_p\omega_{z,0}^2}\cdot\frac{B_2}{B_0}(2\Delta E_+ + 2\Delta E_- - \Delta E_z) \tag{4.7}$$

$$\Delta\omega_L = \frac{\omega_L}{\omega_C}\cdot\Delta\omega_+. \tag{4.8}$$

In Eq. (4.6) and Eq. (4.7), the scaling with the radial energies ΔE_+ and ΔE_- is due to the fact that the axial component of the magnetic field decreases with increasing radius in the magnetic bottle. On the other hand, the dependency on ΔE_z is caused by the increase of B_z with the axial coordinate z. The axial oscillation of the particle leads to a positive shift of the magnetic field seen by the particle since

$$\langle B_2 z(t)^2\rangle = \langle B_2 z_0^2\cos^2(\omega_z t)\rangle = \frac{B_2 z_0^2}{2} = \frac{B_2 E_z}{m_p\omega_z^2}. \tag{4.9}$$

4.2 Larmor resonance line-shape in the magnetic bottle

This section describes the line-shape of the Larmor resonance in presence of the magnetic bottle. When the particle oscillates along the z-axis, the magnetic field seen by the particle changes on the time scale $\tau_z = 1/\omega_z$ as

$$B(z_0,t) = B_0 + B_2 z_0^2\sin^2(\omega_z t), \tag{4.10}$$

where z_0 is the amplitude of the axial oscillation. This leads to a time dependent Larmor frequency

$$\omega_L = \frac{g}{2}\omega_{c,0}\left(1+\frac{B_2}{B_0}z_0^2\sin^2(\omega_z t)\right) = \omega_{L,0}\left(1+\frac{B_2}{B_0}z_0^2\sin^2(\omega_z t)\right). \tag{4.11}$$

Here, $\omega_{L,0}$ is the Larmor frequency in the centre of the trap. By taking the average of Eq. (4.11),

$$\omega_L = \omega_{L,0}\left(1+\frac{B_2}{2B_0}\langle z_0^2\rangle\right). \tag{4.12}$$

As described in chapter 3, in practice the axial amplitude is not constant, since the particle is continuously interacting with the thermal heat bath of the axial detector which has a temperature of $T_z = 8.0(1.0)\,$K. The damping constant $\gamma_z = (q^2 R_{\text{eff}})/(D^2 m_p)$ leads to a fluctuation on the particle's axial energy E_z on timescales $\propto 1/\gamma_z$. Due to the equipartition theorem,

$$\frac{1}{2}m_p\omega_z^2\langle z_0^2\rangle = \frac{1}{2}k_B T_z \leftrightarrow \langle z_0^2\rangle = \frac{k_B T_z}{m_p\omega_z^2}. \tag{4.13}$$

The correction term $\delta\omega_\mathrm{L}$ in Eq. (4.12) for typical thermal amplitudes will be

$$\frac{\delta\omega_\mathrm{L}}{2\pi} = \frac{\omega_{\mathrm{L},0}}{2\pi}\frac{B_2}{B_0}\langle z_0^2\rangle = \frac{\omega_{\mathrm{L},0}}{2\pi}\frac{B_2}{B_0}\frac{k_\mathrm{B}T_z}{m_p\omega_z^2} \approx 5.9\,\mathrm{kHz}\cdot\mathrm{K}^{-1}. \tag{4.14}$$

ω_L is called *linewidth parameter*. Consequently, the interaction between the axial detector causes a broadening of the resonance line. The line-shape is well-described in a reference [56] and given as

$$\chi(\omega) = \frac{4}{\pi}\mathrm{Re}\left[\frac{\tilde{\gamma}\gamma_\mathrm{z}}{(\tilde{\gamma}+\gamma_\mathrm{z})^2}\sum_\mathrm{n}\frac{(\tilde{\gamma}-\gamma_\mathrm{z})^{2\mathrm{n}}(\tilde{\gamma}+\gamma_\mathrm{z})^{-2\mathrm{n}}}{\left(\mathrm{n}+\frac{1}{2}\right)\tilde{\gamma}-\frac{\gamma_\mathrm{z}}{2}-i(\omega-\omega_{\mathrm{L},0})}\right], \tag{4.15}$$

where $\tilde{\gamma} = \sqrt{\gamma_z^2 + 4i\gamma_z\delta\omega_\mathrm{L}}$. Equation 4.15 shows a superposition of Lorentzian functions and the real part of $\tilde{\gamma}$ leads to the line-width of the Larmor resonance. The complex part of $\tilde{\gamma}$ gives a frequency shift, due to the fact that the line-width parameter $\delta\omega_\mathrm{L}$ scales as z^2, and the axial oscillation does not average to zero.

The line-shape $\chi(\omega)$ simplifies in two limits:

- Weak coupling $\delta\omega_\mathrm{L} \gg \gamma_z$.
- Strong coupling $\delta\omega_\mathrm{L} \ll \gamma_z$.

Since our condition is $\delta\omega_\mathrm{L}/\gamma_z \approx 1000\mathrm{K}^{-1}\cdot\mathrm{T_z}$, the first case can be applied. Refer to [56] for the discussion of the second case. When the particle is weakly coupled to the axial detector, the axial amplitude remains constant in a time window $\propto 1/\delta\omega_\mathrm{L}$. In a sequence of idealised measurements of the Larmor resonance, the observed line-shape is a convolution of the unperturbed infinitesimally narrow Lorentzians which is Boltzmann distributed. By solving an integral for the corresponding convolution, it leads to the total line-shape [56] as

$$\chi_\mathrm{week}(\omega) = \frac{\Theta(\omega-\omega_{\mathrm{L},0})}{\delta\omega_\mathrm{L}}\exp\left(-\frac{(\omega-\omega_{\mathrm{L},0})}{\delta\omega_\mathrm{L}}\right). \tag{4.16}$$

Here, $\Theta(\omega-\omega_{\mathrm{L,L}})$ is the Heaviside function. Equation (4.16) shows an exponential function starting at a ”cut frequency $\omega_{\mathrm{L,cut}}$”, which is defined by the zero effective temperature of the Boltzmann distribution $\omega_{\mathrm{L,cut}}(E_z = 0)$. The cut frequency of the line-shape is used to determine the antiproton g-factor in the magnetic bottle (see chapter 11).

4.3 Spin-transition rates

Spin-transitions can be induced by the classical Rabi resonance principle [57]. As will be described in section 11.1, a transverse magnetic rf-field $\vec{b}_\mathrm{rf}$ with frequency ν_rf is generated by a spin-flip coil near the AT, and it will be irradiated at the trapped antiproton. When the drive is on resonance to the Larmor frequency $\nu_{\mathrm{rf}} = \nu_{\mathrm{L}}$, the antiproton's spin starts to precess around $\vec{b}_{\mathrm{rf}}$ with the Rabi oscillation frequency of $\Omega_{\mathrm{R}} = 2\pi\nu_{\mathrm{L}} b_{\mathrm{rf}}/B_0$, which effectively driving spin-flips. This dynamics can be discussed by a time-dependent perturbation theory with

$$H = H_0 + H_{\mathrm{SF}} = H_0 - \mu_{\mathrm{s}} \cdot \vec{b}_{\mathrm{rf}}(t), \tag{4.17}$$

where H_0 is the free Penning trap Hamiltonian and $H_{\mathrm{SF}} = -\mu_{\mathrm{s}} \cdot \vec{b}_{\mathrm{rf}}(t)$ represents the interaction of the spin magnetic moment μ_{s} with the rf-drive. The spin-transition rate when dealing with an inhomogeneous magnetic field is described in a reference [56] and can be expressed as

$$P_{\mathrm{SF}} = \frac{1}{2}\left(1 - \exp\left(-\frac{1}{2}\Omega_{\mathrm{R}}^2 t_0 \chi_{\mathrm{week}}(2\pi\nu_{\mathrm{rf}}, B_2, T_z)\right)\right). \tag{4.18}$$

Here, t_0 is the irradiation time of the rf-drive and $\chi_{\mathrm{week}}(2\pi\nu_{\mathrm{rf}}, B_2, T_z)$ is the line-shape function (Eq.(4.16)). The maximum spin-flip probability $P_{\mathrm{SF}} = 50\,\%$ is achieved for resonant drive and adequate drive amplitude $|\vec{b}_{\mathrm{rf}}|$. In S. Ulmer's PhD thesis [54], it studies in detail how P_{SF} changes by varying t_0, $|\vec{b}_{\mathrm{rf}}|$ and T_z, and how to optimise these parameters to obtain the maximum P_{SF}. According to [54], the axial detector temperature T_z needs to be as small as possible to achieve a high resolution on measuring the Larmor frequency in the magnetic bottle. It can be reduced by applying a negative feedback technique (see section 3.5).

Comparing the spin-transitions to electric dipole transitions, for instance a single quantum transition of the modified cyclotron mode Δn_+, it requires relatively large field strength $|\vec{b}_{\mathrm{rf}}| \approx 2\,\mu\mathrm{T}$ in order to reach the maximum transition probability. Cyclotron quantum transitions can be driven with high transition probability , already with effective $\vec{E}$-field amplitudes in the sub-nV range.

4.4 Double trap method

In the magnetic bottle, the Larmor frequency ω_{L} and the free cyclotron frequency ω_{c} are dependent on the motional amplitudes as shown in Eq.(4.11), which leads to a broadening of the g-factor resonance and ultimately limits the determination of the spin-state to a fractional precision of order parts per million. To overcome this limitation, the spin-state analysis and these frequency measurements are separated to two traps, an analysis trap (AT) and a precision trap (PT). This method has been developed at the University of Mainz by Harmut Häffner and colleagues [58] to measure the magnetic moment of the electron bound to highly charged ions.

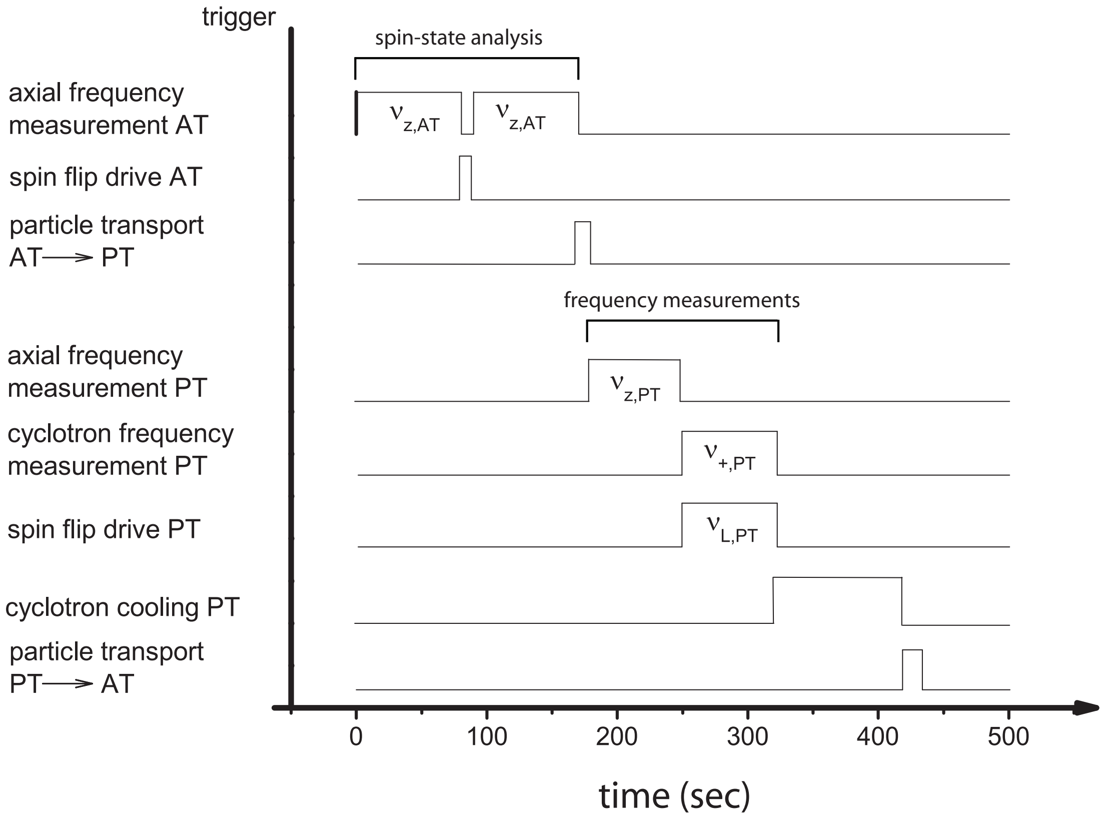
trigger
spin-state analysis
axial frequency measurement AT
ν z,AT
ν z,AT
spin flip drive AT
particle transport AT ⟶ PT
frequency measurements
axial frequency measurement PT
ν z,PT
cyclotron frequency measurement PT
ν +,PT
spin flip drive PT
ν L,PT
cyclotron cooling PT
particle transport PT ⟶ AT
0
100
200
300
400
500
time (sec)

Fig. 4.3: Procedure of the double trap method, which separates the identification of the spin-state and the high-precision frequency measurements to two traps, an analysis trap (AT) and a precision trap (PT).

In the AT, the magnetic bottle is superimposed and the spin-state analysis will be taken place by performing the Stern-Gerlach effect as described in the previous section. In addition to the AT, the PT is utilised, which has a high homogeneous magnetic field at the centre of the trap (see Table 5.2 for numbers). There, the measurements of the cyclotron frequency takes place and spin-transitions are induced. Whether the spin was flipped or not is then determined in the AT. The magnetic field homogeneity in the PT is by a factor of 100 000 times more homogeneous than in the AT. This narrows down the width of the g-factor resonance at the level of p.p.b. and allows for measurements at much improved precision. The BASE experiment at the University of Mainz applied this scheme, the so-called double trap method, to measure the magnetic moment of the proton [24]. The obtained fractional precision from this measurement was 3.3 p.p.b.. The ultimate goal of BASE is to implement this technique for the antiproton in the future.

Figure 4.3 shows the procedure of the double trap method [58]. First, a single particle is trapped in the AT and the spin-state analysis will be performed. Subsequently, the particle is transported to the PT and the free cyclotron frequency ω_c measurement will be carried out. At the same time, a spin-flip drive with frequency ω_{rf} is irradiated. After transporting the particle back to the AT, the spin-state is determined again. From this cycle, it is possible to conclude whether the spin has flipped or not by the rf drive ω_{rf} in the PT. This sequence is repeated over several hundred times for different drive frequencies ω_{rf} and eventually a g-factor resonance will be obtained. This scheme prevents the limitation of the experimental precision and it significantly reduces the line width of the g-factor resonance [24]. An application of this technique is definitely the next step for improving the precision on the antiproton's g-factor, since the current best value is still at sub-p.p.m. level (see chapter 11) and it is expected to be improved by more than a factor of 100.

Part III

Experimental Setup

Chapter 5

BASE experiment

The description of this chapter follows the red line of a review article on the BASE experiment, authored by Chrstian Smorra *et al* [13]. I have contributed to many aspects of assembling and commissioning of the BASE experiment and have co-authored the article.

5.1 Antiproton decelerator and antiproton transfer line

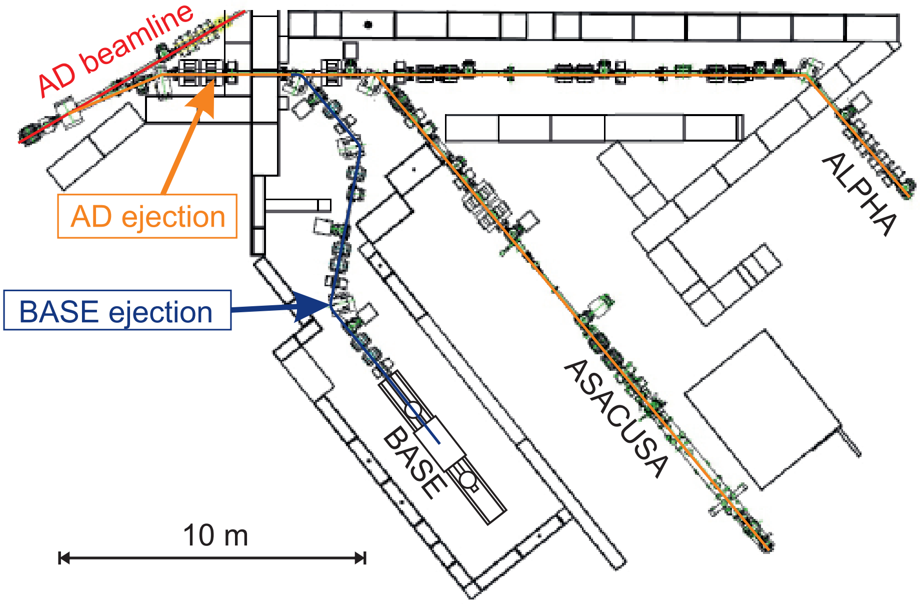
AD beamline
AD ejection
BASE ejection
ALPHA
ASACUSA
BASE
10 m

Fig. 5.1: Top view drawing of the BASE experimental zone and the AD facility. Taken from [13].

The BASE experiment is located at the Antiproton Decelerator (AD) facility of CERN, Geneva, Switzerland. The AD is the only facility which produces and supplies high-intensity pulses of low-energy antiprotons [59]. In order to create antiprotons, first of all protons are accelerated up to a momentum of 26 GeV/c by using a linear accelerator (LINAC), the Proton Synchrotron Booster (PSB), and the Proton Synchrotron (PS) of CERN [60]. After the acceleration process, an intense pulse of 10^{13} protons is focused on an iridium target which generates a highly divergent pulse of antiprotons in pair creation processes. Subsequently, the created antiprotons are focused by a magnetic horn, which allows to transfer about 50 million antiprotons at 3.5 GeV/c momentum from the target into the AD. Once the antiproton beam is injected to the AD, it experiences alternating cooling and deceleration steps. To decrease the transverse emittance, stochastic cooling is applied at the initial momentum of 3.5 GeV/c and after the first deceleration step at 2.0 GeV/c, and electron cooling at the lower momenta of 300 MeV/c and 100 MeV/c. After a cycle length of 120 s, a bunch of approximately 30 million antiprotons with a kinetic energy of 5.3 MeV and a pulse length of about 150 ns is provided to the experiments.

To transfer antiprotons to the BASE apparatus, a new ejection beamline from the AD was constructed. Figure 5.1 shows a top view drawing of the BASE experimental zone at the AD facility. The design of the AD ejection beamline to provide decelerated antiprotons to the BASE apparatus is shown in Fig. 5.2.

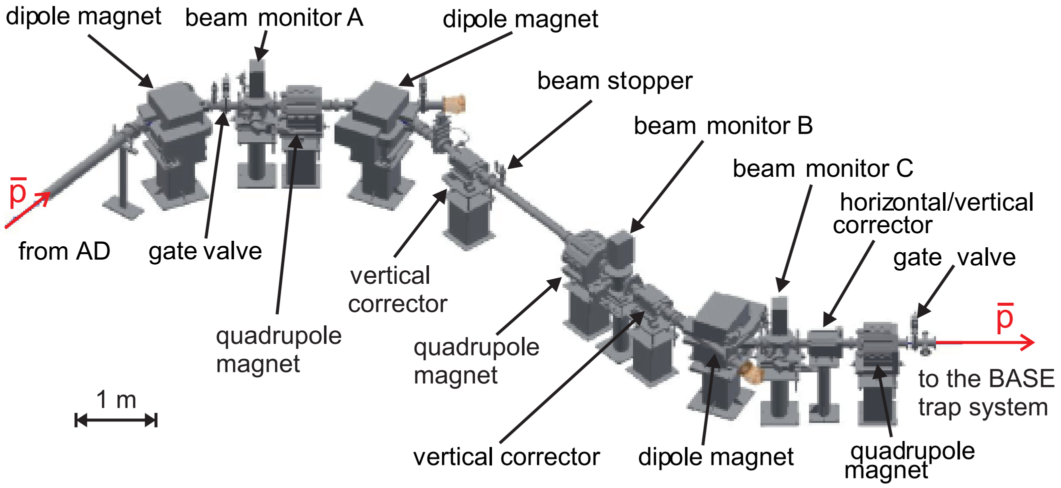
dipole magnet
beam monitor A
dipole magnet
beam stopper
beam monitor B
beam monitor C
horizontal/vertical corrector
gate valve
$\bar{p}$
from AD
gate valve
vertical corrector
quadrupole magnet
quadrupole magnet
$\bar{p}$
to the BASE trap system
1 m
vertical corrector
dipole magnet
quadrupole magnet

Fig. 5.2: Schematic of the BASE beamline. Taken from [13].

5.2 BASE apparatus

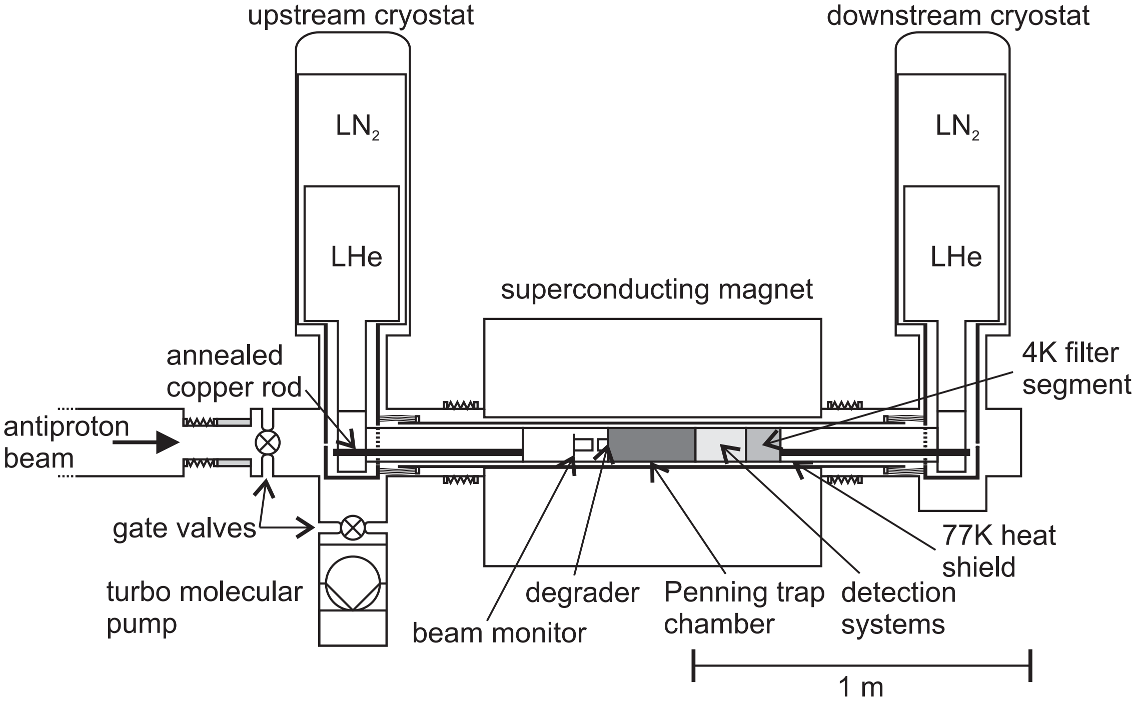
upstream cryostat
downstream cryostat
LN$_2$
LN$_2$
LHe
LHe
superconducting magnet
annealed copper rod
4K filter segment
antiproton beam
gate valves
77K heat shield
turbo molecular pump
degrader
Penning trap chamber
detection systems
beam monitor
1 m

Fig. 5.3: Overview of the BASE apparatus. Taken from [13].

In the BASE zone at the AD facility, an experimental apparatus which is dedicated to high-precision measurements of the fundamental properties of the antiproton was constructed. An overview of the BASE apparatus is shown in Fig. 5.3.

The Penning-trap system is installed inside the horizontal bore of a superconducting magnet (*Oxford instruments*). The trap system is placed inside a hermetically sealed cryogenic vacuum chamber, which is cooled to liquid helium (LHe) temperature by the two cryostats placed upstream and downstream of the superconducting magnet. The LHe stages of the two cryostats hold the trap chamber in the magnet bore inside an isolation vacuum. The axial/cyclotron detection systems, a segment with cryogenic electronics devices and filters for the DC voltage biasing of the Penning-trap electrodes are also installed at the LHe stage next to the trap chamber. The antiprotons provided by the AD are injected into the Penning-trap system through a degrader system, which decelerates the antiprotons to sufficiently low energies so that it allows to capture them by manipulating high voltage potentials (refer to section 7.1 for further details). The degrader system separates the isolation vacuum $< 10^{-8}$ mbar from the trap vacuum. Moreover it has been carefully designed to reduce the energy of a fraction of about a 10^{-4} fraction of antiprotons to energies below 1 kV, which can be handled by the high-voltage electronics used in the experiment. A cryogenic beam monitor is implemented at the upstream of the trap chamber to align the antiproton beam to the trap centre.

5.3 Superconducting magnet

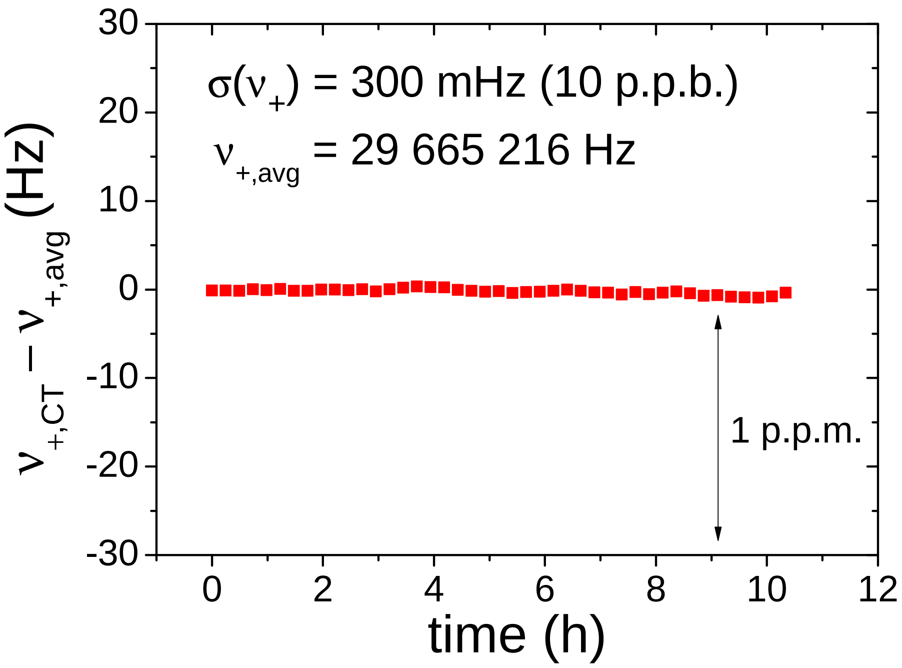

Fig. 5.4: Magnetic field of the superconducting magnet measured with the co-magnetometer particle while a Larmor frequency measurement was carried out in the analysis trap (see chapter 11).

To perform precise measurements of the g-factor as well as the charge-to-mass ratio of the antiproton by using Penning traps, it is necessary to adopt a superconducting magnet which has a highly homogeneous magnetic field with high temporal stability. This is because these magnetic field characteristics are strongly related to the measured precision of the Larmor frequency ν_{L} and the cyclotron frequency ν_{c}. Since the BASE apparatus is located inside of the AD facility where external magnetic field noise caused mainly by operations of the AD, crane actions and neighbouring experiments (these are well described in Takashi Higuchi's master thesis [61]), it is of utmost importance to have a good shielding factor S of self-shielding geometry inside of the magnet. S is the suppression of external magnetic field fluctuations at the centre of the superconducting solenoid by $S^{-1} = 1 + B_i/B_e$. For the superconducting magnet used for the antiproton g-factor measurement, $S \approx 1$. The horizontal room-temperature bore of 150 mm diameter houses the Penning-trap system as shown in Fig. 5.3. The magnet is operated at a field strength of 1.945 T. By adjusting the shim coils, a spatial homogeneity of 0.25 p.p.m./cm around the homogeneous centre and a homogeneity of 5 p.p.m./cm in a cylindrical volume of 9 mm diameter and 120 mm length was obtained. To further improve the self-shielding factor, a self-shielding coil is installed to stabilise the magnetic field flux in the Penning-trap chamber. Careful characterisations and the further improvement of the self-shielding coil will be one of the main projects for the future [62].

The magnitude of magnetic field drifts of the superconducting magnet is characterised by recording the modified cyclotron frequencies in the co-magnetometer trap during the g-factor measurement (see chapter 11). The result is shown in Fig. 5.4. It indicates that the magnetic field drift is $\Delta B_0/B_0 < 6 \times 10^{-9}/\mathrm{h}$ and $\delta B_0/B_0 < 1.5 \cdot 10^{-8}/10\,\mathrm{h}$, which is stable enough to perform the p.p.m. g-factor measurement carried out in the framework of my PhD studies.

5.4 Cryo-mechanical setup

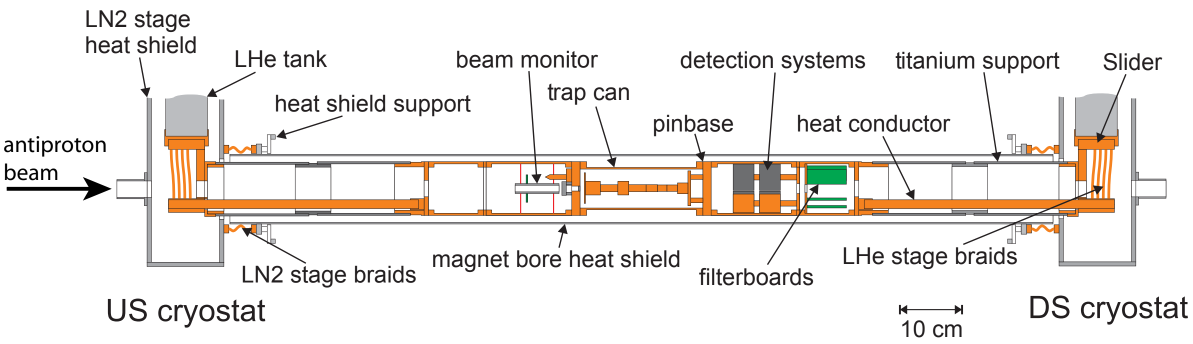
LN2 stage heat shield
LHe tank
beam monitor
detection systems
titanium support
Slider
heat shield support
trap can
pinbase
heat conductor
antiproton beam
LN2 stage braids
magnet bore heat shield
filterboards
LHe stage braids
US cryostat
10 cm
DS cryostat

Fig. 5.5: LN_2 and LHe stages of the BASE apparatus. See the text for the details. Taken from [13].

35 l liquid Nitrogen (LN_2) and 35 l liquid Helium (LHe) reservoirs are installed inside of the two cryostats in order to provide cryogenic temperatures to the experiment. The assembly of the cryostats and the experiment in its entirety is shown in Fig. 5.5. Using a two cryostat construction for a cryogenic experiment in horizontal geometry has the advantage that the LHe stage can be anchored at both ends to the LHe tanks without any needs for an additional support structure. This minimises the conductive heat load from the LN_2 stage on the LHe stage and

ensures a low LHe consumption rate on the LHe reservoirs.

The radiative load on the LHe stage is reduced by thermal shields connected to the LN_2 reservoirs of the cryostats. Inside the cryostats, rectangular heat shields made out of 8 mm thickness of aluminium plates enclose the tail of the LHe tanks and the supports of the 4 K stage. In the magnet bore, an aluminium tube of 127 mm diameter and 3 mm wall thickness is used as a radiation shield. It is mechanically anchored to the vacuum chambers at room temperature by using a fibre glass disk as thermal insulation. As thermal link, oxygen-free high conductivity (OFHC) copper braids of $600\,\mathrm{mm}^2$ cross section in total form a good connection to the cryostat heat shields. This compensates mechanical stress while cooling down to cryogenic temperatures. The complete LN_2 stage is enclosed in 20 layers of multi-layer insulation (MLI) foil. Thereby, a temperature of 80 K at the bottom of the cryostat heat shield and 86 K at the centre of the magnet bore heat shield are reached at a total load of 50 W. The standing time of the LN_2 stage is estimated to be about 70 hours and 58 hours for the upstream and downstream cryostat, respectively. The downstream cryostat has a higher evaporation rate due to the additional load from the trap biasing lines, particularly by the high-voltage lines.

The inlay of the LHe stage consists of a mechanical support, the cryogenic electronics, and the Penning-trap chamber. The latter is a cylindrical indium-sealed cryogenic vacuum chamber (71 mm inner diameter, 234 mm length) located at the centre of the 4 K stage enclosing the Penning-trap system. The chamber is made out of high-purity copper. A flange with cryogenic feedthroughs, the so-called pinbase (see section 5.9.3 for details), closes the trap chamber at the downstream side. All signals for the single-particle detection systems, trap biasing, particle excitation, spin-flip drive and the catching high voltage pulses are connected to the Penning traps via the pinbase. On the upstream side, the Penning-trap chamber is closed by the degrader flange, which has a stainless-steel foil of $25\,\mu\mathrm{m}$ thickness and 9 mm diameter placed in the centre. The foil is vacuum-tight but semi-transparent for the injected 5.3 MeV antiprotons. In addition, the flange has a connection for a pinch-off tube. In order to achieve ultra-high vacuum in the trap chamber, it is pumped out through this connection to a pressure of less than $10^{-6}\,\mathrm{mbar}$. Subsequently, the pumping connection is pinched-off with a cold-weld technique and the chamber is installed into the magnet bore. Placed in an isolation vacuum and cooled by the cryostats, the trap chamber forms an independent vacuum system with $6 \sim 7\,\mathrm{K}$ wall temperature. The residual gas pressure in the chamber drops below the detection threshold of conventional vacuum gauges. It eventually goes down to $10^{-14}\,\mathrm{mbar}$ [63] and can be only determined indirectly by the storage time of the trapped antiprotons. We have reported that the antiproton storage time can exceed one year in reference [14].

The mechanical support of the Penning-trap chamber is designed such that it is symmetric with respect to the centre plane of the superconducting magnet. As a consequence, it allows to avoid a tilt of the trap axis relative to the magnetic field due to unequal deformation of the support structure. Two high-purity copper segments are connected to the Penning-trap chamber on both sides. At the downstream-side, the single-particle detection systems and cryogenic filters for the trap biasing lines are contained. The upstream-side contains the beam monitor and parts of the degrader assembly. As next element, two titanium tubes of 170 mm length and 98 mm diameter with a titanium connection piece are placed on each side around the copper parts in the magnet centre. Even though titanium has a low heat conductivity at 4 K, it is selected for this part of the support structure since it has high stiffness and low weight. At each end of the LHe stage, a short copper tube of 30 mm length and 90 mm diameter rests in the cryostat support structure. To prevent mechanical stress due to the contraction during cool-down, the cryostat support structure is attached to a slider on a ball bearing at the bottom of the LHe reservoir. The slider compensates the mechanical contraction of the inlay.

To achieve a good thermal link of the trap chamber and the superconducting detectors to the LHe reservoirs, the copper segments in the centre of the LHe stage are connected to the cryostats with two heat conductors made from annealed OFHC copper rods of 16 mm diameter. On the trap side, the copper rods are bolted into the last copper segment, and on the cryostat side clamps with OFHC copper braids, which ensures the thermal link to the LHe reservoir. The braids have a total cross section of 360 mm^2 and 125 mm length. The thermal load on the LHe reservoirs by the cryogenic inlay is estimated to be 90 mW from radiative load, 15 mW conductive load due to wiring, and 20 mW load from operations of the cryogenic amplifiers. Considering the intrinsic heat load of the cryostats, the LHe stage is estimated to have a hold time of 120 hours.

5.5 Degrader system

To decelerate the 5.3 MeV antiprotons provided by the AD, degrader foils are implemented at the upstream-side of the trap chamber. Antiprotons lose their energies while penetrating the degrader material via inelastic scattering processes, and are eventually stopped at a certain range. If the thickness of the degrader foil is chosen to be thin enough, low-energy antiprotons are transmitted through the degrader and can be captured in the reservoir trap (see section 7.1)

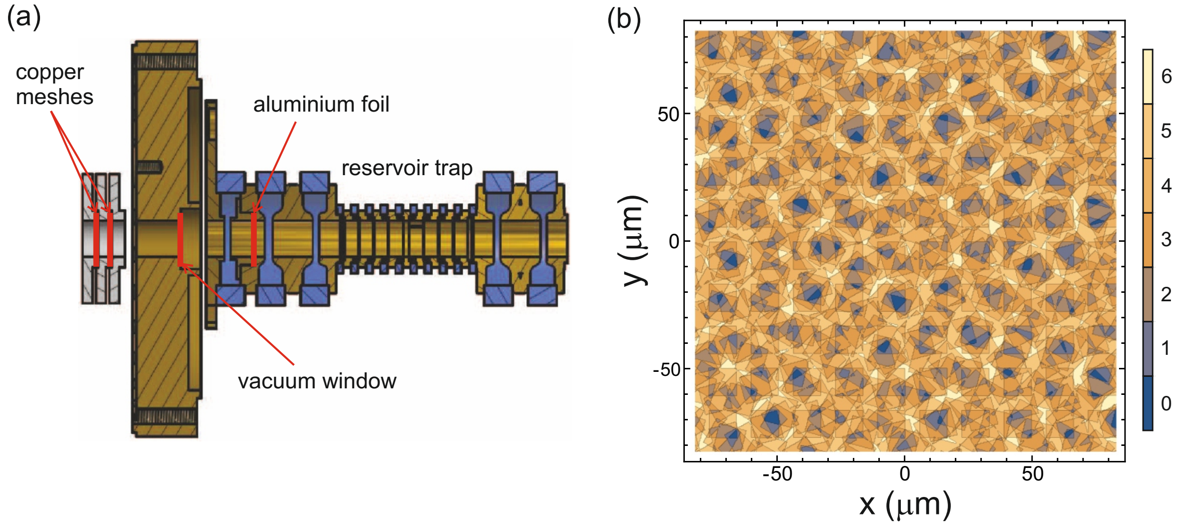

Fig. 5.6: (a) Placement of the degrader foils at the upstream-side of the Penning-trap chamber. There are three copper meshes at each of the two indicated locations. (b) Calculation of the structure generated by the copper mesh assembly. The number of meshes passed by antiprotons as function of the location is shown. For details, refer to the text. The figure is taken from [13].

by fast high-voltage pulses. According to [64], it was studied that the maximum efficiency for the transmission is reached when 50 % of the injected antiprotons are stopped inside the degrader. However, the efficiency of the stopping process is strongly dependent on the degrader material, as well as the thickness and the placement of the degrader components. Moreover, accurate calculations of the stopping power were unexecuted due to the lack of experimental data of the empirical stopping power models at low energies [64, 65]. To account for this, the degrader system used in the BASE apparatus consists of three elements as shown in Fig. 5.6 (a). The first part provides a variable stopping power in order to compensate uncertainties in the stopping power calculations as well as the thicknesses in the production of the degrader foils. It consists out of six stacked copper meshes with a thickness of 2.5 μm rotated by 15 degrees relative to each other. The grid structure of the mesh (15.6 μm, 44 % open area) is much finer than the diameter of the antiproton beam, which is usually around 2 mm at this position. The mesh pattern shown in Fig. 5.6 (b) adds a large possible variation in stopping power with an equivalent thickness of 0 to 24 μm aluminium, depending on the number of meshes $0 < N < 6$ hit by each antiprotons. The probability p for an antiproton to hit N of the meshes are listed in Table 5.1. It is equivalent to the fraction of the area which is covered by the

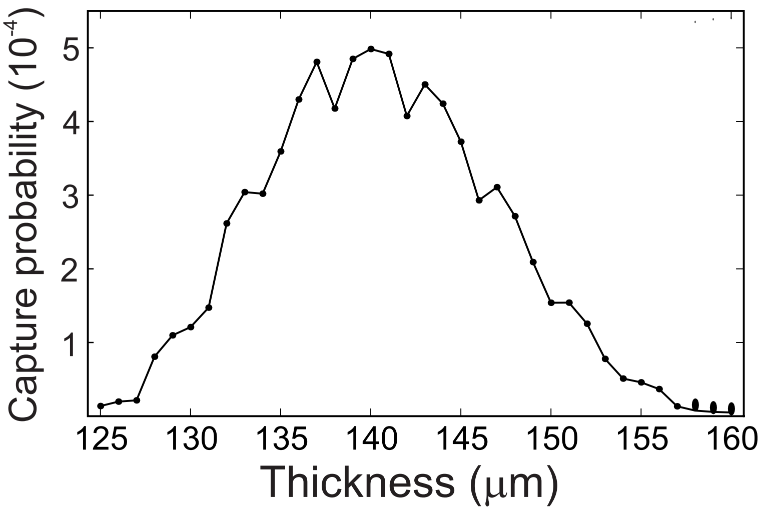

Fig. 5.7: Catching probability of 5.3 MeV antiprotons as function of the thickness of the aluminium degrader calculated with SRIM. The configuration in SRIM consisted of the mesh degrader, the 25 μm stainless steel window, and the aluminium degrader with variable thickness. Particles with a trajectory not exceeding the trap radius of 4.5 mm and with an axial energy below 1 keV are considered as captured. The figure image is taken from [13].

Table 5.1: Probability p of a particle to hit the massive part of N out of the six copper meshes of the mesh degrader. The meshes have an open area of 44 %, therefore the highest probability is obtained for $N = 4$. For further details, refer to the text.

N	0	1	2	3	4	5	6
p	1.09 %	5.55 %	16.51 %	29.32 %	30.07 %	15.03 %	2.44 %

mesh material of N meshes. Since the beam diameter increases as scattering in the degrader foils, the mesh assembly is implemented directly in front of the Penning-trap chamber. The second degrader is the 25 μm stainless-steel vacuum window in the degrader flange. The last degrader is an aluminium foil directly placed in front of the upstream catching electrode. Its purpose is to match the total stopping power of the degrader system for obtaining the maximum number of slow antiprotons. In Fig. 5.7, a calculated result of the catching efficiency using the simulation code SRIM is shown. Antiprotons transmitted through the degrader system with a kinetic energy below 1 keV and has an radial orbit which does not exceed the trap diameter can be captured by high-voltage pulses on the catching electrodes. The total trapping volume of the catching electrodes is 50 mm in the axial direction and 9 mm in diameter, enclosing the reservoir trap. As a whole, the degrader system has a catching efficiency more than 10^{-4} in a broad range around the optimum thickness value. Compared to a single foil with identical stopping power, the maximum efficiency is a factor of three less, but the range in thickness with more than 10^{-4} efficiency is a factor of three higher. Compared to tunable gas chambers [66], the developed degrader system has slightly lower efficiency. However, it is robust, simple, reliable and provides enough antiprotons for single particle experiments.

5.6 Penning-trap system

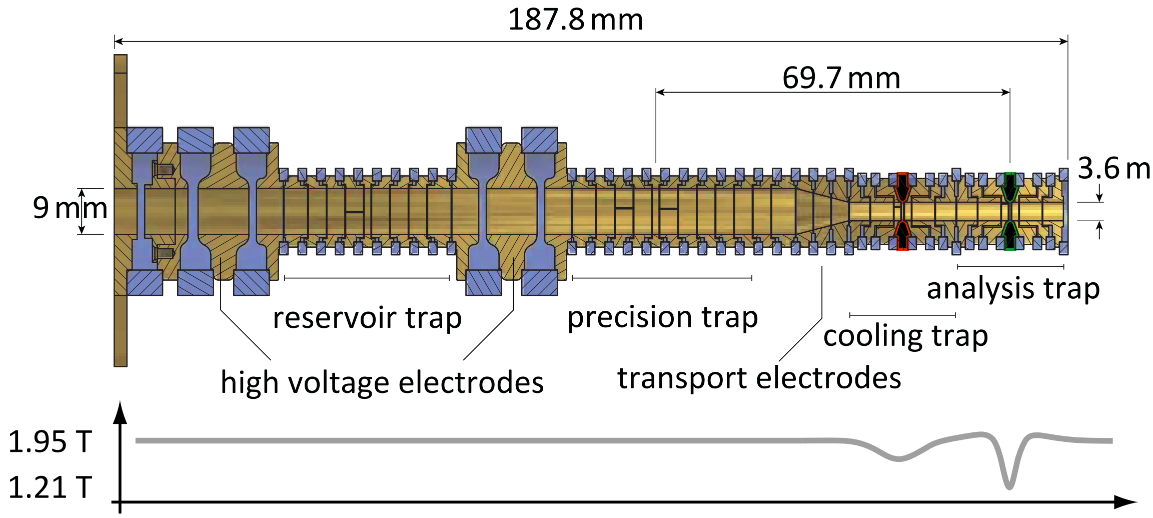

Fig. 5.8: Schematic of the BASE Penning-trap assembly. It consists of four cylindrical Penning-traps interconnected by transport electrodes. The lower graph shows the magnetic field along the z-axis for the entire trap stack. Note that this configuration will be used for the future experiment to measured the antiproton g-factor by using the double trap technique. For the sub-ppm g-factor measurement described in this thesis, the analysis trap and the cooling trap are swapped. Additionally, the electrodes for the cooling trap are grounded, since they were not used for the measurement. The figure is taken from [13].

Figure 5.8 shows the BASE Penning-trap system. It is installed in the homogeneous centre of the superconducting magnet. The trap stack consists of a sequence of four cylindrical Penning traps in a five-electrode orthogonal and compensated design [67]. Each Penning traps are interconnected by transport electrodes in an optimal length-to-diameter ratio. All electrodes are gold-plated to avoid oxidation. Compared to a conventional single particle experiment, which is usually operated less than two Penning traps, the BASE Penning-trap system at CERN is operated in total four traps: a reservoir trap (RT), a precision trap (PT), an analysis trap (AT) and a cooling trap (CT). PT/RT and AT/CT have inner diameters of 9.0 mm and 3.6 mm, respectively. All electrodes are manufactured with an absolute precision better than 5 μm. To separate the individual electrodes and to prevent electrical contacts, the sapphire rings are used. They have a height of 3 mm and a similar machining precision as the electrodes. Table 5.2 summarises the parameters of the every four traps including the magnetic properties B_1 and B_2 at each trap centre.

Table 5.2: Geometry parameters and magnetic field gradients of the four Penning traps in the BASE apparatus.

Trap	Inner Diameter (mm)	C_2 (m^{-2})	B_1 (T/m)	B_2 (T/m^2)
Reservoir trap (RT)	9.0	18 508	< 0.010	< 1
Precision trap (PT)	9.0	18 508	0.022	0.67
Cooling trap (CT)	3.6	116 000	1.900	16 000
Analysis trap (AT)	3.6	116 000	0.100	300 000

5.6.1 Precision trap (PT) and analysis trap (AT)

The Precision trap (PT) and the Analysis trap (AT) are dedicated to be used to perform double Penning-trap measurements [58]. The trap centre of the PT is located in the exact homogeneous centre of the superconducting magnet. This allows to perform frequency measurements with high-precision. On the other hand, a strong magnetic bottle is superimposed in the AT to perform spin-state analysis as described in chapter 4. The basic design of these traps are based on the Mainz experiment [68]. However, several modifications were made for the BASE trap geometry. The inner diameter of the PT was modified from 7 mm to 9 mm. This reduces the systematic shifts in cyclotron frequency measurements caused by potential anharmonicities and image-charge corrections. For the PT in BASE, the systematic shift of the cyclotron frequency is only 40 p.p.t., which is 2.5 times smaller than the Penning-trap system in Mainz. Furthermore, the distance between the centres of the PT and AT is increased from 43.7 mm to 69.7 mm by inserting the cooling trap in between. This effectively reduces the magnetic field inhomogeneities at the centre of the PT compared to the previous setup, since the major contribution to the inhomogeneity is caused by the magnetic bottle in the AT. The magnetic gradient term in the BASE PT is $B_{1,B} = 0.022\,\mathrm{T/m}$, the bottle term is $B_{2,B} = 0.67\,\mathrm{T/m^2}$, which is 4 and 6 times smaller than in the trap used in [24].

5.6.2 Reservoir trap (RT)

One of the important features of the reservoir trap (RT) is to act as a catching trap to capture low energy antiprotons provided by the AD. Therefore, it is placed in between two catching electrodes, which allows the application of DC and pulsed high voltages of up to 8 kV in order to capture antiprotons. In the period between two AD injection pulses, the captured particles in the RT are cooled sympathetically with electrons and transported to the PT to avoid the next injected antiprotons to kick out the accumulated antiprotons from the trap. After the cooling process of the second injected antiprotons, these two antiproton clouds are merged and stocked in the PT.

After all, the apparatus is disconnected from the ejection beamline and the RT functions as a particle reservoir. Single particles can be extracted non-destructively from the RT to supply to the other traps (refer to section 7.3). To avoid any power failure and maintain the reservoir, the entire trap is operated with uninterruptable power supplies which last for 10 h during power-cuts. In this way, the RT enables long-term storage of antiprotons and allows BASE to operate even during accelerator shut-down periods and perform measurements when the magnetic noise in the AD hall is low.

5.6.3 Cooling trap (CT)

The purpose of the Cooling trap (CT) is fast and efficient cooling of the modified cyclotron mode of a single trapped antiproton. This is essential for single spin-flip experiments to prepare particles with low cyclotron energies (refer to section 10.4.1). It was not used in context of this thesis, and we are planning to implement this in future runs.

5.7 Electron gun

The field-emission electron gun is implemented into the trap stack to provide electrons for sympathetic cooling of antiprotons. Additionally, the emitted electrons are used to load the trap with protons. Collided electrons on the degrader release hydrogen atoms out of the surface. These atoms are subsequently electron-impact ionized in the centre of the RT and trapped.

The electron gun consists of a sharp tungsten tip with a high aspect ratio, which is placed close to an acceleration electrode. A biasing voltage applied to the tip defines the energy of the emitted electrons. Electron DC currents in the range of 10 nA to 350 nA are extracted by applying voltages between 500 V and 1.2 kV to the acceleration electrode.

5.8 Trap assembly

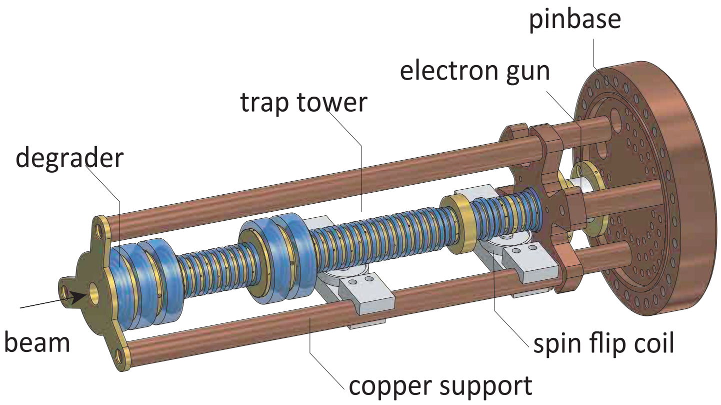

Fig. 5.9: Entire assembly of the experiment.

Figure 5.9 shows the Penning-trap stack inside the trap chamber. The trap electrodes are pressed together by two plates which are fixed on the upper and lower end of a tripod made out of oxygen-free electrolytic (OFE) copper. The electron gun is connected to the lower plate (see Fig. 5.9) and the entire assembly is attached to the pinbase flange by three OFE copper spacers. Spin-flip coils are placed on PTFE supports mounted to the tripod.

5.9 DC and RF wiring

In this section, the configurations of the DC and RF wiring for the BASE apparatus is presented in detail. Figure 5.10 shows a schematic of the entire wiring diagram. Note that the electronics wiring configuration for the cooling trap (CT) is not shown in this figure, since it was not used for neither the charge-to-mass ratio measurement nor the g-factor measurement during my PhD studies. Low DC voltages ($\leq 15\,\mathrm{V}$) are used to bias the Penning-trap electrodes, cryogenic amplifiers, an RF switch, a Q-switch and a field emission electron gun. High DC voltages ($\leq 1\,\mathrm{kV}$) are used to bias the two catching electrodes to capture antiprotons from the AD ejection. Also,

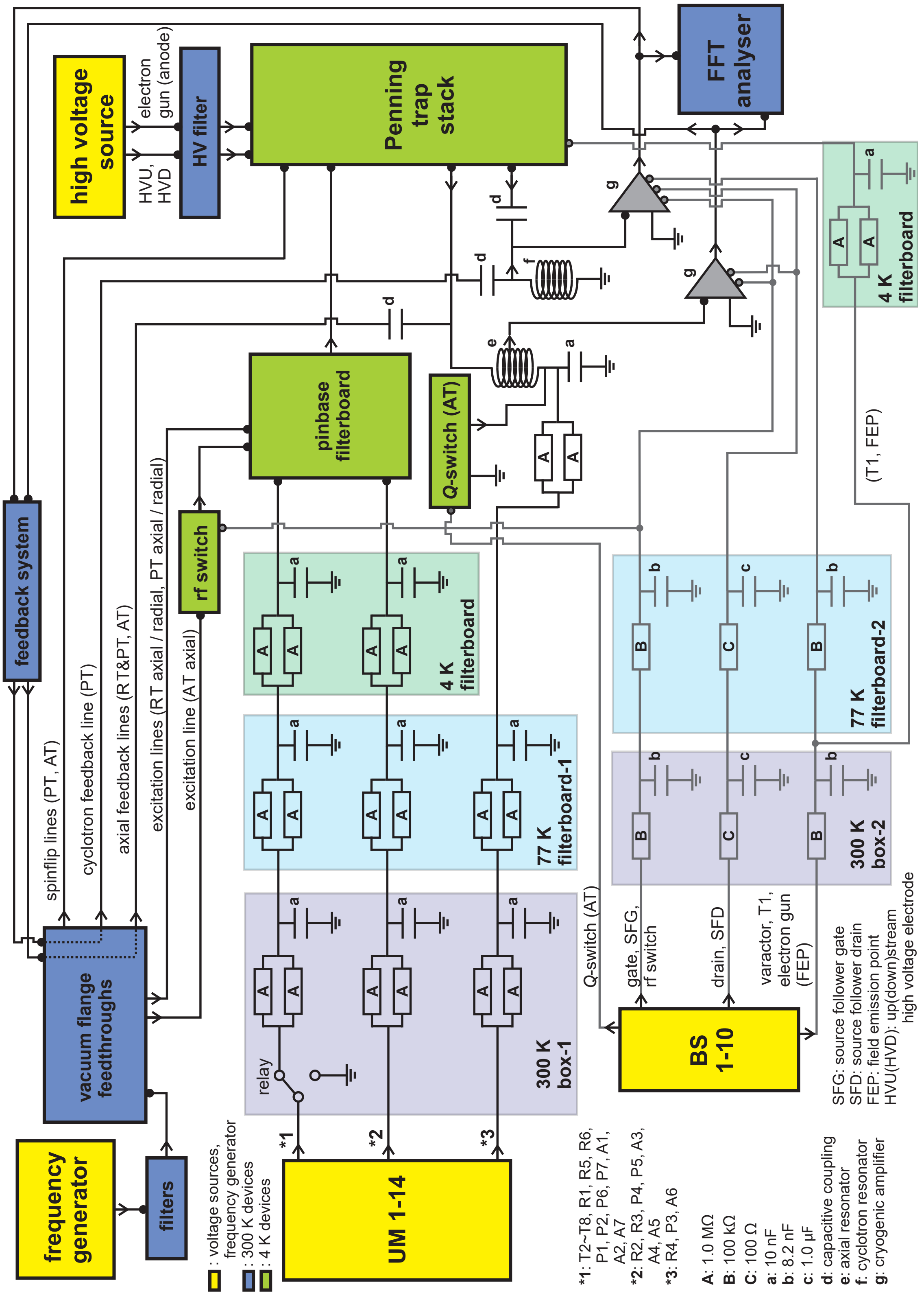
feedback system
high voltage source
HVU, HVD
electron gun (anode)
HV filter
Penning trap stack
FFT analyser
spinflip lines (PT, AT)
cyclotron feedback line (PT)
axial feedback lines (RT&PT, AT)
excitation lines (RT axial / radial, PT axial / radial)
excitation line (AT axial)
rf switch
pinbase filterboard
Q-switch (AT)
4 K filterboard
77 K filterboard-1
300 K box-1
77 K filterboard-2
300 K box-2
vacuum flange feedthroughs
frequency generator
filters
UM 1-14
BS 1-10
relay
*1
*2
*3
Q-switch (AT)
gate, SFG, rf switch
drain, SFD
varactor, T1, electron gun (FEP)
(T1, FEP)
A
B
C
a
b
c
d
e
f
g
: voltage sources, frequency generator
: 300 K devices
: 4 K devices
*1: T2~T8, R1, R5, R6, P1, P2, P6, P7, A1, A2, A7
*2: R2, R3, P4, P5, A3, A4, A5
*3: R4, P3, A6
A: 1.0 MΩ
B: 100 kΩ
C: 100 Ω
a: 10 nF
b: 8.2 nF
c: 1.0 µF
d: capacitive coupling
e: axial resonator
f: cyclotron resonator
g: cryogenic amplifier
SFG: source follower gate
SFD: source follower drain
FEP: field emission point
HVU(HVD): up(down)stream high voltage electrode

Fig. 5.10: Schematic of the electronics diagram. For simplicity, the axial resonator is shown as a solenoid although a toroidal design is actually used for the experiment.

it is used to bias the anode electrode of the electron gun. In order to achieve low-noise as well as stable condition in the apparatus, it is of utmost importance to supply precise DC voltages with small fluctuations to the Penning-trap electrodes as well as to the cryogenic amplifiers. To filter-out spurious noise on the biasing lines, in total four individual *RC* low-pass filters are implemented for the Penning-trap electrodes, one at 300 K box-1, one at 77 K filterboard-1, a first filter stage at 4 K and the final filter stage which is directly mounted on the pinbase as shown in Fig. 5.10. To supply highly stabilised voltages, ultra-high precision voltage sources UM 1-14 from *Stahl Electronics* are utilised to bias the Penning-trap electrodes. The characterisation of these devices is discussed in section 5.9.1. On the other hand, three individual *RC* filter stages are developed and implemented to bias the cryogenic amplifiers, these are the 300 K box-2, 77 K filterboard-2 and one which is directly mounted on the amplifier PCB boards. Precision voltage source BS 1-10 from *Stahl Electronics* are used to provide voltages for the amplifiers. Since no low-pass filters are installed for the high-voltage lines inside of the apparatus, their signal lines are grounded while they are no longer in use. This excludes any possibilities to let unexpected noise to couple into the other lines. For the RF lines, there are 5 excitation lines to manipulate the motions of trapped particles, three feedback lines to decrease the effective detector temperatures, and two spin-flip lines to generate a transverse rf magnetic field at the centre of the trap.

5.9.1 DC biasing for the Penning-trap electrodes

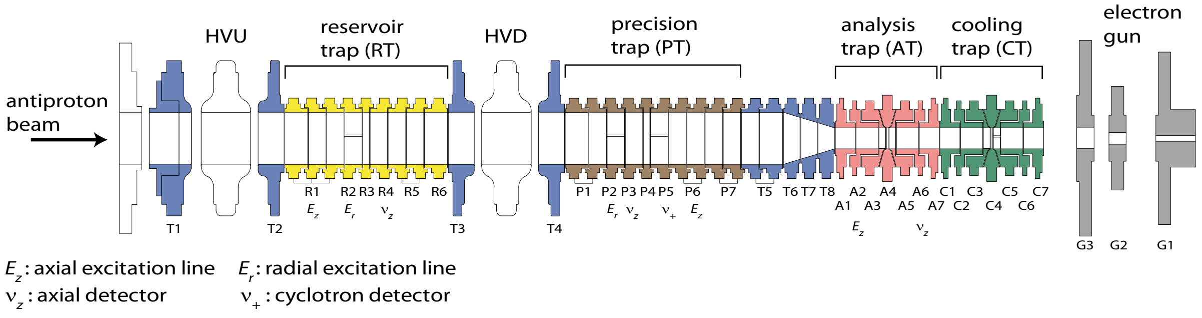
antiproton
beam
HVU
reservoir
trap (RT)
HVD
precision
trap (PT)
analysis
trap (AT)
cooling
trap (CT)
electron
gun
T1
T2
R1
R2 R3 R4
R5
R6
E_z
E_r
ν_z
T3
T4
P1
P2 P3 P4 P5
P6
P7
E_r ν_z
ν_+
E_z
T5
T6 T7 T8
A2 A4 A6
A1 A3 A5 A7
E_z
ν_z
C1 C3 C5 C7
C2 C4 C6
G3
G2
G1
E_z: axial excitation line
ν_z: axial detector
E_r: radial excitation line
ν_+: cyclotron detector

Fig. 5.11: Configuration of the Penning-trap electrodes.

A configuration of the DC voltages applied to the Penning-trap electrodes is shown in Fig. 5.11. Compare with Fig. 5.10.

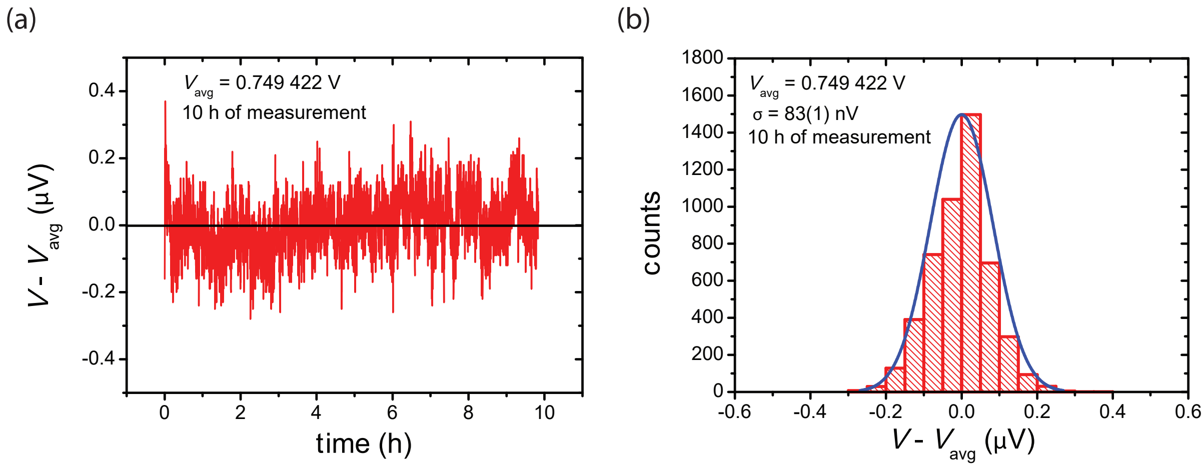

Fig. 5.12: Continuous voltage measurement of UM 1-14 (*Stefan Stahl Electronics*), when it is operated in ultra-high precision mode. Constant voltage of 0.749 422 V is supplied from UM 1-14 and it is recorded continuously for 10 hours by a high-precision multimeter. (a) Shows a measured result. The vertical axis shows measured voltages V substracted by an average voltage V_{avg}, evaluated by the total measurements. (b) Histogram which is directly projected from the data set. Fitted curve represents a Gaussian line-shape which gives a standard deviation of $\sigma = 83(1)\,\mathrm{nV}$. This corresponds to an absolute axial frequency stability of $\Xi_{z,V} = 36(0.5)\,\mathrm{mHz}$, evaluated by using Eq. (5.2)

.

The applied voltages must be as stable as possible, since the axial frequency ν_z is a function of the ring voltage V_{R} as:

$$\nu_z = \frac{1}{2\pi}\sqrt{\frac{2C_2qV_{\mathrm{R}}}{m}}. \tag{5.1}$$

As shown in Fig. 5.10, supplied voltages from UM 1-14 are rectified by four individual stages of *RC* low-pass filters. This configuration allows to filter superimposed noise on the DC voltages. At 300 K box-1, galvanic relays are implemented for particular bias lines, such that it allows switching between signal lines and ground. While precision measurements take place, all electrodes except for the central three trap electrodes of the five-trap assembly are switched to ground.

There are three primary channels (0∼14 V range), three secondary channels for providing a smaller voltage range (diminished by a factor of 4) which are coupled to the primary channels by internal voltage dividers, and 10 add-on auxiliary channels which are intended for no need of extreme stability. The primary and secondary output channels can be run either in ultra high precision mode (featuring highest resolution and stability) or in fast mode. The latter is

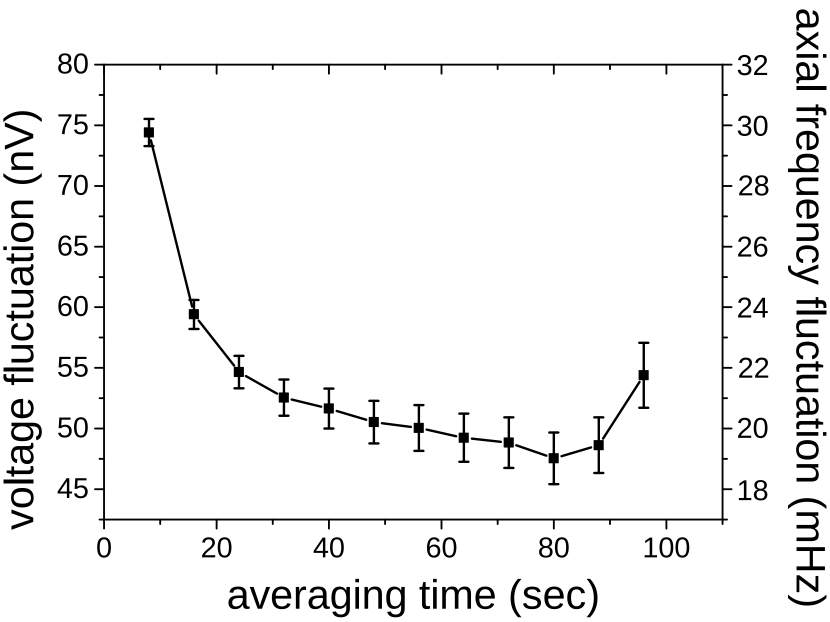

Fig. 5.13: Allan deviation of the voltage/frequency fluctuation, based on 10 hours continuous voltage measurements of UM 1-14, which is operated in ultra-high precision mode. From this evaluation, the voltage fluctuation at 90 s of averaging time is extracted as $\sigma_{90} = 48(2)\,\mathrm{nV}$, which corresponds to the axial frequency fluctuation of $\Xi_{z,V} = 20(1)\,\mathrm{mHz}$.

internally only 16 bit resolved, features less accuracy but faster response time (for instance, suited for transporting antiprotons to other traps). The former offers 25 bit of higher resolution and stability.

To characterise the stability of the individual output channels of the power supply in ultra-high precision mode, a constant voltage of 0.749 422 V is supplied from UM 1-14 and it is recorded continuously for 10 hours by a reference multimeter (*Fluke 8508A*). The result is shown in Fig. 5.12 (a). The vertical axis shows measured voltages V substracted by an average voltage V_{avg}, which is evaluated by the total measurement points. Figure 5.12 (b) shows a histogram which is a projection of Fig. 5.12(a). By fitting this histogram with a Gaussian line-shape, a standard deviation $\sigma = 83\,\mathrm{nV}$ is obtained. By performing error propagations based on Eq. (5.1), an absolute axial frequency stability $\Xi_{z,\bar{V}}$ is evaluated as

$$\Xi_{z,\bar{V}} = \frac{1}{4\pi}\sqrt{\frac{2C_2 q}{mV_{\mathrm{R}}}} \cdot \sigma = \frac{\nu_z \sigma}{2V_{\mathrm{R}}}. \tag{5.2}$$

Inserting properties of the AT (see Table 5.2) into Eq. (5.2), $\Xi_{z,\bar{V}} = 36.0(0.5)\,\mathrm{mHz}$ is obtained. Moreover, the Allan deviation of a sequence of the measured voltages is evaluated as described in section 10.3.1. The result is shown in Fig. 5.13. The voltage fluctuation at 90 s of averaging time is extracted as $\sigma_{90} = 48(2)\,\mathrm{nV}$, which corresponds to the axial frequency fluctuation of $\Xi_{z,V} = 20(1)\,\mathrm{mHz}$. The absolute axial frequency stability $\Xi_{z,\bar{V}}$ as well as the axial frequency fluctuation $\Xi_{z,V}$ caused by fluctuations on the voltage are stable enough to perform Larmor frequency measurements (see section 11.5.2 and section 11.6).

5.9.2 Excitation lines

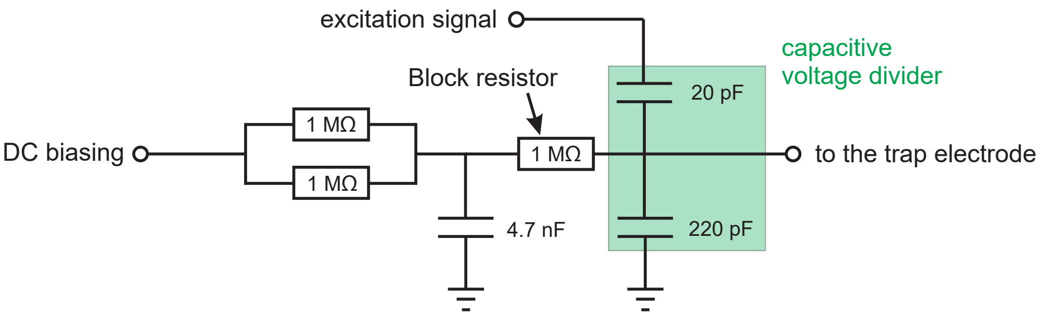

Fig. 5.14: Schematic of the filters at the pinbase. A 20 dB capacitive voltage divider is mounted to suppress stray noise which is potentially picked-up by 20 dB. A 1 MΩ block resistor is implemented to prevent from excitation signals to transmit through the DC bias supplies.

In total, five excitation lines are used to manipulate the motions of the trapped particles (refer to Fig. 5.10). The axial excitation lines are implemented for the RT, PT, and AT. The radial excitation lines are used only for the RT and PT. From the SMA feedthroughs of the vacuum flange to the pinbase filterboard, low-temperature single coaxial cables (*GVL Cryoengineering*) are used. Brass and CuNi are used as a material for the signal line and the shield, respectively. It is suited for a cryogenic environment purposes, since it has a low thermal conductivity. At the pinbase, a 20 dB capacitive voltage divider is implemented for each excitation lines (see Fig. 5.14). This structure suppresses stray noise which is potentially picked-up by 20 dB. Additionally, a 1 MΩ resistor is placed in between the *RC* filter and the capacitive voltage divider to block the rf signals to transmit through the DC biasing supplies. Together with a 220 pF capacitor, it also acts as an *RC* low pass filter for the DC lines. From the pinbase to the inside of the Penning-trap chamber, copper wires are used and they are directly soldered to the electrodes.

5.9.3 Pinbase

The pinbase is an interface which interconnects between the DC/RF lines as well as the spin-flip lines and the trap system. Sapphire feedthroughs are used for the pickup lines of the detection systems, and alumina feedthroughs are used for the rest of the signal lines. Since the pinbase also acts as a vacuum seal for the trap can, it needs to be significantly leak-tight. Before implementing it to the apparatus, many leak tests were carried out until no leaks were found anymore. At the pinbase, a filterboard is mounted to suppress noise to couple on the DC and RF lines as described in section 5.9.2.

5.9.4 RF switch

A transistor switch (SW239 by *MACOM*) is placed at the 4 K stage of the apparatus for switching between the signal line and the ground for the AT axial excitation line. When the excitation line is not in use, we switch it to ground specifically during the spin-flip measurements. Its intention is to achieve noise-less environment as much as possible in the AT.

5.9.5 Feedback lines

In total, three feedback lines are implemented for the experiment. Two axial feedback lines for the small axial detectors (RT and PT) and the big axial detector (AT), and one cyclotron feedback line for the PT cyclotron detector. Low-temperature single coaxial cables (*GVL Cryoengineering*) are guided through the apparatus, and capacitively coupled to the hot-end of the resonators (see Fig. 5.10). In between, there are no filters implemented. From the next run, implementations of filterboards for the feedback lines are planned.

5.9.6 Spin-flip lines

Spin-flip lines are implemented for the PT and the AT. Its configuration is shown in Fig. 5.15. From the vacuum flange, low-temperature twisted-pair coaxial cables (*GVL Cryoengineering*) are guided through the apparatus, and they are soldered to twisted-pair copper wires, which goes through the pinbase filterboard and reaches near the trap electrodes. The end of the twisted copper wires near the trap is wound and act as a spinflip coil.

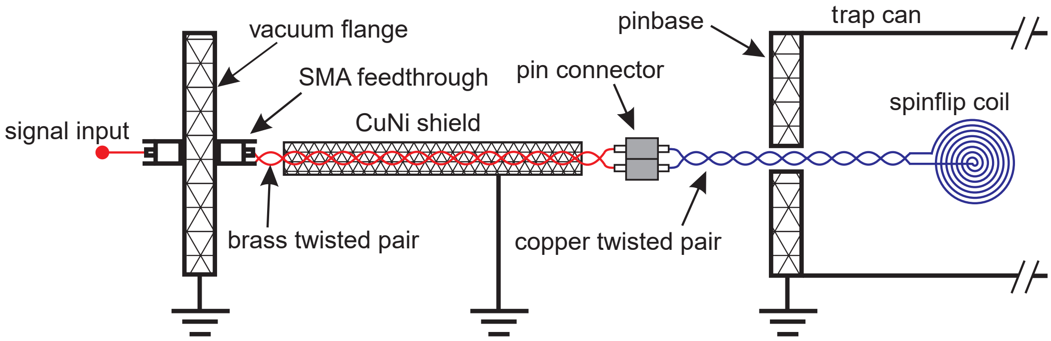
vacuum flange
pinbase
trap can
SMA feedthrough
pin connector
spinflip coil
signal input
CuNi shield
brass twisted pair
copper twisted pair

Fig. 5.15: Schematic of the spinflip line.

5.9.7 High voltage lines for capturing antiprotons

High voltages are used to bias the high voltage upstream (HVU)/downstream (HVD) electrodes, and an anode of the electron gun (see also Fig. 5.10). HVU and HVD are operated with high voltages when capturing process of the antiprotons provided by the AD take place (see section 7.1). Regarding operations on the electron gun, refer to section 5.7.

5.9.8 DC biasing for the cryogenic amplifiers

As mentioned above, three *RC* filters are implemented for the amplifier bias lines (see Fig. 5.10). Constantan wires are used for every connections from 300 K box-2 to the amplifier boards. Constantan also has small thermal expansion coefficient, thus suited for cryogenic usages.

Chapter 6

Single-particle detection systems

6.1 Axial detectors

This section is based on an already published article [15], which I contributed as a corresponding author. The axial detector consists of a superconducting toroidal coil and a cryogenic low noise amplifier for non-destructive detection of the axial frequency. The resonance frequency $\nu_{0,\mathrm{eff}}$ of the detectors is tuned to $550 \sim 800\,\mathrm{kHz}$. The unloaded resonators show quality factors Q_p up to 500 000, which is a factor of 10 improvement compared to the previously used solenoidal designs [69]. Connected to the amplifiers and the trap system, signal-to-noise-ratios of 30 dB at quality factors of $> 20\,000$ are achieved.

Table 6.1: Geometry of the two types of resonators as shown in Fig. 6.1

	AT and CT (mm)	RT and PT (mm)
A	41	36
B	48	41
C	22	23
D	12.5	10
E	19	16

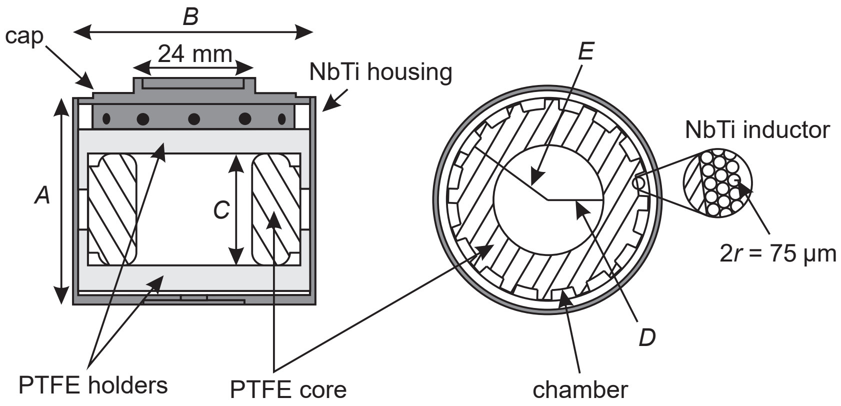
cap
B
24 mm
NbTi housing
E
NbTi inductor
A
C
2r = 75 μm
D
PTFE holders
PTFE core
chamber

Fig. 6.1: Schematic of the superconducting resonator. The toroidal core is made out of PTFE, and PTFE insulated NbTi superconducting wire is used for the windings. The toroid is mounted inside the NbTi housing and kept stable with PTFE holders. It is enclosed by inserting a cap from outside. $A \sim E$ is listed in Table 6.1 for the two types of resonators.

6.1.1 Superconducting axial resonators

A schematic of the resonator is shown in Fig. 6.1. The scaling is different from the big resonators (used for the AT and CT) to the small resonators (used for the RT and PT). The geometry for these two types of resonators is listed in Table 6.1, and it is determined by the geometrical constraints of the electronics chamber (see Fig. 6.2). It is optimised in a way, such that the inner cross-sectional area is maximised at the lowest length of a superconducting wire. Each resonator consists of a toroidal coil in a cylindrical metal housing with an outer diameter B, as shown in Fig. 6.1. The magnetic field flux of a toroid is confined inside the toroid, which

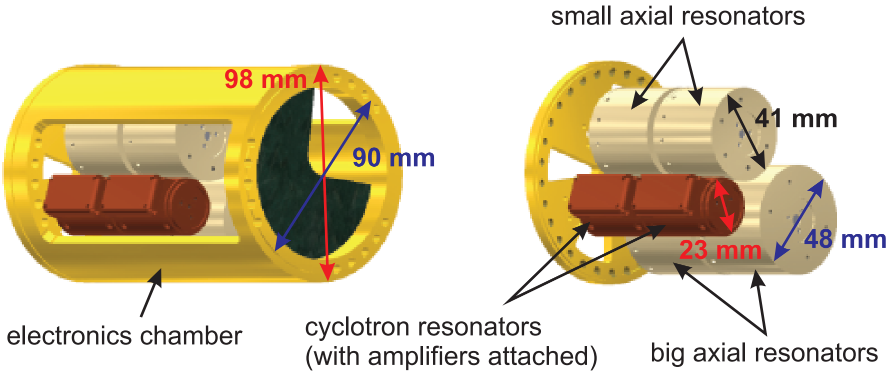
small axial resonators
98 mm
90 mm
41 mm
23 mm
48 mm
electronics chamber
cyclotron resonators
(with amplifiers attached)
big axial resonators

Fig. 6.2: Schematic of the electronics chamber.

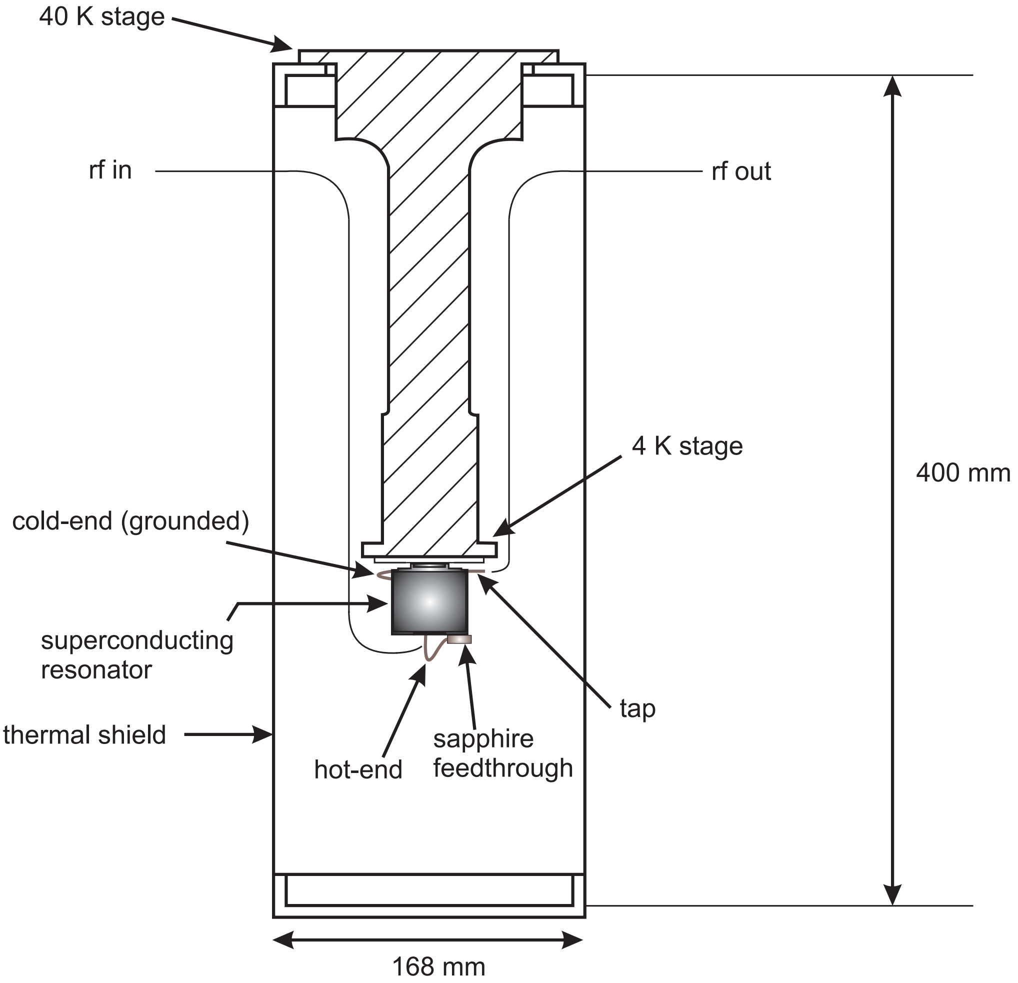

Fig. 6.3: Schematic of the setup for measuring the properties of the unloaded resonators.

prevents eddy current losses in the housing. The coils as well as the housings are made out of type-II superconducting NbTi, which has a high critical magnetic field strength of $B_{C2} = 14.5\,\mathrm{T}$ [70]. This allows to place the resonators close to the Penning-trap system, which is mounted in the high magnetic field $B_0 = 1.9\,\mathrm{T}$. The small length of the connection leads the smaller resistive losses and stray capacitances, which eventually increases the quality factor. Additionally, to keep the parasitic capacitance of the coil small, three-layer chamber windings is used. The individual chambers are machined onto the toroid. The windings are fixed to the core by polytetrafluoroethylene (PTFE) thread seal tape to ensure a good heat contact between the wire and the core. This procedure is exceptionally important, since at the phase transition to the superconducting state, electrons condense to the BCS ground state which leads to a decrease in the heat conduction coefficient of NbTi [71]. Moreover, losses induced by dielectric polarisation effects are kept small by making the cores of the toroids out of PTFE. At cryogenic

Table 6.2: Summary of the characterisation measurements of the unloaded resonators. The left column indicates the name of the dedicated Penning trap in the BASE apparatus: the analysis trap (AT), cooling trap (CT), precision trap (PT), and reservoir trap (RT) [13]. Abbreviations: L - Inductance / C_p - Parasitic capacitance / Q_p - Quality factor / ν_0 - Resonance frequency / N - Number of turns / R_p - Parallel resistance.

	L	C_p	Q_p	ν_0	N	R_p
AT	2.73 mH	9.5 pF	500000	896 kHz	1100	7.7 GΩ
CT	2.14 mH	11 pF	250000	948 kHz	940	3.2 GΩ
PT	1.75 mH	11 pF	194000	1.09 MHz	800	2.3 GΩ
RT	1.71 mH	11 pF	196000	1.07 MHz	800	2.3 GΩ

temperatures for the frequency range of $550 \sim 800\,\mathrm{kHz}$, PTFE has a dielectric loss tangent of $\delta < 0.0001$. For the superconducting wire, PTFE insulated NbTi wire with a diameter of $75\,\mu\mathrm{m}$ is used. At each end of the coil, a 5 cm long copper wire of 0.5 mm diameter is connected. This toroid assembly is placed into PTFE holders, which are mounted into the resonator housing. Afterwards, one end of the coil is directly soldered to ground (cold-end), the other one is kept open, but efficiently thermalised by means of a custom-made sapphire capacitor.

To obtain proper thermalisation of the NbTi housing, copper braids are wrapped around. It is of great importance that the superconducting surfaces are not exposed to thermal radiations. In order to characterise the unloaded-resonator's properties, it is installed to a cryo-cooler as shown in Fig. 6.3. RF signals are generated from the output of a network analyser and capacitively coupled to the hot-end of the resonator. A pickup line is also coupled to the tap of the coil to pick up the transmitted signal and flow it back to the input of the network analyser. Refer to [69] for further details on the measurement principle. From this measurement, the transmission of the resonator is recorded and the resonance spectra are obtained for every axial resonators. In Table 6.2, it shows obtained properties for the resonators. For experimental reasons, different axial frequencies are designed for each traps, and have different inductances L. The following equation reproduces the measured L within an error of 10 %

$$L = \frac{\mu_0 S}{\pi(D+E)} N^2. \tag{6.1}$$

Where, μ_0 is the permeability constant of the vacuum, S the cross-sectional area of a toroid, and N the number of turns. From the transmission, the resonance frequency ν_0 and the 3 dB width $\Delta\nu_r$ are determined and the quality factor Q_p is calculated as $Q_\mathrm{p} = \nu_0/\Delta\nu_r$. To extract the parasitic capacitance C_p, an additional capacitor is connected in parallel to the resonator and the measurement is repeated. Since the capacitance of the additional capacitor C_N is known in advance, following equations can be considered

$$\nu_0 = \frac{1}{2\pi}\frac{1}{\sqrt{LC_\mathrm{p}}} \tag{6.2}$$

$$\nu_1 = \frac{1}{2\pi}\frac{1}{\sqrt{L(C_\mathrm{p}+C_\mathrm{N})}}, \tag{6.3}$$

where ν_1 is the resonance frequency which is obtained from this additional measurement. From Eq. (6.2) and Eq. (6.3), C_p as well as L are extracted. The parallel resistance can be calculated by using a definition of the Q-value for the parallel RLC tuned circuit, $R_\mathrm{p} = 2\pi\nu_0 QL$ (see section 3.1).

The obtained Q-value of more than 190 000 corresponds to effective series resistances $R_\mathrm{s} < 0.06\,\Omega$. This indicates that the measured residual resistance is due to dielectric losses in the PTFE core and in the PTFE insulation of the superconducting wire, as well as small residual resistances in the NbTi-to-Cu joints. Once the detection system is installed in the apparatus, the Q-value is mainly determined by the strength of coupling with the amplifier. Therefore, further optimisation of the Q-value is not of interest. Comparing to the solenoid resonator which has developed previously [69], the achieved Q-values correspond about a factor of 10 improvement.

6.1.2 Axial amplifiers

The description made below is based on a manuscript which is published as a first/corresponding author [15], as well as my master thesis [72]. A schematic of the developed axial amplifier is shown in Fig. 6.4. The amplifier consists of a common-source circuit for the input stage and a source-follower circuit for the output stage. Dual-gate GaAs MES-FETs are utilised for each stages. NE25139 (*NEC*) or 3SK164 (*SONY*) transistors for the input, and CF739 (*Siemens / Tricomp*) for the output stage. The parts are assembled on a high-quality PTFE based laminated printed circuit board material, which has a cryogenic loss-tangent of order $\tan\delta \sim 10^{-4}$. This is important to prevent the reduction of the resonator Q-value by dielectric losses.

After implementation of the amplifiers to the apparatus, it will be cooled down to cryogenic temperatures. Therefore, it is necessary to ensure that these amplifiers conserve their performance and quality even in such a critical environment. Testing the developed amplifiers in a cryogenic environment can be realised by using the pulse tube refrigerator as described previously for testing the superconducting resonators (Fig. 6.3). An equivalent input noise of

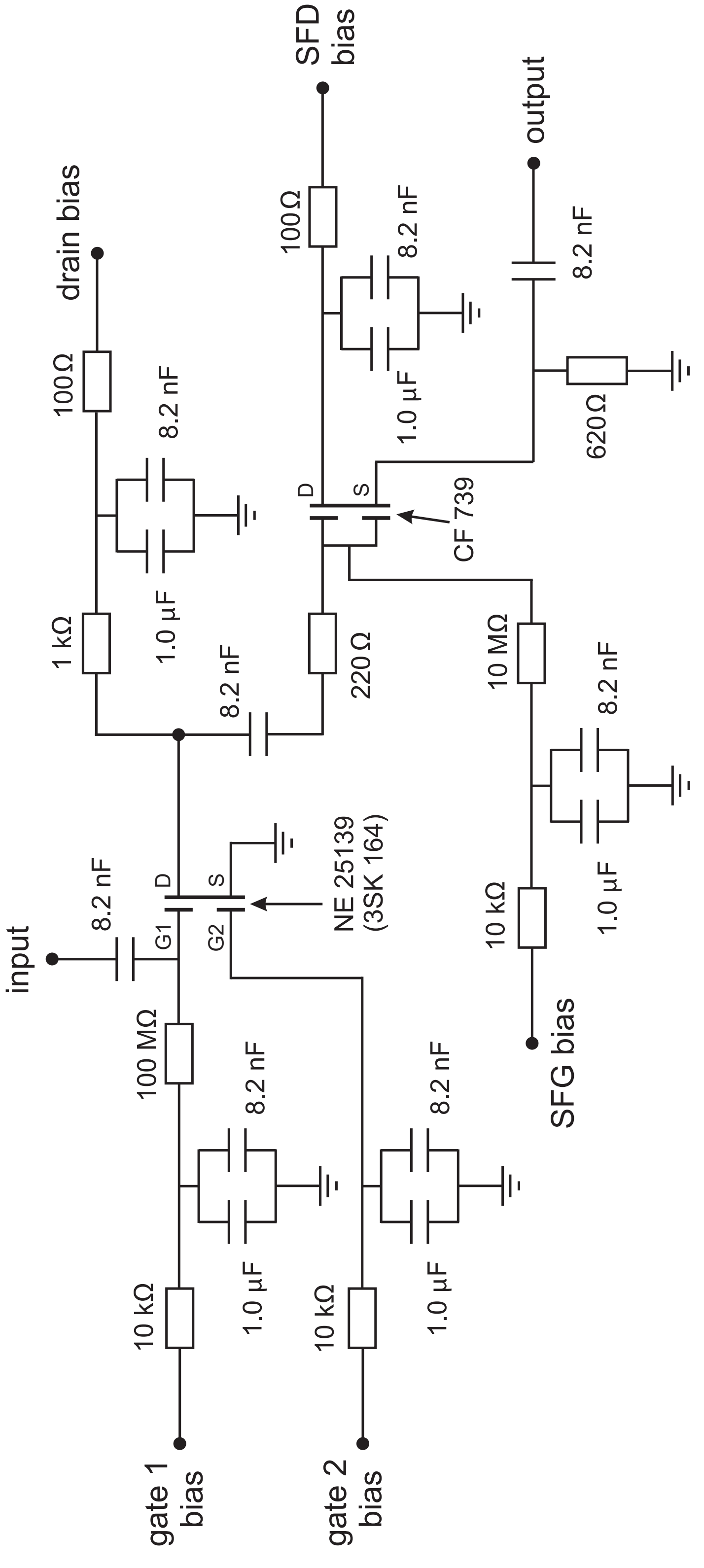
input
8.2 nF
G1
G2
D
S
NE 25139
(3SK 164)
100 MΩ
8.2 nF
1.0 µF
10 kΩ
gate 1 bias
8.2 nF
1.0 µF
10 kΩ
gate 2 bias
drain bias
100Ω
8.2 nF
1.0 µF
1 kΩ
8.2 nF
SFD bias
100Ω
8.2 nF
1.0 µF
D
S
CF 739
220Ω
output
8.2 nF
620Ω
10 MΩ
8.2 nF
1.0 µF
10 kΩ
SFG bias

Fig. 6.4: Schematic of the axial amplifier.

the amplifier e_n is expected to be suppressed when the amplifier is operated in cryogenic temperatures. As described in section 3.3, a dominant source of the noise is the 1st stage of the FET.

There are several contributions to noise in GaAs MES-FET: the thermal noise and the 1/f noise. The thermal noise is the noise of the drain resistance, and it can be reduced by decreasing the temperature. On the other hand, 1/f noise is due to the Generation-Recombination noise (GR noise) and the mobility fluctuations. The GR noise occurs when charge carriers are trapped in substrate impurities and released by thermal fluctuations. The GR noise is mainly present at 300 K where the thermal energy is still large enough to reactivate a trapped carrier. This noise is reduced significantly towards 4 K, where the thermal energy is often too low to release trapped carriers from the trap. The mobility fluctuations are mainly produced by defect scattering of charge carriers. Unlikely as the GR noise, it is not influenced very much by the temperature, and is present even at cryogenic conditions. In this way, it can be concluded that the decrease of the noise e_n when the temperature towards 4 K is mainly due to the reduction of the thermal noise and the GR noise.

In addition to the low noise feature, the following parameters are important to qualify the FET for the experiment: It should have a large input resistance R_in, a small input capacitance C_in, and low power consumption. Moreover, the device should be robust under numerous thermal cycles and insensitive to electric static discharge. To realise this, the design of the amplifier includes several important features:

- Large capacitors are connected in parallel to the Gate 2 of the 1st stage FET. This prevents feedback and parasitic oscillation and is essential for stable amplifier operation.
- A 100 MΩ resistor is applied to the Gate 1 of the 1st stage FET. It prevents the reduction of the effective parallel resistance of the detection system.
- At the input, a single capacitor is applied. Together with the input capacitance C_in, it defines the coupling constant κ_c.
- A relatively small resistor is applied to the drain bias. The drains are biased with small resistor to provide the necessary operation currents.

In order to characterise the amplifier, it is mounted to the pulse tube refrigerator and cooled to 4 K. Then, the gain G_1 as a function of the gate voltages and the equivalent input noise e_n are measured. A schematic of the setup for characterising these properties are shown in Fig. 6.5.

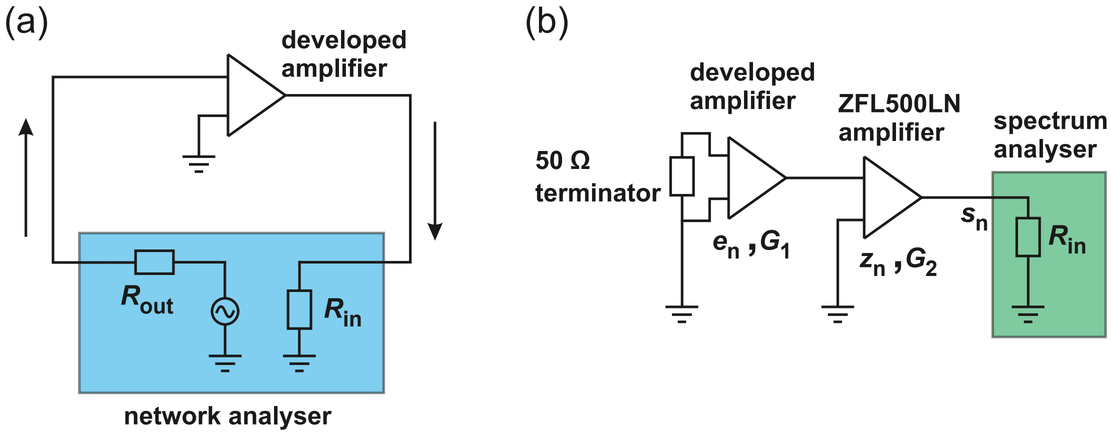

Fig. 6.5: Schematic of the setup for characterising the amplifier. (a) Gain G_1 measurement. (b) Equivalent input noise e_n measurement. Refer to the text for further details.

For the gain measurement, the output of a network analyser, which generates an rf sweep is connected to the input of the amplifier, and the output of the amplifier is connected to the input of the network analyser (Fig. 6.5 (a)). The gain of the amplifier is characterised by changing the gate bias voltages of the first stage. From this method, an optimum gain (working point) is obtained for a certain gate voltage. Regarding the equivalent input noise measurement, a 50 Ω termination is connected to the input of the amplifier, and a coaxial ZFL500LN amplifier (*Mini Circuits*) is connected in between the output of the amplifier and the input of a spectrum analyser (Fig. 6.5 (b)). The 50 Ω termination is connected to the input to prevent from interference signals to couple to the input. To extract the equivalent input noise e_{n} from this method, it is necessary to consider first how the output signal a_{n} $[\text{V}/\sqrt{\text{Hz}}]$ can be expressed, before it is actually detected by using the calibrated noise marker function of the spectrum analyser. Together with Fig. 6.5 (b), the equation for a_{n} can be written as

$$(e_{\text{n}}^2 G_1^2 + z_{\text{n}}^2) G_2^2 + s_{\text{n}}^2 = a_{\text{n}}^2. \tag{6.4}$$

Here, G_2 is the gain of the ZFL500LN amplifier, z_{n} the equivalent input noise of the ZFL500LN amplifier, and s_{n} the baseline noise of the spectrum analyser. By dividing this equation by the input impedance of the spectrum analyser R, the following equation is derived

$$\frac{e_{\text{n}}^2 G_1^2 G_2^2}{R_{\text{in}}} + \frac{z_{\text{n}}^2 G_2^2 + s_{\text{n}}^2}{R_{\text{in}}} = \frac{u_{\text{n}}^2}{R_{\text{in}}} = p_{\text{n}}. \tag{6.5}$$

Where p_{n} is the power density, which has a unit of W/Hz. The second term of the left side of this equation is the power density when only the ZFL500LN is connected to the spectrum

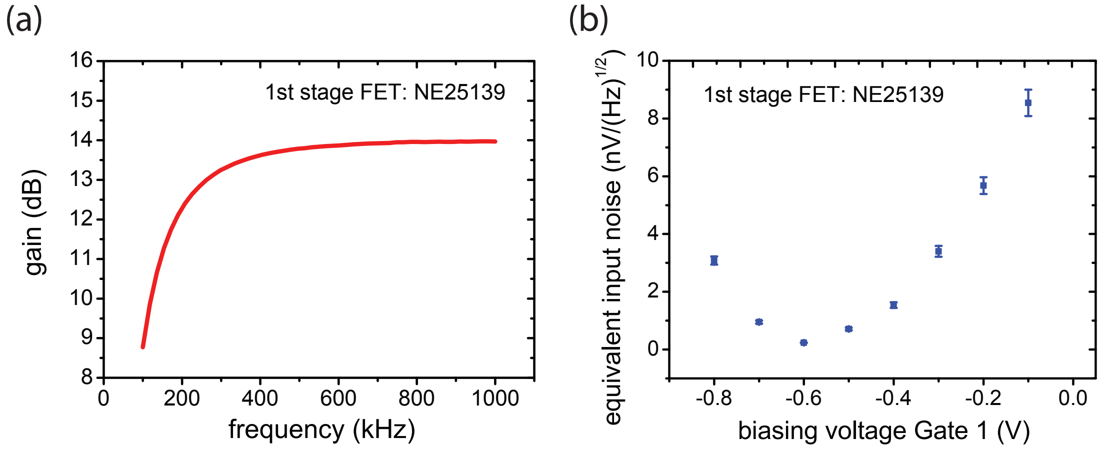

Fig. 6.6: Result of (a) the gain G_1 and (b) the noise e_n (at 600 kHz) of the developed amplifier. For e_n measurement, the voltages are set as shown in Table 6.3 and varied only the Gate 1 voltage.

Table 6.3: Optimum biasing voltages for the amplifier

Gate 1	Gate 2	Drain	Source follower gate	Source follower drain
-0.6 V	0 V	3.0 V	0.7 V	1.9 V

analyser. This can be neglected since it is factor of 100 smaller compared to u_n. Therefore, e_n [V/$\sqrt{\mathrm{Hz}}$] is yielded as

$$e_\mathrm{n} = \frac{\sqrt{R_\mathrm{in} p_\mathrm{n}}}{G_1 G_2}. \tag{6.6}$$

The gain G_1 and the equivalent input noise e_n are obtained as shown in Fig. 6.6. Figure 6.6 (a) shows the gain G_1 (unit in dB) as a function of the frequency with the optimum voltages applied as listed in Table 6.3. For a frequency range of interest 550 $\sim$ 800kHz, G_1 is more or less constant $\sim$ 14 dB. Figure 6.6 (b) shows the noise e_n (at 600 kHz) as a function of the Gate 1 voltage, with the other voltages fixed as listed in Table 6.4.

Table 6.4: Gain and noise of the axial amplifiers at 4 K.

1st stage FET	Gain	Equivalent input noise
NE25139 (NEC)	14 dB	$\sim$0.7 nV/$\sqrt{\mathrm{Hz}}$
3SK164 (SONY)	14 dB	$\sim$0.8 nV/$\sqrt{\mathrm{Hz}}$

Input characteristics of the amplifier C_{in} and R_{in} are measured as the following. C_{in} is measured as the same way as the measurement of the parallel capacitance of the resonator C_{p} (see section 6.1.1). R_{in} can be obtained by coupling the amplifier to the resonator and measure the Q-value at known unloaded parallel resistance R_{p} and inductance L. By inserting these values to Eq. (3.38), R_{in} is extracted. The result of C_{in} and R_{in} is shown in Table 6.5.

Compared to other single particle Penning-trap experiments, the developed amplifiers have a comparably high quality. This is mainly due to careful testing of different FET candidates. The NE25139 transistor has very low equivalent input noise e_{n} at high input resistance R_{in}, which meets the requirements to construct a single particle detection system with very high quality.

Table 6.5: Input characteristics of the axial amplifiers at 1 MΩ.

1st stage FET	Input capacitance C_{in}	Input resistance R_{in}
NE25139 (NEC)	1.95 pF	7.5 MΩ
3SK164 (SONY)	2.0 pF	21 MΩ

6.1.3 Implementation of the axial detectors to the BASE apparatus

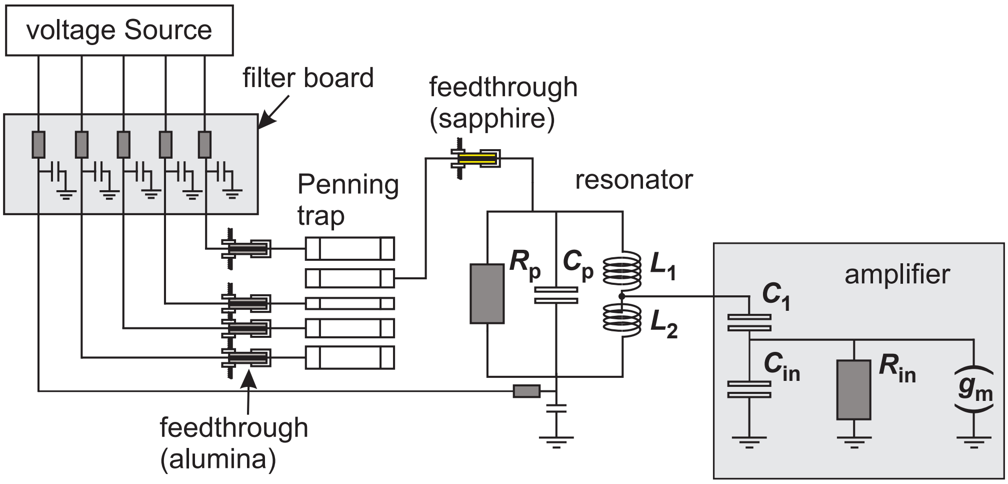

Fig. 6.7: Detailed layout of the detection system.

The developed resonator and amplifier were coupled and implemented to the BASE apparatus as shown in Fig. 6.7. How the coupling has made is described in section 3.3. To connect

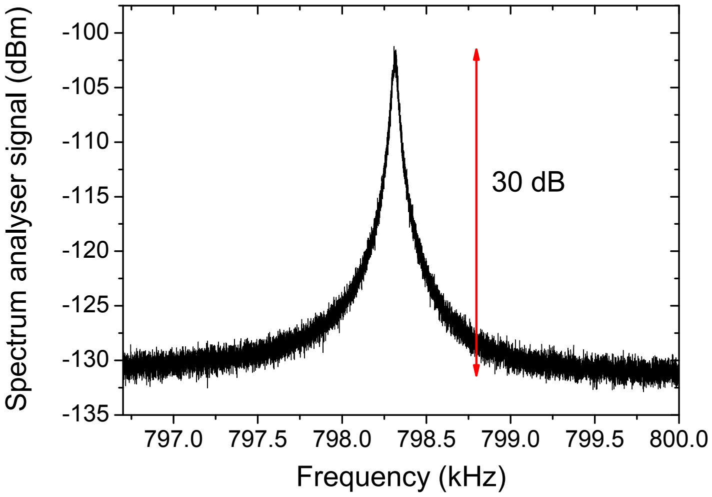

Fig. 6.8: Spectrum of the RT detector. The SNR is 10 dB larger than our previous detection system. This allows much faster and more precise measurements of the axial frequency.

the detectors to the Penning-trap electrode, cryogenic feedthroughs are used. For the previously developed detection systems [69], alumina feedthroughs were utilised, which corresponds to an effective parallel resistance of 120 MΩ. Considering the fact that the parallel resistance of the unloaded resonators are on the order of few GΩ, this contributes to major parasitic losses. To overcome this issue, sapphire feedthroughs (*Kyocera*) were implemented for this setup. This has significantly large effective parallel resistances of $> 7\,\mathrm{G\Omega}$. To characterise the detectors, time transients were recorded with an FFT analyser. From an obtained spectrum, the resonance frequency ν_0 and the Q-value are extracted as the same procedure as the characterisation of the unloaded resonators. The effective parallel resistance of the system R_{eff} is calculated by the obtained Q-value Q_{eff}, ν_0 and the inductance L by using a relation $R_{\mathrm{eff}} = 2\pi\nu_{0,\mathrm{eff}}LQ_{\mathrm{eff}}$. The obtained result is shown in Table 6.6. In case of the RT and the AT detectors, the measured values correspond exactly to the design specifications. Compared to the previously developed detectors [55], the signal-to-noise ratio (SNRr) is improved by up to 10 dB and allows for faster and more precise determinations of the axial frequency. The Q-value of the PT detector is approximately a factor of three smaller than expected. The details of the corresponding limitation have yet to be understood. The effective temperature T_z of our detection systems is 8.0(1.0) K, determined as described in section 10.4.2. This is close to the physical temperature of the apparatus. An obtained resonance spectrum of the RT detector is shown in Fig. 6.8. Regarding discussions of the SNRr consistency to an expected value, refer to [72].

Table 6.6: Summary of the characterisation measurements of the axial detectors. Detectors which are labeled q/m and g-factor is used for the comparison of charge-to-mass ratios of antiproton and proton, and the g-factor measurement of the antiproton, respectively. Abbreviations: SNRr - Signal-to-noise ratio / Q_{eff} - Quality factor / $\nu_{0,\mathrm{eff}}$ - Resonance frequency / R_{eff} - Effective parallel resistance.

	SNRr	Q_{eff}	$\nu_{0,\mathrm{eff}}$	R_{eff}
RT (q/m)	32 dB	11 300	645 kHz	78.8 MΩ
PT (q/m)	23 dB	3600	684 kHz	27 MΩ
RT (g-factor)	30 dB	20 000	798 kHz	170 MΩ
PT (g-factor)	25 dB	6800	676 kHz	49.4 MΩ
AT (g-factor)	27 dB	26 000	674 kHz	275 MΩ

6.2 Cyclotron detector for the precision trap

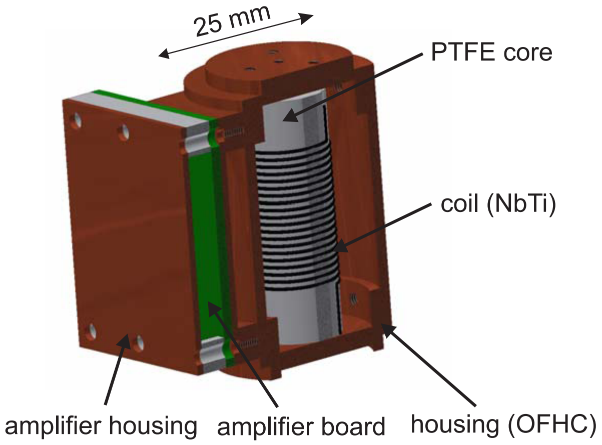

Fig. 6.9: Schematic of the cyclotron detector. Taken from [13].

The cyclotron detection system for the precision trap (PT) is designed to match the modified cyclotron frequency of the antiproton $\nu_{+,\mathrm{PT}} = 29.656\,\mathrm{MHz}$ at a 1.945 T magnetic field. It is dedicated for a purpose of efficient cooling of the modified cyclotron motion. In this respect, the Q-value of the cyclotron detector has to be as large as possible, as for the axial detectors. Moreover, a low equivalent input noise e_{n} is required for the cryogenic amplifier to reach low effective detector temperatures T_+ and sufficiently high signal-to-noise ratios (SNR).

A schematic of the cyclotron detector is shown in Fig. 6.9. The design is based on the general principles reported in [73] and the work described in [74]. Superconducting NbTi solenoids are

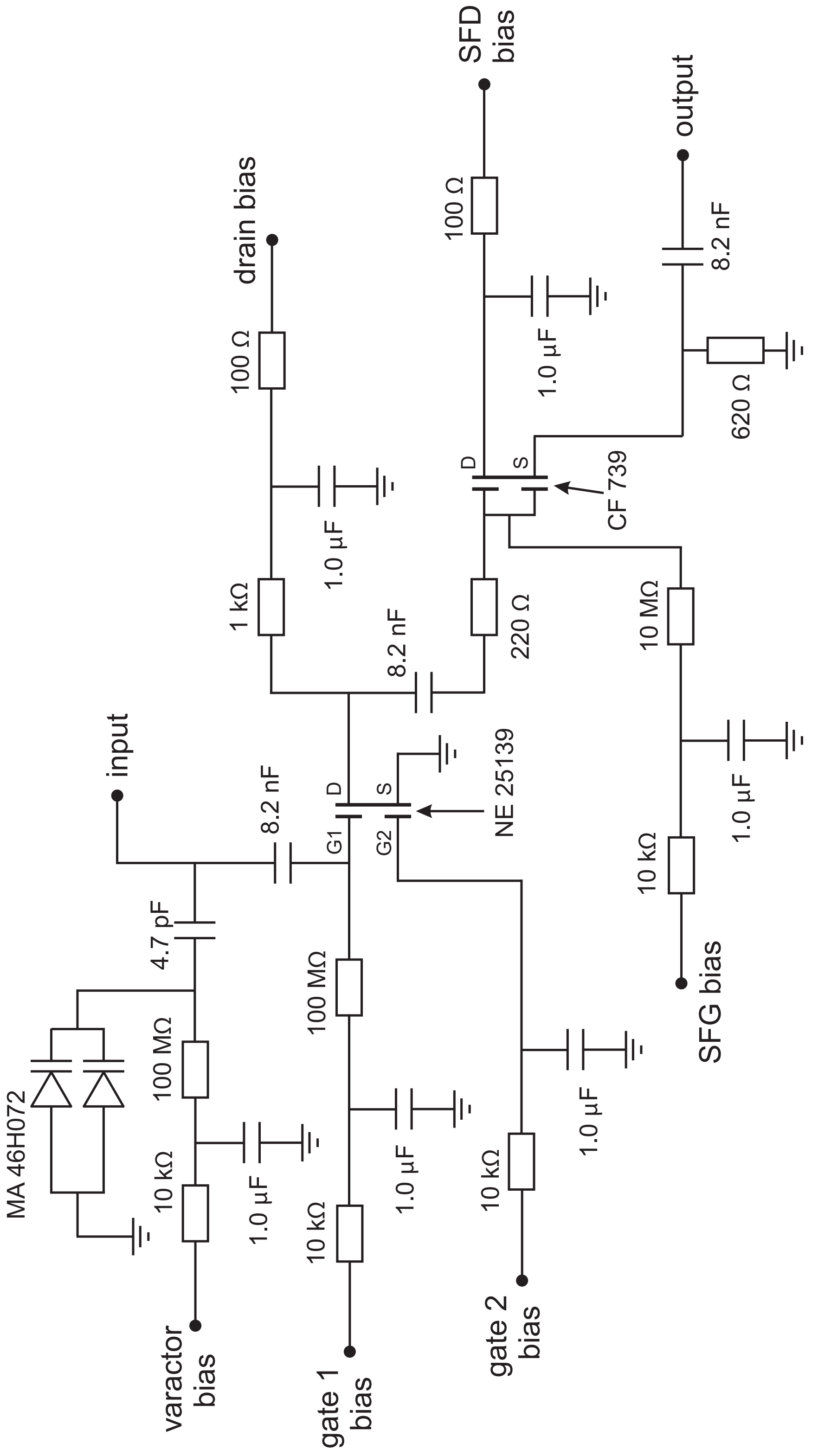
SFD bias
output
drain bias
100 Ω
100 Ω
8.2 nF
1.0 µF
1.0 µF
620 Ω
D
S
CF 739
1 kΩ
220 Ω
8.2 nF
10 MΩ
input
8.2 nF
D
S
G1
G2
NE 25139
1.0 µF
10 kΩ
SFG bias
4.7 pF
MA 46H072
100 MΩ
100 MΩ
10 kΩ
1.0 µF
1.0 µF
10 kΩ
1.0 µF
10 kΩ
1.0 µF
10 kΩ
varactor bias
gate 1 bias
gate 2 bias

Fig. 6.10: Schematic of the cyclotron amplifier.

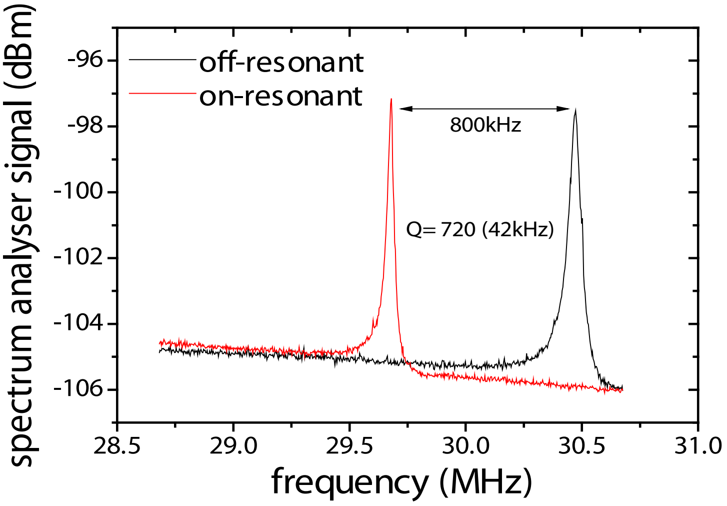

Fig. 6.11: Resonance spectra of the cyclotron detector while tuning the varactor. The black data points represents a spectrum when the varactor is detuned by 800 kHz. By tuning the biasing voltage of the varactor, the resonance frequency is matched to the modified cyclotron frequency of the antiproton in the PT $\nu_{+,\mathrm{PT}} = 29.656\,\mathrm{MHz}$, as represented by the red data points.

used to achieve high Q-values. The coil is wound on a PTFE core with a diameter of 11.5 mm and 1 mm of a pitch. Inductances are defined by the 14 pF parasitic trap capacitance, and are on the order of 1 μH. The coil is inserted to a cylindrical OFHC housing with 23 mm inner diameter and 34 mm length. The unloaded Q-value of the developed resonator is characterised with a setup as shown in Fig. 6.3 and observed in the range of 9000 to 11 000 at resonance frequency of about 90 MHz. Basically, the principle of the cyclotron amplifier is same as for the axial amplifier (section 6.1.2), except for the fact that varactor diodes MA46H072 (voltage dependent capacitor) are implemented at the input in parallel to the resonator, which acts as a 3.6 pF capacitor. This allows to tune the resonance frequency $\nu_{0,\mathrm{eff}}$ to the modified cyclotron frequency $\nu_{+,\mathrm{PT}}$ of the trapped particle by varying biasing voltages. A schematic of the cyclotron amplifier is shown in Fig. 6.10.

A tunability of $\nu_{0,\mathrm{eff}}$ is about $\sim$ 800 kHz. Figure 6.11 shows how the resonance spectrum is manipulated by changing the varactor voltages. The black data points represents a spectrum when the varactor is detuned by 800 kHz. After the varactor voltage is tuned, the spectrum moves towards lower frequencies and eventually the resonance frequency is matched to $\nu_{+,\mathrm{PT}}$ as represented by the red data points. In Table 6.7, it summarises the parameters for the cyclotron detector.

The input resistance of the cyclotron amplifier is $R_{\mathrm{in}} = 170\,\mathrm{k\Omega}$ at 30 MHz and an equivalent

Table 6.7: Summary of the cyclotron detector parameters. Abbreviations: L - Inductance / $\nu_{0,\mathrm{eff,d}}$ - Resonance frequency when the varactor is detuned / $\nu_{0,\mathrm{eff,t}}$ - Resonance frequency when the varactor is tuned / $R_{\mathrm{eff,d}}$ - Effective parallel resistance when the varactor is detuned / $R_{\mathrm{eff,t}}$ - Effective parallel resistance when the varactor is tuned / τ_{d} - Cooling time constant when the varactor is detuned / τ_{t} - Cooling time constant when the varactor is tuned.

L	Q-value	tunability	$\nu_{0,\mathrm{eff,d}}$	$\nu_{0,\mathrm{eff,t}}$	$R_{\mathrm{eff,d}}$	$R_{\mathrm{eff,t}}$	τ_{d}	τ_{t}
$1\,\mu$H	720	~800 kHz	30.472 MHz	29.656 MHz	80 Ω	135 kΩ	30 h	209 s

input noise of $e_{\mathrm{n}} = 0.83\,\mathrm{nV}/\sqrt{\mathrm{Hz}}$ at a 4 K environment. An effective temperature T_+ of the cyclotron detector can be derived by using the AT in addition to the PT. The strong magnetic bottle in the AT couples the cyclotron mode to the axial frequency. Thereby, a cyclotron energy distribution is obtained by performing many thermalisation cycles with the cyclotron detector, and for each cycles transport the particle to the AT and characterise its thermal energy E_+/k_{B}. A result of this measurement is described in section 10.4.1.

Due to space constraints in the setup, the two cyclotron detectors are designed to stack on top of each other (see Fig. 6.2). One is for the PT and the other one is for the CT. The signal wires to the trap and the amplifier are made from annealed OFHC copper wire, which has a resistance of $300\,\mathrm{m\Omega/m}$ for a 30 MHz rf-signal at 4 K. It contributes about $60\,\mathrm{m\Omega}$ series resistance and it is a major limitation for the Q-value. By coupling the resonator to the amplifier and connecting to the trap system, Q-values up to 1500 are achieved when cooled down to 4 K.

6.3 Q-tuner

In this section, development of a superconducting switch which allows continuous tuning of a quality factor of the axial detectors is described. Implementing such a device leads to improve frequency resolution at constant averaging time (refer to section10.3).

The working principle of the Q-tuner is illustrated in Fig. 6.12. A thermal conductor is attached via a galvanic connection to the cold end of the resonator. The other end of the conductor is attached to a metallised dielectric plate with small dielectric losses. A circuit which drives the heater is connected to the lower plate. By dissipating power at the heater, a part of the superconducting coil is heated over the superconducting phase transition. This adds an additional series resistance to the resonator and R_{eff} can be adjusted continuously in a range between 0 Ω and 275 MΩ. This principle allows the continuous tuning of the particle-detector interaction. How-

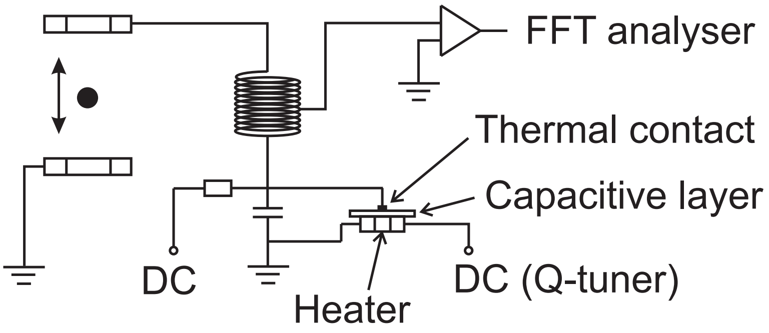

Fig. 6.12: Schematic of the Q-tuner. For details, refer to the text.

ever, compared to GaAs-FET based Q-switches or active feedback techniques [52], no parasitic parallel resistance or spurious thermal noise is added to the detection circuit.

Fig. 6.13 (a) shows FFT spectra of a single trapped antiproton in the AT. The red curve shows the Q-tuner switched off, the black curve represents a noise spectrum where a power of about 10 mW was dissipated at the heater. This decreases the dip width down to $\Delta\nu_w = 1.0$ Hz. In Fig. 6.13 (b), $\Delta\nu_w$ is shown as a function of the dissipated power on the heater. A linewidth of the dip can be adjusted in a range between 3.5 Hz and 0.7 Hz. Characterising the axial frequency stability with Allan deviations for different dip widths, results as shown in Fig. 6.14 is obtained. As expected, the use of the Q-tuner reduces the axial frequency fluctuation which obeys $\propto \Delta\sqrt{R_\mathrm{eff}/\tau}$ (see Eq. (3.30)). Therefore, by using the Q-tuner, it could potentially improve experimental precision for measuring the fundamental properties of particles.

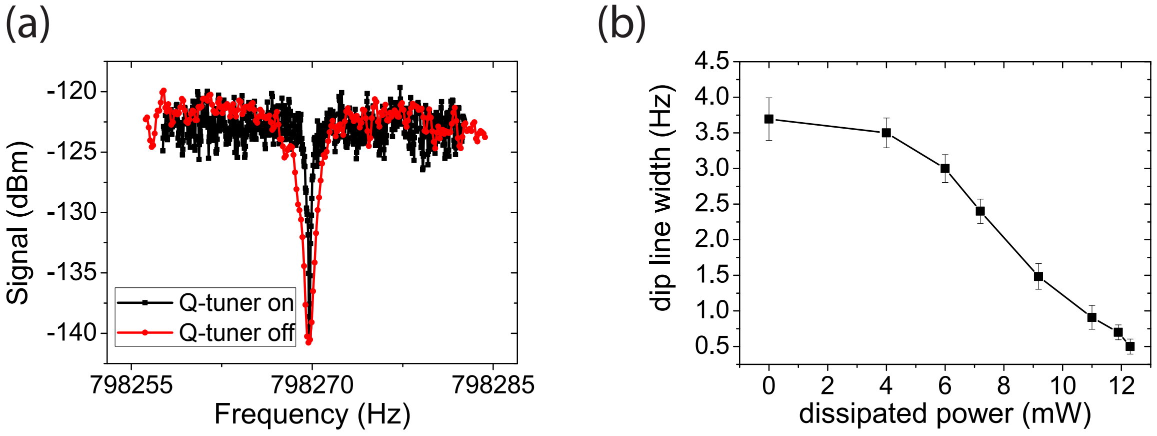

Fig. 6.13: (a) Dip with Q-tuner on and off. (b) Dip linewidth as a function of dissipated power.

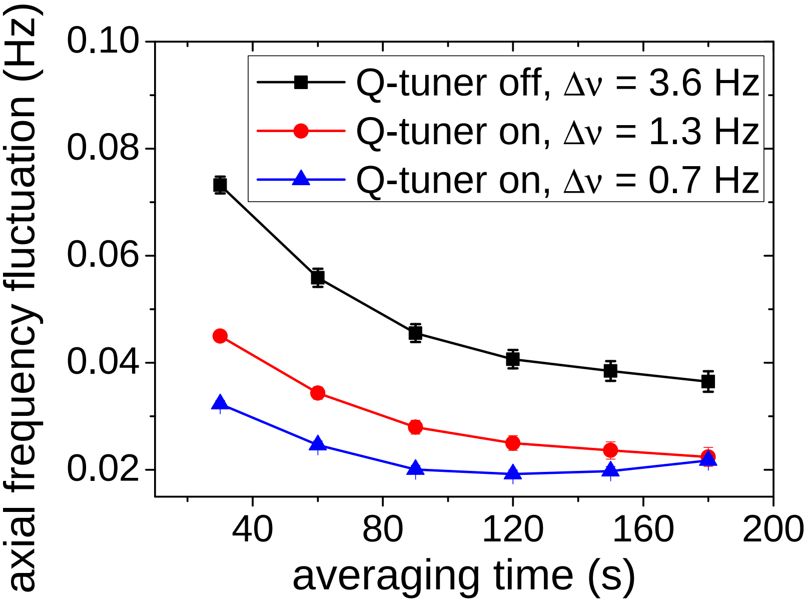

Fig. 6.14: Characterisation of the axial frequency for different dip widths, based on the Allan deviation evaluation. The axial frequency fluctuation obeys $\propto \Delta\sqrt{R_{\mathrm{eff}}/\tau}$ as expected.

Part IV

Experimental Results

Chapter 7

Reservoir trap for antiprotons

The antiprotons used at the BASE experiment are provided by the antiproton decelerator (AD). Since the accelerator operation period is scheduled usually from May to September, data-acquisition time for experiments demanding a continous supply of antiprotons is limited. While the accelerator is operated, the AD produces considerable level of electric and magnetic noise, which effectively induces magnetic field fluctuations to the field of the superconducting magnet on the order of several 10 p.p.b. per one accelerator cycle. The magnetic field fluctuation within this cycle is recorded with a GMR (giant magnetoresistance) sensor and observed to be 100 nT in the BASE experimental area. To overcome these issues, we invented a reservoir trap (RT) for antiproton storages which allows the long-term preservation of an antiproton cloud. This provides the possibility of conducting measurements during accelerator shut down period [75]. Additionally, we developed novel particle manipulation schemes, which allow to extract a single antiproton non-destructively and provide it to the other traps whenever necessary. We call this *potential tweezer scheme* (section 7.3). By detecting clouds of antiprotons for several weeks in the RT, a lower limit for the antiproton storage time of > 1.08 years is obtained [14].

This chapter follows the red line on an existing article [14]. Additionally, this project is a collaborative effort which took place during my PhD studies (see chapter 1.1).

7.1 Catching and cooling of antiprotons

A schematic of the reservoir trap (RT) is shown in Fig. 7.1 . The antiproton beam delivered from the AD, containing about 30×10^6 antiprotons, is injected to the trap from the left side of the figure. The beam trajectory is steered to the centre axis z of the apparatus. In order to tune the focal point to the degrader, the quadrupole magnets which are placed at the upstream of the apparatus

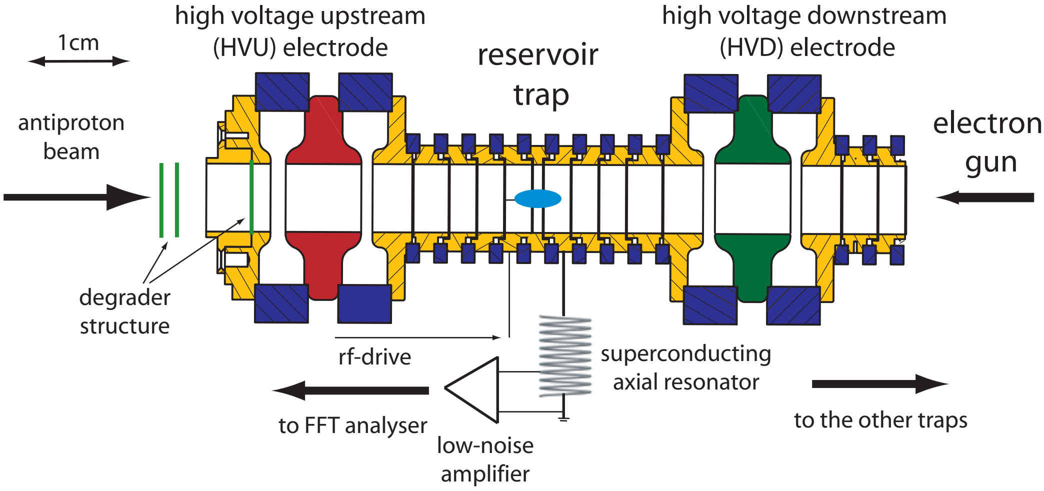
high voltage upstream
(HVU) electrode
1cm
reservoir
trap
high voltage downstream
(HVD) electrode
antiproton
beam
electron
gun
degrader
structure
rf-drive
superconducting
axial resonator
to FFT analyser
low-noise
amplifier
to the other traps

Fig. 7.1: Schematic of capturing antiproton in the reservoir trap. Taken from [14].

are utilised. Additionally, the corrector magnets based on the signal strengths on the channels of a four-fold segmented cryogenic beam monitor are used to correct for displacements of the beam with respect to the axis z. A general signal of impacting antiprotons from the AD on one of the beam-monitor channels is shown in Fig. 7.2. When the beam is centred, a 10^{-4}-fraction of the incident antiprotons is degraded to energies below 1 keV. These decelerated antiprotons are captured by applying a static -1 kV to the high voltage downstream (HVD) electrode, and applying timed voltage pulse -1 kV on the high voltage upstream (HVU) electrode to close the reservoir trap. The injection timing is characterised precisely from a scintillator placed close to the apparatus (a typical scintillation signal is shown in Fig. 7.3 (a)). In order to verify whether the catching process was successful, the antiprotons are extracted to the degrader foil and their annihilation signal is observed by triggering the scintillator on the extraction pulse (Fig. 7.3 (b)). To estimate the number of trapped antiprotons, a calibration of the scintillator by the annihilation signal of an AD pulse with known particle number was conducted. From this, it is estimated that 3000 antiprotons per one AD ejection are confined to the RT. Comparing this number to the expected efficiency from the degrader simulations (see section 5.5) indicates that the actual thickness of the degrader is within the desired range close to the optimum value.

After the capturing procedure, the trapped antiprotons have kinetic energies up to 1 keV and need to be cooled further. To this end, about 15 000 electrons are loaded by utilising the electron gun before the beam injection to perform sympathetic cooling of the trapped antiprotons. A 100 nA electron DC is generated by the electron gun for a few seconds, then the HVU and

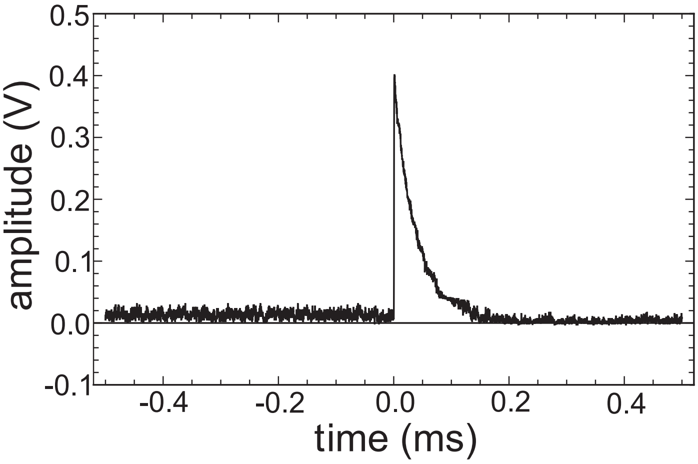

Fig. 7.2: Annihilation signal of antiprotons on the beam monitor. Taken from [13].

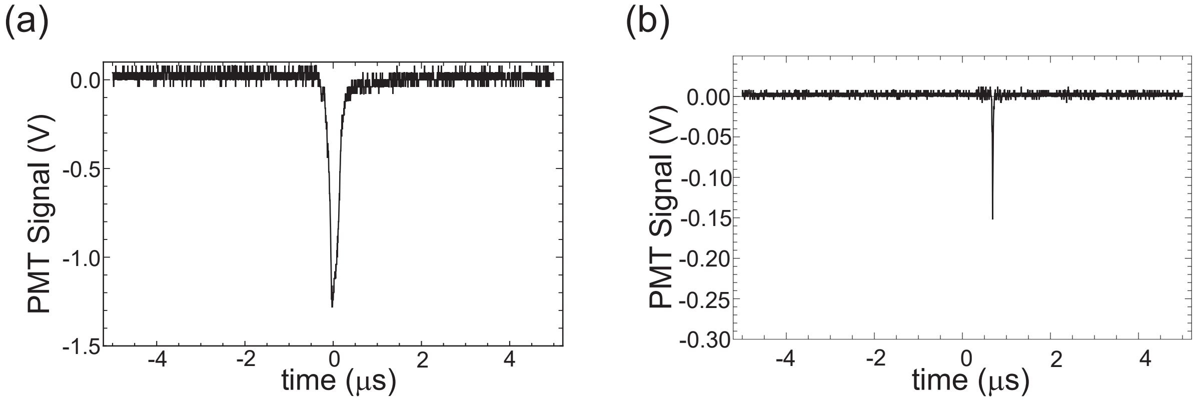

Fig. 7.3: (a) Scintillation signal of antiprotons due to the antiproton beam from the AD. (b) Scintillation signal of 3000 antiprotons extracted from the reservoir. Both figures are taken from [13].

the HVD electrodes are ramped up from 0 V to -1 kV. In the strong magnetic field, the loaded electrons are cooled via synchrotron radiation in the modified cyclotron mode, and fall into the centre of the trap, which is at 14 V. Subsequently, waiting for several seconds, typically 15 000 cooled electrons are prepared for the sympathetic cooling. A sympathetic cooling time of 10 seconds allows to accumulate several hundred antiprotons per AD shot in the RT. The accumulated antiprotons are further cooled resistively via the interaction between the axial detection system at $5.3(1.1)$ K (the detector which is used for this purpose is RT detector (q/m) as shown in Table 6.6). The number of prepared cold antiprotons is typically about a factor of 10 smaller than the initial number of trapped particles which are detected by the scintillation detector, due to the insufficient overlap of the electron cloud and the hot antiprotons and insufficient cooling of particles on large radii.

7.2 Cleaning procedure

After sympathetic cooling of the antiprotons, several cleaning procedures need to take place to eliminate trapped electrons and negatively charged ions. This is important when considering the single antiproton extraction from the cloud, to ensure no contaminants are present in the single particle measurements. The detailed procedure is listed below and its illustration is shown in Fig. 7.4.

1. **Excitation of the electron's axial motion -** An rf signal with an amplitude of 0 dBm and a frequency of 28.7 MHz (corresponds to the axial frequency of the electrons) is generated from a frequency generator and it is applied to the endcap electrode R1 via the RT axial excitation line (see chapter 5.9.2). Due to a capacitive voltage divider, eventually the signal strength is reduced to -21 dBm at R1. This rf drive eliminates a large fraction of the electrons out of the trap. Subsequently, the magnetron motion of the antiprotons is cooled by irradiating a sideband drive at $\nu_z + \nu_-$ to the RT radial excitation line, which centres them in the trap. The axial mode of the electron is excited again and the electric potential is simultaneously ramped up smoothly to 300 mV. This procedure is repeated several times before going to the next step.

2. **Electron kickout -** This technique is used to remove electrons out from the trap by manipulating the voltage potential. See section 10.1 for the basic principle and the detailed description. To kickout remaining electrons from the RT, the HVU electrode, the trans-

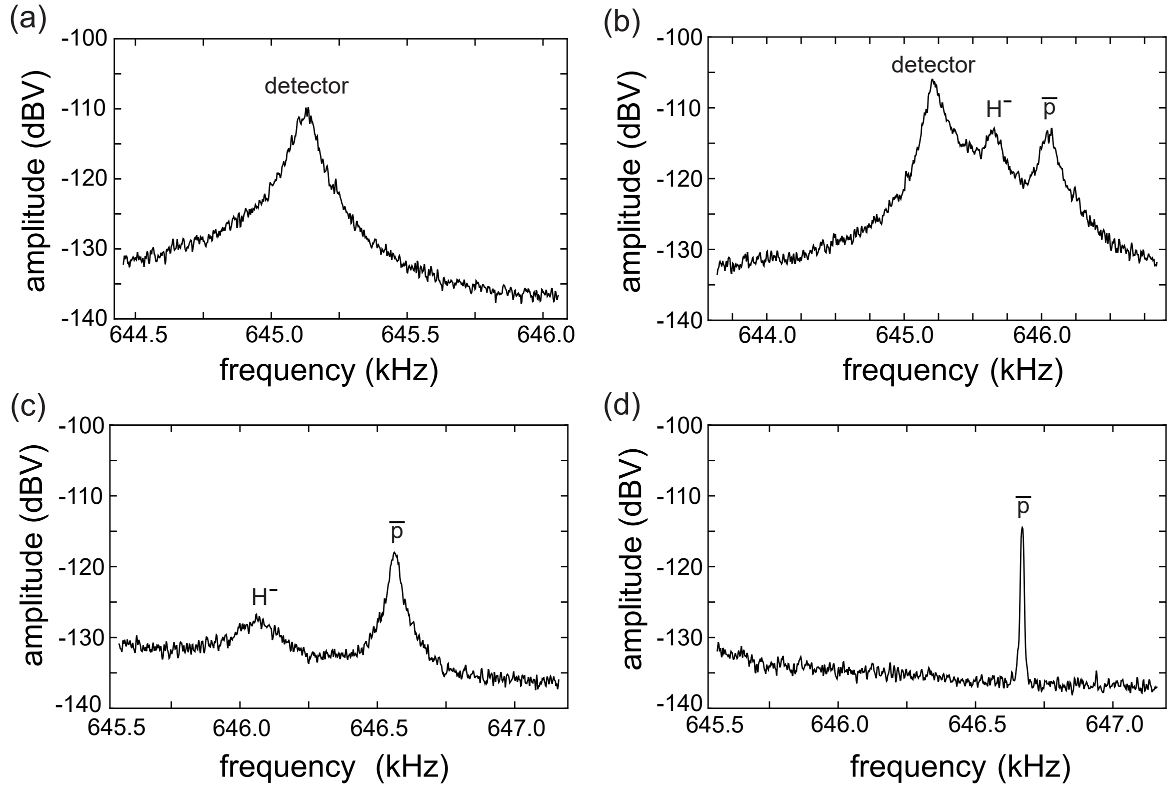

Fig. 7.4: FFT spectra taken during the antiproton preparation procedure. (a) After injecting antiprotons to the trap system, the electrons shield the low axial frequency signals of the antiproton motion and only the thermal noise of the detector can be observed. (b) FFT-spectrum after removing electrons by exciting the electron's axial motion and performing electron kick-out. Subsequently, sideband cooling of the magnetron motion took place. Afterwards, the ring voltage V_R was detuned by $11.5\,\mathrm{mV}$ from the antiproton resonance voltage to observe the H^- and antiproton peak signals $450\,\mathrm{Hz}$ and $800\,\mathrm{Hz}$ above the resonance frequency $\nu_{0,\mathrm{eff}}$, respectively. (c) FFT-spectrum before eliminating the trapped H^- ions. In this case, V_R is detuned by $18.5\,\mathrm{mV}$. (d) After eliminating H^- ions. The spectrum shows only an antiproton signal. All the figures are taken from [14].

port electrode T2, and one of the endcap electrode R1 are utilised, whereas the HVD electrode, T4, and P1 are used to perform the electron kickout for the precision trap (PT) as described in section 10.1. The kickout pulse applied to the HVU electrode is set in the range of 250∼500 ns. Apart from this, basically the procedure is identical to the case for the PT. An FFT spectrum observed after the electron kickout is shown in Fig. 7.4 (b).

3. **Negatively charged ion cleaning -** A major contaminant negative ions are, C^- and O^-. To remove them, a broad-band white noise excitation signal in a frequency band from 20 kHz to 500 kHz is applied to R1 electrode through the RT axial excitation line. This frequency range covers the axial frequency span of the typically present contaminant ion's axial modes except H^- ions. The rf drive is applied for 30 seconds and the electric potential is ramped up gradually to release excited ions from the trap. After this procedure, an FFT spectrum as shown in Fig. 7.4 (c) is obtained .

4. H^- **ion cleaning -** As will be described in chapter 8, the cyclotron frequency of a single H^- ion and an antiproton are measured for a comparison of the antiproton-to-proton charge-to-mass ratio. Therefore, this H^- ion cleaning procedure is performed only for the antiproton g-factor measurement, where H^- ions are not required. To remove H^- ions, axial frequency excitation H^- is not appropriate, since the axial frequency difference between H^- and antiproton is only 350 Hz. Instead, a resonant dipolar drive at their modified cyclotron frequency ν_{+,H^-} is applied and the voltage potential is ramped up again to release the heated H^- ions. After all, an FFT spectrum is recorded as shown in Fig. 7.4(d). It indicates that H^- ions are successfully removed.

By using the procedure described above, 100∼300 antiprotons are prepared in the RT per AD-shot. The number of captured antiprotons can be expected to be further increased by increasing the catching potential up to 5 kV, which can provide a factor 2.6 increased yield according to SRIM calculations [65].

7.3 Potential tweezer scheme

The purpose of this novel technique is to extract a certain amount of antiprotons adiabatically from the RT by manipulating electric potentials. A schematic which illustrates the manipulation of the potential is shown in Fig. 7.5.

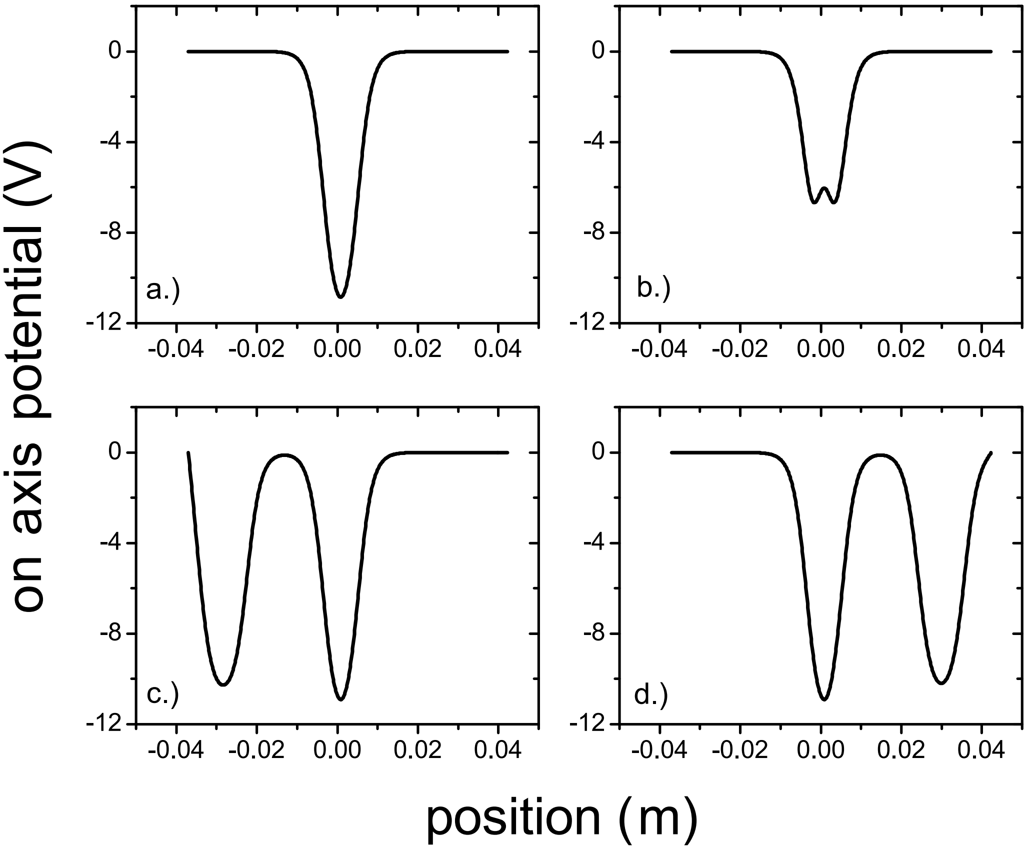

Fig. 7.5: z-axis potentials used for particle extraction from the reservoir trap [reservoir trap]. (a) Initially applied potential. (b) Potential after separation of an antiproton cloud. (c) Potential after shuttling to the upstream high-voltage (HVU) electrode. (d) Potential after shuttling to the downstream high-voltage (HVD) electrode. All the figures are taken from [14].

Initially, the antiproton cloud is confined at the centre of the RT with the ring voltage at 13.5 V. Afterwards, a constant electric field $E = 0.32\,\mathrm{V/m}\cdot\Delta\mathrm{U/V}$ is superimposed on the trap, where ΔU is a potential offset deliberately applied to the correction electrode R4. This superimposed electric field shifts the centre of mass of the axial oscillation with respect to the trap centre (Fig. 7.5 (a)). Subsequently, the ring voltage is ramped up from 13.5 V to -13.5 V (Fig. 7.5 (b)). In this way, it separates the antiproton cloud into two fractions, F_1 and F_2, respectively. F_1 is transported to the HVU electrode, while F_2 is kept in the RT and the number of particles is counted by the axial detection system (Fig. 7.5 (c)). Afterwards, F_2 is shuttled to the HVD electrode, and at the same time F_1 is transported to the RT to count its number as well (Fig. 7.5 (d)). Including transporting particles and the particle number detection of F_1

and F_2, the entire procedure takes in total 120 seconds. Results of this extraction procedure are shown in Fig. 7.6 (a). The horizontal axis represents the centre of mass positions of the particles due to different electric fields superimposed on the RT. The red circles and the black squares show the fractions F_1 and F_2, respectively. The solid lines are from analytical calculations using one-dimensional Boltzmann-statistics $w(E) = k_B T_z \exp(-E/(k_B T_z))$ and integrating

$$N_{\text{down}} = C \cdot \int_{z_0}^{\infty} |z| \exp\left(-\frac{2\pi^2 m(\nu_z z)^2}{k_B T_z}\right) dz, \tag{7.1}$$

with $N = N_{\text{up}} + N_{\text{down}}$, where C is a normalisation constant, N_{up} is the number of particles separated to the HVU electrode, and N_{down} is to the HVD electrode. The obtained data are in perfect agreement with the independently measured effective axial temperature $T_z = 5.3(1.1)\,\text{K}$.

After each individual separation cycle, the fraction of particle clouds F_1 and F_2 were merged by reversing the separation procedure. The green stars indicates the sum of both extracted fractions normalised to the number N_0 of antiprotons counted before the first separation cycle. This implies that during the entire measurement procedure, the particle number was the same within the uncertainties.

In Fig. 7.6 (b), the number of antiprotons which was separated from a RT cloud of about 100 antiprotons is shown. By applying the potential tweezer scheme, it is possible to extract arbitrary numbers of particles, in this measurement starting from 22(1) antiprotons down to a single one. Once a single antiproton is extracted, it can be provided to the other traps for single particle experiments.

By recording the axial frequency dip on the noise spectrum continuously for a certain amount of time using the axial detector, it is possible to investigate whether these particles are annihilated or decayed during this duration (refer also to section 3.2). We accumulated the axial frequency data continuously for three months, however we couldn't observe any changes on the number of trapped particles. This fact allowed us to set a new direct lifetime limit of the antiproton to > 1.08 years.

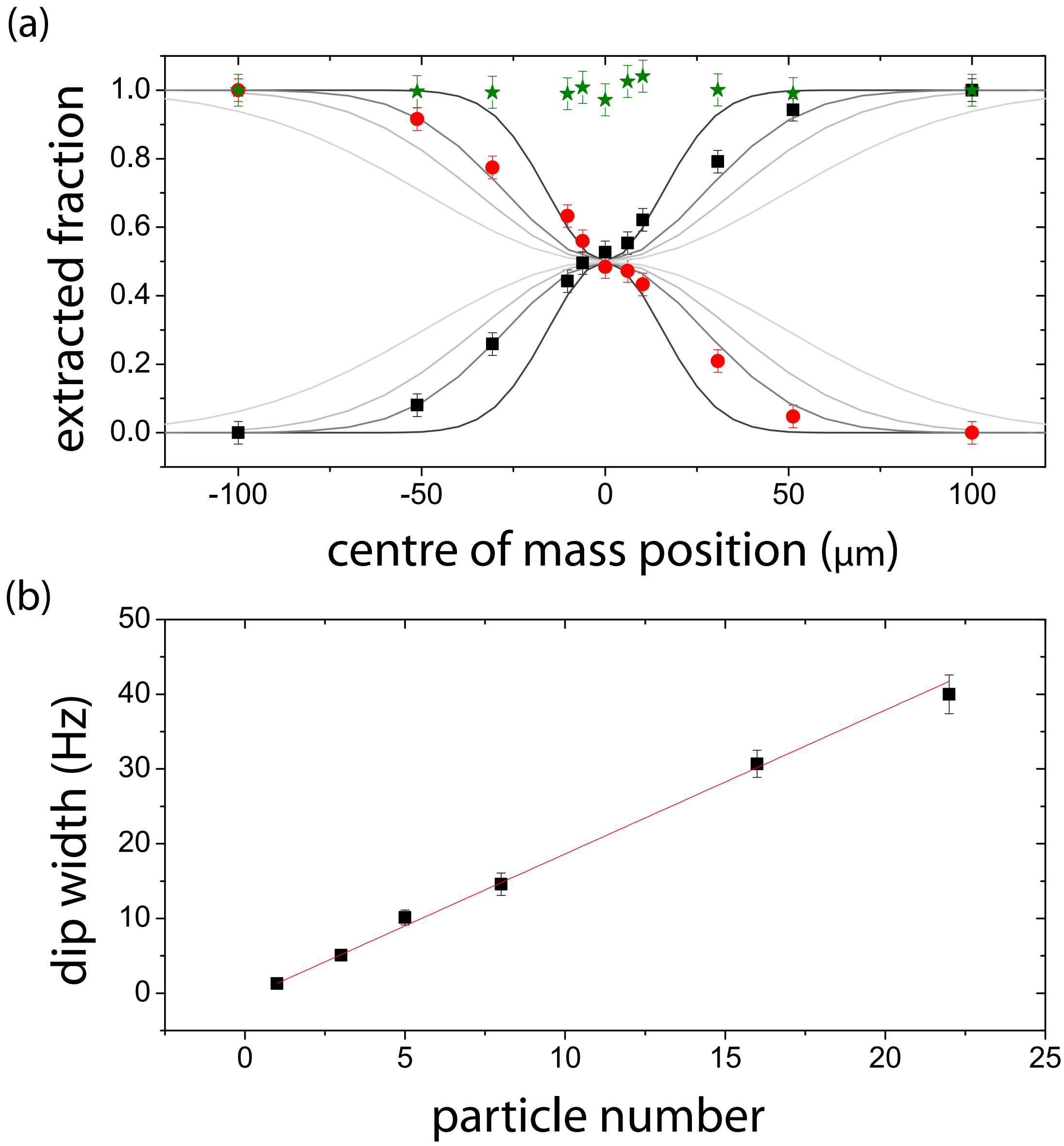

Fig. 7.6: (a) Results of the application of the potential tweezer scheme [14]. The vertical axis shows extracted fractions, and the horizontal axis represents the centre of mass position. For detail, refer to the text. (b) Dip-width as a function of extracted particles [14]. Both figures are taken from [14].

Chapter 8

Comparison of the antiproton-to-proton charge-to-mass ratio

In this chapter, a high-precision comparison of the antiproton-to-proton charge-to-mass ratio is presented. In 2015, we reported the most precise comparison of these fundamental quantities with a fractional precision of 69 p.p.t., by measuring the cyclotron frequencies of a single antiproton and an H$^-$ ion [23]. This achievement exceeds the previous precision which has accomplished by the TRAP collaboration in 1999 [6]. To date, this is the most precise test of CPT invariance with baryon sector. The description of this chapter is based on [13,23]. Additionally, this project is a collaborative effort which took place during my PhD studies (see chapter 1.1).

8.1 Principle of the measurement

In charge-to-mass ratio measurements, the free cyclotron frequency ν_c is measured for the antiproton and H$^-$ ion by using the non-destructive image-current detection of the eigenfrequencies (see chapter 3). The invariance theorem relates these frequencies to ν_c as

$$\nu_\mathrm{c} = \frac{1}{2\pi}\cdot\frac{q}{m}\cdot|\vec{B}| = \sqrt{\nu_+^2+\nu_z^2+\nu_-^2} \approx \sqrt{\nu_+^2+\nu_z^2+\left(\frac{\nu_z^2}{2\nu_+}\right)^2}. \tag{8.1}$$

ν_+ can be measured by the sideband coupling technique as described in section 3.4. Therefore, one ν_c measurement cycle consists of measuring the axial frequency ν_z followed by the modified cyclotron frequency ν_+ of a single antiproton or an H$^-$ ion. Comparisons of the antiproton-to-H$^-$ charge-to-mass ratio can be considered to be equivalent to a direct antiproton-to-proton comparison for our aimed precision, since the mass of the H$^-$ ion m_{H^-} is known with a fractional precision of 0.2 p.p.t. in units of the mass of the proton m_p as

$$m_{\mathrm{H}^-} = m_\mathrm{p}\left(1 + 2\frac{m_\mathrm{e}}{m_\mathrm{p}} + \frac{\alpha_{\mathrm{pol,H}^-}B_0^2}{m_\mathrm{p}} - \frac{E_\mathrm{b}}{m_\mathrm{p}} - \frac{E_\mathrm{a}}{m_\mathrm{p}}\right). \tag{8.2}$$

Here $m_\mathrm{e}/m_\mathrm{p}$ is the electron-to-proton mass ratio [21], $\alpha_{\mathrm{pol,H}^-}B_0^2/m_\mathrm{p}$ is the polarisability shift [76], $E_\mathrm{b}/m_\mathrm{p}$ is the electron binding energy [77] and $E_\mathrm{a}/m_\mathrm{p}$ is the electron affinity of hydrogen [78]. Under the assumption of the CPT invariance, the expected cyclotron ratio is $R = (\nu_\mathrm{c})_{\bar{\mathrm{p}}}/(\nu_\mathrm{c})_{\mathrm{H}^-} = (q/m)_{\bar{\mathrm{p}}}/(q/m)_{\mathrm{H}^-} = 1.001\,089\,218\,754(2)$. The precision is limited by the accuracy of m_p. Moreover, an advantage of using H^- ion instead of proton is the fact that it eliminates the need to invert trap voltages since it has a same polarity of charge as the antiproton. This eliminates a large systematic shift related to the particle position as discussed in section 8.3.

8.2 Preparation procedure

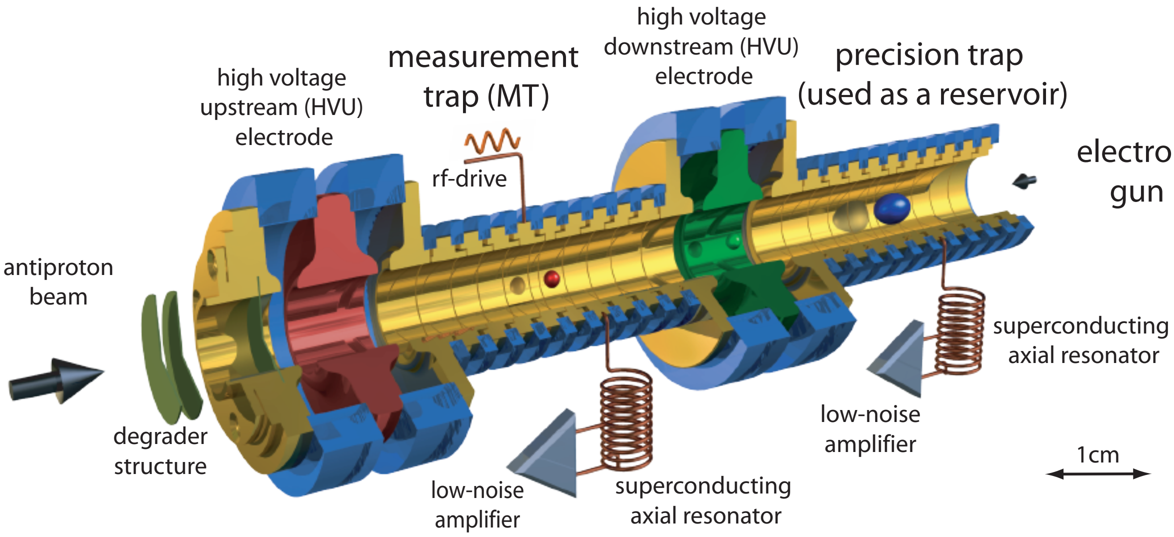
high voltage upstream (HVU) electrode
measurement trap (MT)
high voltage downstream (HVU) electrode
precision trap (used as a reservoir)
electron gun
rf-drive
antiproton beam
degrader structure
low-noise amplifier
superconducting axial resonator
low-noise amplifier
superconducting axial resonator
1cm

Fig. 8.1: Schematic of the charge-to-mass ratio measurement. Taken from [23].

Figure 8.1 shows the measurement setup. For the entire measurement, the reservoir trap (RT), precision trap (PT), high voltage downstream electrode (HVD) and high voltage upstream electrode (HVU) are used to trap particles. Regarding the RT, it was used as the measurement trap (MT) for determination of the cyclotron frequencies of a single antiproton or an H^- ion in this case. It is exposed to the magnetic field generated by the superconducting magnet, which has a field strength of $B_0 = 1.946\,\mathrm{T}$ at the centre of the trap. The PT is used as a reservoir to stock a cloud of particles for this measurement. The characteristics of the used detection systems are summarised in Table 6.6. HVD is used to park an H^- ion when the measurement of the cyclotron frequency of an antiproton is taking place in the MT, and vice versa, the HVU is used to park the antiproton when the cyclotron frequency of the H^- ion is being measured.

To load the trap, the antiproton beam provided by the antiproton decelerator (AD) is injected through the degrader system, which releases hydrogen molecules from the degrader foil. H^- ions are produced from molecular hydrogen which is frozen out on the degrader either by asymmetric dissociation of H_2 ($\mathrm{H}_2 \rightarrow \mathrm{H}^- + \mathrm{H}^+$) or by electron capture ($\mathrm{H} + \mathrm{e}^- \rightarrow \mathrm{H}^-$) process. A detailed study of the production mechanism has yet to be performed. These H^- ions are captured together with the antiprotons during the catching procedure (refer to section 7.1). Eventually, typically $100 \sim 350$ cold antiprotons and about a fraction of a third of H^- ions are trapped per a single ejection from the AD.

The number of the trapped particles can be counted non-destructively by measuring the dip-widths of their independent axial frequencies for the different species (see section 3.2). The ring voltage has to be tuned to match the axial frequency and the resonance frequency of the detector, since they differ for the antiproton and the H^- ion. For the antiproton, we need to apply $V_{\mathrm{R},\bar{\mathrm{p}}} = 4.662035\,\mathrm{V}$, whereas $V_{\mathrm{R},\mathrm{p}^-} = 4.667038\,\mathrm{V}$ is required for the H^-.

8.3 Measurement procedure

The entire measurement procedure is shown in Fig. 8.2 (a). Initially, the antiproton is parked in the MT and the H^- ion is parked in the HVD (see Fig. 8.2 (b)). The ring voltage is set to $V_{\mathrm{R},\bar{\mathrm{p}}} = 4.662035\,\mathrm{V}$ to tune the axial frequency of the antiproton to the resonance. The ν_c measurement is synchronised to the AD cycle, which is typically 110∼120 seconds. This is exceptionally important to avoid systematic shifts induced by beats between the measurements and ambient field fluctuation caused by the AD itself. Immediately after the injection trigger of the AD, the magnetron motion of the antiproton is cooled for 10 seconds by applying upper-sideband frequency $\nu_z + \nu_-$. Subsequently, the axial frequency $\nu_{z,\bar{\mathrm{p}}}$ is measured, followed by the measurement of the modified cyclotron frequency $\nu_{+,\bar{\mathrm{p}}}$. These two measurements take 30 seconds and 48 seconds, respectively. From this, $\nu_{-,\bar{\mathrm{p}}} \approx \nu_{z,\bar{\mathrm{p}}}^2/2\nu_{+,\bar{\mathrm{p}}} = 7.02\,\mathrm{kHz}$ is extracted, resulting in $\nu_{\mathrm{c},\bar{\mathrm{p}}} \approx 29.663\,\mathrm{MHz}$. Afterwards, the antiproton is transported to the HVU by ma-

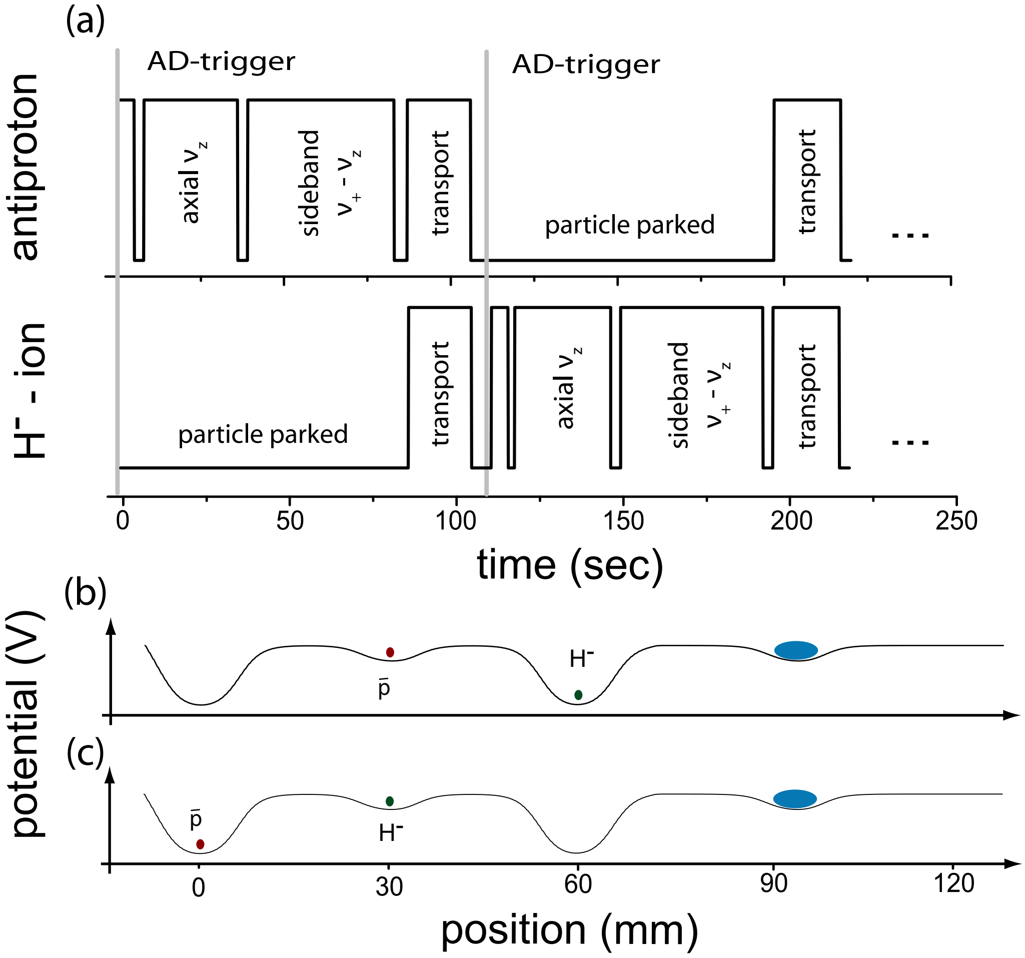
(a)
AD-trigger
AD-trigger
antiproton
axial ν_z
sideband ν_+ - ν_z
transport
particle parked
transport
...
H⁻ - ion
particle parked
transport
axial ν_z
sideband ν_+ - ν_z
transport
...
0
50
100
150
200
250
time (sec)
(b)
potential (V)
p̄
H⁻
(c)
p̄
H⁻
0
30
60
90
120
position (mm)

Fig. 8.2: (a) Detailed procedure of the charge-to-mass ratio measurement. (b) Potential configuration for antiproton cyclotron frequency measurement. (c) Potential configuration for H$^-$ cyclotron frequency measurement. All figures are taken from [23] and partly modified.

nipulating the voltage potential, and at the same time the H$^-$ ion is transported to the MT as shown in Fig. 8.2 (c). Now, the ring voltage is changed to $V_{\mathrm{R,p^-}} = 4.667038\,\mathrm{V}$, in order to tune its axial frequency to the resonance. By repeating the same procedure as for the measurement of $\nu_{\mathrm{c,\bar{p}}}$, $\nu_{\mathrm{c,H^-}} \approx 29.635\,\mathrm{MHz}$ is obtained. Therefore, a single q/m ratio comparison takes two AD cycles, which corresponds to 220 $\sim$ 240 seconds. To obtain the final experimentally determined frequency ratio $R_{\mathrm{exp}} = (q/m)_{\bar{\mathrm{p}}}/(q/m)_{\mathrm{H^-}}$ from all measurements, data points which are measured when magnetic field changes caused by activities in the AD hall were excluded. These changes are identified by an array of GMR (giant magneto resistance), Hall and flux-gate magnetic field sensors.

To remove systematic ratio shifts caused by the intrinsic magnetic-field drift $1/B_0 \times (\Delta B/\Delta t) = -5(1) \times 10^{-9}$ per hour of the superconducting magnet, the antiproton cyclotron frequencies are interpolated as

$$\nu_{\mathrm{c},\bar{\mathrm{p}},k}(t) = \nu_{\mathrm{c},\bar{\mathrm{p}},k} + \frac{(\nu_{\mathrm{c},\bar{\mathrm{p}},k+1} - \nu_{\mathrm{c},\bar{\mathrm{p}},k}) \times t}{t_{k+1} - t_k}, \tag{8.3}$$

where k is the index of individual measurements. Then, the ratio of the k-th measurement $R_{\mathrm{exp,k}}$ is defined as

$$R_{\mathrm{exp,k}} = \frac{\nu_{\mathrm{c},\bar{\mathrm{p}},k}(t_{\mathrm{H^-,k}})}{\nu_{\mathrm{c,H^-,k}}}. \tag{8.4}$$

Here, $t_{\mathrm{H^-,k}}$ is the centre time of the $\nu_{\mathrm{c,H^-,k}}$ determination. To estimate the uncertainty of the mean, the correlation matrix of the extracted ratios are evaluated and we calculate the standard error of the cross-correlated data. This avoids underestimation of the error caused by frequencies which are used in multiple ratios owing to the linear interpolation approach. All considered ratios are shown in Fig. 8.3 (a). These are 6521 frequency ratios, which were measured within 35 days. Breaks in the time sequence are due to maintenance of the apparatus or systematic measurements. Figure 8.3 (b) shows the results projected to a histogram. Additionally, for all frequency ratios, the Allan deviation (see section 10.3) is evaluated and its double-log plot is presented in Fig. 8.3 (c). By performing a linear fit to the plot, it gives a slope of $\alpha = -0.501(2)$. This confirms the Gaussian white-noise nature of the ratio fluctuations and justifies the data analysis.

The antiproton-to-H$^-$ charge-to-mass ratio extracted from this data evaluation is

$$R_{\mathrm{exp}} = 1.001\,089\,218\,872(64). \tag{8.5}$$

To ensure the reliability of the data analysis and the experiment, the cyclotron frequency ratios for identical particles $R_{\mathrm{exp,id}}$ are also evaluated. For these direct comparisons,

$$R_{\mathrm{exp,id}} - 1 = -3(79) \times 10^{-12} \tag{8.6}$$

is obtained, which is consistent with 1. The increased uncertainty is caused by the random walk in the magnetic field, which leads to slightly higher ratio fluctuations owing to the doubled time interval between subsequent measurements of identical particles. Several systematic corrections enter into the measured antiproton-to-H$^-$ charge-to-mass ratio R_{exp}. The dominant systematic shift is related to particle exchange and the 5 mV detuning of the voltage potential, which is required to tune the axial frequencies of both particles to the centre of the axial detector. Slightly different contact and offset potentials as well as machining imperfections are present at each individual trap electrode. As a consequence, the change of the ring voltage causes a relative shift of the antiproton-to-H$^-$ equilibrium position. In the presence of a magnetic gradient term

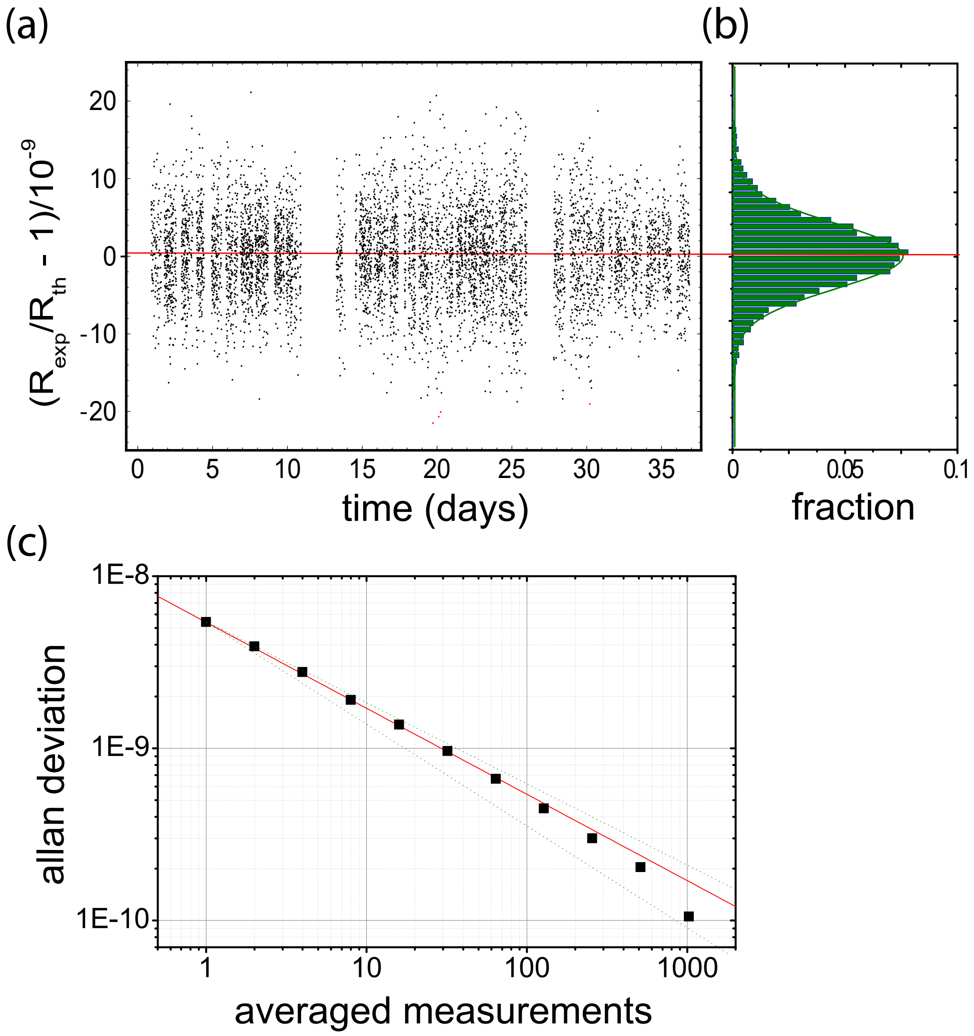

Fig. 8.3: (a) All measured antiproton-to-H^- cyclotron frequency ratios as a function of time. (b) Measured ratios projected to a histogram. (c) Allan deviation of the measured ratios. All figures are taken from [23].

of $B_1 = 7.58(42)\,\mathrm{mT\,m^{-1}}$ (where B_1 is the strength of the magnetic gradient) the cyclotron frequencies $\nu_{c,\bar{p}}$ and ν_{c,H^-} are inherently measured at slightly different magnetic fields, leading to a systematic ratio shift. In this measurement, the adjustment of the trapping voltage shifts the H^- ion towards lower magnetic fields, and R_{exp} has to be corrected by -114(26) p.p.t.. Refer to the supplementary materials of reference [23] for further information. The systematic uncertainty arises from the uncertainty in the determination of the offset voltages and the magnetic gradient B_1.

In addition to the particle position, the magnitude of the octupolar coefficient C_4 of the trapping potential (see section 2.2) also changes when the trap voltage is adjusted. The resulting ratio correction is at -3(1) p.p.t., the error being due to uncertainties extracted from potential theory and the determination of the effective axial temperature T_z of the particle. Eventually, the stability of our rubidium frequency reference clock contributes a systematic scatter of 3 p.p.t. per ratio comparison. In summary, the ratio has to be corrected by -117(26) p.p.t., leading to the final result

$$R_{\mathrm{exp,final}} = 1.001089218755(64)(26) \tag{8.7}$$

which corresponds to an antiproton-to-proton mass ratio of

$$\frac{(q/m)_{\bar{p}}}{(q/m)_{p}} - 1 = 1(64)(26) \times 10^{-12}. \tag{8.8}$$

This is in agreement with CPT conservation.

Chapter 9

Single antiproton in the analysis trap

While the work described up to here was either technical or collaborative, the following chapters describe the original experimental work of my PhD thesis.

9.1 Overview

In the analysis trap (AT), the strong magnetic bottle is superimposed to couple the spin-states of a single trapped antiproton to its axial motion. This allows to detect spin-flips of the antiproton non-destructively, which is required to measure the *g*-factor. When a spin-flip takes place in the AT, the axial frequency will be shifted by 183 mHz out of 674 kHz for our designed trap system (refer to section 9.2.4). Therefore, the axial frequency needs to be stable enough to resolve such a tiny change. To realise this, it is important to understand the behaviour of the trapped antiproton in a well-characterised AT in the first place.

In the first part of this chapter, the characterisation of the AT is described. The description starts from the detection procedure of a single antiproton in the AT, followed by the optimisation of the trapping potential in order to obtain a high signal-to-noise ratio of axial frequency dip signals. Subsequently, a direct measurement of the magnetic bottle by using the trapped antiproton is presented.

9.2 Characterisation of the analysis trap

Before actually performing precision measurements in the AT, it is necessary to understand and characterise its characteristics, such as offset potentials on the electrodes, strength of the superimposed magnetic bottle as a function of the axial position, noise level on the electrodes, and so on in detail. To characterise these basic properties, a single antiproton is extracted from the reservoir trap (RT) and transported to the AT via the precision trap (PT). Note, that it is impossible to perform these characterisation by using more than one antiproton, unlike in the RT and the PT. This is due to the fact that the strong magnetic bottle couples the radial modes to the axial frequency, and continuous interactions among antiprotons perturb the radial modes which also continuously shift the axial frequency. This prevents us from observing a dip signal on the FFT analyser, therefore it is important to ensure that there is only one antiproton trapped in the PT before transporting it to the AT. Obviously, excluding contaminants in advance is required, which could already carried out in the RT (refer to chapter 7).

Dealing with a single particle in the AT is much more challenging compared to operating the RT and the PT. First of all, the AT is constructed with much smaller inner diameter for the ring electrode (3.6 mm) than the other two (9.0 mm) and is much more sensitive to surface defects and geometric imperfections of the trap electrodes. Moreover ferromagnetic material FeCo is used for the ring electrode to create a strong inhomogeneous magnetic field at the centre of the trap. As described above, it couples not only the spin magnetic moment but also the radial magnetic moments to the axial frequency ν_z, which makes ν_z dependent on the energy of the radial motions. After cooling the modified cyclotron mode with the cyclotron detector in the PT and shuttling the particle to the AT, the frequency range of the expected axial frequency is $\sim 40\,\mathrm{kHz}$ out of $674\,\mathrm{kHz}$, which is quite significant (see section 9.2.4). On the other hand, the frequency range due to the variation of the magnetron energy after sideband cooling in the PT is relatively small $\sim 10\,\mathrm{Hz}$, therefore it is negligible in the context of seeking for particle signals. Required precisions on the ring voltage as well as the tuning ratio to observe a particle signal in such a small trap are extremely high (see section 9.2.2). Considering these issues, it is exceptionally difficult to observe particle signals in the AT in the first place. It is one of the first obstacles which needs to be carried over before actually dealing with characterisation of the AT with a trapped particle. As will be discussed in section 9.2.3, the parametric excitation of the axial motion is used to overcome these problems.

After observing a dip signal, careful optimisation of the voltage potential took place. The signal-to-noise ratio of the dip is very sensitive to the tuning ratio for such a small trap. Additionally, a direct measurement of the magnetic bottle is performed to characterise the strength of the magnetic bottle. Afterwards the antiproton was tuned to the centre of the bottle to suppress systematic shifts for the g-factor measurement (refer to section 11.5.2).

9.2.1 Adiabatic shuttling of a single antiproton from the RT to the AT

By using the potential-tweezer scheme (see section 7.3), a single antiproton is extracted from the RT and transported to the PT. Subsequently, the magnetron motion is cooled via the upper-sideband drive. The modified cyclotron motion is cooled by the interaction of the particle with the PT cyclotron detector. A waiting time of more than a cooling time constant of the detector τ ($\sim$ 3 min) is necessary for the particle to reach thermal equilibrium. The particle is shuttled from the PT to the AT also by manipulating transport electrodes which interconnect the both traps.

9.2.2 Acceptance of the ring voltage and the tuning ratio

In a small trap as the AT, the required voltage on the ring electrode to tune the axial frequency to the resonance frequency of the detector $\sim$674 kHz is at 0.877 V, calculated by using geometrical parameters of the trap design code. Therefore, by taking into account that an offset voltage on the ring electrode due to patch effects, leakage currents, and thermal contact potentials can be on the order of up to 300 mV, the actual ring voltage as well as the tuning ratio can be quite off from the predicted values. On the other hand, in order to observe a dip, the trap voltage as well as the tuning ratio need to be known to the per-mille level. Fig. 9.1 shows the initial uncertainty of the tuning ratio as well as the ring voltage, and the required precision to observe a particle signal on the FFT analyser. The red curve represents the effective tuning ratio $\mathrm{TR}_{\mathrm{eff}}(\mathrm{V}_{\mathrm{off}})$ which is defined as:

$$\mathrm{TR}_{\mathrm{eff}}(V_{\mathrm{off}}) = \mathrm{TR}_0 \left(\frac{1}{1 + V_{\mathrm{off}}/V_{\mathrm{R}}} \right), \tag{9.1}$$

where TR_0 and V_{R} are the expected tuning ratio 0.882 and the ring voltage 0.877 V, respectively. V_{off} is an offset voltage on the ring electrode. The initial uncertainty is represented by the black rectangular region with sparse pattern. To observe a particle signal, the ring voltage and the tuning ratio should be known to a level of 0.04 % and 0.06 %, which is shown as a small blue dot on the figure.

In addition, since the axial frequency depends strongly on the principal quantum number of the modified cyclotron motion in the AT, searching particle signals without any predictions consumes a considerable amount of time. This problem can be solved by exciting the axial motion parametrically to effectively decrease the required precision to find a particle signal.

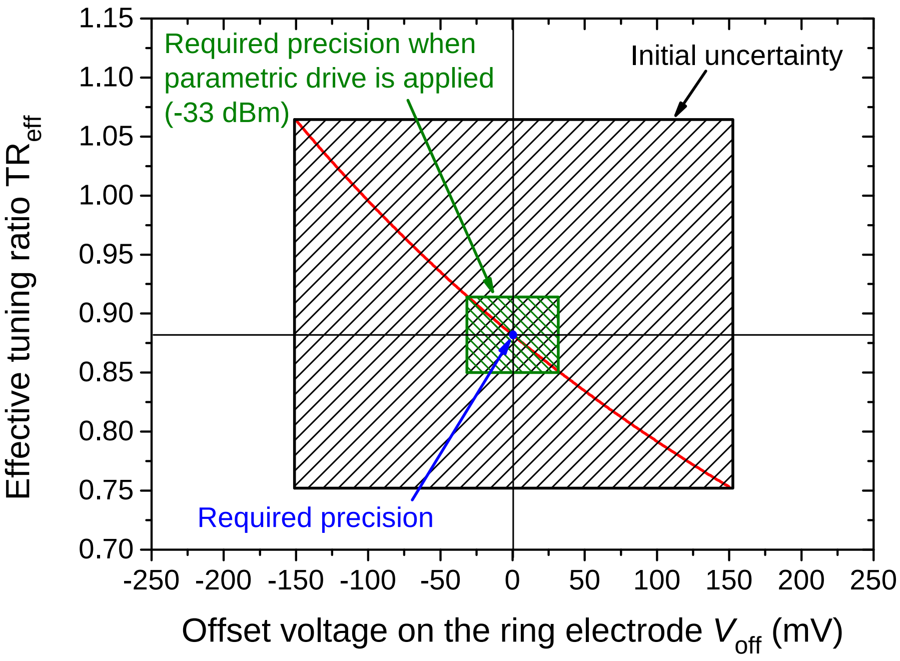

Fig. 9.1: Required precision to observe a particle signal. The red curve represents the effective tuning ratio $\mathrm{TR}_{\mathrm{eff}}$, which is defined by Eq. 9.1. The initial uncertainty of the tuning ratio and the ring voltage are shown as the black rectangular region with sparse pattern. The required precision to observe a particle signal is expressed as a small blue dot. Therefore, searching particle signals without any predictions consumes a considerable amount of time. By using a parametric resonance scheme, it is possible to decrease the required precision depending on a strength of the parametric drive. A green rectangle with sparse pattern shows the required precision when the amplitude -33 dBm is applied to the correction electrode A3. For further details, refer to section 9.2.3.

9.2.3 Parametric excitation of the axial motion

This section follows a part of the description of reference [79]. To understand the parametric excitation from the physics point of view, it is convenient to start from a model of a one-dimensional harmonic oscillator. The equation of motion of the axial motion without any external drives can be expressed as

$$\ddot{z} + \omega_z^2 z = 0 \tag{9.2}$$

where ω_z is the axial angular frequency and z the axial coordinate. When a dipolar rf drive is applied to the trap electrode, it manipulates the voltage potential V and ω_z becomes a time dependent function $\omega_{z,\mathrm{rf}}(t)$. Then Eq. (9.2) modifies to

$$\ddot{z} + \omega_{z,\mathrm{rf}}^2(t) z = 0. \tag{9.3}$$

Since $\omega_{z,\mathrm{rf}}(t)$ is a periodic function, $\omega_{z,\mathrm{rf}}(t+T) = \omega_{z,\mathrm{rf}}(t)$ (T is the period). Therefore, Eq. (9.3) is also invariant under a conversion of $t \rightarrow t+T$. By assuming $z_1(t)$ and $z_2(t)$ are the two independent solutions for Eq. (9.3), they need to satisfy $z_1(t+T) = \mu_1 z_1(t)$ and $z_2(t+T) = \mu_2 z_2(t)$, respectively. Consequently, the general expression of these two solutions will become

$$z_1(t) = \mu_1^{t/T} \Pi_1(t) \tag{9.4}$$

$$z_2(t) = \mu_2^{t/T} \Pi_2(t), \tag{9.5}$$

where, $\Pi_1(t)$ and $\Pi_2(t)$ are periodic functions which both have a same period T. By inserting z_1 and z_2 to Eq. (9.3), followed by multiplying z_2 and z_1 for each equations and subtract them from each other, eventually the following relation will be obtained

$$\dot{z_1} z_2 - z_1 \dot{z_2} = \text{const.} \tag{9.6}$$

Eq. (9.6) must hold for arbitrary functions (9.4) and (9.5). This condition leads to obtain

$$\mu_1 \mu_2 = 1. \tag{9.7}$$

We are only interested in a situation when both μ_1 and μ_2 are real, thus Eq. (9.4) and (9.5) can be rewritten as

$$z_1(t) \quad = \quad \mu^{t/T} \Pi_1(t) \tag{9.8}$$

$$z_2(t) \quad = \quad \mu^{-t/T} \Pi_2(t). \tag{9.9}$$

According to the discussion above, by assuming that the applied drive frequency is close to the double of the axial frequency and the resultant time dependent frequency $\omega_{z,\mathrm{rf}}(t)$ is nearly the same as ω_z, then the equation of motion and its general solution can be expressed as

$$\ddot{z} + \omega_z^2 [1 + \eta \cos(2\omega_z + \varepsilon)t] z = 0 \quad (0 < \eta << 1) \tag{9.10}$$

$$z = a\mathrm{e}^{st} \cos(\omega_z + \frac{1}{2}\varepsilon)t + b\mathrm{e}^{-st} \sin(\omega_z + \frac{1}{2}\varepsilon)t. \tag{9.11}$$

By substituting Eq. (9.11) for (9.10) and neglecting second derivatives (this approximation is only possible when e^{st} and e^{-st} are varying slowly) and neglecting also non-resonant terms which must be present in small amounts, we obtain

$$2as\mathrm{e}^{2st} + b\varepsilon + \frac{1}{2}\eta b \omega_z = 0 \tag{9.12}$$

$$2bs\mathrm{e}^{-2st} + a\varepsilon - \frac{1}{2}\eta a \omega_z = 0, \tag{9.13}$$

therefore,

$$s = \pm\frac{1}{2}\sqrt{\varepsilon^2 - \frac{1}{4}\eta^2\omega_z^2}. \tag{9.14}$$

To drive the parametric resonance, the condition must be

$$-\frac{1}{2}\eta\,\omega_z < \varepsilon < \frac{1}{2}\eta\,\omega_z. \tag{9.15}$$

By defining $V(t)$ as voltage variation when the parametric drive is applied to the electrode, and V_0 as voltage which is necessary to tune the axial frequency to ω_z, the following equation is obtained also by considering Eq. (9.10)

$$V(t) = V_0 + \frac{\eta m\omega_z^2}{2C_2 q}\cos(2\omega_z + \varepsilon)t = V_0 + V_{\mathrm{drive}}\cos(2\omega_z + \varepsilon)t, \tag{9.16}$$

where V_{drive} is an amplitude unit in volts of the parametric drive applied to the electrode. Therefore, Eq. (9.15) can be rewritten as

$$-\frac{C_2 q V_{\mathrm{drive}}}{m\omega_z} < \varepsilon < \frac{C_2 q V_{\mathrm{drive}}}{m\omega_z}. \tag{9.17}$$

Eq. (9.17) implies that the required precision to observe a parametrically excited signal depends on the amplitude V_{drive} of the rf drive. Therefore, the search can start from applying a relatively large amplitude and scan the TR and V_{R} to obtain a rough region where the signal was observed. Afterwards, we can decrease the amplitude and pin down the region even further. By using this principle, it is possible to get close to the point which doesn't require to apply parametric drives to observe particle signals. To illustrate the dependency of the amplitude to the required precision, here is an example. For instance, if $V_{\mathrm{drive}} = 5\,\mathrm{mV}$ is used (-33 dBm is applied to the correction electrode A3), a condition of $|\varepsilon| < 14\,\mathrm{kHz}$ is derived from Eq. (9.17). The precision which is required to find a particle signal with this drive amplitude is shown as the green rectangle with sparse pattern in Fig. 9.1. When these two parameters are in this region while applying the parametric drive, the amplitude z increases by time and it generates a large peak on a FFT analyser. Figure 9.2 shows a simulated example based on Eq. (9.11), how the axial amplitude evolves when parametric resonance drive is continuously applied to a trapped particle. In practice, the amplitude saturates after a certain period, due to the higher order potential coefficients C_4 and C_6 which shift the resonance frequency of the parametric excitation at large amplitudes. A detailed procedure of pinning down the TR as well as V_{R} towards the blue dot as shown in Fig. 9.1 is as follows:

1. Fix the TR and sweep V_{R} at a range of interest. If a peak is observed only at a certain voltage, sweep the voltage again from the other direction. If the peak still appears only at

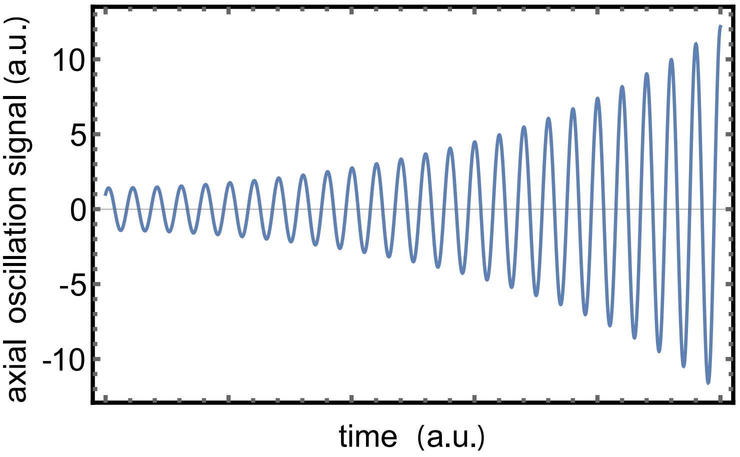

Fig. 9.2: Simulation on the parametrically excited axial motion based on Eq. (9.11).

the same voltage as the first attempt, V_R and the TR is more or less optimised. Decrease the drive amplitude V_{drive} and repeat the procedure until the TR is sufficiently optimised.

2. If a peak appeared from a certain V_R but still observable while sweeping the voltage, this is an indication that the TR is not optimised. If this phenomenon is observed while ramping up the voltage potential, this is due to $C_4 > 0$, therefore the TR should be smaller. On the other hand, if this happened while ramping down, it means $C_4 < 0$ and the TR should be larger.

Figure 9.3 shows an example of the parametric resonance scheme applied to a single trapped antiproton in the AT. The vertical axis indicates the input signal level (dBm) as a function of the frequency close to the resonance frequency $\nu_{0,\text{eff}}$ read out by an FFT analyser (see also Fig. 9.4 (a)).

The entire measurement shown in Fig. 9.3 was done by sweeping up V_R from 0.7350 V to 0.7491 V in steps of 0.3 mV (it corresponds to ramping down the voltage potential) while the parametric drive was applied with an amplitude of -30 dBm and a frequency of 1.35 MHz. Note that a capacitive voltage divider is implemented for the AT axial excitation line at the 4 K stage, which reduces the drive strength by 21.5 dB. Therefore, -51.5 dBm is actually applied to the electrode, which acquire the parametric resonance condition of $|\varepsilon| < 1.7$ kHz (required precision of $V_R = \pm 0.36\,\%$, TR $= \pm 0.35\,\%$). This is relatively close to the precision which is required to observe a dip signal. The black rectangular plot is a measurement when the TR was fixed to 1.0275, and it indicates that the TR is too small according to the procedure described above. By increasing the TR up to 1.0300 and repeating the same measurement, the parametric resonance

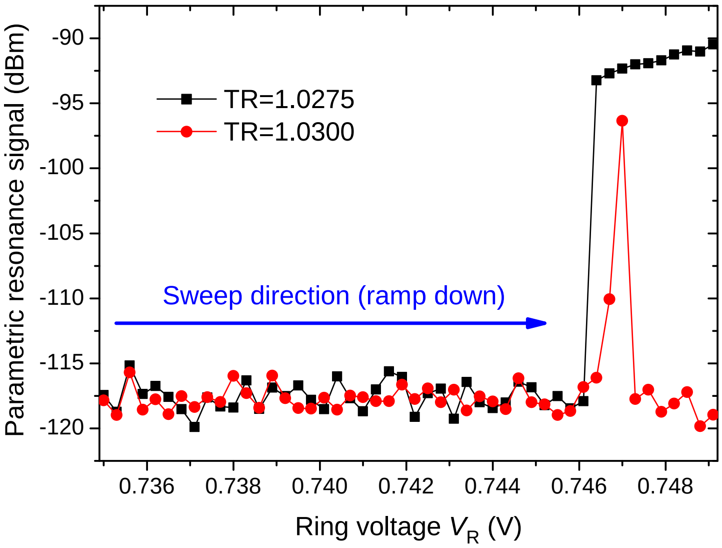

Fig. 9.3: Measurement result of the parametric resonance scheme. The black and red dots represent parametric resonance signals when the tuning ratio (TR) was fixed to 1.0275 and 1.0300, respectively. For both measurements, the ring voltage (V_R) was swept up from 0.7350 V to 0.7491 V in steps of 0.3 mV. The parametric drive with an amplitude of -51.5 dBm and a frequency of 1.35 MHz was applied to the correction electrode A3. From the figure, it is possible to conclude that the TR of 1.0275 is too small and 1.0300 is relatively close to the optimum value. For further details, refer to the text.

occurred only at a certain voltage (∼0.747 V). This implies that a particle signal should be visible at TR=1.03 and V_R =0.747 V even after the parametric drive is switched off. In Fig. 9.4, (a) it shows a peak signal of the parametrically excited particle, and (b) a dip signal after the drive is turned off. In this case, anharmonic terms of the trapping potential (particularly, C_4 and C_6) are still present to some extent, since the TR was not sufficiently optimised. This causes continuous shifts on the axial frequency and leads to decrease the SNR. In this context, the SNR is a good measure to optimise the TR. The result is shown in Fig. 9.5 (a). This measurement was done after the particle is tuned to the centre of the magnetic bottle by applying an offset voltage of -37.1 mV on A5 (see section 9.2.4), and also after the axial frequency is stabilised (see section 10). The extracted optimum TR is 1.0378. This indicates that there is an offset potential of $\approx$ 130 mV on the ring electrode. In Fig. 9.5 (b), it shows a dip spectrum after the TR optimisation.

The dip spectrum is fitted by using an appropriate line-shape as described in section 3.2, and its fit uncertainty σ is proportional to $\mathrm{SNR}^{-\frac{1}{4}}$ as shown in Eq. 3.30.

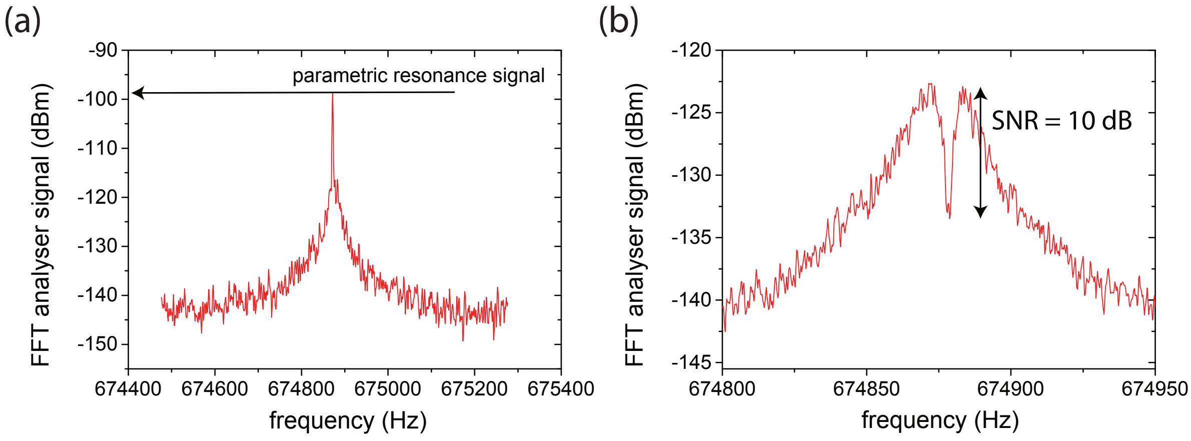

Fig. 9.4: (a) It shows a peak signal of the parametrically excited particle. (b) A dip signal after the drive is turned off. Further optimisation of the TR is required to increase the signal-to-noise ratio (SNR) of the dip.

Additionally, the axial frequency as a function of the TR is measured to characterise D_2, which is the orthogonality parameter of the trap (see section 2.2). The result is shown in Fig. 9.6. The extracted slope $\Delta\nu_z/\Delta\mathrm{TR} = -128(3)\,\mathrm{Hz/mU}$ is quite different from the potential theory $\Delta\nu_z/\Delta\mathrm{TR} = 37\,\mathrm{Hz/mU}$. This implies that there was a misalignment of the electrodes while assembling the trap system, which leads to a loss of orthogonality. As a second consequence, the higher order potential coefficients C_4 and C_6 can not be compensated simultaneously at the same TR, which prevents the particle dip to short the detector thermal noise.

9.2.4 Direct measurement of the magnetic bottle

As mentioned previously, offset potentials on the electrodes prevent the simple-minded prediction of the actual ring voltage as well as the tuning ratio to observe a particle signal. The existence of offset potentials on the correction electrodes changes the ideal voltage potential and make its shape asymmetric. This shifts the position of the trapped particle in the axial direction z and it is no longer trapped at the centre of the magnetic bottle. Centering the particle to the minimum of the bottle is important to reduce systematic errors for the g-factor measurement in the AT (see section 11.5.2).

In order to tune the particle to the centre of the trap, first of all the magnetic field B has to be measured as a function of the axial position z of the particle. The magnetic bottle couples the principal quantum number of the modified cyclotron motion n_+, the magnetron motion n_-,

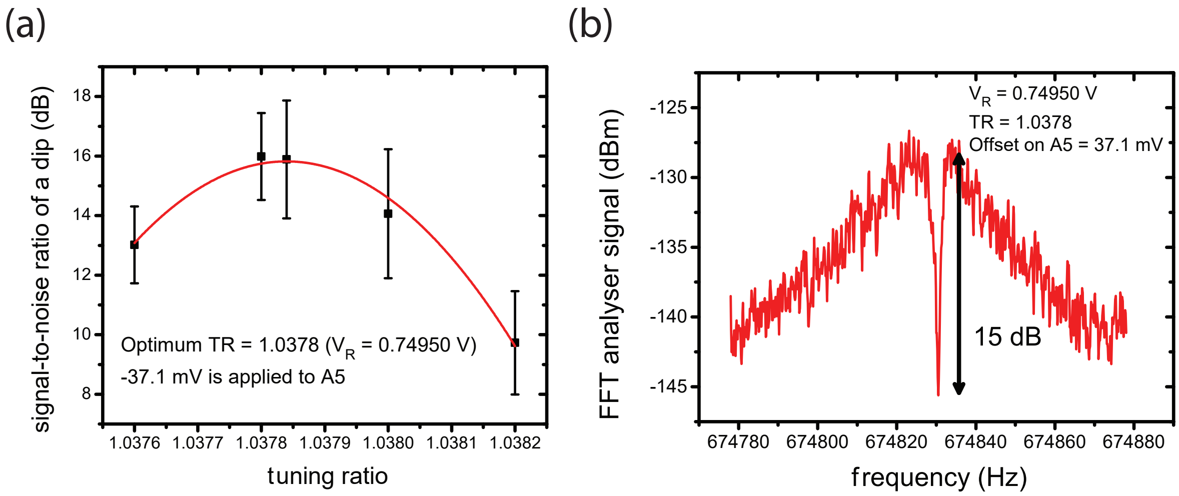

Fig. 9.5: (a) Signal-to-noise ratio (SNR) of the dip as a function of the tuning ratio (TR). By fitting the data with a parabolic curve, optimum tuning ratio of 1.0378 is extracted. This measurement was done after the particle is tuned to the centre of the magnetic bottle by applying an offset voltage of -37.1 mV on A5 (see section 9.2.4) and the axial frequency is stabilised (see section 10). The optimum ring voltage $V_\mathrm{R} = 0.74950\,\mathrm{V}$ indicates that there is an offset potential of $\sim$130 mV on the ring electrode. (b) Dip spectrum when the optimum tuning ratio of 1.0378 and the ring voltage of 0.74950 V is applied.

and the spin-state m_s to the axial frequency of the particle ν_z as

$$\nu_z(n_+, n_-, m_\mathrm{s}) = \nu_{z,0} + \frac{h\nu_+}{4\pi^2 m_\mathrm{p}\nu_z} \times \frac{B_2}{B_0} \times \left(n_+ + \frac{1}{2} + \frac{\nu_-}{\nu_+}\left(n_- + \frac{1}{2}\right) + \frac{g m_\mathrm{s}}{2}\right). \tag{9.18}$$

Equation 9.18 indicates that the axial frequency ν_z changes when quantum transitions of n_+ occur. By applying rf drives to the trapped antiproton via the spin-flip coil, they can excite the modified cyclotron mode n_+ when it is on resonance with the particle's modified cycltron frequency. This leads to an increase of the fluctuation of the axial frequency ν_z. The details of the axial frequency fluctuation measurements are described in section 10.3.1. A schematic of the setup to excite the cyclotron motion is shown in Fig. 9.7. A high-pass filter and a band-pass filter are used such that it has a high transmission at the modified cyclotron frequency $\approx$ 18.727 MHz, and low transmissions at the other frequencies. The developed setup has -120 dBm transmission at the magnetron frequency, which is around 12 kHz in the AT. The attenuation is large enough to prevent spurious noise to significantly heat the magnetron mode. The measurement procedure to directly measure the magnetic bottle is as follows:

1. Apply a certain offset voltage V_off to the correction electrode A5 and optimise the trap

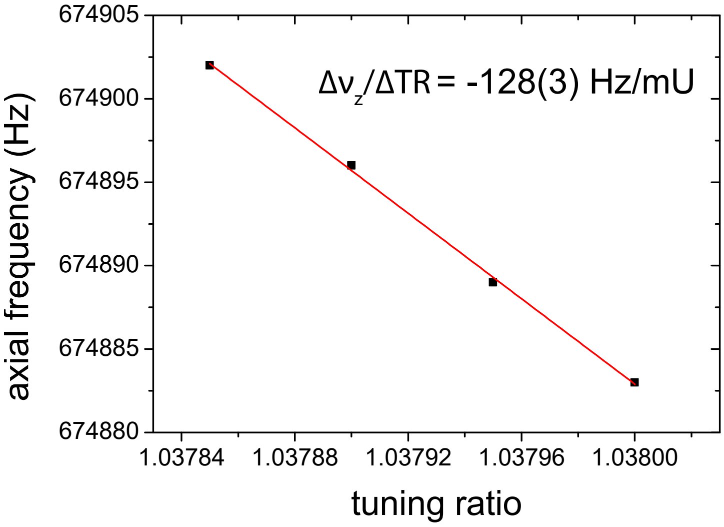

Fig. 9.6: Characterisation of orthogonality parameter D_2 by measuring the axial frequency as a function of the tuning ratio (TR). By fitting the data points by a linear function, $\Delta\nu_z/\Delta\mathrm{TR} = -128(3)\,\mathrm{Hz/mU}$ is extracted.

(V_R and TR) for the new parameters. This effectively changes the particle position and the relative shift can be calculated from potential theory.

2. Sweep up the rf drive frequency until it is on resonance with the modified cyclotron motion. In this case we start to observe large axial frequency fluctuations. The drive strength is tuned (-90 dBm is applied at the input of the AT spinflip line on the vacuum flange), so that it increases the heating rate up to around $dn_+/dt \approx 4\,\mathrm{s}^{-1}$. In this situation, the axial frequency fluctuation will be around 500(50) mHz on resonance and it is large

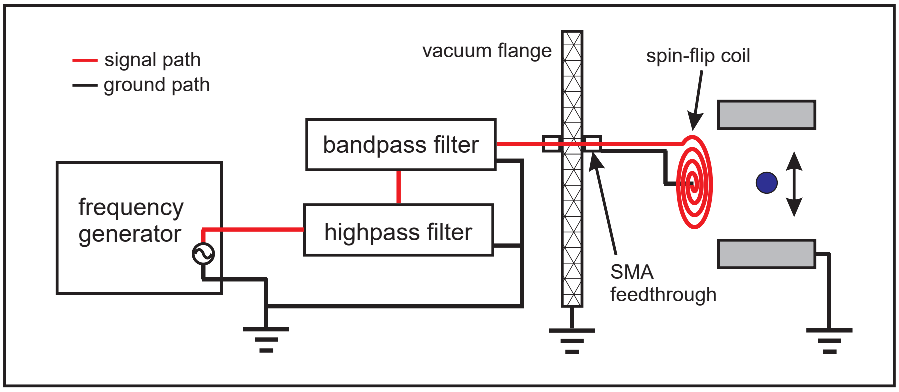

signal path
ground path
vacuum flange
spin-flip coil
bandpass filter
frequency generator
highpass filter
SMA feedthrough

Fig. 9.7: Experimental setup for the magnetic bottle measurement.

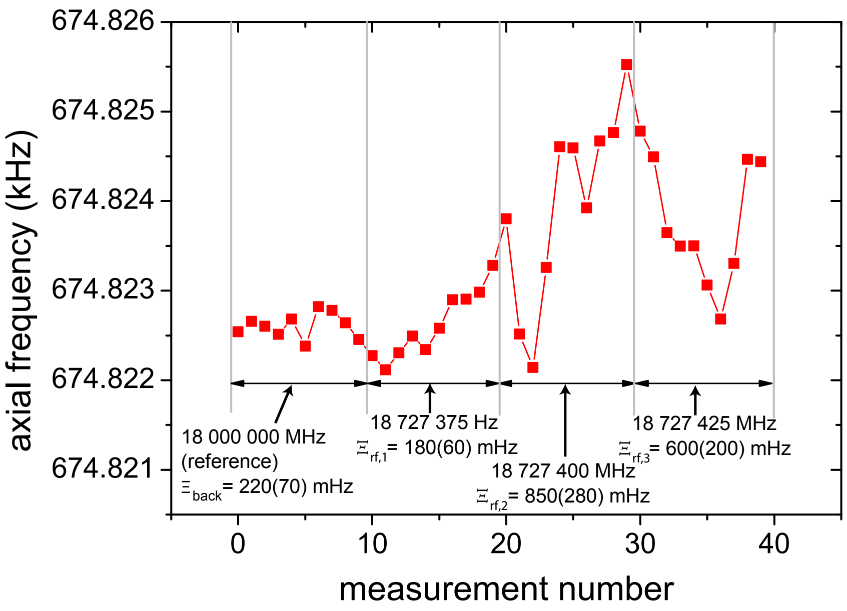

Fig. 9.8: Example of the axial frequency fluctuation caused by external rf drives in the magnetic bottle.

enough to distinguish it from off resonance. An example of this procedure is shown in Fig. 9.8. First, an off-resonant drive $\nu_{\mathrm{ref}} = 18\,000\,000\,\mathrm{Hz}$ is continuously applied, meanwhile ten axial frequencies are recorded (30 s of averaging time per each). Evaluated the axial frequency fluctuation as $\Xi_{\mathrm{back}} = 220(70)\,\mathrm{mHz}$. Then, we changed the rf-drive frequency to $\nu_{\mathrm{rf},1} = 18\,727\,375\,\mathrm{Hz}$, evaluated its fluctuation in the same procedure as for the off-resonant drive and we obtained $\Xi_{\mathrm{rf},1} = 180(60)\,\mathrm{mHz}$. By increasing the drive frequency in steps of 25 Hz, the axial frequency fluctuation started to increase drastically from $\nu_{\mathrm{rf},2} = 18\,727\,400\,\mathrm{Hz}$. This indicates that the resonance frequency of the modified cyclotron frequency is in between $\nu_{\mathrm{rf},1}$ and $\nu_{\mathrm{rf},2}$.

3. The frequency of the resonant rf drive is recorded. By using the invariance theorem [44], the magnetic field strength $B(V_{\mathrm{off}})$ for the given position is extracted.

4. Turn off the rf drive and shift the particle position by applying a different offset voltage V_{off} on A5. To visualise B_2, shift should be $\sim 50\,\mu\mathrm{m}$ which corresponds to $\sim 30\,\mathrm{mV}$. This is calculated from potential theory (see section 2.2).

5. Repeat this procedure for different offset voltages V_{off}.

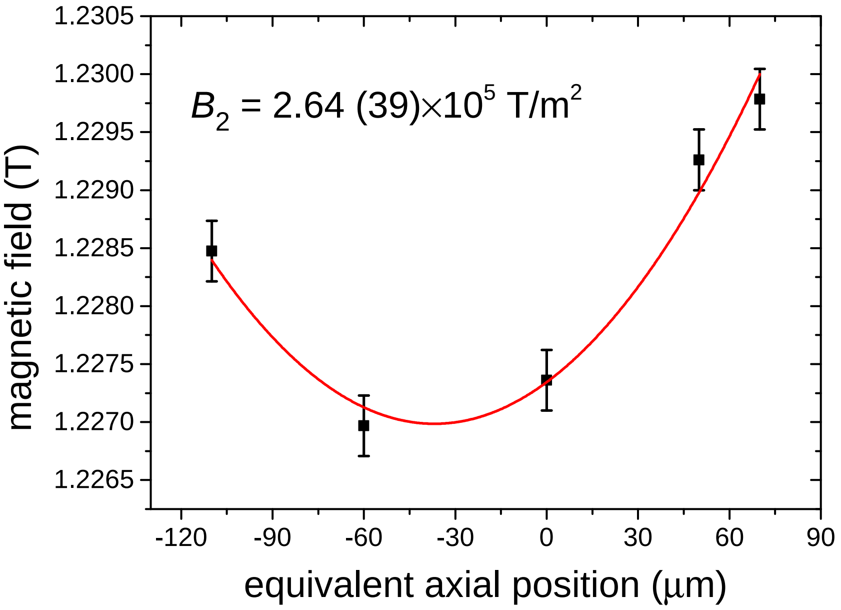

Fig. 9.9: Direct measurement of the magnetic field in the AT. For details on the measurement principle, see the text. By fitting the data with a parabolic function, $B_2 = 2.64(39) \times 10^5\,\mathrm{T/m^2}$ is extracted.

The result is shown in Fig. 9.9. By fitting this graph with a quadratic function, $B_2 = 2.64(39) \times 10^5\,\mathrm{T/m^2}$ is extracted. This is consistent within the error bars with the simulation by a potential theory as shown in Fig. 4.2. Inserting the obtained value in Eq. (9.18) and performing simple calculations results $\Delta\nu_{z,+} = \pm 65$ mHz, $\Delta\nu_{z,-} = \pm 42$ μHz, and $\Delta\nu_{z,s} = \pm 180$ mHz. By performing a fine measurement with an offset voltage range of -48∼-28 mV yielded the potential minimum at -37.1 mV.

Chapter 10

Axial frequency stability in the magnetic bottle

In this chapter, the characterisation and optimisation of the axial frequency stability in the AT are described. Apart from the coupling of the principal quantum number of radial modes n_+ and n_- to the magnetic bottle (see section 9.2.4), there are several possible factors which can affect the stability. The major factors are, interactions between the particle and trapped contaminants, the quality of the electrical ground of the apparatus, and fluctuations of the voltages applied to the Penning-trap electrodes. By using high precision voltage source UM 1-14 by Stahl Electronics together with our handmade multi-stage RC filters, the applied voltages on the electrodes are sufficiently stabilised (refer to section 5.9.1 for their specifications). Therefore, techniques to eliminate the other major factors are described here in detail. In the last part of the chapter, measurements of the thermal energies of the modified cyclotron mode and the magnetron mode are described. The axial frequency stability is dependent on the energy states of the radial motions, and it is understood that the lower the energies are, the higher the stability becomes (see section 10.4.1). Since the radial modes are cooled via the interaction with the thermal bath of the detection systems, which possess a certain effective temperature, it is necessary to characterise its temperature so that the preparation time required to prepare a sufficiently cold particle in the AT can be estimated.

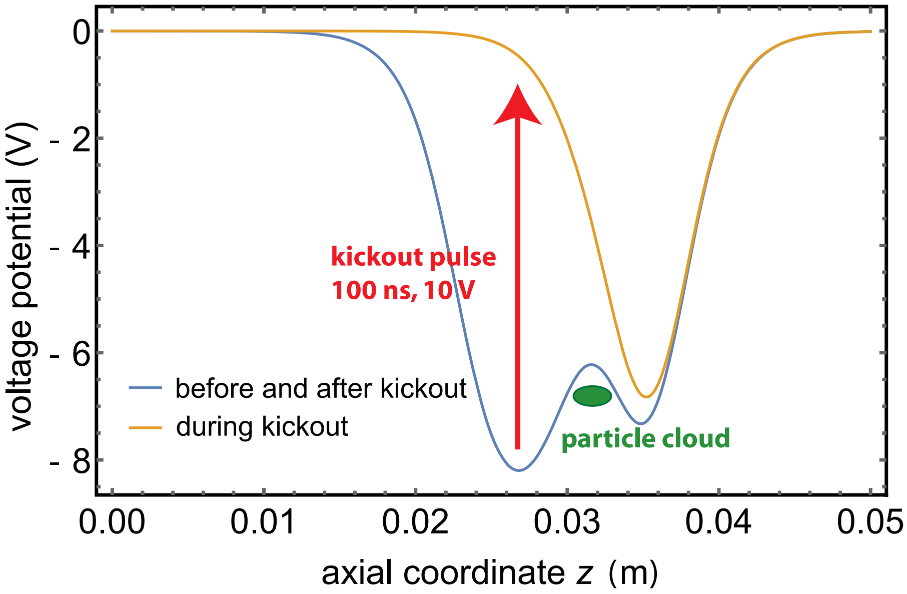

Fig. 10.1: Schematic of the electron kickout. The actual voltage potentials before and after the kickout pulse is applied to HVD electrode are shown.

10.1 Electron kickout scheme

A very important step is to remove co-trapped electrons from the antiproton's potential well. One of the most efficient ways to get rid of electrons out of the trap is to perform the electron kickout scheme. Figure 10.1 shows voltage potentials before and after the electron kickout was performed. The basic idea is to use the fact that the mass of the antiproton is about 1836 times larger than that of the electron. This causes a big difference on the axial frequency between the antiproton and the electron. The electron has a factor of 43 larger axial frequency than that of the antiproton in the same trapping potential, which corresponds to the oscillation period of roughly a factor of 40 smaller for the antiproton than the electron. A pulse signal is applied to a certain electrode in a way that one side of the potential well opens for some time, which is long enough for electrons to escape from the potential well but short enough for the antiproton to leave the potential well.

In practice, the antiproton is transported from the AT and parked at the transport electrode T4 which is located next to the downstream high voltage electrode (HVD). $-2\,\mathrm{V}$ is applied to T4, $-10\,\mathrm{V}$ to HVD, and $-13\,\mathrm{V}$ to P1. In this situation, the antiproton has an axial frequency of around 700 kHz and 30 MHz for electrons. Subsequently, a pulse signal which has a pulse width of 100 ns and an amplitude of 10 V is applied to HVD and let the trapped electrons escape. In order to prepare a clean antiproton, we repeat this scheme for multiple times before we use the electron cleaned antiproton for spin-flip experiments. Including particle shuttling and cooling of the magnetron motion in the PT a single electron kick-out procedure typically takes 120 s.

10.2 Optimisation of the ground structure

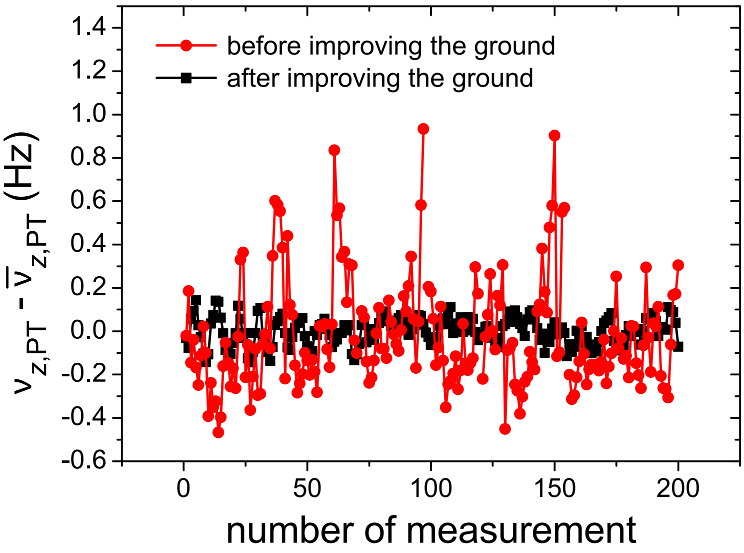

Fig. 10.2: Comparison of the axial frequency stability between before improving the ground of the apparatus (red circle points) and after the action (black rectangular points). $\bar{\nu}_{z,\mathrm{PT}}$ is the mean frequency evaluated from the individual measurements.

Fluctuations on the ground potential can be effectively considered as spurious noise on the Penning-trap electrodes, which can lead to an increase of the heating rate of n_+ and n_-. According to Eq. (9.18), this directly affects the axial frequency stability. Even if there was a significant effort made to stabilise the voltage source itself, having an improper grounding makes this effort to go down the drain.

A preferable ground should be made out of a metal (good conductor), which has a large surface area, and close to the system. Therefore, the most suitable ground of the system is the vacuum flange, which supplies the electrical signals of the entire apparatus. To avoid generating unwanted noise, voltage differences at different parts of the ground should be avoided. To realise this situation, all ground parts of the devices related to the experiment should be unified to this vacuum flange and connected via a short path as possible. Good ground connections can be made by soldering or screwing tightly. In addition, to avoid any ground loops

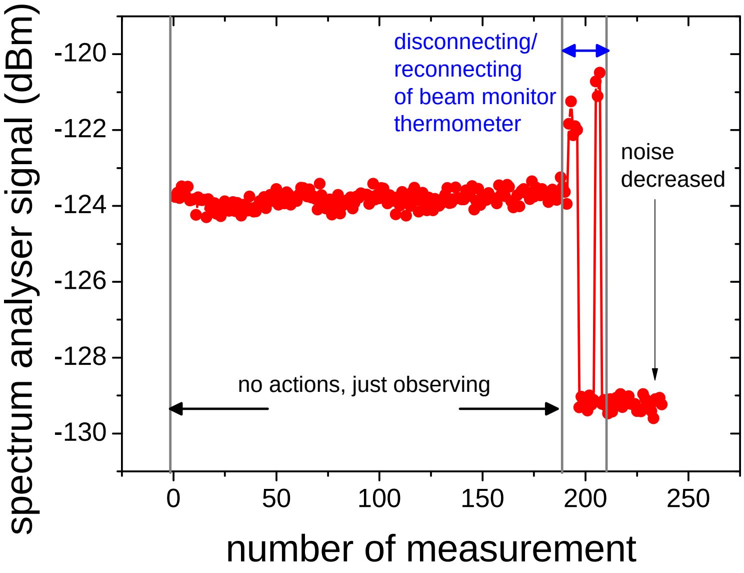

Fig. 10.3: Monitoring the noise level on the resonance frequency of the cyclotron detector, while performing grounding actions. After disconnecting a thermometer for the beam monitor, the noise level decreased by -5 dB. For details, see the text.

a local reference point was defined and the ground of all the devices must be always guided from this point. Before having such a proper grounding action, the amount of noise present on the apparatus was considerably higher that it was already possible to quantify the noise level by recording the axial frequency of a single antiproton in the precision trap (PT), while the cyclotron detector was tuned to the particle's modified cyclotron frequency. The result is shown as the red circle points in Fig. 10.2. Each point is a frequency measurement averaged by 50 s. By using Eq. (10.22) and evaluating the effective temperature T_+ of the cyclotron detector as described in section 10.4.1, $T_+ \approx 500\,\mathrm{K}$ is extracted. This is approximately 120 times higher than the physical temperature of the apparatus, which implies that it is almost impossible to prepare a cyclotron-wise cold particle in the AT to perform g-factor measurements. The detector temperature directly affects the time which is required to prepare a sufficiently cold particle in the AT (see section 10.4.1). As a conclusion, it turned out that the major contribution to such a large T_+ was related to a thermometer for the cryogenic beam monitor. Figure 10.3 shows the signal level [dBm] on the resonance frequency of the cyclotron detector as a function of a number of measurement points. Equation 3.15 indicates high T_+ leads to have high SNRr, therefore the noise level on the cyclotron detector can be a suitable measure of T_+ while improving the ground. Around measurement number 200, the detector signal fluctuated within a range of

$-129\,\mathrm{dBm} \sim -120\,\mathrm{dBm}$, by disconnecting and reconnecting the thermometer. After disconnecting it completely and make it an open circuit, the noise level was more or less constant at $-129\,\mathrm{dBm}$, which is $5\,\mathrm{dB}$ smaller than before this action took place. A detailed investigation for this effect is yet to be performed. The black square points in Fig. 10.2 shows a measurement after the thermometer was disconnected. The axial frequency became much more stable so that T_+ was no longer possible to be resolved in the PT. Further investigations on T_+ is possible by using the AT, as described in section 10.4.1.

After this action, rearrangement of all electronic instruments which are involved in our measurement schemes took place, since the axial frequency stability in the AT was still not good enough to resolve spin-flips. For each instrument used for the experiment, we consider how the individual signal/ground lines should be guided. As described above, it should have a common ground and the power cables must be distributed with a structured cabling. Eventually, the distributed power cables need to be unified to one power socket, which is connected to the AD mains supply. A schematic of how the entire instruments are distributed after this action is shown in Fig. 10.4.

Additionally, it is also important to make sure that the apparatus is electrically isolated from the AD beamline to achieve a stable ground condition. Since the dipole/quadrupole magnets distributed in the AD are operated with large currents, they induce not only ambient magnetic field, but also electric noise. To prevent that the electric accelerator noise couples into the ground structure of our apparatus, the beamline is electrically isolated by connecting to the main recuperation by vacuum tubes made out of Polyetheretherketone (PEEK). A pump which continuously pumps the OVC of the magnet is also decoupled by using a tube made out of this material.

The final result obtained after all these optimisation steps is presented in the next section.

10.3 Characterisation of the axial frequency stability

10.3.1 Definition of the axial frequency fluctuation

Quantifying the axial frequency stability is important to investigate whether the apparatus is well-optimised or not. Specifically, it is important measure to tell if it is stable enough to resolve spin-flip transitions $\Delta\nu_{z,\mathrm{SF}} = 183\,\mathrm{mHz}$ in the AT.

Assume that the axial frequency is continuously recorded and N data-points are accumu-

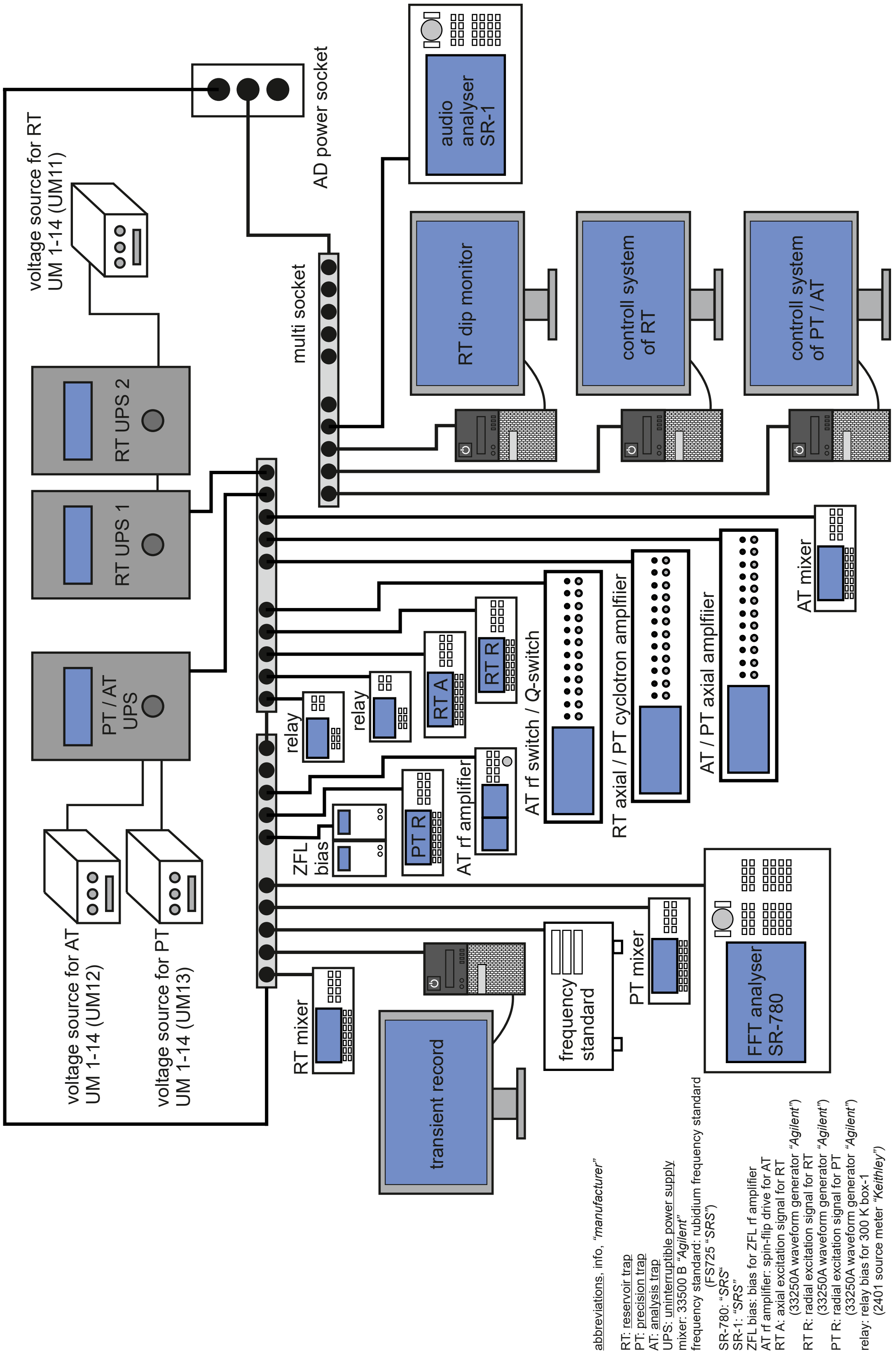
voltage source for RT
UM 1-14 (UM11)
AD power socket
audio
analyser
SR-1
multi socket
RT UPS 2
RT UPS 1
PT / AT
UPS
RT dip monitor
controll system
of RT
controll system
of PT / AT
relay
relay
RT A
RT R
PT R
ZFL
bias
AT rf amplifier
AT rf switch / Q-switch
RT axial / PT cyclotron amplfiier
AT / PT axial amplfiier
AT mixer
voltage source for AT
UM 1-14 (UM12)
voltage source for PT
UM 1-14 (UM13)
RT mixer
transient record
frequency
standard
PT mixer
FFT analyser
SR-780
abbreviations, info, “manufacturer”
RT: reservoir trap
PT: precision trap
AT: analysis trap
UPS: uninterruptible power supply
mixer: 33500 B “Agilent”
frequency standard: rubidium frequency standard
(FS725 “SRS”)
SR-780: “SRS“
SR-1: “SRS”
ZFL bias: bias for ZFL rf amplifier
AT rf amplifier: spin-flip drive for AT
RT A: axial excitation signal for RT
(33250A waveform generator “Agilent”)
RT R: radial excitation signal for RT
(33250A waveform generator “Agilent”)
PT R: radial excitation signal for PT
(33250A waveform generator “Agilent”)
relay: relay bias for 300 K box-1
(2401 source meter “Keithley”)

Fig. 10.4: Power cable distribution of the electric instruments.

lated. The measured axial frequencies are defined as $\nu_{z,k}\,(k = 1,2,3\cdots N)$. Then, the axial frequency fluctuation Ξ_z and its standard error $\Delta\Xi_z$ are

$$\Xi_z = \frac{1}{N-1}\sum_{i=1}^{N-1}(\Delta\nu_{z,i}-\Delta\bar{\nu}_z)^2 \tag{10.1}$$

$$\Delta\Xi_z = \frac{\Xi_z}{\sqrt{2\cdot(N-1)-2}}, \tag{10.2}$$

where,

$$\Delta\nu_{z,i} = \nu_{z,i+1}-\nu_{z,i} \tag{10.3}$$

$$\Delta\bar{\nu}_z = \frac{1}{N-1}\sum_{k=1}^{N-1}\Delta\nu_{z,k}. \tag{10.4}$$

The same argument can be also applied for characterising voltage supplies [54, 55].

10.3.2 Allan deviation

In the time domain, the axial frequency signal of a single particle can be expressed as a simple sinusoidal function

$$V(t) = V_0\sin(\omega_z t+\phi(t)), \tag{10.5}$$

where ω_z is the average frequency, and $\phi(t)$ the phase variation, respectively. By defining the instantaneous phase $\Phi(t) = \omega_z t+\phi(t)$, the instantaneous frequency $\omega(t)$ can be expressed as

$$\omega(t) = \frac{d\Phi(t)}{dt} = \omega_z+\frac{d\phi(t)}{dt}. \tag{10.6}$$

For a convenience of the further discussions, the two following functions which are related to the variation of the frequency are defined

$$y(t) = \frac{\omega(t)}{\omega_z}-1 = \frac{1}{\omega_z}\frac{d\phi(t)}{dt} \tag{10.7}$$

$$x(t) = \int y(t)dt = \frac{\phi(t)}{\omega_z}. \tag{10.8}$$

In practice, unlikely to Eq. (10.7), the axial frequency fluctuation can only be measured as a value which averaged over the measurement interval τ

$$\bar{y}_m(\tau) = \frac{x(t_m+\tau)-x(t_m)}{\tau} = \frac{1}{\tau}\int_{t_m}^{t_m+\tau} y(t)dt. \tag{10.9}$$

Therefore, the standard variance of the axial frequency fluctuation $\langle\bar{y}_m(\tau)^2\rangle$ with a duration of τ will be

$$\begin{aligned}\langle\bar{y}_m(\tau)^2\rangle &= \lim_{M\to\infty}\frac{1}{M}\sum_{m=1}^{M}\bar{y}_m(\tau)^2 = \left\langle\frac{[x(t_m+\tau)-x(t_m)]^2}{\tau^2}\right\rangle \\ &= \frac{\langle x(t_m+\tau)^2\rangle+\langle x(t_m)^2\rangle-2\langle x(t_m+\tau)x(t_m)\rangle}{\tau^2}.\end{aligned} \tag{10.10}$$

By introducing autocorrelation functions

$$R_x(\tau) = \lim_{T\to\infty} \frac{1}{T}\int_0^T x(t)x(t+\tau)dt \tag{10.11}$$

$$R_y(\tau) = \lim_{T\to\infty} \frac{1}{T}\int_0^T y(t)y(t+\tau)dt, \tag{10.12}$$

Eq. (10.10) can be rewritten as

$$\langle \bar{y}_m(\tau)^2 \rangle = \frac{2[R_x(0) - R_x(\tau)]}{\tau^2}. \tag{10.13}$$

Recalling that these autocorrelation functions are related to power spectrum density $S_{x,y}(f)$ via Fourier transform

$$S_{x,y}(f) \;=\; 4\int_0^\infty R_{x,y}(\tau)\cos(2\pi f\tau)d\tau \tag{10.14}$$

$$R_{x,y}(\tau) \;=\; \int_0^\infty S_{x,y}(f)\cos(2\pi f\tau)df, \tag{10.15}$$

Eq. (10.13) can be written as

$$\langle \bar{y}_m(\tau)^2 \rangle = \frac{4}{\tau^2}\int_0^\infty S_x(f)\sin^2(\pi f\tau)df. \tag{10.16}$$

Since the time derivative corresponds to multiplying $2\pi f$ for the frequency domain,

$$S_y(f) = 4\pi^2 f^2 S_x(f). \tag{10.17}$$

Therefore, Eq. (10.16) eventually becomes

$$\langle \bar{y}_m(\tau)^2 \rangle \;=\; \int_0^\infty S_y(f)\frac{\sin^2(\pi f\tau)}{(\pi f\tau)^2}df = \int_0^\infty H_{\mathrm{SV}}df \tag{10.18}$$

$$S_y(f) \;=\; h_{-2}f^{-2} + h_{-1}f^{-1} + h_0 f^0 + h_1 f^1 + h_2 f^2, \tag{10.19}$$

where f^{-2} is the random walk FM noise, f^{-1} the flicker FM noise, f^0 the white FM noise, f^1 the flicker PM noise, and f^2 the white PM noise, respectively. By inserting the equation (5.34) to (5.33) and integrating, it turns out that $\langle \bar{y}_m(\tau)^2 \rangle$ diverges to infinity for f^{-2} and f^{-1}. This implies that if there is a random walk or flicker FM noise component superimposed on the axial frequency evolution, the axial frequency deviates from ω_z by performing a large amount of sampling, independent on the averaging time τ. Consequently, characterising the axial frequency stability by using the standard variance is not suited for a general stability standard. Instead, the Allan variance $\sigma_y^2(\tau)$ can be considered:

$$\sigma_y^2(\tau) = \frac{1}{2}\langle(\bar{y}_{m+1} - \bar{y}_m)^2\rangle = 2\int_0^\infty S_y(f)\frac{\sin^4(\pi f\tau)}{(\pi f\tau)^2}df = 2\int_0^\infty H_{\mathrm{AV}}df. \tag{10.20}$$

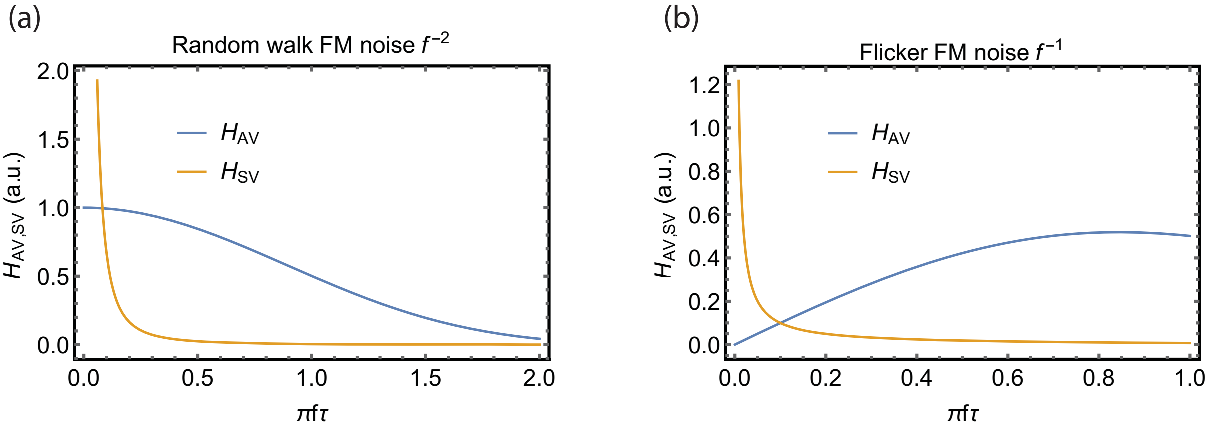

Fig. 10.5: Comparison of the Allan and Standard variance by using H_{SV} and H_{AV}. (a) Presence of random walk FM noise f^{-2} diverges H_{SV} to infinity, inherently $\langle \bar{y}_m(\tau)^2 \rangle \to \infty$. On the other hand, H_{AV} converges to a certain value, although a random walk component is present. This is also the case for (b), when considering that flicker FM noise f^{-1} is superimposed. Therefore, the Allan variance is much more suitable than the Standard variance as a measure for frequency stability.

The Allan variance does not converge to infinity even in a presence of f^{-2} and f^{-1}. Fig. 10.5 shows a comparison of the functions H_{SV} and H_{AV} for (a)f^{-2} and (b)f^{-1}. In practice, the axial frequency fluctuation is expected to be a superposition of the white FM noise f^0 and the random walk FM noise f^{-2}. The white noise mainly comes from voltage fluctuations and an uncertainty of fitting dip spectra. On the other hand, the random walk is mainly due to the voltage drift and quantum transitions on the radial modes. Figure 10.6(a) shows a simulation of the Allan deviation $\sigma_y(\tau)$ when a certain amount of a white noise and a random walk are present. Therefore, it is possible to disentangle these two components, no matter how large the sampling number is. From this aspect, the Allan variance is suited for characterising the axial frequency evolution in time domain. Figure 10.6(b) shows the axial frequency stability characterised by the Allan deviation $\sigma_y(\tau)$ in the AT before and after optimising the system. The black dots are measured on 7th of December 2015, after performing electron kickout and the previously described stabilisation of the apparatus. The data-set represented by the red dot was measured on 29th of November 2015, before these actions. Note that within this period, the antiproton was trapped in the AT all the time and we didn't perform any thermalisation cycles with the cyclotron detector. This ensures that the difference shown in Fig. 10.6(b) is not due to different thermal energies E_+/k_{B}, but the proper grounding action led to decrease considerably the spurious noise density on the electrodes. By fitting the black curve with a non-linear least squares, the cyclotron heating transition rate of $dn_+/dt \approx 0.1\,\mathrm{s}^{-1}$ is obtained (the cyclotron energy was $E_+/k_\mathrm{B} \approx 1\,\mathrm{K}$). This corresponds to the spurious noise density of $50{\sim}200\,\mathrm{pV}/\sqrt{\mathrm{Hz}}$, see Eq. (10.21). The Allan deviation reaches $\sim 100\,\mathrm{mHz}$ after this optimisation work. Since the spin-flip shift is around 180 mHz, it is possible to apply the statistical method for spin-flip detection [55].

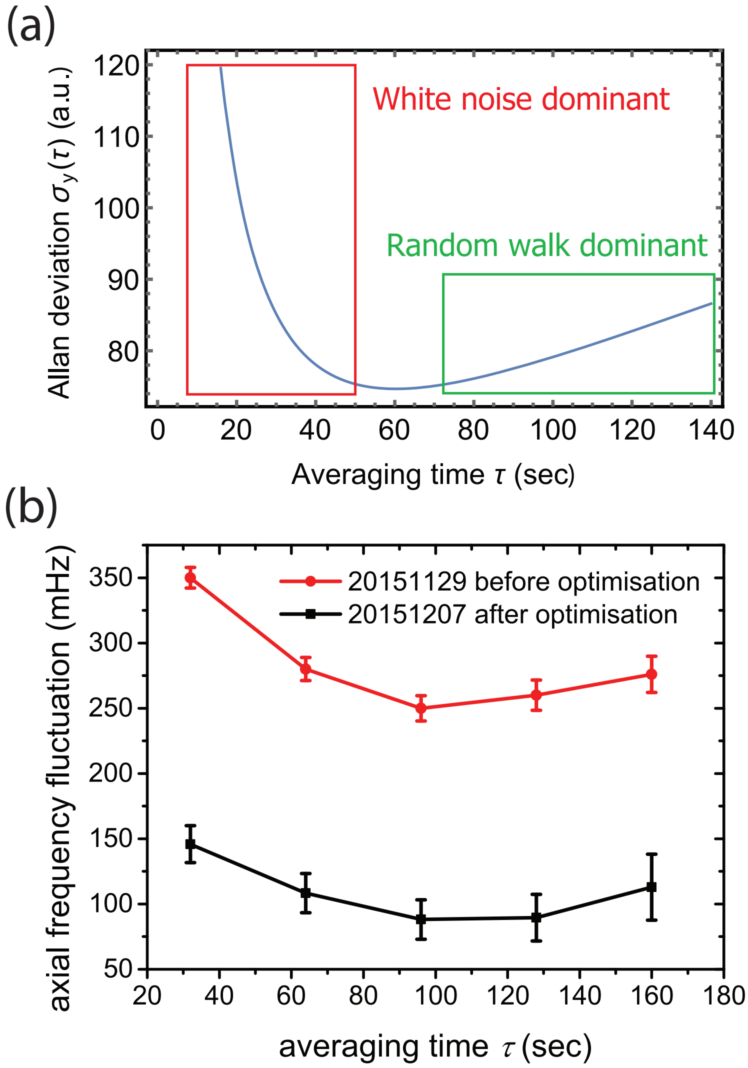

Fig. 10.6: (a) Simulation of the Allan deviation $\sigma_y(\tau)$ when a certain amount of white noise and the random walk are present. (b) Axial frequency stability characterised by using the Allan deviation $\sigma_y(t)$. The black dots are measured on 7th of December 2015, after performing the electron kick-out scheme and the stabilisation of the ground potential. The red dot is measured on 29th of November 2015, before these actions. Refer to the text regarding interpretations of this result.

10.4 Temperature measurements of the radial motions

The axial frequency stability is related to the heating rate of the radial modes as [80]:

$$\frac{dn_{+,-}}{dt} \approx \frac{q^2}{2m_p h\nu_{+,-}} n_{+,-} \Lambda^2 \langle e_n(t), e_n(t-\tau)\rangle, \tag{10.21}$$

where $\langle e_n(t), e_n(t-\tau)\rangle$ is the spurious noise density on the electrode. According to this equation, not only the spurious noise affects the heating rate but also the principal quantum number of the radial modes $n_{+,-}$ contributes. Therefore, it is important to cool the radial modes as much as possible to obtain a good stability on the axial frequency. The modified cyclotron mode n_+ is cooled by the cyclotron detector in the PT, and the magnetron mode n_- is cooled by applying upper-sideband drive in the AT. The background noise amplitudes which we were observing when the axial frequency stability is on the order of 100 mHz correspond to noise densities of order 10 to $100\,\mathrm{pV}/\sqrt{\mathrm{Hz}}$. Such amplitudes can only be observed with cold particles in traps.

10.4.1 Temperature of the modified cyclotron mode

To measure the temperature of the modified cyclotron mode, first the particle is brought to resonance with the cyclotron detector. After the particle has reached thermal equilibrium with the detector, the cyclotron energy is Boltzmann distributed. The actual measurement procedure of T_+ is as the following:

1. Transport the antiproton from the AT to the PT.
2. Vary the DC-bias voltage of the varactor, which is implemented on the amplifier board of the PT cyclotron detector, and tune the resonance frequency of the detector to the modified cyclotron frequency of the antiproton ∼29.65 MHz.
3. Wait until the cyclotron mode has reached thermal equilibrium (waiting time depends on the cooling time constant τ. In our case, it is typically around 3 min).
4. Transport the antiproton from the PT to the AT.
5. Tune the dip to the centre of the AT axial detector and record the applied ring voltage (keep the tuning ratio constant).
6. Repeat this procedure until the distribution can be clearly seen, and a particle below a certain temperature threshold has been found .

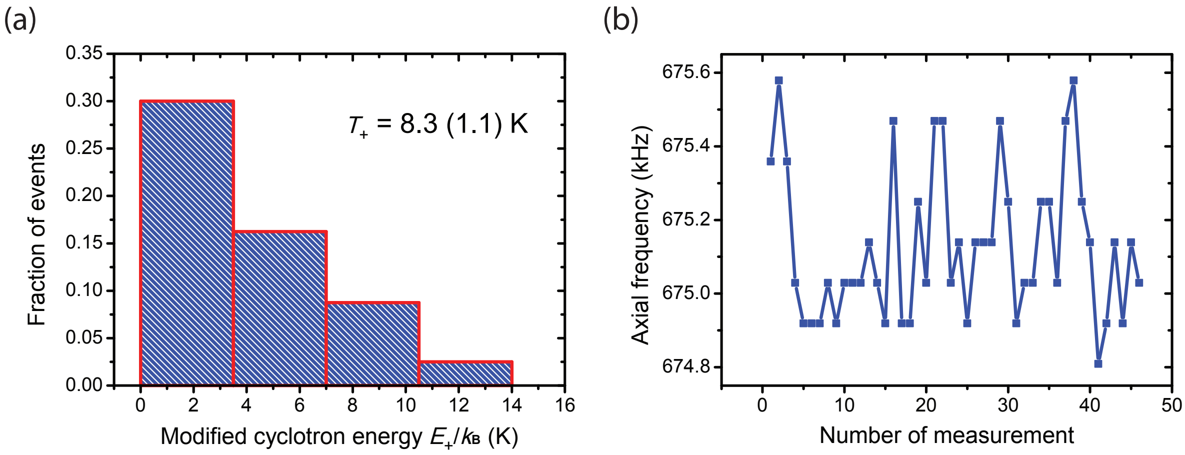

Fig. 10.7: (a) Histogram of the energy of the modified cyclotron motion. It is measured after optimisation of the apparatus. First, a single trapped antiproton in the AT is transported to the PT and its modified cyclotron mode is cooled by the cyclotron detector. Subsequently, it is transported back to the AT and the energy of the modified cyclotron mode is measured based on Eq. (9.18). Repeating this procedure for many times ends up at obtaining a Boltzmann distribution of the energy as shown in the figure. By fitting with an appropriate function, the temperature of the cyclotron detector $T_+ = 8.3(1.1)\,\mathrm{K}$ is extracted. (b) Axial frequency distribution due to different cyclotron energies as a function of a number of measurements.

The obtained ring voltage distribution $F(V_\mathrm{R})$ is converted to the axial frequency distribution $F(\nu_z)$ by using the relation $440\,\mathrm{kHz}/V_\mathrm{R}$. By subtracting the cut frequency $\nu_{z,0}$ from each measured ν_z, $\Delta\nu_z$ is obtained, which allows to determine the cyclotron energy:

$$E_+ = 4\pi^2 m\nu_{z,0}\Delta\nu_z \frac{B_0}{B_2}. \tag{10.22}$$

Converting the distribution to $F(E_+/k_\mathrm{B})$, we can fit an exponential function $\alpha \mathrm{e}^{-E_+/k_\mathrm{B}T}$ ($\alpha \subset \mathbb{R}$) to the distribution to extract the temperature T_+. From integrating the probability density function $\frac{1}{k_\mathrm{B}T_+}\mathrm{e}^{-E_+/k_\mathrm{B}T_+}$ within an energy range of interest, it is possible to extract a probability to obtain a particle energy which is in this respective range. Therefore, it is required to decrease the temperature T_+ as much as possible to increase the probability to observe a cold particle in the AT, which consequently leads to decrease the preparation time for the measurements. This is exceptionally important for eventually performing the double-trap g-factor measurement [35]. Although the physical temperature of the cyclotron detector is 6.4 K, it does not necessary mean that T_+ is at the same temperature since T_+ is defined only as the effective temperature of the detector. The effective temperature T_+ increases if external noise is coupled into the system, which then adds up to the thermal noise. Therefore, it is important to eliminate external noise sources, which is a difficult task in an accelerator hall. Figure 10.7 (a) shows a histogram of the Boltzmann distribution of the modified cyclotron energy E_+/k_B after optimising the apparatus. By evaluating the temperature T_+ as described above, $T_+ = 8.3(1.1)\,\mathrm{K}$ is extracted. Figure 10.7 (b) shows the axial frequency as a function of a number of measurements.

10.4.2 Temperature of the magnetron mode

The magnetron motion is cooled by applying a sideband drive at $\nu_z + \nu_+$ in the AT via the spin-flip coil. The basic idea is similar to the cooling procedure of the modified cyclotron motion, except for the fact that the PT is not required for this procedure. As discussed previously, the magnetic bottle couples the magnetron mode via n_- to the axial frequency ν_z as expressed in Eq. (9.18). Therefore, it is necessary to reproduce a Boltzmann distribution on the magnetron energy E_- to characterise a required axial frequency ν_z, when its stability is sufficiently high. The experimental result is shown in Fig. 10.8. Since the magnetron mode is coupled to the axial detector when the sideband drive is applied, it is possible to extract not only the magnetron temperature T_- but also the axial temperature T_z (refer to section 3.4 for further detail). By fitting the histogram with a function $\alpha \mathrm{e}^{-E_-/k_\mathrm{B}T}$ ($\alpha \subset \mathbb{R}$), T_- =125(15) mK is obtained. In addition, by recalling the relation:

$$\frac{E_z}{T_z} = \frac{E_-}{T_-}, \tag{10.23}$$

$$T_z = \frac{\nu_z}{\nu_-} T_- \tag{10.24}$$

T_z =8.0(1.0) K is extracted. After cooling the particle and optimising the stability, we obtain an axial frequency stability of $\sim$ 100 mHz. In this condition, it becomes possible to observe antiproton spin-transitions.

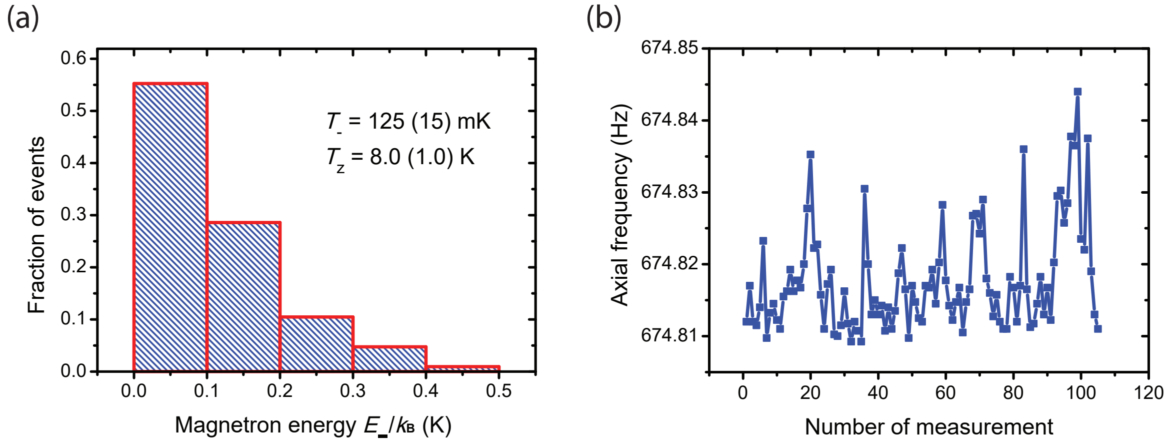

Fig. 10.8: Histogram of the magnetron energy measured in the AT by using sideband drives. From the distribution, the temperature of the magnetron mode T_- when coupled to the axial detector of the AT is extracted as $T_- = 125(10)\,\mathrm{mK}$. From Eq. (10.24), the corresponding axial temperature is $T_z = 8.0(1.0)\,\mathrm{K}$.

Chapter 11

Measurement of the magnetic moment of the antiproton

In this chapter, a measurement of the magnetic moment of the antiproton with a fractional precision of 0.8 p.p.m. is presented [25]. The fractional precision of the obtained value is by six times more precise than reported by the ATRAP collaboration in 2013 [22]. The result is consistent with the most precise measurement of the magnetic moment of the proton, reported by the BASE collaboration at the University of Mainz [24] and supports CPT invariance.

The measurement was performed by using in total three Penning traps: the reservoir trap (RT), the precision trap (PT), and the analysis trap (AT). As described in chapter 7, the RT is used to contain a cloud of antiprotons and supplies single ones to the other traps whenever needed. The PT is originally implemented to measure the particle's oscillation frequencies with high precision, however, in these measurements it is used as a co-magnetometer trap. Continuous measurement of the modified cyclotron frequency ν_+ of a single antiproton in the PT provides continuous sampling of the trap's magnetic field, with an absolute resolution of a few nanotesla. The AT has the strong magnetic bottle of $B_2 = 2.88 \times 10^5\,\mathrm{T/m^2}$ superimposed. In this trap, the actual g-factor measurement took place. In the AT, the trapped antiproton is tuned to the centre of the bottle by applying an offset voltage of $-37.1\,\mathrm{mV}$ to the correction electrode A5 (see Fig. 9.9). This is crucial to suppress systematic shifts (refer to section 11.5.2). In this condition, the antiproton in the AT experiences a magnetic field of $B_0 \sim 1.23\,\mathrm{T}$, which corresponds to a modified cyclotron frequency ν_+ and a Larmor frequency ν_L of $\nu_+ \approx 18.727\,\mathrm{MHz}$ and $\nu_\mathrm{L} \approx 52.337\,\mathrm{MHz}$, respectively.

The determination of the g-factor requires precise measurements of ν_+ and ν_L. As shown in Eq. (9.18), the modified cyclotron motion and the spin-state are coupled to the axial frequency

ν_z by the strong B_2. Therefore, these frequencies can be measured by applying radio-frequency (rf) drives to the particle in the AT and characterise its axial frequency fluctuation (see section 10.3.1) for different drive frequencies ν_{rf}. First, the principle of frequency measurements in the magnetic bottle is described.

11.1 Principle of frequency measurements in the magnetic bottle

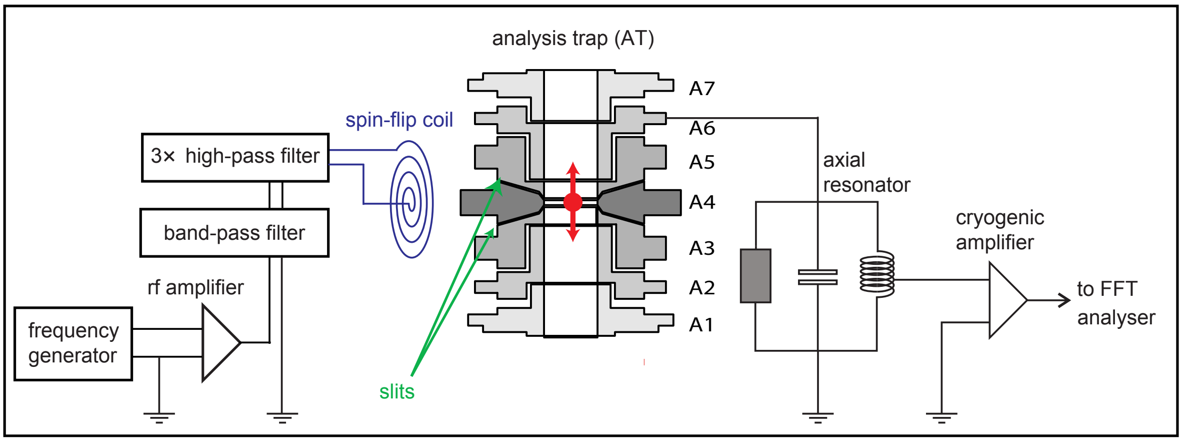
analysis trap (AT)
A7
A6
A5
A4
A3
A2
A1
spin-flip coil
3× high-pass filter
band-pass filter
rf amplifier
frequency generator
slits
axial resonator
cryogenic amplifier
to FFT analyser

Fig. 11.1: Schematic of frequency measurements in the analysis trap (AT). This setup is used for Larmor frequency measurements. A frequency generator signal is first amplified by an rf amplifier, subsequently passes through a band-pass filter and three high-pass filters. In total four filters are implemented to achieve -120 dB transmission at the magnetron frequency $\nu_- \approx$ 12 kHz. The attenuation is large enough to prevent the rf drive to heat up the magnetron motion. For further details, refer to the text.

A schematic of the AT including electronics details is shown in Fig. 11.1. The trap consists of seven electrodes used as four end caps (A1, A2, A6, and A7), two correction electrodes (A3 and A5) and one ring electrode A4 which is made out of Co/Fe. The superconducting detection system is connected to the end cap electrode A6, which allows to measure the axial frequency ν_z of a single trapped antiproton non-destructively. The specifications of the detector are shown in in Table 6.6. Recalling that the radial modes with their main quantum numbers n_+ and n_- and the spin-state with quantum number m_s are strongly coupled to the axial frequency ν_z in the magnetic bottle as

$$\nu_z(n_+,n_-,m_\mathrm{s}) = \nu_{z,0} + \frac{h\nu_+}{4\pi^2 m_\mathrm{p}\nu_z} \times \frac{B_2}{B_0} \times \left(n_+ + \frac{1}{2} + \frac{\nu_-}{\nu_+}\left(n_- + \frac{1}{2}\right) + \frac{g m_\mathrm{s}}{2}\right), \tag{11.1}$$

the Larmor frequency ν_L and the modified cyclotron frequency ν_+ can be measured by exciting these two modes n_+, m_s directly by applying rf-drives to the particle, and characterising the axial frequency fluctuations as a function of the drive frequencies ν_rf. To irradiate the rf signals, a spin-flip coil is mounted close to the AT electrodes. Since the coil is galvanically isolated from the particle, contributions of electric noise on the spin-flip line to the particle is suppressed by more than $-80\,\mathrm{dB}$. By applying rf drives to the coil, a transverse magnetic rf field $\vec{b}_\mathrm{rf}$ is generated and transmits through the electrodes via the slits (see Fig. 11.1). The trapped particle is oscillating in the strong magnetic bottle along the axial direction, and in this way the particle experiences a large magnetic field gradient within one oscillation cycle. In this condition, the spin-state interacts with the rf magnetic field incoherently. An effective magnetic field strength b_rf which is required to obtain 50 % of spin-flip probability can be calculated by using Eq. (11.11). Inserting our experimental conditions and the irradiation time $t_0 = 10\,\mathrm{s}$ to this equation, a Rabi oscillation frequency $\Omega_\mathrm{R}/2\pi = 80\,\mathrm{Hz}$ is extracted. This corresponds to a field strength $b_\mathrm{rf} = (B_0\Omega_\mathrm{R})/(2\pi\nu_\mathrm{L}) = 1.9\,\mu\mathrm{T}$. By also considering the attenuation of the slits, it requires a significant amount of current on the spin-flip coil to actually drive spin-transitions [81]. Therefore, it is necessary to develop a system to drive high power rf-field at the Larmor frequency ν_L to actually drive spin-flips in the AT.

As shown in Fig. 11.1, an rf amplifier followed by one band-pass filter and three high-pass filters are implemented in between a frequency generator and the spin-flip coil. With this configuration, output powers of up to $\sim$30 dBm at $\nu_\mathrm{L} \approx 52\,\mathrm{MHz}$ on the spin-flip line, with less than $-100\,\mathrm{dBm}$ transmission at $\nu_+ \approx 18\,\mathrm{MHz}$ and $\nu_- \approx 12\,\mathrm{kHz}$. Transmission characteristics are very important to prevent heating the radial modes while applying a spin-flip drive. If the drive frequency ν_rf is resonant with ν_L and induces a spin transition, it shifts the axial frequency ν_z by $\pm 183\,\mathrm{mHz}$. This tiny change will be observed by the axial detection system. For further experimental details on the Larmor frequency ν_L measurement, refer to section 11.6.

The modified cyclotron frequency ν_+ can be also measured by detecting the axial frequency changes while applying perturbation rf-drives via the spin-flip coil. This has been discussed already in the context of measuring B_2 (see section 9.2.4). The spin-transition requires an effective magnetic field strength of microtesla in the AT. Cyclotron quantum transitions are electric dipole transitions and can be driven with high transition probability, already with effective $\vec{E}$-field amplitudes in the sub-nV range. Additionally, since there is no upper limit on the occupation number n_+, the drive power can be tuned to generate many quantum transitions per frequency measurement to observe an easily detectable frequency shifts. Taking these facts into account, the rf amplifier is not required for ν_+ measurement, instead several high-pass filters and band-pass filters are connected in between the input flange on the apparatus and the frequency generator to obtain a low transmission on the magnetron frequency ν_-. In our case, the resonant drive perturbs n_+ by $dn_+/dt \approx 4\,\mathrm{s}^{-1}$ using a drive amplitude -90 dBm on the input flange of the apparatus, with less than -100 dB transmissions at 12 kHz.

In the next section, a line-shape study on the resonance curve of ν_L and ν_+ when the measurement takes place in the magnetic bottle is described.

11.2 Line-shape study

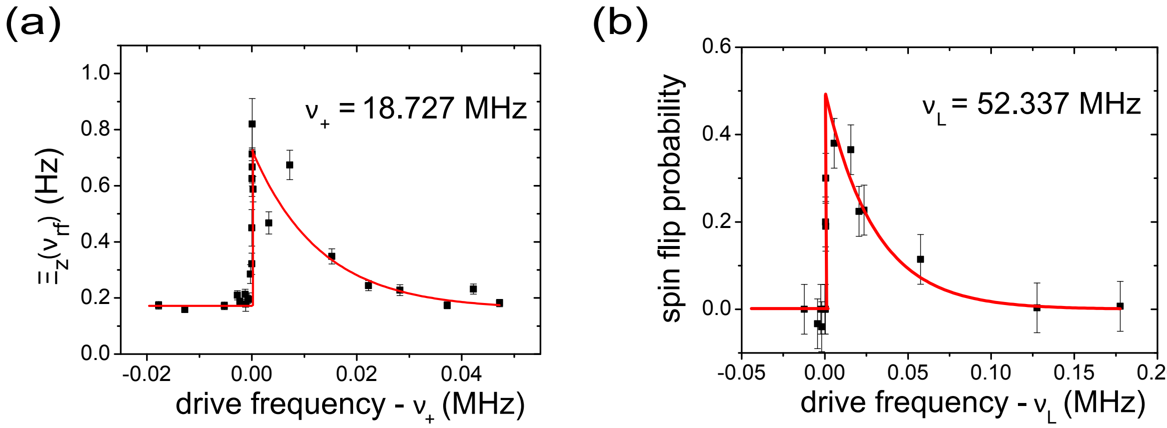

Fig. 11.2: Examples of a measured cyclotron resonance (a) and a Larmor resonance (b). The red lines represent fit functions based on Eq. 11.2. (a) An rf drive at amplitude -90 dBm and the frequency $\approx$ 18.727 MHz is applied to the spin-flip line to excite the cyclotron quantum state n_+. The axial frequency fluctuation $\Xi_z(\nu_\mathrm{rf})$ is evaluated for each drive frequency. (b) Measurement setup is shown in Fig. 11.1. RF drive (30 dBm at $\approx$ 52.337 MHz) is applied to the spin-flip coil to produce a transverse magnetic field $\vec{b}_\mathrm{rf}$ to drive spin-flips. The drive frequency is varied and characterised the spin-flip probability for each.

As described in the previous section, the axial energy E_z is Boltzmann distributed due to the interaction with the axial detector. Moreover, the magnetic field B experienced by the particle in the magnetic bottle depends on its axial position z as $B(z) = B_0 + B_2 z^2$. Therefore, the resonance curve of the Larmor frequency and the modified cyclotron frequency in the magnetic bottle reflect the Boltzmann shape. The experiment is operated in the weak coupling range described in detailed calculations in reference [54] and the line-shape $\chi(\nu_{\mathrm{rf}}, \nu_j, \nu_{\Delta\nu_j})$ of both, the resonant response lines for modified cyclotron transitions and the Larmor transitions are

$$\chi(\nu_{\mathrm{rf}}, \nu_j, \Delta\nu_j) = \frac{\Theta(\nu_{\mathrm{rf}} - \nu_j)}{2\pi\Delta\nu_j} \cdot \exp\left(-\frac{\nu_{\mathrm{rf}} - \nu_j}{\Delta\nu_j}\right), \tag{11.2}$$

where ν_j are the resonance frequencies of the modified cyclotron frequency $\nu_+(E_z = 0) = \nu_{+,\mathrm{cut}}$ and Larmor frequency $\nu_{\mathrm{L}}(E_z = 0) = \nu_{\mathrm{L,cut}}$ at vanishing axial energy E_z, and $\Theta(\nu_{\mathrm{rf}} - \nu_j)$ is the Heaviside function. The linewidth parameter

$$\Delta\nu_j = \nu_j \frac{B_2}{B_0} \frac{k_{\mathrm{B}} T_z}{4\pi^2 m_{\bar{\mathrm{p}}} \nu_z^2} \tag{11.3}$$

is a measure for the width of the resonance line.

This line-shape is a direct result of the continuous contact of the particle with the axial detection system. The interaction of the antiproton with the detection system at temperature T_z thermalises the particle continuously with a correlation time constant $\tau_c = 33\,\mathrm{ms}$. The resulting resonance line is a convolution of unperturbed Lorentz profiles and the Boltzmann distribution $\frac{1}{k_{\mathrm{B}} T_z} \cdot \exp(-E_z/(k_{\mathrm{B}} T_z))$ (also refer to section 10.4.1 and 10.4.2). Note that for frequencies $\nu_{\mathrm{rf}} < \nu_j$, the line-shape function $\chi(\nu_{\mathrm{rf}}, \nu_j, \Delta\nu_j) = 0$ and for $\varepsilon > 0 \rightarrow \chi(\nu_j + \varepsilon, \nu_j, \Delta\nu_j) = 1/(2\pi\Delta\nu_j)$, which means that for infinitely stable magnetic and electric field conditions the $\frac{d}{d\nu_{\mathrm{rf}}} \chi(\nu_{\mathrm{rf}}, \nu_j, \Delta\nu_j)|_{\nu_{\mathrm{rf}} = \nu_j} \rightarrow \infty$.

Examples of a measured cyclotron resonance and a Larmor resonance are shown in Fig. 11.2. By fitting the data-points with the best fit [56], the temperature of the axial detection system is derived $T_z = 7.8(1.2)\,\mathrm{K}$, which is consistent with the value extracted by measuring the magnetron energy distribution coupled to the thermal bath of the axial detector $T_z = 8.0(1.0)\,\mathrm{K}$ (see section 10.4.2).

11.3 Procedure of the *g*-factor measurement

In Fig. 11.3, a schematic of the Penning-trap system used for the *g*-factor measurement is shown. To prepare the initial conditions of the measurement, first of all, the modified cyclotron mode is cooled by the PT cyclotron detector and subsequently the particle is transported to the AT. Afterwards the cyclotron energy is determined by measuring the axial frequency (Eq. (11.1)). This sequence is repeated until a particle is found with $E_+/k_{\mathrm{B}} < 1.1\,\mathrm{K}$. Secondly, the magnetron mode is cooled by using sideband coupling in the AT until $E_-/k_{\mathrm{B}} < 4\,\mathrm{mK}$ is achieved. For these

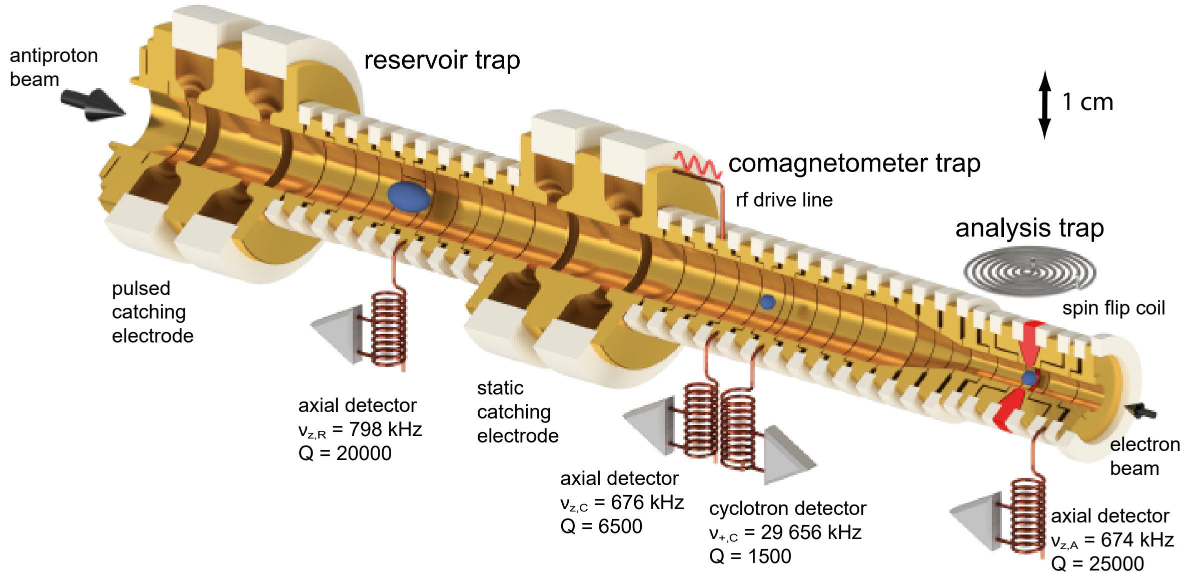
antiproton beam
reservoir trap
1 cm
comagnetometer trap
rf drive line
analysis trap
spin flip coil
pulsed catching electrode
axial detector
$\nu_{z,R}$ = 798 kHz
Q = 20000
static catching electrode
axial detector
$\nu_{z,C}$ = 676 kHz
Q = 6500
cyclotron detector
$\nu_{+,C}$ = 29 656 kHz
Q = 1500
electron beam
axial detector
$\nu_{z,A}$ = 674 kHz
Q = 25000

Fig. 11.3: Schematic of the Penning-trap system used for the *g*-factor measurement of the antiproton.

conditions, the axial frequency fluctuation without any drives applied is $\Xi_{z,\mathrm{back}} < 100(20)\,\mathrm{mHz}$ for more than 90 seconds of averaging time. Finally, another single antiproton is extracted from the RT and transported to the PT. This particle is dedicated for monitoring the magnetic field to characterise its stability during the actual *g*-factor measurements.

As will be described in section 11.4, the precision of the *g*-factor which can eventually be achieved is limited by the ability to resolve the cut frequencies; $\nu_{+,\mathrm{cut}}(E_z = 0)$ and $\nu_{\mathrm{L,cut}}(E_z = 0)$. To extract these frequencies, the resonance lines only in a close range around the cut-frequencies need to be scanned. The actual *g*-factor measurement procedure is illustrated in Fig. 11.4. It consists of:

1. Cooling of the magnetron motion.
2. Measurement of the modified cyclotron frequency $\nu_{+,\mathrm{AT},1}$. It lasts for typically less than 1 h.
3. Measurement of the Larmor frequency ν_{L}. It typically takes 9 h to 14 h.
4. Measurement of the modified cyclotron frequency $\nu_{+,\mathrm{AT},2}$.
5. The cycle ends by cooling the magnetron motion.

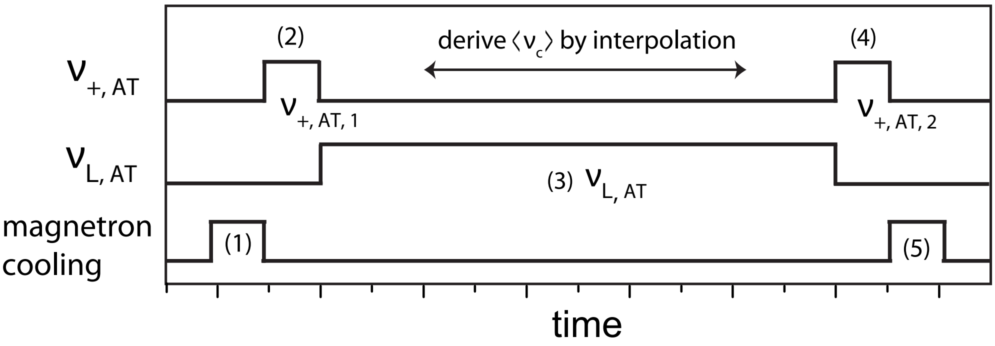

Fig. 11.4: Measurement sequence of the g-factor. First, centre the particle in the trap by cooling the magnetron motion to $E_-/k_\mathrm{B} < 4\,\mathrm{mK}$. Subsequently, measure the modified cyclotron frequency $\nu_{+,\mathrm{AT},1}$. Then, scan the Larmor resonance $\nu_{\mathrm{L,AT}}$ and measure the modified cyclotron frequency again $\nu_{+,\mathrm{AT},2}$. Afterwards, re-cool the magnetron motion. For further details on the sequence, refer to the text.

To derive a g-factor, the modified cyclotron frequencies $\nu_{+,\mathrm{AT},1}$ and $\nu_{+,\mathrm{AT},2}$ are converted to the free cyclotron frequencies $\nu_{\mathrm{c},1}$ and $\nu_{\mathrm{c},2}$ by using the invariance theorem [44]. Then, a mean cyclotron frequency $\langle\nu_\mathrm{c}\rangle$ and its standard error $\langle\Delta\nu_\mathrm{c}\rangle$ are calculated by evaluating $\langle\nu_\mathrm{c}\rangle = (\nu_{\mathrm{c},1}+\nu_{\mathrm{c},2})/2$ and $\langle\Delta\nu_\mathrm{c}\rangle = (\Delta\nu_{\mathrm{c},1}^2+\Delta\nu_{\mathrm{c},2}^2)^{0.5}$, respectively. Here, $\Delta\nu_{\mathrm{c},1}$ and $\Delta\nu_{\mathrm{c},2}$ are 95 % confidence intervals evaluated in a way as described in section 11.9. Finally, the g-factor $g_{\bar{\mathrm{p}}}/2$ and its relative uncertainty $\Delta g_{\bar{\mathrm{p}}}/g_{\bar{\mathrm{p}}}$ are obtained as calculating

$$\frac{g_{\bar{\mathrm{p}}}}{2} = \frac{\nu_\mathrm{L}}{\langle\nu_\mathrm{c}\rangle} \tag{11.4}$$

$$\frac{\Delta g_{\bar{\mathrm{p}}}}{g_{\bar{\mathrm{p}}}} = \left(\left(\frac{\Delta\nu_\mathrm{L}}{\nu_\mathrm{L}}\right)^2+\left(\frac{\langle\Delta\nu_\mathrm{c}\rangle}{\langle\nu_\mathrm{c}\rangle}\right)^2\right)^{0.5}, \tag{11.5}$$

where $\Delta\nu_\mathrm{L}$ is the 95 % confidence interval of the Larmor frequency ν_L. The detail of the evaluation is described in section 11.7.

11.4 Line-shape modifications

The line-shape given in section 11.2 assumes stable magnetic field conditions, so that $\nu_{\mathrm{L,cut}}(E_z = 0,t)$ and $\nu_{+,\mathrm{cut}}(E_z = 0,t)$ are constant for the entire sampling time which is required to resolve the resonance line. However, different drift effects soften the slope of the resonance line and $\frac{d}{d\nu_\mathrm{rf}}\chi(\nu_\mathrm{rf},\nu_j,\Delta\nu_j)|_{\nu_\mathrm{rf}=\nu_j} = \alpha < \infty$.

These are,

- drifts of the external magnetic field $\xi_B(t)$,
- voltage drifts of the trap-biasing supplies $\xi_V(t)$,
- a noise-driven random walk $\xi_+(t)$ in the modified cyclotron mode, and
- a noise-driven random walk $\xi_-(t)$ in the magnetron mode.

By summarising all these effects to an effective $\xi(t)$, the line-shape modifies to

$$\chi\left(\nu_{\mathrm{rf}},\nu_j,\Delta\nu_j,\tau_{\mathrm{m}},\xi(t)\right)=\frac{1}{\tau_{\mathrm{m}}}\int_0^{\tau_{\mathrm{m}}}dt\frac{\Theta(\nu_{\mathrm{rf}}-(\nu_j+\xi(t)))}{2\pi\Delta\nu_j}\cdot\exp\left(-\frac{\nu_{\mathrm{rf}}-(\nu_j+\xi(t))}{\Delta\nu_j}\right), \quad (11.6)$$

where τ_{m} is the time required to resolve the cut frequency. Each measured line is consequently a convolution of the unperturbed line over the random processes $\xi_k(t)$. The correlation time constants τ_k of the random drifts $\xi_k(t)$ are large compared to the required measurement time; $\tau_k \gg \tau_{\mathrm{m}}$. As a result of this discussions of measurement uncertainties need to be based either on Monte-Carlo simulations or distributions approximated by diffusion models.

As a conclusion, the final g-factor precision depends on how precise one can resolve the cut frequencies $\nu_{+,\mathrm{cut}}$ and $\nu_{\mathrm{L,cut}}$. Therefore, it needs to be investigated how much extent each drifts can soften the slope during the measurements.

11.5 Drift effect studies

In this section, possible origins which may cause effective drifts of the magnetic field experienced by the particle during Larmor frequency ν_{L} and cyclotron frequency ν_+ measurements are described in detail. This study is crucial to eventually define $\nu_{+,\mathrm{AT},1}$, $\nu_{+,\mathrm{AT},2}$ and ν_{L}, and their 95 % confidence intervals based on each resonances.

11.5.1 External magnetic field drifts

The magnetic field drift of the superconducting magnet is described in section 5.3. Intrinsic drifts of the field of the superconducting magnet are small compared to the fractional precision of the measurements reported in this thesis, therefore it can be neglected. This assumption is supported by ν_+ measurement with the comagnetometer particle in the PT which showed a magnetic field drift of $\Delta B_0/B_0 < 6\cdot 10^{-9}/\mathrm{h}$.

11.5.2 Voltage stability

Drifts of the biasing voltages of the trap lead to spatial shifts of the antiproton in the magnetic bottle and consequently to a shift of the magnetic field B_0 which is experienced by the particle. Voltage drifts on the correction electrodes contribute the most significant shifts in particle position. A voltage drift of 1 mV shifts the antiproton in the trap by 1.25 μm. Depending on the equilibrium position z_0 of the particle in the magnetic bottle, this leads to position dependent frequency shifts

$$\frac{1}{\nu}\frac{d\nu}{dz}z_0 = 0.49 \cdot \frac{\text{p.p.m.}}{\mu\text{m}} \cdot z_0. \tag{11.7}$$

To account for this effect, the antiproton is tuned carefully to the centre of the magnetic bottle. For the actual procedure, refer to section 9.2.4. This allows for tuning the antiproton to the centre with a spatial resolution of $\approx 1.2\,\mu$m.

The voltage stability is directly measured using a reference multimeter and is for a typical measurement time to resolve the Larmor frequency, $\approx$ 10 h, at 83(1) nV at $\approx$ 0.75 V. As a consequence, the error in the cyclotron frequency, caused by voltage drifts, is in the worst case of correlated drifts of opposite sign on the two correction electrodes of our 5-electrode compensated Penning trap (see section 2.2) of order $\Delta\nu_+/\nu_+ < 0.3$ p.p.b..

11.5.3 Cyclotron random walk

The random walk in the cyclotron mode is estimated by measuring the axial frequency ν_z as a function of the cyclotron energy E_+. The cyclotron energy is calibrated by thermalising the particle in the co-magnetometer trap and measuring the axial frequency shift in the analysis trap after each thermalisation cycle, see Fig. 10.7 (a) and (b).

$$\nu_z(n_+) = \nu_{z,0} + \frac{h\nu_+}{4\pi^2 m\nu_z}\frac{B_2}{B_0}\left(\left(n_+ + \frac{1}{2}\right)\right). \tag{11.8}$$

To extract the heating rate $dn_+/dt(E_+)$, the axial frequency fluctuation $\Xi_z(E_+, \tau_\text{m})$ as a function of E_+ and for different averaging times τ_m is measured, and fit functions $\Xi_z(E_+, \tau_\text{m}) = (\Xi^2_{z,\text{back}} + dn_+/dt(E_+) \cdot \Delta\nu^2_{z,+} \cdot \tau_\text{m}/\sqrt{2})^{0.5}$ to the measured data, see Fig. 11.5. Combining the data of all modified cyclotron energies, a heating rate of $dn_+/dt(E_+) = 0.08 \cdot E_+/k_\text{B}(\text{s}\cdot\text{K})^{-1}$ is extracted. All measurements reported in this thesis were carried out with particles at cyclotron energies $E_+/k_\text{B} < 1.1$ K. One cyclotron quantum transition changes the magnetic field experienced by the particle by $\Delta B_0/B_0 = 3 \cdot 10^{-10}$, and for typical measurement times of order 1 h to 20 h, the cyclotron walk contributes at maximum a fractional shift in the cyclotron frequency of 20 p.p.b..

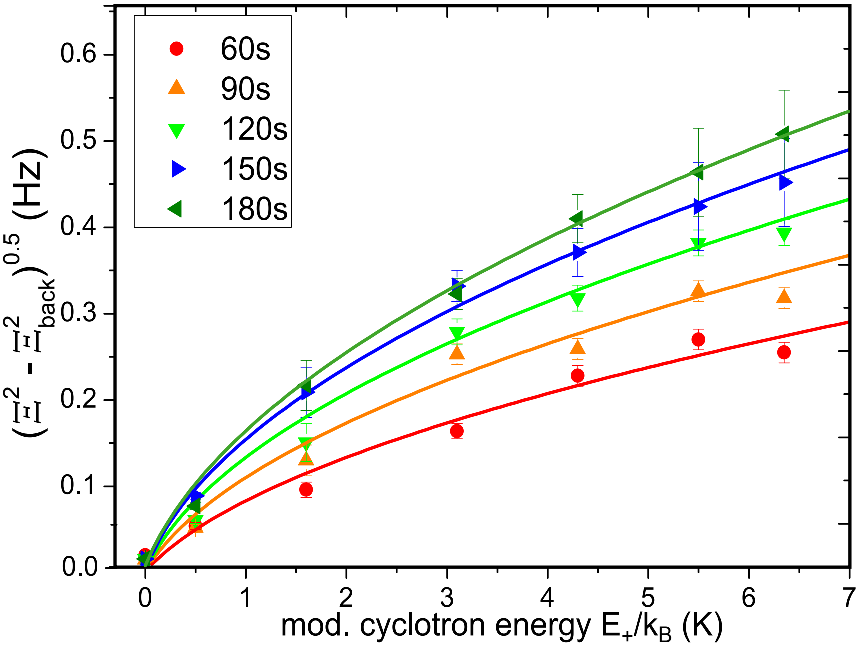

Fig. 11.5: Axial frequency fluctuation Ξ_z for different averaging times and different cyclotron energies E_+. From the fits, we extracted the cyclotron heating rate, as described in the text.

Within the experimental resolution achieved in a framework of my PhD studies, the effect of the random walk $\xi_+(t)$ in the cyclotron mode is negligibly small.

11.5.4 Magnetron random walk

To characterise the magnetron heating rate dn_-/dt during Larmor frequency measurements, first the modified cyclotron frequency $\nu_{+,1}$ is measured, subsequently the scan of the Larmor frequency ν_L is performed before the modified cyclotron frequency $\nu_{+,2}$ is measured again. Since the magnetic field is stable at the level $\delta B_0/B_0 < 1.5 \cdot 10^{-8}/10\,\mathrm{h}$ (see section 11.5.1), and a typical measurement to resolve the Larmor frequency takes 10 hours, the measured cyclotron frequency difference can be accounted solely to a change in the magnetron radius. From a set of 20 long-term measurements, a distribution is obtained

$$\frac{dn_-}{dt} = \sqrt{2}\frac{(\nu_{+,2} - \nu_{+,1})^2}{\tau_m(\Delta\nu_+/\Delta n_-)^2}, \tag{11.9}$$

with $\Delta\nu_+/\Delta n_- = 0.0024\,\mathrm{Hz}$ being the cyclotron frequency shift per magnetron quantum transition. From the width of the distribution, $dn_-/dt = 18.5(3.0) \cdot 10^3/\mathrm{s}$ is obtained. Consequently, the magnetron random walk $\xi_-(t)$ in the magnetron mode leads to an average root mean square drift of the cyclotron frequency at $\Delta\nu_+/\nu_+(t) = 8.4 \cdot 10^{-7}\sqrt{t}/\sqrt{h}$, and constitutes the dominant drift mechanism which softens the slope of the resonance. However, we can decrease the uncertainty induced by the magnetron random-walk by using the ν_+ and ν_z measurements to constrain the evolution of the magnetron radius. The analytical and Monte-Carlo evaluation methods used for this purpose are described in section 11.7 and 11.9.

11.6 Larmor frequency ν_L measurement

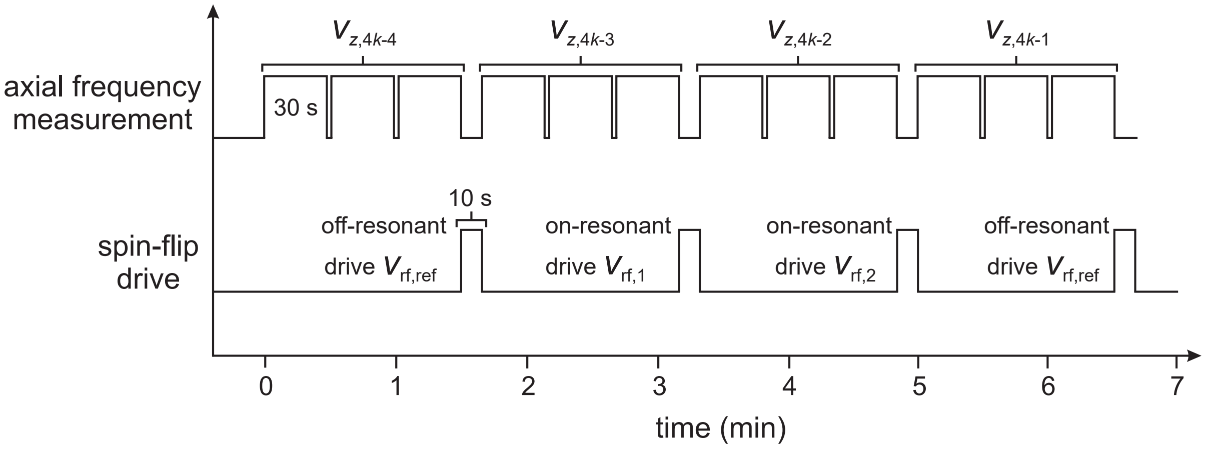

$\nu_{z,4k\text{-}4}$
$\nu_{z,4k\text{-}3}$
$\nu_{z,4k\text{-}2}$
$\nu_{z,4k\text{-}1}$
axial frequency measurement
30 s
10 s
spin-flip drive
off-resonant drive $V_{\mathrm{rf,ref}}$
on-resonant drive $V_{\mathrm{rf,1}}$
on-resonant drive $V_{\mathrm{rf,2}}$
off-resonant drive $V_{\mathrm{rf,ref}}$
0
1
2
3
4
5
6
7
time (min)

Fig. 11.6: Schematic of the Larmor frequency ν_L measurement.

The axial frequency stability achieved within these PhD studies is 100(20) mHz at 90 seconds of averaging time, therefore it was stable enough to detect spinflips with the statistical method described in [55]. Further stabilisation is subject of on going research efforts.

The basic measurement sequence of detecting spin-flips is shown as below (also see Fig. 11.6):

1. measure the axial frequency $\nu_{z,4k-4}$,

2. irradiate a reference drive with $\nu_{\mathrm{rf,ref}} < \nu_\mathrm{L}$,

3. measure the axial frequency $\nu_{z,4k-3}$,

4. irradiate a resonant drive close to resonance $\nu_{\mathrm{rf},1} \approx \nu_\mathrm{L}(E_z = 0)$ but slightly below $\nu_\mathrm{L}(E_z = 0)$,

5. measure the axial frequency $\nu_{z,4k-2}$,

6. irradiate another drive close to resonance $\nu_{\mathrm{rf},2} \approx \nu_{\mathrm{L}}(E_z = 0)$ with slightly above $\nu_{\mathrm{L}}(E_z = 0)$,
7. and conclude the sequence by another measurement of the axial frequency $\nu_{z,4k-1}$.

This sequence is repeated for $N > 80$ times and we subsequently evaluate:

1. the standard deviation $\sigma(\nu_{z,4k-4} - \nu_{z,4k-3}) := \Xi_{z,\mathrm{back}}$ for the off-resonant reference drive,
2. the standard deviation $\sigma(\nu_{z,4k-3} - \nu_{z,4k-2}) := \Xi_z(\nu_{\mathrm{rf},1})$ for the first drive close to $\nu_{\mathrm{L}}(E_z = 0)$ as well as
3. the standard deviation $\sigma(\nu_{z,4k-2} - \nu_{z,4k-1}) := \Xi_z(\nu_{\mathrm{rf},2})$ for the second drive close to $\nu_{\mathrm{L}}(E_z = 0)$.

In the first case, the reference fluctuation $\Xi_{z,\mathrm{back}}$ is obtained. In the second case and the third case, the potentially induced spin transitions add frequency jumps $\Delta\nu_{z,\mathrm{SF}} = 183\,\mathrm{mHz}$ to the background fluctuation and the measured axial frequency fluctuations $\Xi_z(\nu_{\mathrm{rf},1})$ and $\Xi_z(\nu_{\mathrm{rf},2})$ is increased to

$$\Xi_z(\nu_{\mathrm{rf,k}}) = \sqrt{\Xi^2_{z,\mathrm{back}} + P_{\mathrm{SF}}(\nu_{\mathrm{rf,k}}, \nu_{\mathrm{L}}, \Delta\nu_{\mathrm{L}})\Delta\nu^2_{z,\mathrm{SF}}}, \tag{11.10}$$

where $P_{\mathrm{SF}}(\nu_{\mathrm{rf,k}}, \nu_{\mathrm{L}}, \Delta\nu_{\mathrm{L}})$ is the frequency dependent spin-flip probability [56] at a given drive strength Ω_{R} of a radio frequency drive at frequency ν_{rf} which is irradiated for a time $t_0 = 10\,\mathrm{s}$:

$$P_{\mathrm{SF}}(\nu_{\mathrm{rf,k}}, \Delta\nu_{\mathrm{L}}) = \frac{1}{2}\left(1 - \exp\left(-\frac{1}{2}\Omega^2_{\mathrm{R}} t_0 \chi(\nu_{\mathrm{rf,k}}, \nu_{\mathrm{L}}, \Delta\nu_{\mathrm{L}})\right)\right). \tag{11.11}$$

Here, $\Delta\nu_{\mathrm{L}}$ is the line-width parameter and $\chi(\nu_{\mathrm{rf,k}}, \nu_{\mathrm{L}}, \Delta\nu_{\mathrm{L}})$ is the line-shape function (see section 11.2). Figure 11.7 shows the very first result of a statistical detection of a single antiproton spin-flips in BASE. For this measurement, it was intended to detect spin-flips unrelated to the actual g-factor measurement. Therefore, only the off-resonant reference drive ν_{ref} and the on-resonant drive $\nu_{\mathrm{rf},1}$ were irradiated. It shows the cumulative background fluctuation $\Xi_{z,\mathrm{back}}$ (red data points) as well as $\Xi_z(\nu_{\mathrm{rf},1})$ (black data points) as a function of measurement number N, the solid lines represent the calculated error bands $\Delta\sigma(\nu_{\mathrm{rf},1}, N) = \Xi_z(\nu_{\mathrm{rf},1})/(2N-2)^{0.5}$ of the measurement. From this result, it is also possible to inversely calculate the magnetic bottle B_2. We extracted $2.88 \times 10^5\,\mathrm{T/m^2}$, which is consistent with the value obtained from measuring the magnetic bottle directly $2.64(39) \times 10^5\,\mathrm{T/m^2}$ (refer to section 9.2.4).

Additionally, the drive strength was characterised. The result is shown in Fig. 11.8. The red curve represents the best fit based on Eq. (11.11), and the green curves are its error bands. For all data-points, the particle was tuned to the centre of the magnetic bottle, and the extracted spin-flip probabilities are consistent within the errorbars with the fit function in Eq. (11.11).

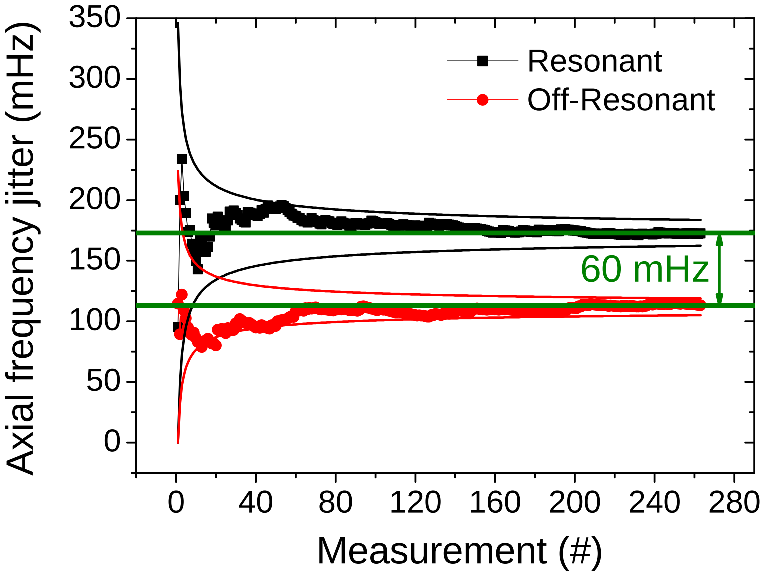

Fig. 11.7: First observation of spinflips of a single trapped antiproton in BASE. By using this result, $B_2 = 2.88 \times 10^5\,\mathrm{T/m^2}$ is extracted. This is consistent with the value obtained from measuring the magnetic bottle directly $2.64(39) \times 10^5\,\mathrm{T/m^2}$.

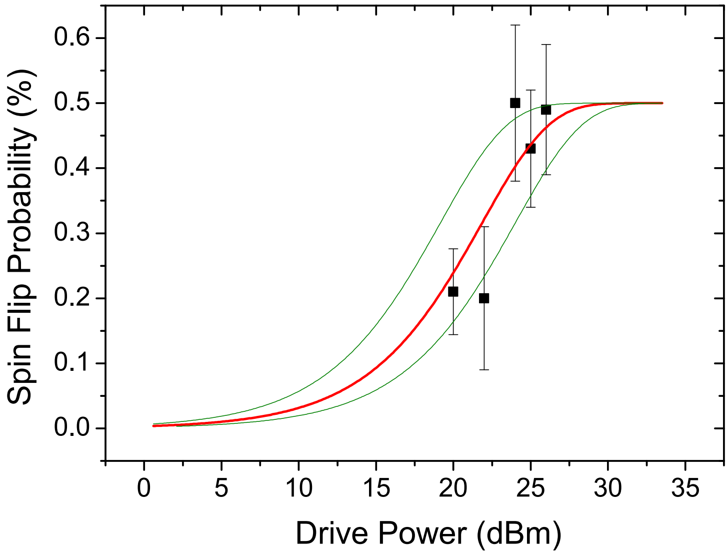

Fig. 11.8: Power characterisation of spin-flip drive. The red curve represents the best fit based on Eq. (11.11), and the green curves are its error bands. The theoretical detail on the line-shape are discussed in section 4.2.

11.7 Larmor frequency ν_{L} evaluation

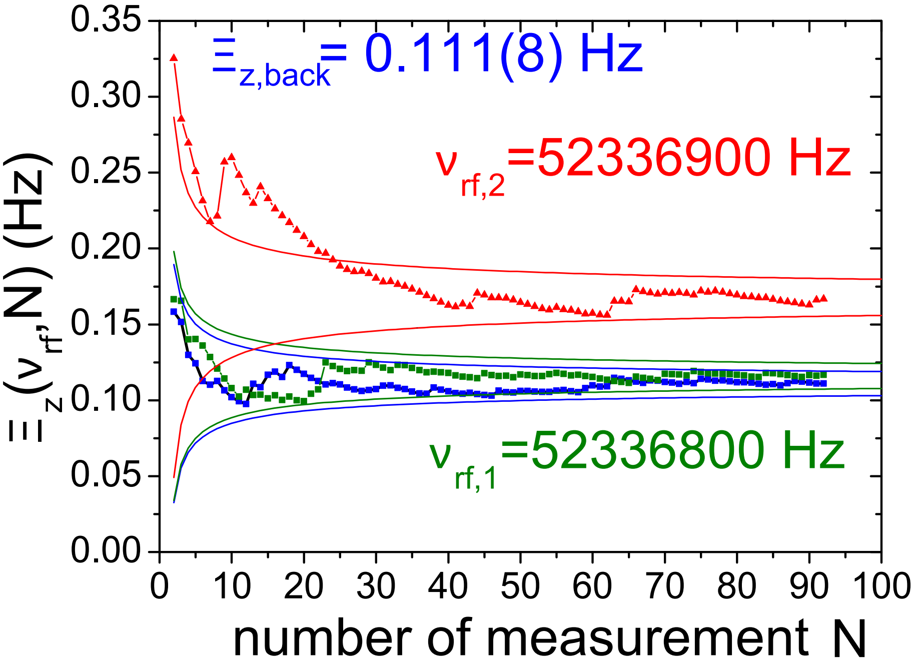

Fig. 11.9: Cumulative plot of frequency fluctuations for different spin-flip drive frequencies. The blue data-points represent the background measurement. For the green data-points, a drive at $\nu_{\mathrm{rf},1} = 52\,336\,800\,\mathrm{Hz}$ was irradiated, for the red data-points, a drive at $\nu_{\mathrm{rf},2} = 52\,336\,900\,\mathrm{Hz}$ was applied. The solid lines represent the 68 % confidence interval of Ξ_z for the respective measurement.

In some Larmor frequency measurements, as e.g. the one shown in Fig. 11.9, the cut frequency was undersampled, which means that the diffusion of $\nu_+(E_z = 0, \tau_m) - \nu_+(E_z = 0, 0)$ was smaller than the sampling interval $\Delta\nu_{\mathrm{rf}}$ which was chosen in the frequency scan. Under these conditions, at 68 % confidence level

$$\Xi_z(\nu_{\mathrm{rf},1}) = \Xi_{z,\mathrm{back}}$$

and

$$(\Xi_z(\nu_{\mathrm{rf},2}) - \Xi_{z,\mathrm{back}})/\sigma(\Xi_z(\nu_{\mathrm{rf},2}), \Xi_{z,\mathrm{back}}) > 3.5.$$

From the experiment sequence, $\nu_{+,1}$, the information from the Larmor measurement, as well as $\nu_{+,2}$ are available information to constrain the evolution of the magnetron radius. To give in this case of undersampling an appropriate error estimate, the following case needs to be discussed:

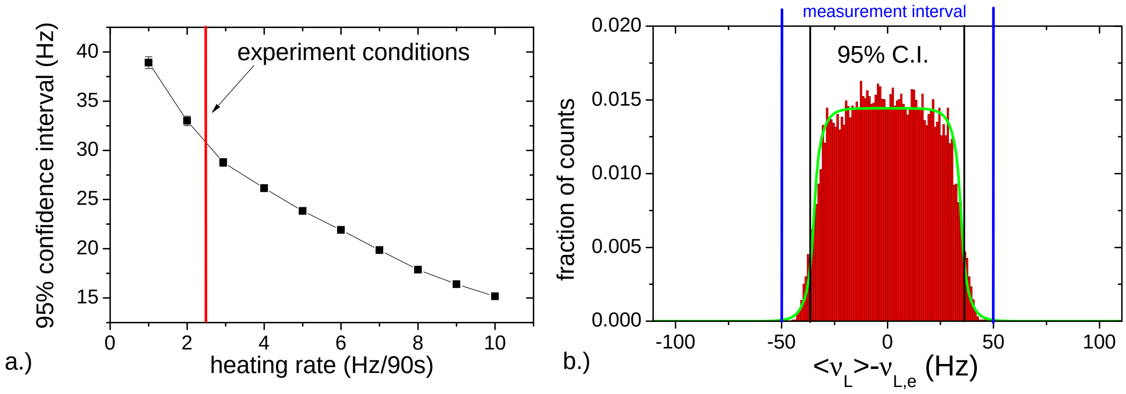

Fig. 11.10: (a) 95 % confidence level of the distribution $\langle \nu_{\rm L} \rangle - \nu_{\rm L,e}$ as a function of the magnetron heating rate. (b) Distribution $\langle \nu_{\rm L} \rangle - \nu_{\rm L,e}$ for the magnetron heating rates which are observed in this experiment. The blue lines indicate the measurement interval, black lines the 95 % confidence interval of $\nu_{\rm L,e} = 0.5(\nu_{\rm rf,1} + \nu_{\rm rf,2})$. The light green line is a result of an explicit calculation, which is consistent with the Monte-Carlo simulated data.

Given the input parameters of the experiment $\nu_{+,1}$ and $\nu_{+,2}$, including their uncertainties, an appropriate estimate of the uncertainty needs to be derived.

To realise this, random walk Monte-Carlo simulations with defined parameters $\tau_{\rm m}$ and $\nu_{+,1} - \nu_{+,2}$ are executed. The start frequency $\nu_{+,1}$ and the heating rate $\xi_{-}(t)$ are varied. Random walks which reproduce the following conditions are only accepted to represent the actual measurement, if

- within the 68 % C.L., $\Xi_z(\nu_{\rm rf,1}) = \Xi_{z,\rm back}$ and
- $(\Xi_z(\nu_{\rm rf,2}) - \Xi_{z,\rm back})/\sigma(\Xi_z(\nu_{\rm rf,2}), \Xi_{z,\rm back}) > 3.5$.

The mean frequency of the simulated walk $\langle \nu_{\rm L} \rangle$ is calculated and compared to the frequency $\nu_{\rm L,e} \equiv 0.5(\nu_{\rm rf,1} + \nu_{\rm rf,2})$ which would have been extracted from the measurement. Based on 1000 simulations for each parameter $\nu_{+,1}$, the distribution $\langle \nu_{\rm L} \rangle - \nu_{\rm L,e}$ is evaluated, we integrated $\nu_{+,1}$ in boundaries $\nu_{\rm rf,1}$ to $\nu_{\rm rf,2}$ and calculated the 95 % confidence interval of the integrated distribution. Figure 11.10(a) shows the scaling of the 95 % confidence level of the distributions $\langle \nu_{\rm L} \rangle - \nu_{\rm L,e}$ for different magnetron heating rates dn_{-}/dt. The red line indicates the experimental conditions. Note that the uncertainty of the distribution $\langle \nu_{\rm L} \rangle - \nu_{\rm L,e}$ increases with reduced heating rate, which is caused by the boundary conditions $\nu_{+}(t=0) = \nu_{+,1}$ and $\nu_{+}(t=\tau_{\rm m}) = \nu_{+,2}$. Walks which fulfill the boundary conditions at high heating rates trace the frequency interval $\nu_{\rm rf,2} - \nu_{\rm rf,1}$ more equally than walks at low heating rate. The probability to reproduce the true mean frequency in case of a strong walk by the arithmetic mean is inherently enhanced. Figure 11.10 (b) displays the integrated distribution of $\langle\nu_\mathrm{L}\rangle - \nu_\mathrm{L,e}$ for the magnetron heating rates $dn_-/dt = 18.5(3.0)\cdot 10^3\,\mathrm{s}^{-1}$, which are observed in this experiment. The blue lines indicate the measurement interval, the black lines represent the 95 % confidence level of $\nu_\mathrm{L,e} \equiv 0.5(\nu_\mathrm{rf,1} + \nu_\mathrm{rf,2})$. Based on this evaluation, the 95 % confidence interval is defined as $\Delta\nu_\mathrm{L} = 33\,\mathrm{Hz}$.

A purely analytical treatment to derive the distribution $w(\langle\nu_\mathrm{L}\rangle - \nu_\mathrm{L,e})$ shown in Fig. 11.10 (b) requires integration of the mean of distributions in the resolved frequency interval, derivation of a scaling function which reflects the fraction of walks which meet the boundary conditions of the experiment for different heating rates, the evaluation of $\langle\nu_\mathrm{L}\rangle - \nu_\mathrm{L,e}$ based on a diffusion model and the integration of the results over all possible heating rates. Rather than explicitly quoting the formulas, the result of such an analytical treatment together with the Monte-Carlo simulated data is shown as light green line in Fig. 11.10 (b).

11.8 Modified cyclotron frequency ν_+ measurement

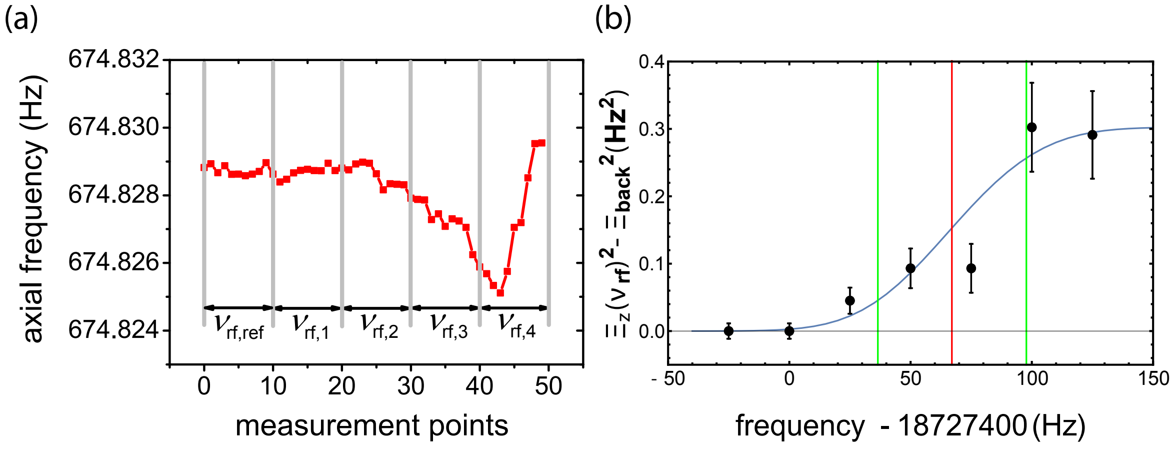

Fig. 11.11: Measurement of the modified cyclotron frequency. (a) Sequence of axial frequency measurements of 30 s averaging time while a radial dipolar drive at $\nu_\mathrm{rf,k}$ is applied. The drive frequency is adjusted after each 10 measurements. Once the drive is on resonance to the cyclotron frequency $\nu_{\mathrm{rf},k} \approx \nu_{+,\mathrm{cut}}$, the axial frequency fluctuation increases. (b) Projection of axial frequency data to axial frequency fluctuation $\Xi_z(\nu_\mathrm{rf})$. The red and green vertical lines indicate the determined mean value $\nu_{+,\mathrm{cut}}$ and its 95 % C.L. uncertainties, respectively. The blue solid line is a fit based on the data-analysis described in the text.

The basic principle is same as in the measurement of the magnetic bottle (see section 9.2.4). When the particle is on resonance to the external drive frequency, the cyclotron heating rate dn_+/dt increases which leads to an increase of the axial frequency fluctuation Ξ_z as well. By measuring the axial frequency fluctuations as a function of the drive frequencies $\nu_{\mathrm{rf},k}$ with a fixed drive power (-90 dBm at the input of the spinflip line on the vacuum flange), a resonance spectrum is extracted as shown in Fig. 11.2 (a).

As described previously, rf-drives are irradiated only close to the cut frequency $\nu_{+,\mathrm{cut}}$ for actual g-factor measurements. To determine the modified cyclotron frequency, a drive which induces on resonance a heating rate of $dn_+/dt(\nu_{\mathrm{rf}} = \nu_{+,\mathrm{AT}}(E_z = 0)) \approx 4\,\mathrm{s}^{-1}$ is applied. Starting with a background measurement at $\nu_{\mathrm{rf,ref}} \approx \nu_{+,\mathrm{AT}} - 100\,\mathrm{Hz}$, we scan the drive frequency ν_{rf}, typically in steps of 25 Hz over the resonance. For each individual drive frequency $\nu_{\mathrm{rf,k}}$, ten axial frequency data-points are recorded, each averaged by $t = 30\,\mathrm{s}$, and the axial frequency fluctuation $\Xi_z(\nu_{\mathrm{rf},k})$ is evaluated. This scheme is repeated until the resonance line is clearly resolved, which means that for a resonant excitation frequency $\nu_{\mathrm{rf,e}}$ the condition $(\Xi_z(\nu_{\mathrm{rf,e}}) - \Xi_{z,\mathrm{back}})/\sigma(\Delta\Xi_z(\nu_{\mathrm{rf,e}}), \Delta\Xi_{z,\mathrm{back}}) > 3$ is fulfilled. Here $\Delta\Xi_z(\nu_{\mathrm{rf},k}) = \Xi_z(\nu_{\mathrm{rf},k})/(2N - 2)^{0.5}$ is the 68 % confidence interval of the measurement, N is the number of accumulated data-points per drive frequency $\nu_{\mathrm{rf,k}}$ and $\sigma(\Delta\Xi_z(\nu_{\mathrm{rf,e}}), \Delta\Xi_{z,\mathrm{back}})$ the propagated standard error of $\Xi_z(\nu_{\mathrm{rf,e}}) - \Xi_{z,\mathrm{back}}$. As an example, a sequence of fifty axial frequency measurements with applied rf-drives at $\nu_{\mathrm{rf},k}$ is shown in Fig. 11.11 (a). The first data-sets at $\nu_{\mathrm{rf},1}$ and $\nu_{\mathrm{rf},2}$ are consistent with the undriven background fluctuation $\Xi_{z,\mathrm{back}}$. At $\nu_{\mathrm{rf},3}$ and $\nu_{\mathrm{rf},4}$ the applied rf-drive induces cyclotron quantum transitions which clearly increases the measured axial frequency fluctuation to $\Xi_z(\nu_{\mathrm{rf},k}) = (\Xi^2_{z,\mathrm{back}} + \Delta\nu^2_{z,+} \cdot dn_+/dt(\nu_{\mathrm{rf},k}) \cdot t/\sqrt{2})^{0.5}$. Figure 11.11 (b) displays a projection of measured axial frequencies of an entire measurement sequence to axial frequency fluctuation $\Xi_z(\nu_{\mathrm{rf},k})$ as a function of the applied rf-drive frequency.

11.9 Modified cyclotron frequency ν_+ evaluation

Compared to the spin system with eigenstates $\pm\hbar/2$, the quantum numbers of the cyclotron oscillator are $n_+ \geq 1$. Many transitions can be induced within one excitation cycle, and as a consequence, the resolution of the slope around $E_z = 0$ affords significantly shorter measurement time. The axial frequency fluctuation $\Xi_z(\nu_{\mathrm{rf}})$ is measured while irradiating a radial rf-drive at $\nu_{\mathrm{rf,k}}$. There are two different approaches to study the cyclotron cut, an analytical method and Monte-Carlo simulations.

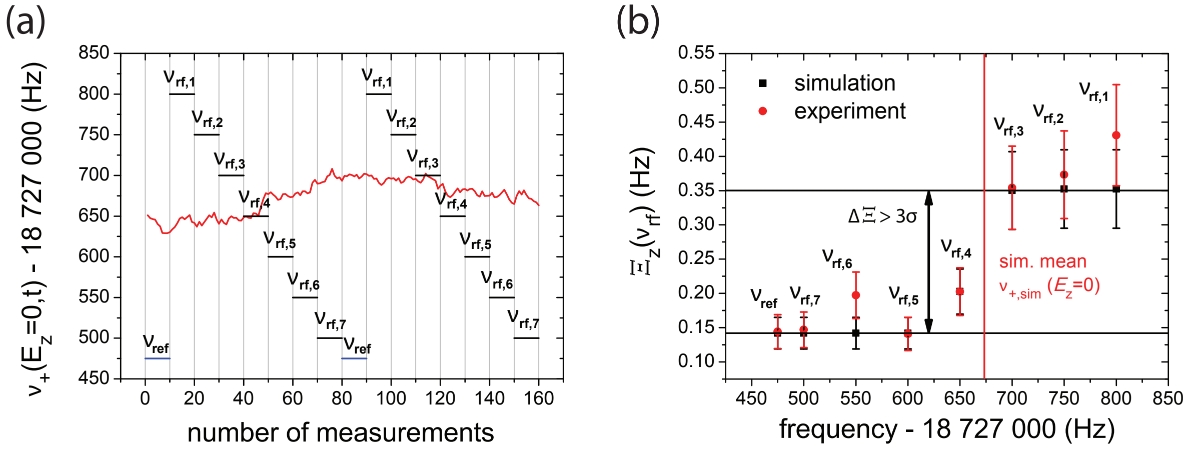

Fig. 11.12: (a) Simulated walk of the cyclotron frequency. In this simulation, the generating function of the walk has a strength of $\xi_- = 4\,\mathrm{Hz}/30\,\mathrm{s}$. The red lines show the result of a simulated walk of the cyclotron cut frequency, and the black lines indicate the excitation frequencies $\nu_{\mathrm{rf},k}$. (b) Projection of the simulated result to frequency fluctuation $\Xi_z(\nu_{\mathrm{rf}})$. The red line represents the actual mean frequency $\langle \nu_{+,\mathrm{sim}}(E_z = 0, t)$ of the simulated data.

The analytical method uses the fact that the measured distribution of points $\Xi_z(\nu_{\mathrm{rf,k}})$ allows to constrain the random walk $\xi_-(t)$ in the magnetron mode which has taken place during the frequency scan. Each individual measurement can be associated to a gaussian sub-distribution $w_k(\nu, \nu_+(0) + \xi_-(t))$

$$\Xi_z(\nu_{\mathrm{rf},k}) = \Upsilon \int_0^{\nu_{\mathrm{rf},k}} d\nu \int_0^{\tau_{\mathrm{m}}} dt \cdot w_k(\nu, \nu_+(0) + \xi_-(t)) := f(w_k(\nu_{\mathrm{rf},k}, \langle \nu_+(0) + \xi_-(\tau_{\mathrm{m}})\rangle)), \tag{11.12}$$

where τ_{m} is the measurement time, Υ a scaling factor, and $\nu_+(0) + \xi_-(t)$ the time dependent modified cyclotron frequency while $\nu_{\mathrm{rf},k}$ was irradiated. The distribution of modified cyclotron frequencies during the entire measurement $w = \sum_k w_k$ is reconstructed by minimising $\sum_k (f(w_k(\nu_{\mathrm{rf},k}, \langle \nu_+(0) + \xi_-(\tau_{\mathrm{m}})\rangle)) - \Xi_z(\nu_{\mathrm{rf},k}))^2$ with the strength of the walk ξ_- as a free parameter. From the reconstructed distribution, an expected mean value and its 95 % confidence interval is evaluated based on w.

The another approach is based on Monte-Carlo simulations. From the obtained results $\Xi_z(\nu_{\mathrm{rf},k})$, the distribution w of cyclotron frequencies during the measurement sequence is reconstructed by using Monte-Carlo simulations. To visualise the Monte-Carlo based reconstruction of w, Fig. 11.12 illustrates a basic example. The red lines in (a) show the result of a simulated walk of the cyclotron cut frequency, and the black lines indicate the excitation frequencies $\nu_{\mathrm{rf},k}$.

In Fig. 11.12 (b), the projection to measured frequency fluctuation is shown. Simulations for different start/stop frequencies are performed, and different heating rates of the walks. We select walks which reproduce the measured data points within their 68 % error bars. For each heating rate, a sub-distribution $\tilde{w}_k$ is obtained. Finally, all possible sub-distributions $\tilde{w}_k$ are integrated to obtain a final distribution of cyclotron mean values, calculated the expectation value of $\tilde{w}$ and quote its 95 % confidence level as the uncertainty.

11.10 Final result

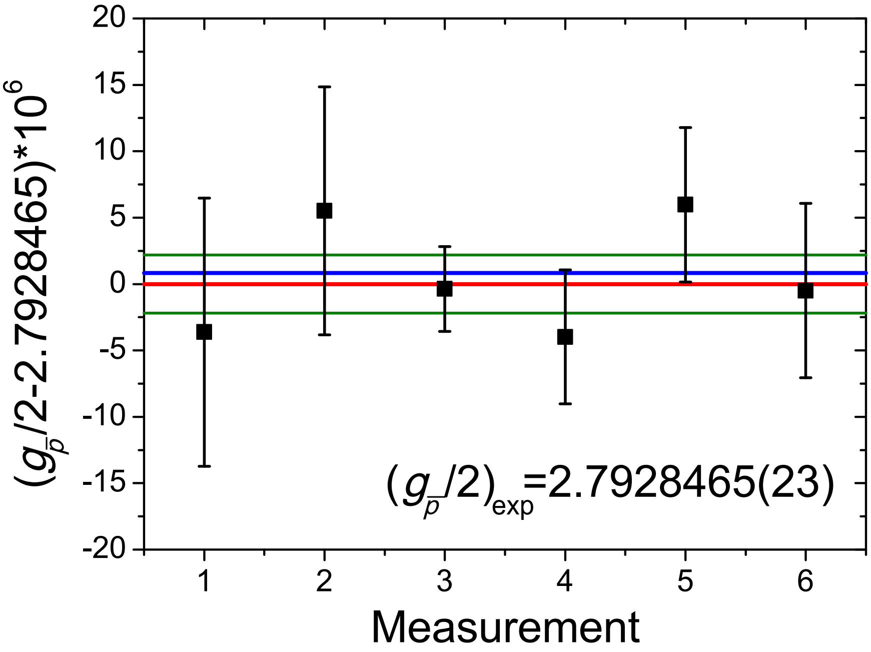

Fig. 11.13: Results of the six g-factor measurements carried out during CERN's 2015/2016 accelerator shutdown between the 20th of February 2016 and 5th of March 2016. Based on this set of measurements, $(g_{\bar{p}}/2)_{\mathrm{exp}} = 2.7928465(23)$ is extracted. The red and green lines show the final g-factor value $(g_{\bar{p}}/2)_{\mathrm{exp}}$ and its final error, respectively. The blue line represents the proton g-factor $(g_p/2)$ [24]. The measured antiproton g-factor is consistent with the proton g-factor, inherently in agreement with CPT invariance.

In total, six g-factor measurements were carried out. All of them were performed during weekend or night-shifts when magnetic field noise in the accelerator hall is low. Table 11.1 summarises all measured modified cyclotron and Larmor frequencies which enter the g-factor evaluation. For all g-factor measurements, the axial frequency was in a range of 674 823 Hz to

674 841 Hz. To evaluate the final value of the g-factor, the weighted mean of the entire data-set

Table 11.1: Summarises all measured modified cyclotron and Larmor frequencies.

g-factor	$\nu_{+,1}$ (Hz)	ν_{L} (Hz)	$\nu_{+,2}$ (Hz)
1	18 727 430(30)	52 336 760(155)	18 727 454(71)
2	18 727 452(35)	52 336 800(166)	18 727 338(14)
3	18 727 438(11)	52 336 850(33)	18 727 467(32)
4	18 727 476(34)	52 336 900(77)	18 727 513(11)
5	18 727 452(33)	52 336 895(86)	18 727 400(33)
6	18 727 601(48)	52 337 350(77)	18 727 664(48)

is calculated and extracted,

$$\left(\frac{g_{\bar{\mathrm{p}}}}{2}\right)_{\mathrm{stat}} = 2.792\,846\,5(22)(6). \tag{11.13}$$

The first number in brackets represents the 95 % confidence interval of the measured mean, the second number in brackets represents the scatter of the error according to t-test statistics. The individual g-factor values are shown in Fig. 11.13. The final error is calculated by standard error propagation and obtained

$$\left(\frac{g_{\bar{\mathrm{p}}}}{2}\right)_{\mathrm{exp}} = 2.792\,846\,5(23). \tag{11.14}$$

The fractional precision achieved from this measurement is 0.8 p.p.m., which is six times more precise than reported by the ATRAP collaboration in 2013 [22]. Compared to the g-factor measurement by the BASE collaboration at the University of Mainz [24]

$$\frac{g_{\mathrm{p}}}{2} = 2.792\,847\,350(9), \tag{11.15}$$

the value of the magnetic moment of the antiproton in units of the nuclear magneton measured is in agreement with CPT invariance.

11.11 Application of the Standard Model Extension

In this section, the sensitivity of the measurement with respect to the parameters of the Standard Model Extension (SME) [9, 43, 82], a model which allows discussion of the sensitivity of experiments with respect to CPT violating coefficients based on an effective field theory, is

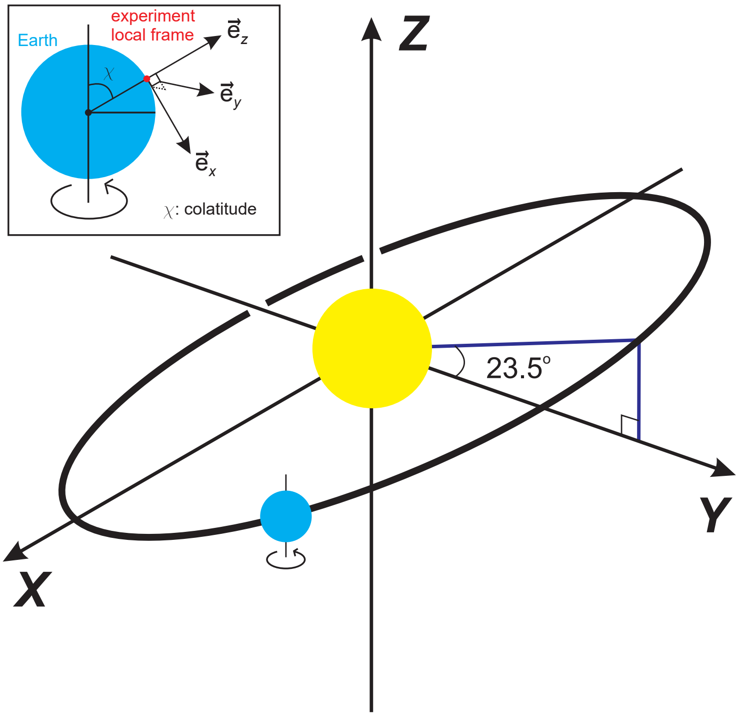

Fig. 11.14: Standard Sun-centred inertial reference frame. It is to define the geometrical conventions of the Standard Model Extension. The yellow and the blue circle represents the Sun and the Earth, respectively.

presented. In this evaluation, the formalism of a very recent publication on the application of the SME to Penning trap based magnetic moment measurements is applied [43]. Details to obtain constraints on SME coefficients by comparing results of experiments performed at different magnetic field strengths, orientations, and locations are outlined in Eq. (65), Eq. (67), Eq. (76) and Eq. (80) of reference [43].

To derive new constraints on the coefficients $\tilde{b}_{\mathrm{p}}^{Z}$, $\tilde{b}_{\mathrm{F,p}}^{XX}+\tilde{b}_{\mathrm{F,p}}^{YY}$, and $\tilde{b}_{\mathrm{F,p}}^{ZZ}$ for protons, and $\tilde{b}_{\mathrm{p}}^{*Z}$, $\tilde{b}_{\mathrm{F,p}}^{*XX}+\tilde{b}_{\mathrm{F,p}}^{*YY}$ and $\tilde{b}_{\mathrm{F,p}}^{*ZZ}$ for antiprotons, we follow [43] and compare our 2014 $(g/2)_{\mathrm{p}} = 2.792\,847\,350(9)$ g-factor measurement, which was performed at the University of Mainz, to the antiproton g-factor measurement which is presented in this thesis. Both experiments are in horizontal design. As local coordinate systems to define the orientations of the superconducting magnets, the local zenith is defined as $\vec{e}_z = \cos(\phi)\sin(\chi)\vec{e}_X + \sin(\phi)\sin(\chi)\vec{e}_Y + \cos(\chi)\vec{e}_Z$, here small indices represent the local laboratory frame and capital indices represent the standard frame used in the SME, with Z-component along the earth's rotational axis (compare Fig. 11.14). The angle χ is the local colatitude, $\chi_{\mathrm{C}} \approx 44°$ for the CERN experiment and $\chi_{\mathrm{M}} \approx 40°$ for the Mainz experiment. As local y-component, the vector which points eastwards is used, as local x-component is defined as the vector which points southwards. It is assumed that the azimuthal component ϕ averages out due to the earth's rotation. In the local Mainz experiment frame, the magnetic field is oriented southwards $\gamma_{\mathrm{M}} \approx 0^\circ$, in the CERN experiment the axis of the magnet is oriented $\gamma_{\mathrm{C}} \approx 120^\circ$ with respect to the local x-axis. The angle γ is defined as positive when rotated counter-clockwise from the local axis.

To derive constraints on SME coefficients based on these two measurements, the g-factors of the proton $(g/2)_{\mathrm{p}}$ and the antiproton $(g/2)_{\bar{\mathrm{p}}}$ can be compared as

$$\left(\frac{g}{2}\right)_{\mathrm{p}} - \left(\frac{g}{2}\right)_{\bar{\mathrm{p}}} = \frac{2}{\omega_{\mathrm{c}}^{\mathrm{p}}\omega_{\mathrm{c}}^{\bar{\mathrm{p}}}}(\Sigma\omega_{\mathrm{c}}^{\mathrm{p}}\Delta\omega_{\mathrm{a}}^{\mathrm{p}} - \Delta\omega_{\mathrm{c}}^{\mathrm{p}}\Sigma\omega_{\mathrm{a}}^{\mathrm{p}}), \tag{11.16}$$

where

$$\begin{aligned}
\Delta\omega_{\mathrm{c}}^{\mathrm{p}} &= \frac{1}{2}(\omega_{\mathrm{c}}^{\mathrm{p}} - \omega_{\mathrm{c}}^{\bar{\mathrm{p}}}) && (11.17)\\
\Sigma\omega_{\mathrm{c}}^{\mathrm{p}} &= \frac{1}{2}(\omega_{\mathrm{c}}^{\mathrm{p}} + \omega_{\mathrm{c}}^{\bar{\mathrm{p}}}) && (11.18)\\
\Delta\omega_{\mathrm{a}}^{\mathrm{p}} &= \frac{1}{2}(\delta\omega_{\mathrm{a}}^{\mathrm{p}} - \delta\omega_{\mathrm{a}}^{\bar{\mathrm{p}}}) && (11.19)\\
\Sigma\omega_{\mathrm{a}}^{\mathrm{p}} &= \frac{1}{2}(\delta\omega_{\mathrm{a}}^{\mathrm{p}} + \delta\omega_{\mathrm{a}}^{\bar{\mathrm{p}}}). && (11.20)\\
& && (11.21)
\end{aligned}$$

$\omega_{\mathrm{c}}^{\mathrm{p}}$ and $\omega_{\mathrm{c}}^{\bar{\mathrm{p}}}$ are the cyclotron angular frequencies of the proton and the antiproton, respectively, while $\delta\omega_{\mathrm{a}}^{\mathrm{p}}$ and $\delta\omega_{\mathrm{a}}^{\bar{\mathrm{p}}}$ are the shifts in the anomaly frequencies due to hypothetical CPT violating effects:

$$\begin{aligned}
\delta\omega_{\mathrm{a}}^{\mathrm{p}} &= 2\tilde{b}_{\mathrm{p}}^{x} - 2\tilde{b}_{\mathrm{F,p}}^{xx}B && (11.22)\\
\delta\omega_{\mathrm{a}}^{\bar{\mathrm{p}}} &= -2\tilde{b}_{\mathrm{p}}^{*z} + 2\tilde{b}_{\mathrm{F,p}}^{*zz}B^{*}. && (11.23)
\end{aligned}$$

For explicit expressions of $\Delta\omega_{\mathrm{a}}^{\mathrm{p}}$ and $\Sigma\omega_{\mathrm{a}}^{\mathrm{p}}$, refer to Eq. (68) and Eq. (69) in [43]. This gives:

$$\begin{aligned}
\Delta\omega_{\mathrm{a}}^{\mathrm{p}} = -\tilde{b}_{\mathrm{p}}^{Z}\sin(\chi_{\mathrm{M}}) - \frac{1}{2}(\tilde{b}_{\mathrm{F,P}}^{XX} + \tilde{b}_{\mathrm{F,P}}^{YY})B\cos^2(\chi_{\mathrm{M}}) - \tilde{b}_{\mathrm{F,P}}^{ZZ}B\sin^2(\chi_{\mathrm{M}})\\
-\tilde{b}_{\mathrm{p}}^{*Z}\sin(\chi_{\mathrm{C}})\cos(\gamma_{\mathrm{C}}) - \frac{1}{2}(\tilde{b}_{\mathrm{F,P}}^{*XX} + \tilde{b}_{\mathrm{F,P}}^{*YY})B^{*}\left(\cos^2(\chi_{\mathrm{C}})\cos^2(\gamma_{\mathrm{C}}) + \sin^2(\gamma_{\mathrm{C}})\right)\\
-\tilde{b}_{\mathrm{F,P}}^{*ZZ}B^{*}\sin^2(\chi_{\mathrm{C}})\cos^2(\gamma_{\mathrm{C}}) \qquad (11.24)\\
\Sigma\omega_{\mathrm{a}}^{\mathrm{p}} = -\tilde{b}_{\mathrm{p}}^{Z}\sin(\chi_{\mathrm{M}}) - \frac{1}{2}(\tilde{b}_{\mathrm{F,P}}^{XX} + \tilde{b}_{\mathrm{F,P}}^{YY})B\cos^2(\chi_{\mathrm{M}}) - \tilde{b}_{\mathrm{F,P}}^{ZZ}B\sin^2(\chi_{\mathrm{M}})\\
+\tilde{b}_{\mathrm{p}}^{*Z}\sin(\chi_{\mathrm{C}})\cos(\gamma_{\mathrm{C}}) + \frac{1}{2}(\tilde{b}_{\mathrm{F,P}}^{*XX} + \tilde{b}_{\mathrm{F,P}}^{*YY})B^{*}\left(\cos^2(\chi_{\mathrm{C}})\cos^2(\gamma_{\mathrm{C}}) + \sin^2(\gamma_{\mathrm{C}})\right)\\
+\tilde{b}_{\mathrm{F,P}}^{*ZZ}B^{*}\sin^2(\chi_{\mathrm{C}})\cos^2(\gamma_{\mathrm{C}}). \qquad (11.25)
\end{aligned}$$

By inserting these equations together with Eq. (11.17) and Eq. (11.18) into Eq. (11.16),

$$\begin{aligned} |\tilde{b}_{\mathrm{p}}^{Z} &- 0.83\tilde{b}_{\mathrm{p}}^{*Z} \\ &+ (1.7\times 10^{-16}\mathrm{GeV}^2)(\tilde{b}_{\mathrm{F,p}}^{XX}+\tilde{b}_{\mathrm{F,p}}^{YY}) \\ &+ (2.4\times 10^{-16}\mathrm{GeV}^2)\tilde{b}_{\mathrm{F,p}}^{ZZ} \\ &+ (3.7\times 10^{-17}\mathrm{GeV}^2)(\tilde{b}_{*\mathrm{F,p}}^{XX}+\tilde{b}_{*\mathrm{F,p}}^{YY}) \\ &+ (6.9\times 10^{-17}\mathrm{GeV}^2)\tilde{b}_{\mathrm{F,p}}^{*ZZ}| \lesssim 2.1\times 10^{-22}\,\mathrm{GeV} \end{aligned} \tag{11.26}$$

is obtained. The SME coefficients are constrained as described in [43] and derived as listed in Table 11.2. For comparison, the coefficients published in [43] are also listed. The leading coefficients are improved by a factor of 11 and 22, respectively. Note that the g-factor results shown in this thesis are evaluated at 95 % confidence level. In [43], it is assumed that the experimental uncertainties are at 68 % confidence level and to approximate the 95 % confidence level, the coefficients were constrained using twice the quoted uncertainty in a reference [22].

Table 11.2: Derived constraints on the Standard Model Extension parameters by the g-factor measurement.

SME coefficient	[6]	this measurement
$\lvert\tilde{b}_p^Z\rvert$	$< 2\times 10^{-21}\,\mathrm{GeV}$	$< 2.1\times 10^{-22}\,\mathrm{GeV}$
$\lvert\tilde{b}_p^{*Z}\rvert$	$< 6\times 10^{-21}\,\mathrm{GeV}$	$< 2.5\times 10^{-22}\,\mathrm{GeV}$
$\lvert\tilde{b}_{F,P}^{XX}+\tilde{b}_{F,P}^{YY}\rvert$	$< 1\times 10^{-5}\,\mathrm{GeV}^{-1}$	$< 1.2\times 10^{-6}\,\mathrm{GeV}^{-1}$
$\tilde{b}_{F,P}^{ZZ}$	$< 1\times 10^{-5}\,\mathrm{GeV}^{-1}$	$< 8.8\times 10^{-7}\,\mathrm{GeV}^{-1}$
$\lvert\tilde{b}_{F,P}^{*XX}+\tilde{b}_{F,P}^{*YY}\rvert$	$< 2\times 10^{-5}\,\mathrm{GeV}^{-1}$	$< 8.3\times 10^{-7}\,\mathrm{GeV}^{-1}$
$\tilde{b}_{F,P}^{*ZZ}$	$< 8\times 10^{-6}\,\mathrm{GeV}^{-1}$	$< 3.0\times 10^{-6}\,\mathrm{GeV}^{-1}$

Chapter 12

Conclusion and Outlook

During my PhD studies, three independent measurements related to the fundamental properties of the antiproton were carried out by using a cryogenic Penning-trap system:

1. By recording the antiproton reservoir for three months, a new direct lifetime limit of the antiproton is set to > 1.08 years [14].

2. Compared the charge-to-mass ratio of the antiproton and the proton with a fractional precision of 69 p.p.t. [23]. This improves the previous precision [6] and is in agreement with CPT invariance. To date, it is the most precise test of CPT invariance with baryon sector.

3. The antiproton's g-factor is measured with a relative precision of 0.8 p.p.m., which corresponds to a factor of six improvement compared to the previous best value [22]. In this measurement, we applied the continuous Stern-Gerlach effect in a Penning trap where a strong magnetic bottle is superimposed to resolve antiproton spin resonance-frequencies. This result is in agreement with the recent best value of the proton's g-factor [24], as a consequence agrees with CPT invariance and is to date the most precise test of CPT invariance with baryonic vector. Moreover, we improved the direct limit on the g-factor related CPT violating coefficients of the prominent Standard Model Extension by a factor of 11 and 22.

To go beyond these achievements, the following strategies could be applied for the individual measurements (the item numbers below have a one-to-one correspondence to the previous ones):

1. Accumulate more numbers of antiprotons in the reservoir and record for a span of years. With the current understanding of our apparatus, it is possible to store about 100 antiprotons in the reservoir and feasible to keep it trapped for a year. This improves already the lifetime limit approximately by a factor of 100.

2. The FWHM of the obtained ratio distribution shown in Fig. 8.3 (b) is mainly due to the magnetic field fluctuation of the superconducting magnet ($\sim$5.5 p.p.b.) and the voltage fluctuation in the Penning-trap electrodes ($\sim$2.0 p.p.b.). Therefore, it is possible to make the width smaller by implementing a self-shielding coil with a high shielding factor to effectively reduce the magnetic field fluctuation. Concerning the voltage fluctuation, it is also possible to minimise the contribution to the width by measuring cyclotron frequencies with the phase sensitive detection [83–85], which allows us to determine a frequency of interest in several seconds, whereas it typically takes about 30 seconds for our dip detection. Additionally, the decrease on the measurement time consequently increases the number of statistics N of the cyclotron frequency ratio, and in this way decreases the statistical uncertainty by $\propto 1/\sqrt{N}$. Further more, there was a 26 p.p.t. systematic uncertainty which arised from measuring the cyclotron frequency of an antiproton and an H^- ion at a different magnetic field, due to the necessity of tuning the trapping potential to match their axial frequencies to the fixed resonance frequency of the detector. This effect can be eliminated by tuning the magnetic field to higher homogeneity and implementing advanced detector tuning techniques.

3. Application of the double trap method [58] to further improve the precision to the p.p.b. level. The principle of this method is described in section 4.3.

Acknowledgements

In the course of writing this thesis, I have amassed many debts of gratitude. First and foremost, I owe a special debt of gratitude to Dr Stefan Ulmer who leads the BASE (Baryon Antibaryon Symmetry Experiment) multinational collaboration at CERN. It is primarily due to his valued and continuing support that I have been able to produce a high-quality and substantive final PhD thesis. Thanks to Dr Ulmer's encouragement, guidance and investment in my potential, I was able to work within his BASE team at CERN, throughout the course of my PhD. His outstanding knowledge concerning the BASE experiment and physics itself has inspired me and motivated me to become a similarly committed and accomplished physicist. Dr Ulmer is not only an excellent physicist; he is also a skilled and untiring team leader. During my research, Dr Ulmer was always able to find time in his schedule to speak with me should I have any problems or questions. At such times, this was often not a brief discussion and instead continued until I was either satisfied or could be persuaded to pursue another direction in my research. The opportunity to spend these precious hours speaking with such a knowledgeable physicist during my time working within BASE was invaluable and truly transformative for me in the context of my life in science.

I am also very grateful and indebted to Dr Christian Smorra. Thanks to his knowledge, direction and advice, I have been able to learn an immense amount about the BASE experiment. Dr Smorra and I worked within BASE as one of the experiment's initial, core members. As initial members, we formed part of a team that eventually designed and constructed the main BASE apparatus and commissioned the experiments. In this process, we experienced both moments of great elation and moments of seemingly insurmountable difficulty. At those times when we encountered obstacles in the experiment, it was Dr Smorra who kept us motivated. His motivational words and encouragement enabled me to persist and confront the issues we faced. Whilst working on my thesis, Dr Smorra was incredibly generous with his time, and made several excellent suggestions for ways in which I could develop my thesis. Without his valued assistance, I may not have been able to raise the standard of my analysis overall. Needless to say, the times we could share occasional informal moments together and exchange our concerns over a long dinner have also been invaluable and a space for much needed creative exchange.

In order to carry out the extensive data analysis required for this thesis, I also owe an immense debt to the expertise of Dr Stefan Sellner. Dr Sellner's excellent advice and tutorship concerning coding with Mathematica raised the precision and speed of my own analyses. He further instilled in me a great enthusiasm for analysis and the process of simulating experiments with Mathematica. Dr Sellner also has a clear passion and talent for baking and for holding fantastic social events. From time to time, Dr Sellner organised wonderful gatherings and coffee breaks for our BASE group members. At those parties he entertained us with his delicious homemade cakes. I believe it is thanks to Dr Sellner's cake that a strong bond has formed between us all.

I am further indebted to Mr Takashi Higuchi. As fellow Tokyo University PhD students and Junior Research Associates at RIKEN (Saitama, Japan), we have offered each other both moral support and academic counsel during our time in Geneva. Mr Higuchi has shown a great deal of enthusiasm concerning our experiment and especially our simulations. His contributions to our group discussions have been consistently interesting and filled with passion. I have truly enjoyed working alongside him.

My other huge debt is to another friend and colleague, Mr James Harrington. Mr Harrington joined the BASE team as a PhD student after I had just completed the main project for my PhD. In other words, my focus at this time became directed at my writing and the trials and tribulations that can entail; particularly as someone writing in a second language. Throughout this period, Mr Harrington kindly assisted me with my writing and offered helpful suggestions concerning some of my common errors in English. His great passion for physics has also had a huge impact on me and has fired up my own ardour for the subject. It has been wonderful spending time with Mr Harrington and working alongside him at CERN.

I am further grateful to Mr Matthias Borchert with whom I spent many hours working in the laboratory to develop our central, experimental devices. We shared a very happy moment together at CERN one night, when we found the very first particle signal in the analysis trap at the antiproton decelerator facility. Without his stamina and kind support during the CERN's Christmas shutdown period in 2015, this completed PhD might well not have been possible. It has been an invaluable time working with him within BASE.

My thanks go too, to Mr Toya Tanaka. Mr Tanaka's friendly and warm personality brought much happiness to our days working together at CERN. We had many enthusiastic discussions together regarding the axial detection systems, which are crucial for our experiment. These discussions often continued over into dinner in the CERN canteen. Mr Harrington would also join us there and our conversations often offered up new possibilities for developments in our experiment.

Beyond CERN, I owe a significant debt of gratitude to Dr Yasuyuki Matsuda, my official supervisor in the Matsuda group at the University of Tokyo, Japan. Without his cooperation, it would not have been possible for me to have had to opportunity to work within the BASE team. Dr Matsuda gave me extensive and invaluable advice regarding this thesis, which was exceptionally helpful and allowed to take a proper shape. I would like to offer my immense thanks to him again, for his long and continuing support throughout my graduate studies. Within the Matsuda group at the University of Tokyo, I would also like to thank Dr Hiroyuki Torii and Dr Naofumi Kuroda. They have guided me and supported me across both my Master's degree and PhD and offered me a great deal of advice concerning my research.

Finally, I remain indebted to all the BASE members at the University of Mainz, and the Matsuda group; summer students of BASE; members of ASACUSA; and the secretaries of Ulmer Initiative Research Unit at RIKEN.

I would like to conclude this acknowledgement by thanking my family, friends and fiancée, who have offered me their constant love and encouragement during the course of my PhD studies.

References

[1] M. Dine and A. Kusenko. Origin of the matter-antimatter asymmetry. *Rev. Mod. Phys.*, **76**(1), 2003.

[2] G. Lüders. Proof of the TCP theorem. *Annals of Physics*, **2**(1), 1957.

[3] R. Van Dyck Jr, P. Schwinberg, and H. Dehmelt. New high-precision comparison of electron and positron *g* factors. *Phys. Rev. Lett.*, **59**(26), 1987.

[4] B. Schwingenheuer *et al.* CPT tests in the neutral Kaon system. *Phys. Rev. Lett.*, **74**(4376), 1995.

[5] J.P. Miller, E. De Rafael, and B.L. Roberts. Muon (g-2) experiment and theory. *Rep. Prog. Phys.*, **70**(795), 2007.

[6] G. Gabrielse, A. Khabbaz, D. Hall, C. Heimann, H. Kalinowsky, and W. Jhe. Precision mass spectroscopy of the antiproton and proton using simultaneously trapped particles. *Phys. Rev. Lett.*, **82**(3198), 1999.

[7] M. Hori *et al.* Two photon laser spectroscopy of antiprotonic helium and the antiproton to electron mass ratio. *Nature*, **475**(484), 2011.

[8] M. Ahmadi *et al.* An improved limit on the charge of antihydrogen from stochastic acceler ation. *Nature*, **529**(373), 2016.

[9] V.A. Kostelecký and N. Russell. Data-tables on Lorentz and CPT Violation. *Rev. Mod. Phys.*, **83**(11), 2011.

[10] ALICE Collaboration. Precision measurement of the mass difference between light nuclei and anti-nuclei. *Nat. Phys.*, **11**(811814), 2015.

[11] N. Kuroda *et al.* A source of antihydrogen for in-flight hyperfine spectroscopy. *Nat. Commun.*, **5**(3089), 2014.

[12] C. Amole *et al.* The ALPHA antihydrogen trapping apparatus. *Nucl. Instr. Meth. Phys. Res. A*, **735**(319), 2014.

[13] C. Smorra *et al.* The BASE Experiment. *Eur. Phys. J. S.T.*, **224**(3055), 2015.

[14] C. Smorra *et al.* A reservoir trap for antiprotons. *Int. J. Mass Spectrom.*, **389**(10), 2015.

[15] H. Nagahama *et al.* Highly sensitive superconducting circuit at $\sim$700 kHz with tunable quality factors of image-current detection of single trapped antiprotons. *Rev. Sci. Instrum.*, **87**(113305), 2016.

[16] K. Blaum. High-accuracy mass spectrometry with stored ions. *Phys. Rep.*, **425**(1), 2006.

[17] E.G. Myers. The most precise atomic mass measurements in Penning traps. *Int. J. Mass Spectrom*, **349-350**(107), 2013.

[18] L. Gastaldo *et al.* The Electron Capture ^{163}Ho Experiment ECHo. *J. Low Temp. Phys.*, **176**(876), 2014.

[19] S. Rainville *et al.* World year of physics: A direct test of $e = mc^2$. *Nature*, **438**(1096), 2005.

[20] A. Wagner *et al.* g factor of Lithiumlike Silicon Si^{11+}. *Phys. Rev. Lett.*, **110**(033003), 2013.

[21] S. Sturm *et al.* High-precision measurement of the atomic mass of the electron. *Nature*, **506**(476), 2014.

[22] J. DiSciacca *et al.* One-particle measurement of the antiproton magnetic moment. *Phys. Rev. Lett.*, **110**(130801), 2013.

[23] S. Ulmer *et al.* High-precision comparison of the antiproton-to-proton charge-to-mass ratio. *Nature*, **524**(196), 2015.

[24] A. Mooser *et al.* High-precision measurement of the magnetic moment of the proton. *Nature*, **509**(596), 2014.

[25] H. Nagahama *et al.* Sixfold improved single particle measurement of the magnetic moment of the antiproton. *Nat. Commun.*, **8**(14084), 2017.

[26] I. Estermann and O. Stern. Über die magnetische Ablenkung von Wasserstoffmoleklen und das magnetische Moment des Protons. i. *Z. Phys. a: Hadrons Nucl.*, **85**(4), 1933.

[27] R. Frisch and O. Stern. Über die magnetische Ablenkung von Wasserstoffmoleklen und das magnetische Moment des Protons. ii. *Z. Phys. a: Hadrons Nucl.*, **85**(17), 1933.

[28] J.M.B. Kellogg, I.I. Rabi, N.F. Ramsey, and J.R. Zacharias. The Magnetic Moments of the Proton and the Deuteron. The Radiofrequency Spectrum of H_2 in Various Magnetic Fields. *Phys. Rev.*, **56**(728), 1939.

[29] E. M. Purcell, H. C. Torrey, and R. V. Pound. Resonance Absorption by Nuclear Magnetic Moments in a Solid. *Phys. Rev.*, **69**(37), 1946.

[30] F. Bloch, W.W. Hansen, and M. Packard. Nuclear Induction. *Phys. Rev.*, **69**(127), 1946.

[31] H.M. Goldenberg, D. Kleppner, and N.F. Ramsey. Atomic hydrogen maser. *Phys. Rev. Lett.*, **5**(361), 1960.

[32] H.M. Goldenberg, D. Kleppner, and N.F. Ramsey. Absolute Value of the Proton g Factor. *Phys. Rev. Lett.*, **17**(405), 1966.

[33] P.F. Winkler, D. Kleppner, T. Myint, and F.G. Walther. Magnetic Moment of the Proton in Bohr Magnetons. *Phys. Rev. A*, **5**(83), 1972.

[34] P.J. Mohr, B.N. Taylor, and D.B. Newell. CODATA recommended values of the fundamental physical constants: 2010. *Rev. Mod. Phys.*, **84**(1527), 2012.

[35] A. Mooser *et al.* Demonstration of the double Penning Trap technique with a single proton. *Phys. Lett. B*, **723**(78), 2013.

[36] A. Kreissl *et al.* Remeasurement of the magnetic moment of the antiproton. *Z. Phys. C*, **37**(557), 1988.

[37] T. Pask *et al.* Antiproton magnetic moment determined from the HFS of $\bar{p}He^+$. *Phys. Lett. B*, **678**(55), 2009.

[38] H.G. Dehmelt and P. Ekström. Continuous Stern-Gerlach effect: Principle and idealized apparatus. *Proc. Natl. Acad. Sci.*, **83**(2291), 1986.

[39] D. Colladay and V.A. Kostelecký. CPT violation and the standard model. *Phys. Rev. D*, **55**(6760), 1997.

[40] V.A. Kostelecký and S. Samuel. Spontaneous breaking of lorentz symmetry in string theory. *Phys. Rev. D*, **39**(683), 1989.

[41] V.A Kostelecký and R. Potting. CPT and strings. *Nucl. Phys. B*, **359**(545), 1991.

[42] V.A Kostelecký and R. Potting. CPT, strings, and meson factories. *Phys. Rev. D*, **51**(3923), 1995.

[43] Y. Ding and V.A. Kosteleck y. Lorentz-violating spinor electrodynamics and Penning traps. *Phys. Rev. D*, **94**(056008), 2016.

[44] L.S. Brown and G. Gabrielse. Precision spectroscopy of a charged particle in an imperfect Penning trap. *Phys. Rev. A.*, **25**(2423), 1982.

[45] L.S. Brown and G. Gabrielse. Geonium theory: Physics of a single electron or ion in a Penning trap. *Rev. Mod. Phys.*, **58**(233), 1986.

[46] G. Schneider. Development of a Penning trap system for the high precision measurement of the antiprotons magnetic moment. Master's thesis, The University of Mainz, 2014.

[47] J. Johnson. Thermal Agitation of Electricity in Conductors. *Phys. Rev.*, **32**(97), 1928.

[48] H. Nyquist. Thermal Agitation of Electric Charge in Conductors. *Phys. Rev.*, **32**(110), 1928.

[49] E.A. Cornell, R.M. Weisskoff, K.R. Boyce, and D.E. Pritchard. Mode coupling in a Penning trap: π pulses and a classical avoided crossing. *Phys. Rev. A*, **41**(213), 1990.

[50] J. Verdù. *Ultrapräzise Messung des elektronischen g-Faktors in wasserstoffähnlichem Sauerstoff.* PhD thesis, The University of Mainz, 2003.

[51] H. Häffner. *Präzisionsmessung des magnetischen Moments des Elektrons in wasserstoffähnlichem Kohlenstoff.* PhD thesis, The University of Mainz, 2000.

[52] H. Dehmelt, W. Nagourney, and J. Sandberg. Self-excited mono-ion oscillator. *Proc. Natl. Acad. Sci. U. S. A.*, **83**(5761), 1986.

[53] B. D'Urso, B. Odom, and G. Gabrielse. Feedback Cooling of a One-Electron Oscillator. *Phys. Rev. Lett.*, **90**(043001), 2003.

[54] S. Ulmer. *First Observation of Spin Flips with a Single Proton Stored in a Cryogenic Penning Trap.* PhD thesis, The University of Heidelberg, 2011.

[55] S. Ulmer *et al.* Observation of spin flips with a single trapped proton. *Phys. Rev. Lett.*, **106**(253001), 2011.

[56] L.S. Brown. Geonium lineshape. *Ann. Phys.*, **159**(62), 1985.

[57] I. Rabi, J. Zacharias, S. Millman, and P. Kusch. A New Method of Measuring Nuclear Magnetic Moment. *Phys. Rev.*, **53**(318), 1938.

[58] H. Häffner *et al.* Double Penning trap technique for precise g factor determinations in highly charged ions. *Eur. Phys. J. D - At. Mol. Opt. Plas. Phys.*, **22**(163), 2003.

[59] S. Maury. The Antiproton Decelerator: AD. *Hyp. Int.*, **109**(43), 1999.

[60] M. Benedikt *et al.* LHC Design Report, CERN-2004-003-V-3., 2004.

[61] T. Higuchi. High precision measurement of the cyclotron frequency of the single-trapped antiproton. Master's thesis, The University of Tokyo, 2015.

[62] T. Higuchi. *To be submitted.* PhD thesis, The University of Tokyo, 2018.

[63] W. Thompson and S. Hanrahan. Characteristics of a cryogenic extreme highvacuum chamber. *J. Sci. Vac. Technol*, **14**(643), 1977.

[64] M.H. Holzscheiter. Slowing down and trapping of MeV antiprotons. *Physica Scripta*, **46**(272), 1992.

[65] J.F. Ziegler. Stopping of energetic light ions in elemental matter. *J. Appl. Phys.*, **85**(1249), 1999.

[66] G. Gabrielse *et al.* Barkas effect with use of antiprotons and protons. *Phys. Rev. A*, **40**(481), 1989.

[67] G. Gabrielse, L. Haarsma, and L.S. Rolston. Open-endcap Penning traps for high precision experiments. *Int. J. Mass Spec*, **88**(319), 1989.

[68] C.C. Rodegheri *et al.* An experiment for the direct determination of the *g*-factor of a single proton in a Penning trap. *N. J. Phys.*, **14**(063011), 2012.

[69] S. Ulmer *et al.* The quality factor of a superconducting rf resonator in a magnetic field. *Rev. Sci. Instrum.*, **80**(123302), 2009.

[70] Y. Shapira and L.J. Neuringer. Upper Critical Fields of Nb-Ti Alloys: Evidence for the Influence of Pauli Paramagnetism. *Phys. Rev.*, **140**(A1638), 1965.

[71] W. Buckel and R. Kleiner. *Superconductivity: Fundamentals and Applications.* Wiley-VHC, 2004.

[72] H. Nagahama. Development of Low Noise Electronics for the Measurement of the Magnetic Moment of the Antiproton. Master's thesis, The University of Tokyo, 2014.

[73] W.W. Macalpine *et al.* Coaxial Resonators with Helical Inner Conductor. *Proc. IRE*, **47**(2099), 1959.

[74] S. Ulmer *et al.* A cryogenic detection system at 28.9 Mhz for the non-destructive observation of a single proton at low particle energy. *Nucl. Instr. meth. Phys. Res. A*, **705**(55), 2013.

[75] S. Ulmer *et al.* Letter of Intent to the CERN SPSC., 2012.

[76] J.K. Thompson, S. Rainville, and D.E. Pritchard. Cyclotron frequency shifts arising from polarization forces. *Nature*, **430**(58), 2004.

[77] C.G. Parthey *et al.* Improved measurement of the hydrogen 1S-2S transition frequency. *Phys. Rev. Lett.*, **107**(203001), 2011.

[78] A.K. Bhatia and R.J. Drachmann. Polarizability of helium and the negative hydrogen ion. *J. Phys. B: At. Mol. Optl. Phys.*, **27**(1299), 1994.

[79] L.D. Landau and E.M. Lifshitz. *Mechanics -Course of Theoretical Physics, Volume 1-*. Butterworth-Heinemann, 1976.

[80] T.A. Savard, K.M. O'Hara, and J.E. Thomas. Laser-noise-induced heating in far-off resonance optical traps. *Phys. Rev. A*, **56**(R1095), 1997.

[81] A. Mooser. Untersuchung des Magnetfelds zur Spinflipanregung eines Protons in einer Penningfalle. Master's thesis, The University of Mainz, 2009.

[82] R. Bluhm, V.A. Kostelecký, and N. Russell. CPT and Lorentz tests in Penning traps. *Phys. Rev. D.*, **57**(3932), 1998.

[83] E.A. Cornell *et al.* Single-ion cyclotron resonance measurement of $M(CO^+)/M(N_2^+)$. *Phys. Rev. Lett.*, **63**(1674), 1989.

[84] S. Stahl *et al.* Phase-sensitive measurement of trapped particle motions. *J. Phys. B*, **38**(297), 2005.

[85] S. Sturm, A. Wagner, B. Schabinger, and K. Blaum. Phase-Sensitive Cyclotron Frequency Measurements at Ultralow Energies. *Phys. Rev. Lett.*, **107**(143003), 2011.